UNIVERSITÀ DEGLI STUDI DI MODENA E REGGIO EMILIA

Facoltà di Scienze Matematiche, Fisiche e Naturali

Tesi per il conseguimento del titolo di Dottore di Ricerca in Fisica

Engineering Silicon Nanostructures: theoretical study of the effects of doping with Boron and Phosphorus

Candidate:

Federico Iori

Supervisors:

Prof. Stefano Ossicini
Dott.ssa Elena Degoli

Coordinators:

Prof. Stefano Frabboni
Prof. Stefano Ossicini

DOTTORATO DI RICERCA IN FISICA XX CICLO - Dicembre 2007

Ai miei genitori Gisella e Umberto,
ai nonni Benilde e Gino,
a Francesca.
La mia Famiglia.

Contents

Contents 7

Preface 9

1 Introduction 13
1.1 The Silicon Connection . . . 13
1.2 Let be there Light, let be there Silicon! . . . 17
1.3 Doping goes to nano . . . 19
1.4 Physical Properties of undoped SiNC . . . 22
1.5 Physical Properties of undoped SiNW . . . 24

2 Density Functional Theory 25
2.1 The Many-Body Problem . . . 25
2.2 Another brick in the wall: a brief DFT survey . . . 29
2.2.1 The form of E_{xc} . . . 36
2.2.2 The Meaning of Kohn-Sham eigenvalues . . . 45
2.3 The Plane Wave Pseudopotential approach . . . 51
2.4 Excited states in DFT . . . 64

3 Many Body Perturbation Theory: "a stairway to heaven" 67
3.1 Theoretical Spectroscopies . . . 67
3.1.1 External Perturbation and dielectric function . . . 68
3.1.2 Electronic Spectra in practice . . . 75
3.2 Quasiparticles and Green Functions approach . . . 76
3.2.1 Quasiparticle representation and Spectral Function . . . 78
3.2.2 An "alchemic circle": the Hedin's pentagon . . . 80
3.2.3 The GW Approximation . . . 82
3.3 The Bethe-Salpeter approach . . . 83

4 The Systems 89
4.1 Model System . . . 89
4.2 Formation Energy . . . 91
4.3 What about doping Silicon Nanocrystals? . . . 92
4.4 Codoping: Structural Properties . . . 96
4.5 Codoping: Formation Energy . . . 103

5 Back to the future: OptoElectronics 111
5.1 Electronic Properties . . . 111
5.2 Optical Properties . . . 125
5.2.1 Computational details . . . 126
5.2.2 Absorption and Emission: RPA results . . . 129
5.2.3 Absorption, Emission and Stokes Shift: IP-RPA results 135
5.2.4 Absorption, Emission and Stokes shift: Many-Body results . . . 141

6 Multidoping... is better 145
6.1 The systems . . . 145
6.2 Structural properties and Formation Energy . . . 147
6.3 Electronic structure . . . 150
6.4 Optical Absorption . . . 153

7 Codoped Silicon Nanowires 157
7.1 The systems . . . 158
7.2 Formation Energy . . . 162
7.3 Electronic Properties . . . 171
7.4 Optical Features . . . 180
7.4.1 Many Body Absorption Spectra . . . 186

Conclusions 189

Curriculum Vitae 193

Full list of publications 199

Bibliography 201

Preface

Bisogna esser duri senza perder mai la tenerezza.

ERNESTO GUEVARA DE LA SERNA

The great amount of breakthroughs in Silicon-based technology in the last decade has switched the traditional electronic branch into a new fascinating research field: the Silicon Photonics. Squeezing of light out of Silicon is becoming one of the most intriguing task of the Silicon research field: in particular because over the past few years the trend of continued down-scaling of the "traditional" Silicon integrated circuits to increase speed is reaching the limit. Thus the necessity to speed up the level of *communications* has been dictated not only by the digital processing of information or by the developing of interconnections to carry the information, but also simply by the requirement to *communicate* between people all around the world; this has determined an acceleration to improve the interface between the *traditional Silicon electronics* and the newest *Silicon Photonics*, a very challenging task, high on the agenda in the field of optoelectronics. Propelled by pioneering research conducted in the 1980s and 1990s, **Silicon photonics** has enjoyed spectacular progress in particular in the past decade.

Several recent papers confirm that Silicon-based active optical components are nowadays becoming reliable and interesting in order to leverage the infrastructure of Silicon microelectronics technology for the fabrication of optoelectronic devices. Moving towards dimension of just few nanometers seems to be the ultimate and very useful way to overcome the physical limitations of overlapping electrical fields and current leakage of the two-dimensional field-effect transistors. New devices incorporating Silicon

nanostructures (like nanocrystals, nanowires, nanorods) have attract effort of research for their optical features in the photonics and Nanophotonics branch.

Aim of this PhD thesis work will be the investigation of the role played by doping with donor and acceptor impurities like Boron and Phosphorous Silicon based nanostructures, like Silicon nanocrystals and nanowires. Doping - the intentional introduction of impurities into a material is fundamental to control the properties of bulk semiconductors, and also to engineer the electronic and optical properties of nanocrystals and nanowires for optoelectronic applications. Doping Silicon nanostructures can be an useful tool in order to render the emission of light from nanocrystals and nanowires more efficient, bypassing through the insertion of acceptor and donor impurities several competitive processes, like the absorption of free carriers and the Auger non radiative recombination of electron-hole pairs, that quench and degrade the emission of light from these Silicon nanostructures.

Till now very few theoretical works about doping Silicon nanocrystals and nanowires are appeared in literature and the majority concerns the single doping of nanostructures for transport applications. Aim of this research will be therefore the study of the effects produced by **codoping simultaneously with Boron and Phosphorus Silicon nanocrystals and nanowires**. Supported by the recent experimental outcomes by Minoru Fujii and coworkers on the possibility to tune the photoluminescence emission from codoped Silicon nanocrystals, we performed the **first theoretical *ab initio* study** based on a *plane wave pseudopotential method* on **codoped Silicon nanostructures** focusing the attention on how the codoping modifies the stability and the structures of nanoclusters and nanowires and how the electronic and optical features can be engineered according to the experimental evidence.

The thesis is organized as follow: after a brief Introduction which describes the technological and scientific interests that lies behind the Silicon Nanostructures, in the First and Second Chapter will be described the theoretical background on which are based the present first principle calculations, moving from the basic knowledge of DFT to the Many Body Perturbation Theory framework; moreover the codoped Silicon Nanocrystals will be describe in terms of Formation Energy and Structural Stability in Chapter Three, pointing out the effects of doping on electronic and optical properties on Chapter Four. More specifically, for the first time it has been performed an ab initio calculation of the emission spectrum for one of the codoped nanocrystals studied, comparing the IP-RPA spectra with the one obtained through the Many-Body approach by including GW corrections and excitonic effect via

Bethe-Salpeter equation. Next the attention will be focused in Chapter Five on multidoped Silicon Nanocrystals, with more than two impurities inserted into the core. Finally the Chapter Six will be devoted to the description of codoped Silicon Nanowires of different diameters and unit cell size in terms of electronic and optical IP-RPA absorption.

1 Introduction

Zemian!
tgnirev strec a cla piopa
elta, saca e slanzeda
chl a-s ciama Ghirlandeina

SANDRONE, FAMIGLIA PAVIRONICA

1.1 The Silicon Connection

Silicon, the second most abundant element (after oxygen) in the Earth crust, making up 25.7% of the crust by mass, is one of most (probably the absolute) striking material for electronic and technological applications. Silicon has be defined the material where *the extraordinary is made ordinary* [1], where enormous performance improvements and manufacturing cost reductions over the last fifty years have been coupled by the basic research field and the applied one. Thus integration and economy of scale are the two keys ingredient for the Silicon technological success, as demonstrated since the early 1947 when the "electronic age" started with the invention of the *transistor* by J. Bardeen, W. H. Brattain and W. B. Shockley then has become a reality when the first electronic integrated circuit was developed by J. S. Kilby in 1957.

Silicon has thus become the leading and most prominent building-block material for electronics. Silicon has an indirect band-gap of 1.12 eV that is ideal for room temperature operation and an oxide SiO_2 that allows the processing flexibility to place today more than 10^9 devices on a single chip. However all the single transistors and electronic devices have transferred information to length scale which are relevant with respect to their

nanometric scale. Pushing down the dimension of Silicon-based devices toward the nanometric scale determines an high concentration of transistor on a single Silicon crystal (around 200 mm for the moment) that have permitted with an high integration level high-speed device performances and unprecedented interconnection levels. As the famous empirical law coined by Gordon Moore in 1960 asserts, *the number of transistors on an integrated circuit would be double every 12 months (lately corrected to 18 months)* (see Fig. 1.1) and at the same time the chip interconnections length (15 Km of connection today, 91 till ten years!) and the power density (too high to keep the components at low working temperature) supplied by the components will increase uncontrolled.

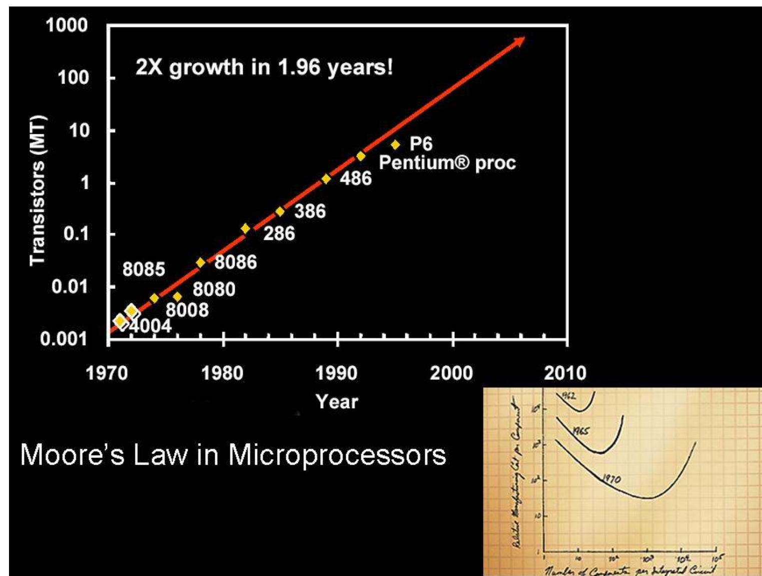

Figure 1.1: The Moore's law: number of transistor integrated from 1970's to nowadays and the hand-sketched note by G. Moore. This empirical trend will saturate if either new technologies in Integrated Circuits (IC) are going to be introduced or new devices concepts developed (*Courtesy of Intel*).

The present interconnection degree is sufficient to cause interconnect propagation delays, overheating and information latency between single devices, generating the so-called **interconnection bottleneck**, depicted in Fig. 1.2 . Overcome these problematic is together the main motivation and opportunity for the present-day Silicon microphotonics, where attempts to combine photonics and electronic components on a single Si chip or wafer are strongly pursued. In addition, photonics aims to combine the power of Silicon microelectronics with the advantages of photonics: the challenge

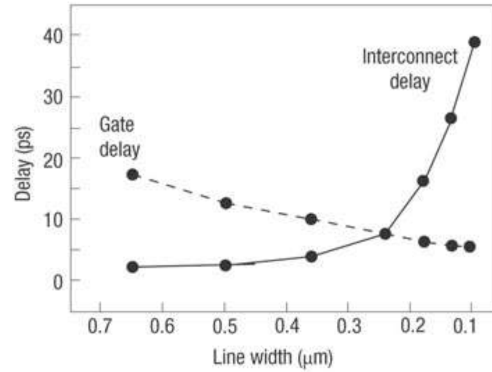

Figure 1.2: Trends in transistor gate delay (switching time) and interconnect delay (propagation time for an aluminium/Silicon dioxide system) with IC fabrication technology. The crossover point represents the start of the **interconnect bottleneck**, where optical technology could have come to the rescue. With copper wires and advanced dielectric materials, the crossover happened at a linewidth of 0.18 μm, from [2].

is to turn Silicon into the ***photonics material*** per excellence where the convergence between electronic and photonics is realized, to make the extraordinary happen again in Silicon.

Silicon photonics has boomed in recent years and all the various photonics devices have been demonstrated, focusing in particular the attention to the emitting, guiding and modulating light features that could be the key to creating short-distance ultrafast optical interconnects for data communication applications: Si-based optical waveguides with extremely low losses and small curvature radii [3], tuneable optical filters, fast switches (ns) [4] and fast optical modulators (GHz)[5], fast CMOS photodetectors [6], integrated Ge photodetectors for 1.55 μm radiation [7, 8] are only a little fraction of the new promising generation technology.

The main difficult that slows the progress is nowadays the lack of practical *Si-based light sources*, such as efficient Si light emitting diodes (LED) or all Si injection lasers. Thus since Silicon is an indirect band-gap material, light emission is a phonon-mediated process with low probability (spontaneous recombination lifetimes are in the *ms* range) and with low intensity emission in the near infrared. Moreover, in bulk Silicon, the competitive non-radiative recombination rates are much higher than the radiative ones and most of the excited e-h pairs recombine non-radiatively. This yields very low internal quantum efficiency ($\eta_i \approx 10^{-6}$) for bulk Silicon luminescence. In addition, fast non-radiative processes such as Auger or free carrier

absorption processes severely prevent population inversion for Silicon optical transitions at the high pumping rates which is instead needed to achieve optical amplification.

Despite of all, during the nineties many different strategies have been employed to overcome these materials limitations. The most successful ones are based on the exploitation of **low dimensional Silicon structures** where the electronic properties of free carriers are modified by quantum confinement effects [9, 10].

1.2 Let be there Light, let be there Silicon!

The roadmap for Si photonics has been traced but is only with several recent breakthrough in the last decade that the exploitation of optical phenomena in Silicon on the nanoscale, Silicon nanophotonics, is opening up a diverse field of study that promises to deliver technological solutions. The way to achieve light from Silicon and more important, to increase the emission efficiency of Silicon is to turn it into a low dimensional material and, hence, to exploit quantum confinement effects to increase the radiative probability of carriers. The first attempt has been pioneered in 1990 (by chance at the beginning) by the work of L. Canham which showed that when Silicon is partially etched in an HF solution via an electrochemical attack, the surviving structure is formed by small nanocrystals and nanowires which show bright red luminescence at room temperature [11]. This material, assimilated to a "quantum sponge", is called Porous Silicon, shown in Fig. 1.3 and it has been deeply studied since its discover [12, 13]. The explanation of

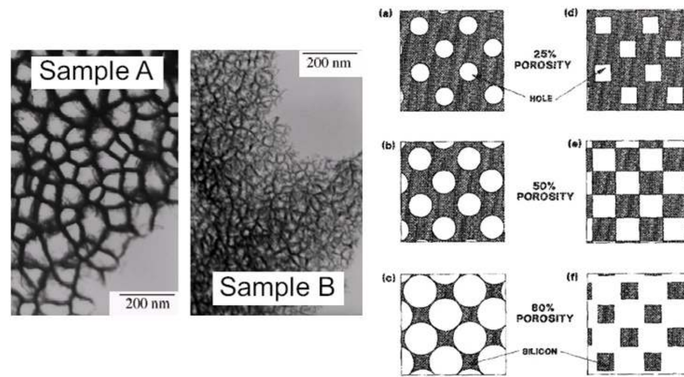

Figure 1.3: Porous Silicon sample at TEM on the left, and scheme of the different level of porosity which gives rise to different confined nanostructures (from [11]).

the observed high luminescence internal quantum efficiency was: i) quantum confinement which leads to an enlargement of the band-gap and to an increased recombination probability, ii) the spatial confinement of the free carriers which prevent them to reach non radiative recombination centers, iii) the reduction of the refractive index of the material which increases the extraction efficiency via refractive index matching. This result has motivated many research efforts in order to exploit these properties in visible light emitting devices such as LED based on Porous Silicon [14].

Furthermore one of the main point of attraction on Silicon photonics lies in the possibility to achieve not only light from Silicon-based devices, but prominently to achieve *gain of light* from this dispositive, as shown in Fig. 1.4. In particular great attention has been payed to Silicon nanostruc-

Figure 1.4: Left: first light from Silicon. Nanocrystalline Silicon emits red light when stimulated by an argon-ion laser (green light). Right: experimental setup to observe emission of visible light from Silicon Nanocrystals.

tures such as Silicon nanocrystals (Sinc) and nanowires (Sinw) (in Fig. 1.5) since the first **optical gain** in Sinc has been demonstrated by Lorenzo Pavesi and coworker in 2000 [15]. By firing high-energy Silicon ions into quartz (Silicon dioxide), and then heating the material to 1100 C, Pavesi and his colleagues generated Silicon particles about 3 nm across that were embedded in the quartz. These researchers showed that not only do the nanocrystals emit red light when energized with a laser beam, but they can also amplify a 'probe' beam of the same wavelength as the emission. Known as **optical gain**, this phenomenon is one of the fundamental features of laser emission. Sinc embedded in silica matrix have shown strong photoluminescence emission and in particular the possibility to gain as a measure of amplified spontaneous emission or as a superlinear increase of the luminescence intensity or as probe amplification in transmission experiments under high pumping excitation [16, 17, 18]. Light emission has not been observed only in Porous Silicon [19, 12, 20], but also in low dimensional Si systems such as Silicon nanocrystals [21], Silicon/insulator superlattices [22, 23] and Silicon nanopillars [24].

Moreover by considering from the early experimental outcomes of Canham the Porous Silicon as a substance made up of a network of nanowires, also these one-dimensional systems has attracted the attention of research. Illuminating Silicon nanowires with laser light to create pairs of negative and positive charge carriers determines suddenly Porous Silicon glows with visible light; this process has revealed to be 10,000 times more efficient in the nanowires than in normal Silicon. Nanowires such as nanocrystals have thus found application for new photonics devices, such as LED: several experimental groups have been able to build crossed-wire p-n junctions that efficiently emit light in the visible region [25, 26, 27].

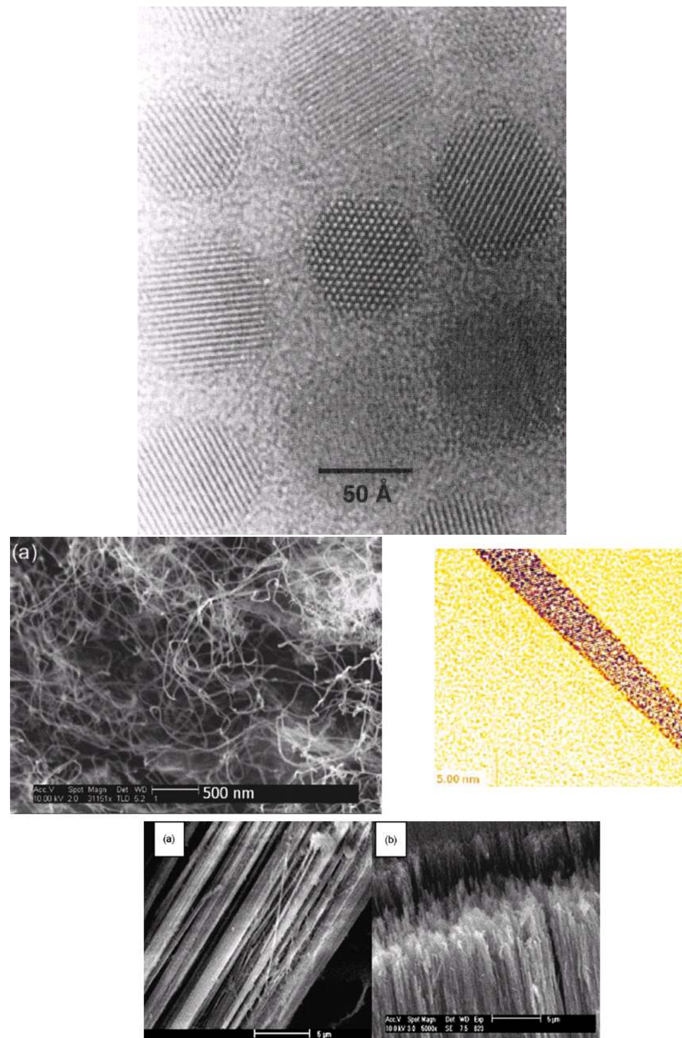

Figure 1.5: Top: TEM image of Silicon nanocrystals embedded in an oxide matrix. Bottom: TEM and SEM images of bunch of Silicon nanowiress.

1.3 Doping goes to nano

Although the great effort in the research for a Si based emitting light source and even if it has been found that Si nanocrystals band-gap increases with decreasing size with a luminescence external efficiency in excess of 23%, Si nanocrystals (Sinc) still have a memory of the indirect band gap of the bulk phase and this is evidenced by the clearly observed structures related to momentum-conserving phonons [28, 29]. Although in Silicon nanocrystals the quantum confinement breaks the **k**-vector selection rule and allows direct radiative transitions even without phonon assistance, the calculated radiative lifetime remains long, more than 10 μs, for Sinc

containing more than 20 atoms as confirmed by theoretical [30] and experimental [31] evidence. Since the Auger lifetimes τ lie between 10^{-1} and 10^{2} nanoseconds (ns), these non radiative recombination process are much faster and more competitive than the radiative ones. This drawback can be circumvented by *doping* Silicon nanostructures, thus by introducing *isoelectronic* [32] or *n*- and *p*- type impurities [29, 12, 33] within both nanocrystals and nanowires in order to sustain more the radiative transitions and diminish the competitive quenching action of the Auger decay processes.

Yet impurities play a central role in semiconductor technology. Performance of a semiconductor device is dictated by shallow dopants. Shallow dopants like Boron (B) and Phosphorus (P) alter the conductivity of bulk Silicon by several orders of magnitude. Deep defects, on the other hand, are known to degrade device performance. These properties are expected to be significantly altered in highly confined systems such as Sinc. Important questions arise as to whether dopants will continue to play a role similar to that in bulk semiconductors and whether new applications will become possible. Experimental studies of impurities in Sinc have been slow to address such issues, the major part due to difficulties in preparation of samples in a controllable manner. To date, efforts have focused almost exclusively on: (i) studies of Boron-doped or Phosphorus-doped Si nanowires [34, 35], materials that have enabled the assembly and fabrication of field-effect transistors and biosensors, and (ii) the possible control of the photoluminescence properties of Si nanodots by n- and p-type impurities [36, 37]. Concerning these experiments several questions are still open: in some cases a very low conductivity is measured, thus it is not clear whether or not the doping of Sinc provides a generation of free charge carriers. In the case of Si nanowires a decrease in mobility with decreasing dopant concentration has been observed that contrasts the usual behaviour in bulk Si, where increase in dopant concentration leads to increased scattering and a reduction in mobility; it is not clear if this effect is intrinsic or not to the one-dimensional geometry of the wires.

In the last years the experimental group of Minoru Fujii has demonstrated that the *simultaneously* insertion of *n*- and *p*- type impurities, such as Boron and Phosphorus, within the Silicon nanocrystals tends to suppress the PL quenching that normally arise in undoped Sinc or when stand-alone donor or acceptor impurity are individually present [36, 37, 38]. It has been demonstrated infact by Kovalev and coworkers [39] that, when single donor or acceptor impurities are present within the nanocrystals, due to the spatial localization of excitons in the vicinity of neutral impurities the effective concentration of the carriers (two photogenerated + one intrinsic) is very high on the order of 10^{18} to 10^{19} cm^{-3}: at these concentrations the most effective recombination mechanism in Si is the Auger process. Thus the crystallites

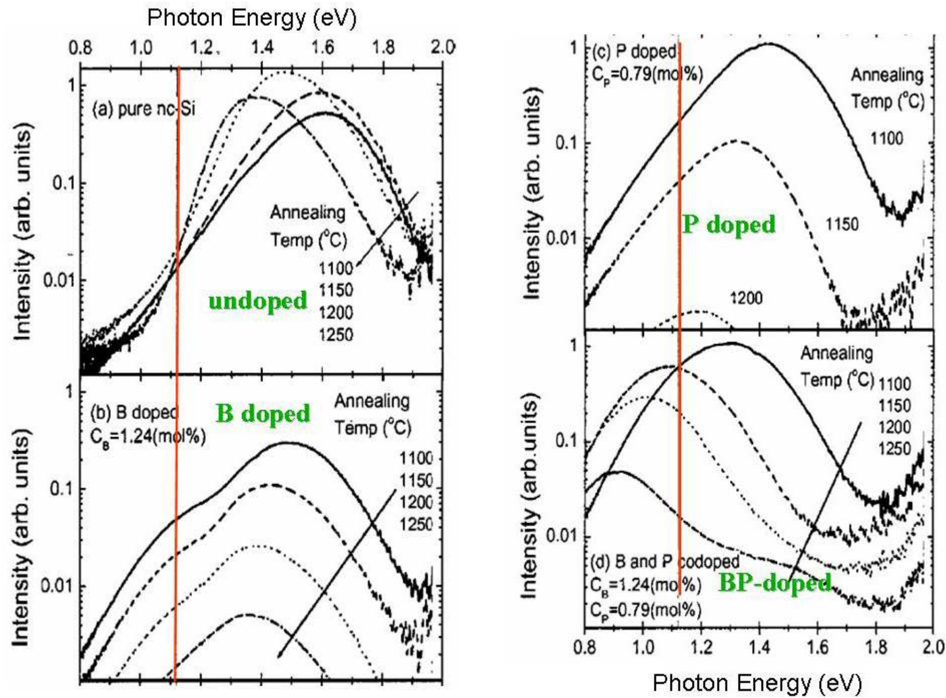

Figure 1.6: Annealing temperature dependence of (a) pure nc-Si, (b) B-doped nc-Si (left side) and (c) P-doped nc-Si, and (d) B- and P-codoped nc-Si (right side). All spectra are taken at the same condition. The vertical red line is drawn at the band-gap energy of bulk Si crystals s1.12 eV.

containing a single shallow impurity are ”dark” [33, 40, 41].

By simultaneously doping Silicon nanocrystals instead, Fujii demonstrate that PL properties of P and B codoped Sinc’s assemblies have the PL maximum below the band-gap energy of bulk Si crystals and also that the mechanism of the PL is different from that of pure Sinc’s. Under resonant PL excitation condition, impurity codoped samples exhibit quite different PL spectra from those of pure Sinc’s.

In particular B and P codoping suppress the quenching of photoluminescence that occurs when only Boron or Phosphorus are singularly present; furthermore the codoped nc exhibit stronger PL peaks shifted to lower energies with respect to the corresponding undoped and single doped Sinc and in particular below the bulk Silicon band gap limit as in Fig. 1.6, thus demonstrating that by simultaneously doping n- and p- type impurities in Sinc, it’ s possible to change the indirect band-gap nature of pure Sinc to direct ones without losing the intensity as shown in panel (d) of Fig. 1.6. This approach may further improve the luminescence efficiency of Sinc as well as extend the tunable range of the luminescence energy. However, to

make the benefit of this effect maximum, carriers in all nanocrystals in a sample should be compensated.

Since impurity doping is expected to change significantly the electronic band structure of nanocrystals, there is a need of a detailed theoretical knowledge of their electronic states, crucial to fully understand their optical and electrical transport properties. Theoretical studies of impurities in quantum dots and wires have lagged relative to calculations for pure, undoped systems. To the best of our knowledge only few theoretical studies exist in literature related to the role of doping on Silicon nanostructures and, for what concern the nanowires, mostly of them are mainly focused on the electronic conductance and transport properties of n- or p- type single doped nanowires and based on semi-empirical tight binding approach [42]. Impurity surface segregation strongly affects the conductance with respect to the undoped Sinw. Boron or phosphorus single doping leads to significantly different conductance properties in wires compared to bulk; in particular, single P- doped wires subdue to a drop of conductance due to a strong resonant backscattering that reduces the mobility of carriers at selected energies.

The idea of this thesis comes form the fact that very few and/or not conclusive theoretical studies exist on the role played by single and co- doping on the optical properties of Sinc and in particular on Sinw [43]. In particular our aim is to focus the attention on the role played by simultaneous substitutional impurities like Boron and Phosphorus on the electronic and optical properties of these nanostructured systems, finding out what does also really change in the electronic structures and in the optical response when we move from 3D confined nanodots to 2D confined nanowires by a first principle calculations. Absorption and emission spectra will be calculated within a Many-Body approach by means of the GW self energy corrections and excitonic effects in order to bring out the most reliable study to shed more light on the possibility to engineer and tune the emission of light from codoped Silicon nanostructures.

1.4 Physical Properties of undoped SiNC

Silicon nanocrystals are quasi 0- dimensional nanosized system that can be synthesized in different ways. Deposition techniques from silane decomposition in gas phase or from laser ablation permit to obtain Sinc with accurate size and concentrations. Other techniques such as the chemical vapor deposition (CVD) or the ion implantation produce Sinc embedded in an Oxide matrix compatible with integrated circuits (IC) applications. They have crystalline structure that preserve most of the symmetry properties of the infinite bulk crystal, and can be treated as spherical [44] or facetted [45] nc.

- due to the quantum confinement they have quasi-direct energy gap with discrete quantized energy level with respect the indirect behaviour of bulk Silicon; the energy gap can be considered direct at the Γ k-point due to the band folding; it decreases with the increasing of the nc diameter approaching to the bulk limit value as the size augment.

- the Sinc present a breakdown of the k-conservation rule: the spatial confinement of electrons and holes increases the uncertainty of their crystal momentum thus allowing optical transition which don't require the mediation of phonons as instead happen in indirect band gap semiconductor.

- Sinc are able to emit light after being excited with optical laser. In particular this photoluminescence emission of light (PL) is enhanced when dealing with Sinc ranging from 1 to 5 nm of diameter (dispersion in size). From several experimental works, it comes out that Sinc are characterized by a Stokes shift between absorption and emission processes. This phenomenon could be related to the relaxation that the nanocrystals subdue after the optical excitation process. This amount of difference between the absorption and emission energies is a decreasing function of the nc diameter: it's bigger for smaller nanocrystals, while it tends to be negligible when the size increase toward the bulk limit.

- several theoretical works have been realized in the last decade concerning the simulation of isolated-free standing hydrogenated Si nanocrystals [44, 46, 47, 48, 45, 49, 50, 51]. Through different approach (DFT-LDA, Time Dependent DFT, Quantum Montecarlo, Real Space approach) these nanocrystals have been studied in order to understand and reproduce the electronic and optical features of Porous Silicon which has been demonstrated to be constituted, as prepared, by a robust network of interconnected Si nanostructures that move from the nanowires to the nanocrystals size as the porosity increases. Moreover, after the demonstration that light emission can be achieved both from aged Porous Silicon samples and from Si nanocrystals embedded in an oxide (SiO_2) matrix [52, 15], several work has been realized in order to bring out which role plays the oxygen at the surface on the optical features [53, 20, 54, 55, 56, 57, 45] by comparing theoretical results with the experimental outcomes. In particular, among the numerous calculations done, the more sophisticated tend to go beyond the simple DFT-LDA approach related to total energy calculation of the Ground State but aspire to shed some more lights on the study of the Excited State, by taking explicitly into account the electron-hole interaction through different kind of approach, such as Green function approach,

Constrain DFT scheme or Time Dependent DFT.

1.5 Physical Properties of undoped SiNW

Silicon nanowires are quasi one-dimensional systems. As for Silicon nanocrystals several growth techniques exist, and for each of them different applications can be realized. The most common fabrication technique is the Vapor-Solid-Liquid (VSL) growth, in which a metal particle is used to catalyze the growth reaction of the nanowires. The main effects of low dimensionality are:

- size scaling of the optical gap. The effect of uni-dimensional spatial confinement of carriers along the two direction perpendicular to the wire axis determines that electrons holes are free to move all along the wire axis. This determines an opening of the band gap which varies as a function of the wire diameter. The optical properties instead, don't depend so much on the wire diameter, but indeed on the wire orientation. This anisotropic behaviour could help in the identification of the different wires grown in a sample.

- as already said for Silicon nanocrystals, the Silicon nanowires present a direct optical gap, due to the band folding of the energy bands on the axis of the nanowires.

- Sinw show strong electron-hole interaction effects when compared to the bulk compounds. As before, the spatial confinement of the carriers along the wire axis, determines a strong overlap of their wavefunctions that results in an increasing of the interaction effects. It has been found that strong bounded exciton present a binding energy 10^3 times bigger with respect to the corresponding value in bulk Silicon.

2

Density Functional Theory

Queremos la luz, para nosotros nada
queremos la luz, para todos todo.

La lunga notte, Cisco

Since this work concerns of theoretical simulations of real (or that pretend to be almost real!) systems for ponderable technological application, we adopt the most used and efficient technique to deal with success in this kind of study. To understand the electronic ground-state properties of the systems we have taken benefit of *ab initio* approach based on the density functional theory (DFT) scheme. But, although the well known and tested efficiency of DFT, we had to recourse to the Many-Body Perturbation Theory (MBPT) to treat in the proper way the excited-state features, that means charged and neutral excitations, such as optical absorption and emission.

Thus this section will pursue with a brief description of some important and, of course, well known features of DFT and MBPT scheme implemented in the *ab initio* computer codes used in the present work to investigate our systems of interest.

2.1 The Many-Body Problem

One of the principal aim of condensed matter physics and quantum chemistry is the theoretical study of the electronic properties. To understand the behaviour of systems ranging from atoms, molecules and nanostructures to more complex bulk systems, the resolution of the Schrödinger equation has become the fundamental and the main task of the many-body problem. Since the Coulomb or electrostatic interaction between electrons is

very strong, the analytical solution of this equation is possible only for a small number of very simple systems and in particular numerical solutions could be found only for a few number of atoms and molecules. The main and computational demanding problem lies in the many-body nature of the Hamiltonian H that governs the evolution of any systems composed by electrons (labelled by coordinates (position and spin) $\{\mathbf{r_i}\}$, momenta $\mathbf{p_i}$, mass m_i) and atomic nuclei (represented by coordinates $\{\mathbf{R_I}\}$ and momenta $\mathbf{P_I}$ with mass M_I and atomic charge Z_I):

$$H\big[\{\mathbf{r},\mathbf{p}\}\,\{\mathbf{R},\mathbf{P}\}\big] = \sum_{i=1}^{N}\frac{\mathbf{p_i}^2}{2m_i}+\sum_{i=1}^{M}\frac{\mathbf{P_I}^2}{2M_I} + \sum_{I<J}\frac{e^2}{|\mathbf{r_i}-\mathbf{r_j}|} + \\ - \sum_{i<j}\frac{Z_I\,e^2}{|\mathbf{r_i}-\mathbf{R_I}|} + \sum_{I<J}\frac{Z_I\,Z_J\,e^2}{|\mathbf{R_I}-\mathbf{R_j}|}$$

and that is also applied to the many-body wavefunctions

$$\Psi_{MB} = (\{\mathbf{r}_1,...,\mathbf{r}_n\}\,;\{\,\mathbf{R}_1...,\mathbf{R}_N\})$$

describing the eigenstates of the complex real system, in terms of electrons and atoms contributions through a many-body secular equation

$$\hat{H}\big(\{\mathbf{r_i}\},\{\mathbf{R_I}\}\big)\ \Psi_{MB}\big(\{\mathbf{r_i}\},\{\mathbf{R_I}\}\big) = E_{tot}\ \Psi_{MB}\big(\{\mathbf{r_i}\},\{\mathbf{R_I}\}\big) \tag{2.1}$$

Due to the huge number of interactions involved this problem is enormously complex to resolve and also nowadays very tough also for the most powerful supercomputer. Thus the physics and chemistry community has been obliged to find some approximation that worked to simplify the task. The first one, exploited by M. Born and M. J. Oppenheimer during 1927, introduces a hierarchy of approximation due to different scales of energy. The so called *Born-Oppenheimer or adiabatic approximation* [58] tends in fact to decouple the nuclear and the electronic degrees of freedom. Since electrons move much faster than nuclei it can be assumed that electrons are in the lowest energy state for the given nuclear configuration: electrons and nuclei moves on different energy and time scale so that electrons follow *adiabatically* the slow "motion" of nuclei.

Thus, according to the *Born-Oppenheimer Approximation*, we can separate the electronic variable from the nuclei ones factorizing the many-body wavefunction into two contributes:

$$\Psi_{MB} \;\backsimeq\; \Psi_{BO} \;=\; \varphi(\{\mathbf{r}\},\{\mathbf{R}\})\ \Phi(\{\mathbf{R}\}) \tag{2.2}$$

Then the secular eigenvalues equation Eq. [2.1]

$$(T_e + T_I + V_{ee} + V_{Ie} + V_{II})\ \Psi_{MB}(\{\mathbf{r_i}\},\{\mathbf{R_I}\}) = E_{tot}\ \Psi_{MB}(\{\mathbf{r_i}\},\{\mathbf{R_I}\})$$

(where the sum terms have been replaced by T for the kinetic energy and V for the potential energy) can be separated into two coupled equations

$$\begin{aligned} \left[T_e + V_{ee} + V_{Ie}\right] \varphi(\{\mathbf{r}\},\{\mathbf{R}\}) &= E\left(\{\mathbf{R}\}\right) \varphi(\{\mathbf{r}\},\{\mathbf{R}\}) \\ \left[T_I + V_{II} + C\left(\{\mathbf{R}\}\right)\right] \Phi(\{\mathbf{R}\}) &= E_{tot}\, \Phi(\{\mathbf{R}\}) \end{aligned} \tag{2.3}$$

This means that now the properties of electrons depend on the nuclei coordinates $\{\mathbf{R}_I\}$ in a *parametric* way: since the nuclei (or ions) are supposed to be *frozen* we can see that the ionic potential enter as a parameter in the equation for electrons Eq. [2.3] and the electrons in the ionic counterpart equation via the *adiabatic* parametric energy term $C\left(\{\mathbf{R}\}\right)$, which represents a sort of *electronic glue* for the lattice. Note that the energy term $C_{\mathbf{R}}$, called *adiabatic diagonal correction*, is an operator that acts on the nuclear wave function $\Phi(\{\mathbf{R}\})$ and is generally quite small and is mostly neglected altogether.
Once the electron equation has been separated by the ionic counterpart, there's still another open question blinking on the paper: how to resolve the electron eigenvalues equation from the quantum theory point since it describes (with the V_{ee}) interactions between 10^{23} electrons per material and the index of the wavefunction $\varphi(\{\mathbf{r}\},\{\mathbf{R}\})$ runs over N-electrons?
We have again to deal with a "*many-body Schrödinger equation*"!

Several models have been proposed during the last century to treat in a simply but proper way this new formidable "many-body task" of interacting electrons. Most of this approximate theories concerns with finding a good single-particle approximation for the Coulomb term.
The earliest attempt is due to D. R. Hartree in 1928 [59]. The main features of the *Hartree approximation* are:

- the *non local* Coulomb potential is replaced by a **local** Coulomb potential (**Hartree potential**) averaged by all the electrons of the systems

$$V_H = \sum_{N}^{j=1} \int d^3r'\, \varphi_j^*(r')\, \varphi_j(r')\, \frac{1}{\mid r - r' \mid} = \int d^3r'\, \rho(r')\, \frac{1}{\mid r - r' \mid} \tag{2.4}$$

- the many-body electron wavefunction $\varphi(\{\mathbf{r}\},\{\mathbf{R}\})$ is separated into a product of N single-particle function satisfying a one-electron Schrödinger equation.

$$\varphi(\{\mathbf{r}\},\{\mathbf{R}\}) \backsimeq \varphi_H = \varphi_i(\mathbf{r}_1)\, \varphi_i(\mathbf{r}_2)\, \varphi_i(\mathbf{r}_3) \ldots \varphi_i(\mathbf{r}_j) \tag{2.5}$$

Although the *Hartree approximation* gives reasonable results, it miss the effect of exchange and correlation between electrons (that are partially

cancelled each other) and also doesn't take into account the Pauli exclusion principle, so neglecting the spin component effect.

Taking into account Fermi-Dirac statistic the wavefunction can be describe as a Slater's determinant of single-particle wavefunction, in order to treat the wavefunction as anti-symmetric with respect to any interchange of two electrons,

$$\varphi(\{\mathbf{r}\},\{\mathbf{R}\}) \backsimeq \varphi_{HF} = \frac{1}{\sqrt{N!}}\, det\, [\,\varphi_i\,(\mathbf{r}_j)\,]$$

it's possible to go beyond the Hartree potential obtaining the so called *Hartree-Fock method* where an additional **non local spin-dependent exchange** term appears in the Hamiltonian [60]:

$$\int d^3r'\, V_x(r,r')\ \varphi_i(r') = -\sum_{j=1}^{Noccup} \int d^3r'\, \varphi_j^*(r')\ \frac{1}{\mid r-r'\mid}\ \varphi_j(r)\varphi_i(r') \quad (2.6)$$

In this new approach the exchange contribution V_x is now treated exactly and improves the total energy predictions for atoms and molecules although fails describe solid state systems, such as insulators for which the energy gap is overestimated. What the Hartree-Fock methods miss is the correlation between electrons with different spin and therefore the screening. One possibility to go beyond Hartree-Fock approximation is done in the *configuration interaction (CI)* scheme [61]. In this method a set of Slater determinants is considered as a basis for many-body wavefunction, but the number of configurations scales very rapidly with the number of electrons making the method extremely demanding (linear combination of the determinants are considered to describe the lowest-lying state, but the increasing number of configurations with increasing number of electrons means that only systems with a few number of electrons can be calculated with high accuracy).
All these method belong to the class of *mean field* approximation: all the electrons experience an "averaged" potential due to the electrostatic interaction with the *charge density* formed by all other electrons in the systems.

A different approach was adopted by Thomas and Fermi (1927-1928) [62, 63] who proposed to cast the many-body problem into a semiclassical variational framework in which the degrees of freedom of the systems were condensed into the electron density $n(r)$ only. Extensions of this method were suggested by Dirac (1930) [64] introducing the exchange interaction between electrons as a functional of the density, and by Slater who introduced correlations effects. These were the basis for the development of the Density Functional Theory.

2.2 Another brick in the wall: a brief DFT survey

Although in the Thomas-Fermi model is possible to introduce correction (such as exchange and correlations effects or gradient density with the extension of Dirac) that can lead to really good results, it can't be considered that a first simpler version of the density functional theory. The first theoretical foundation of *Density Functional Theory (DFT for friends!)* was introduced in 1964 by P. Hohenberg and W. Kohn in a famous paper [65] that was worth the Nobel Prize for Chemistry to Kohn in the 1998. They demonstrated that all the electronic properties of the system in its non-degenerate **ground-state (GS)** configuration can be completely described by its **electron density** $n(\mathbf{r})$; moreover the total energy and the potentials can be described as **functional** of the electron density n($\mathbf{r}$) only.
One year later, in 1965, moving from the H-K theorem, W. Kohn and L. J. Sham provided a *self-consistent* scheme in order to map the interacting many-body problem into a set of *non interacting* single particle equation reformulating the mean-field method into a *variational principle* on the basis of the electron density only [66]. The first milestones of Density Functional Theory can therefore considered the Hohenberg-Kohn theorem and the Kohn-Sham equations.

The Hohenberg-Kohn theorem

The Hohenberg-Kohn (H-K) theorem succeeded to demonstrate that the properties linked to the electronic structure of a system in its fundamental non-degenerate ground-state are completely and univocally described by its **electronic ground-state density** n($\mathbf{r}$). The theorem asserts that:

"the ground-state density n($\mathbf{r}$*) of a bound system of interacting electrons in some external potential v(r) determines this potential uniquely"*

where *uniquely* means "up to an additive constant" (defined in the Hohenberg-Kohn paper, uninteresting) and in the case of degenerate ground-state, the lemma refers to any ground-state density n($\mathbf{r}$). Taking into account a N-electron system interacting in presence of an external potential $V_{ext}(\mathbf{r})$, the Hamiltonian results

$$\hat{H} \;=\; \hat{T} + \hat{V}_{ext} + \hat{W}$$

a sum of a kinetic term

$$\hat{T} \;=\; -\frac{1}{2}\sum_{i}^{N} \nabla_i^2$$

an electron-electron interaction Coulomb potential term

$$\hat{W} \;= \frac{1}{2}\sum_{i\neq j} v_{ij}\;(\,|\mathbf{r_i} - \mathbf{r}_j|\,)$$

and a term representing the interaction with the external potential $V_{ext}(\mathbf{r})$

$$\hat{V}_{ext} = \sum_{i}^{N} v_{ext}(\mathbf{r_i})$$

the ground-state many-body wavefunction can be defined as $\varphi(\mathbf{r}_1 \ldots \varphi_N)$ and the ground-state electronic density (supposed to be non-degenerate) is

$$n(\mathbf{r}_1) \;=\; N \int \varphi^*(\mathbf{r}_1 \ldots \varphi_N)\; \varphi(\mathbf{r}_1 \ldots \varphi_N)\, d\mathbf{r}_2 \ldots d\mathbf{r}_N$$

The H-K theorem asserts that φ and V_{ext}[1] are univocally determined by the electronic density n($\mathbf{r}$) only and they're called *unique functional of the electronic charge density*. From the eigenvalues equation

$$\begin{aligned} \hat{H}\,|\,\varphi(\mathbf{r})\,\rangle \;&=\; E_{GS}|\,\varphi(\mathbf{r})\,\rangle \\ \left(\hat{T} + \hat{V} + \hat{W}\right)|\,\varphi(\mathbf{r})\,\rangle \;&=\; E_{GS}|\,\varphi(\mathbf{r})\,\rangle \end{aligned} \tag{2.7}$$

although T and W are univocally specified through the H-K theorem, on the other hand, the potential v, supposed in the original paper [65] to be local, bounded and spin-independent, can be considered an element of the $\mathscr{V}$ ensemble containing all the external potential that generate a non-degenerate ground-state for the system. Each v can be related to a ground-state wavefunction φ_{GS} to which belong a unique electronic charge density $n_{GS}(\mathbf{r})$:

$$n_{GS}(\mathbf{r}) \;=\; \langle\, \varphi_{GS}\,|\,\hat{n}(\mathbf{r})\,|\,\varphi_{GS}\,\rangle$$

All the densities that satisfy this relation belong to the ensemble $\mathscr{N}$ and are called $\mathbf{v}$-*representable* because are ground-state electronic densities of the hamiltonian $\hat{H} \;=\; \hat{T}{+}\hat{W}{+}\hat{V}$ obtained from different $v_{ext} = \int\, v(\mathbf{r})\, n(\mathbf{r})\, d\mathbf{r} \;\; \in \mathscr{V}$. It's possible to construct a map between a set of external potential $v(\mathbf{r})$ and the corresponding ground-state densities n($\mathbf{r}$) through:

$$\mathcal{G}\,:\; v(\mathbf{r}) \rightarrow \;|\,\varphi(\mathbf{r})\,\rangle$$

and since the H-K theorem shows that $\mathcal{G}$ is surjective and injective, thus biunivocal and fully invertible:

$$\mathcal{G}^{-1}\,:\; n(\mathbf{r}) \rightarrow\; v(\mathbf{r})\; + c$$

the ground-state density could be considered the basic variable in the electronic problem. The application $\mathcal{G}$ is surjective for construction but to prove that is also injective one can shows that two different systems subjected to two external potentials that differ only for a constant, $v(\mathbf{r}) \neq\; v'(\mathbf{r}) + \mathrm{c}$ they

[1] From now on the external potential will be simply indicated by v

cannot have the same electronic density for the ground-state, $n(\mathbf{r}) = n'(\mathbf{r})$ leads to an *absurdum*.
This implies that the ground-state expectation value of any physical observable is a *unique functional* of the ground-state electron density n($\mathbf{r}$):

$$\langle \varphi[n] | \hat{O} | \varphi[n] \rangle = O[n]$$

In particular according to these findings we can define the total energy of the N-electron system as the expectation value calculated on the ground-state wavefunction $|\varphi\rangle$:

$$E[n(\mathbf{r})] = \left\langle \varphi[n] \right| \hat{H} \left| \varphi[n] \right\rangle$$

and defining the ***universal functional*** $F_{HK}[n]$:

$$F_{HK}[n] = \left\langle \varphi[n] \right| (\hat{T} + \hat{W}) \left| \varphi[n] \right\rangle \tag{2.8}$$

the total energy become:

$$E_v[n(\mathbf{r})] = \int v(\mathbf{r})\, n(\mathbf{r})\, d\,\mathbf{r} + F_{HK}[n] \tag{2.9}$$

It is worth pointing out that $F_{HK}[n]$ is a *universal functional* because it doesn't depend on the external potential and it is the same density functional for atoms, molecules and solids since in all cases $\hat{W}$ is the Coulomb repulsion between the electrons and $\hat{T}$ their kinetic energy.
The second part of the H-K theorem establish that through a reformulation of the *Rayleigh-Ritz variational principle* in term of the electron density $n(\mathbf{r})$ is possible to *minimize the $E_v[n]$ functional in the class of the regular functions $n(\mathbf{r})$ satisfying the condition $\int n(\mathbf{r})\, d\,\mathbf{r} = N$ for the exact ground-state density* [67]. The minimization process leads to

$$E = min_{\tilde{n}(\mathbf{r})} E_v[\tilde{n}] = min_{\tilde{n}(\mathbf{r})} \left\{ \int v(\mathbf{r})\tilde{n}(\mathbf{r}) d\mathbf{r} + F[\tilde{n}] \right\} \tag{2.10}$$

where here $\tilde{n}(\mathbf{r})$ refers to all functions of the $v-$*representable* class cited above. The minimum is attained when $\tilde{n}(\mathbf{r})$ coincides with the $n(\mathbf{r})$ ground-state density for a non-degenerate case; for a degenerate case, instead, $\tilde{n}(\mathbf{r})$ is only one of the ground-state densities. The constraint on the number of particles (that assures the conservation) is resumed with

$$\frac{\delta E[n(\mathbf{r})]}{\delta n(\mathbf{r})} = \mu. \tag{2.11}$$

where μ mathematically defined as a *Lagrange multiplier* represents the **chemical potential** of the system.
The formidable problem of finding the minimum of $\langle \widetilde{\Psi} \mid H \mid \widetilde{\Psi} \rangle$ with respect to the $3N-$ dimensional trial function $\widetilde{\Psi}$ has been transformed into the

seemingly trivial problem of finding the minimum of $E_v[\tilde{n}]$ with respect to the three-dimensional trial function $\tilde{n}(\mathbf{r})$. However the main difficulty in the determination of the ground-state density is the form of the functional Eq. [2.8]: fixed the external potential $v_{ext}(\mathbf{r})$ the lack of a proper analytical definition of the $F_{HK}[n]$ functional leads straight the use of approximations for the minimization of $E_v[\tilde{n}(\mathbf{r})]$ for the calculation of E_{tot} and $n(\mathbf{r})$.

The Kohn-Sham equations

A particulary important strategy to solve the problem of the practical DFT implementations was introduced by Kohn and Sham [66].
They considered an auxiliary system of N non-interacting electrons subjected to an *effective potential* $v_{eff}^{KS}(\mathbf{r})$ and described by the Hamiltonian:

$$\hat{H}^{KS} = \hat{T}^{KS} + \hat{v}_{eff}^{KS}. \tag{2.12}$$

by moving from the initial Hartree formulation of the Schrödinger equation for *noninteracting* electrons in the external potential v_{eff} and from the H-K minimal principle. According to the theorem of Hohenberg and Kohn, for a non-interacting N-particle system, the energy is a functional of the density:

$$E_s[n] = T_s[n] + \int v_s(\mathbf{r})\tilde{n}(\mathbf{r})d\mathbf{r} \tag{2.13}$$

The central assertion used in establishing the Kohn-Sham scheme is the following: **''for any interacting system, there exists a local single particle potential $v_{ks}(\mathbf{r})$ such that the exact ground-state density n(r) of the interacting systems is equal to the ground-state density of the auxiliary system $\tilde{n}(\mathbf{r})$, i.e. that $n(\mathbf{r}) = \tilde{n}(\mathbf{r})$''.**

We limit our discussion to non degenerate systems, for a more general approach see [67].
Minimizing the energy functional for the Kohn-Sham system of N-independent particles, with the constrain on the number of electrons and considering that the density $\tilde{n}(\mathbf{r})$ must be constructed for an independent-particle system (one-single Slater determinant), we obtain a set of equations:

$$\left[-\frac{\hbar^2}{2m}\nabla^2 + v_s(\mathbf{r})\right]\varphi_i(\mathbf{r}) = \epsilon_i\varphi_i(\mathbf{r}) \tag{2.14}$$

The density has a unique representation in term of the (lowest) N single-particle orbitals:

$$n(\mathbf{r}) = \tilde{n}(\mathbf{r}) = \sum_{i=1}^{N} \mid \varphi_i(\mathbf{r}) \mid^2 \tag{2.15}$$

where the constraint on the density became equivalent to the orthonormality of the wavefunctions:

$$\int d\mathbf{r}\varphi_j^*(\mathbf{r})\varphi_i(\mathbf{r}) = \delta_{ij} \tag{2.16}$$

Once the existence of a potential $v_s(\mathbf{r})$ generating a given interacting density n($\mathbf{r}$) is assumed, the uniqueness of $v_s(\mathbf{r})$ follows from the Hohenberg-Kohn theorem.
Thus the single-particle orbitals are unique functional of the density: n($\mathbf{r}$), $\phi_i(\mathbf{r}) = \phi_i([n(\mathbf{r})])$ and the non interacting kinetic energy $T_s[n(\mathbf{r})]$ is a unique functional of n($\mathbf{r}$) as well.

Starting from the interacting system subject to an external potential $v(\mathbf{r})$ we can rewrite the total energy functional of Eq. [2.9] splitting $F_{HK}[n]$ as:

$$F_{HK}[n] = \frac{1}{2}\int\int d\mathbf{r}d\mathbf{r}'\frac{n(\mathbf{r})n(\mathbf{r}')}{|\mathbf{r}-\mathbf{r}'|} + T_s[n] + E_{xc}[n] \tag{2.17}$$

and obtaining in this way:

$$E_v[n] = T_s[n] + \int d\mathbf{r}\, v(\mathbf{r})n(\mathbf{r}) + \frac{1}{2}\int\int d\mathbf{r}\, d\mathbf{r}'\,\frac{n(\mathbf{r})\,n(\mathbf{r}')}{|\mathbf{r}-\mathbf{r}'|} + E_{xc}[n] \tag{2.18}$$

where we have inserted three terms in $F_{HK}[n]$ such as:

- the Hartree energy term $\frac{1}{2}\int\int d\mathbf{r}d\mathbf{r}'\frac{n(\mathbf{r})n(\mathbf{r}')}{|\mathbf{r}-\mathbf{r}'|}$ describing interaction between electrons
- the kinetic energy T_s of the non-interacting system
- the term $E_{xc}[n]$ called ***exchange-correlation energy*** and unfortunately still *unknown*, defined as

$$E_{xc}[n] = F_{HK}[n] - \frac{1}{2}\int\int d\mathbf{r}d\mathbf{r}'\frac{n(\mathbf{r})n(\mathbf{r}')}{|\mathbf{r}-\mathbf{r}'|} - T_s[n] \tag{2.19}$$

but from Eq. [2.8] we can see that E_{xc} consists of a potential and a kinetic part:

$$E_{xc}[n] = \left(W[n] - \frac{1}{2}\int\int d\mathbf{r}d\mathbf{r}'\frac{n(\mathbf{r})n(\mathbf{r}')}{|\mathbf{r}-\mathbf{r}'|}\right) + \left(T[n] + T_s[n]\right) \tag{2.20}$$

The Hohenberg and Kohn variational principle ensures that $E_v[n]$ is stationary for small variations of $\delta n(\mathbf{r})$ around the minimum density $n(\mathbf{r})$:

$$\delta E_v[n] = E[n+\delta n] - E[n] = 0$$

$$\int \delta\tilde{n}(\mathbf{r})\left\{v(\mathbf{r})+\frac{\delta\, T_s[\tilde{n}]}{\delta\tilde{n}(\mathbf{r})}+\frac{1}{2}\int\frac{\tilde{n}(\mathbf{r})}{\mid\mathbf{r}-\mathbf{r}'\mid}d\mathbf{r}'+\frac{\delta\, E_{xc}[\tilde{n}]}{\delta\tilde{n}(\mathbf{r})}-\mu\right\}_{\tilde{n}\equiv n} d\mathbf{r}=0 \tag{2.21}$$

Applying the Euler-Lagrange equations

$$\frac{\delta T_s[n(\mathbf{r})]}{\delta\tilde{n}(\mathbf{r})}+v(\mathbf{r})+\frac{1}{2}\int\frac{\tilde{n}(\mathbf{r}')}{|\mathbf{r}-\mathbf{r}'|}d\mathbf{r}'+\frac{\delta\, E_{xc}[n(\mathbf{r})]}{\delta n}-\mu=0 \tag{2.22}$$

introducing an **exchange-correlation potential** v_{xc} defined as:

$$v_{xc}(\mathbf{r})=\frac{\delta E_{xc}[n]}{\delta n(\mathbf{r})}.$$

and an **effective potential**

$$v_{eff}^{KS}(\mathbf{r})=v(\mathbf{r})+\frac{1}{2}\int\frac{n(\mathbf{r}')}{|\mathbf{r}-\mathbf{r}'|}d\mathbf{r}'+v_{xc}(\mathbf{r})$$

one can finally get the so called *self-consistent Kohn-Sham (KS) equations* [66]:

$$\left\{-\frac{1}{2}\nabla^2+v_{eff}^{KS}(\mathbf{r})-\varepsilon_i^{KS}\right\}\varphi_i^{KS}=0 \tag{2.23}$$

where the ε_i^{KS} and φ_i^{KS} are the Kohn-Sham respectively eigenvalues and eigenvectors. It can be observed that since

$$\begin{aligned}\sum_i^N\varepsilon_i &= \sum_i\langle\varphi_i\mid -\frac{1}{2}\nabla^2+v_{eff}(\mathbf{r})\mid\varphi_i\rangle= \\ &= T_s[n(\mathbf{r})]+\int v_{eff}\; n(\mathbf{r})d\mathbf{r}= \\ &= T_s+\int v(\mathbf{r})\,n(\mathbf{r})\,d\mathbf{r}+\frac{1}{2}\int\frac{n(\mathbf{r})n(\mathbf{r}')}{|\mathbf{r}-\mathbf{r}'|}d\mathbf{r}d\mathbf{r}'+ \\ &+ \int v_{xc}(\mathbf{r})n(\mathbf{r})d\mathbf{r}\end{aligned} \tag{2.24}$$

and

$$E_v[n]=T_s+\int v(\mathbf{r})n(\mathbf{r})d\mathbf{r}+\frac{1}{2}\int\frac{n(\mathbf{r})\,n(\mathbf{r}')}{\mid\mathbf{r}-\mathbf{r}'\mid}d\mathbf{r}d\mathbf{r}'+E_{xc}[n]$$

then the *total energy* of the interacting system can be expressed in this way:

$$\begin{aligned}E_{tot}=T_s[n]+\int v_{ext}(\mathbf{r})n(\mathbf{r})\,d\,\mathbf{r}+\frac{1}{2}\int\frac{n(\mathbf{r})n(\mathbf{r}')}{|\mathbf{r}-\mathbf{r}'|}d\mathbf{r}d\mathbf{r}'+E_{xc}[n]= \\ \sum_i^N\varepsilon_i-\frac{1}{2}\int\frac{n(\mathbf{r})n(\mathbf{r}')}{|\mathbf{r}-\mathbf{r}'|}d\mathbf{r}d\mathbf{r}'+E_{xc}[n]-\int v_{xc}(\mathbf{r})n(\mathbf{r})\,d\,\mathbf{r}\end{aligned} \tag{2.25}$$

If one neglects the E_{xc} and the v_{xc} terms altogether, the KS equations (2.2, 2.23, 2.25) reduce to the self-consistent Hartree equations. The same must holds also for the non-interacting systems and we can write:

$$0 = \delta E_s[n] = E_s[n + \delta n] - E_s[n] = \delta T_s + \int d\mathbf{r}\, \delta n(\mathbf{r}) v^{KS}(\mathbf{r}) \qquad (2.26)$$

This leads to the final expression as seen above:

$$v_{eff}^{KS}(\mathbf{r}) = v_{ext}(\mathbf{r}) + \int d\mathbf{r}' \frac{n(\mathbf{r}')}{|\mathbf{r} - \mathbf{r}'|} + v_{xc}(\mathbf{r}) \qquad (2.27)$$

The Kohn-Sham formalism relies on the link between an actual N electrons system and a fictitious non-interacting counterpart through the potential $v_{xc}(\mathbf{r})$. Hence, $v_{xc}(\mathbf{r})$ contains essential information about many-body correlations which Many-Body Perturbation Theory describes [68, 69] in terms of non local dynamical terms.

It may be realized that the mapping between ground-state densities and Kohn-Sham potentials $v^{KS}[n](\mathbf{r})$ depends on $n(\mathbf{r})$ in a very peculiar and sensitive way. In fact the actual functional relation between $n(\mathbf{r})$ and $v_{xc}(\mathbf{r})$ is highly non-analytical: small or even infinitesimal changes in the density may induce substantial variations in the xc potential. It is highly non local, i.e. changes in the density at a given point $\mathbf{r}$ may induce substantial variations of the xc potential at a point $\mathbf{r}'$.

The KS equation can be regarded as the exact formalization of the Hartree scheme: with the exact E_{xc} and v_{xc} all the many-body effects are completely taken into account by principle, and the main effort of DFT lies in the practical usefulness of ground-state when the good approximation (simply to use but accurate) for the xc functional is found.

Some remarks:

1. *the Hartree potential* gives an exact estimation of the exchange potential but tends to neglect the correlation effects between electrons of the system: for that reason the Hartree equations tend to underestimate the total energy;

2. *the KS equation*, instead, take into account both the effects of exchange and correlation contained in the $E_{xc}[n]$ functional;

3. *the effective single-particle potential* V_{eff} can be regarded as a unique external potential which leads for noninteracting particles, to the same density $n(\mathbf{r})$ as that for the interacting electrons in the physical external potential $v(\mathbf{r})$;

4. the initial N-electron many-body problem (very computational demanding) is simplified to *a set of* n *single-particle equations describing a fictitious system of noninteracting electrons with electron density of the real system of interacting electrons*;

5. the single-particle KS wavefunction $\varphi_i^{KS}(\mathbf{r})$ are considered *"density optimal"* while the Hartree-Fock wavefunction φ_j^{HF} are *"total energy optimal"* because their normalized determinant leads to the lowest ground-state energy attainable with a single determinant

Within the Kohn-Sham scheme the problem of the interacting system is now simpler, but it is still not solved: it is necessary, in fact, to find a good approximation for the exchange-correlation energy E_{xc}.
Once a good approximation for E_{xc} is obtained, the Kohn-Sham equations must be solved self-consistently and then it is possible to obtain the ground-state density of the interacting system and its total energy, as depicted in Fig. 2.1.

2.2.1 The form of E_{xc}

Since there's no exist an exact analytical expression for the E_{xc} functional, the total energy calculations require some approximations for it. In the next section I'll fix the attention on three of these approximations that are used in this work: the Local Density Approximation (LDA), the Local Spin Density Approximation and the Generalized Gradient Approximation.

The Local Density Approximation

According to this approximation, disclose to be the simplest and most used one, the *xc* functional is defined as a *local function* of the density of a

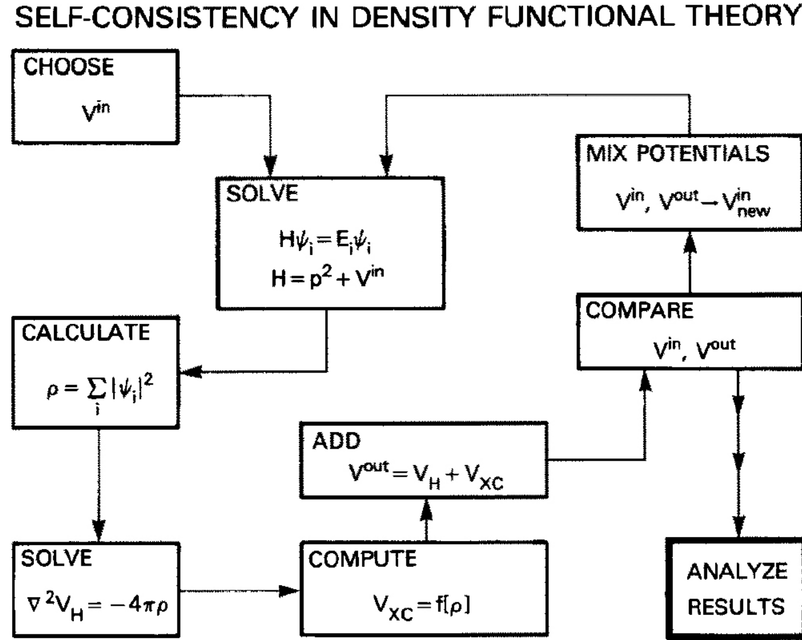

Figure 2.1: The main Self-Consistent Algorithm

homogeneous electron gas:

$$E_{xc} = \int d\mathbf{r}\, \epsilon_{xc}^{hom}(n(\mathbf{r}))$$

where ϵ_{xc}^{hom} is the *exchange-correlation energy per electron* of the homogenous and uniform electron gas. Taking into account an interacting *homogeneous* electron gas, we can say that the exchange-correlation energy per electron is in this case a *function of the density* and not a functional since the density is constant for this kind of system: thus $\epsilon_{xc}[n(\mathbf{r})] \rightarrow \epsilon_{xc}(n(\mathbf{r}))$ and multiplying for the number of electron we get $E_{xc}[n] = N\epsilon_{xc}(n(\mathbf{r}))$. In the Local Density approximation, the *inhomogeneous* electron gas is handled in the same way: the exchange-correlation energy is the sum of the contribution of each portion of the *non uniform* gas as it was **local uniform**. Thus the exchange-correlation potential become:

$$v_{xc}^{LDA}(\mathbf{r}) = \frac{\partial E_{xc}[n]}{\partial n(\mathbf{r})} = \frac{\partial \int \epsilon_{xc}(n\mathbf{r})n(\mathbf{r})d\mathbf{r}}{\partial n(\mathbf{r})} = \frac{\partial [n(\mathbf{r})\epsilon_{xc}(\mathbf{r})]}{\partial n(\mathbf{r})} = \epsilon_{xc}(n\mathbf{r}) + n(\mathbf{r})\left(\frac{\partial \epsilon_{xc}(n)}{\partial n}\right)_{n(\mathbf{r})} \equiv \mu_{xc}(n(\mathbf{r})) \quad (2.28)$$

where $\mu_{xc}(n(\mathbf{r}))$ is the exchange-correlation contribution to the chemical potential for an uniform system. The approximation is said to be **local** be-

cause $\epsilon_{xc}(\mathbf{r})$ depends from the local value of the density $n(\mathbf{r})$ in the $\mathbf{r}$ position only. The LDA works well for systems with a *slowly varying density* and has proven very successful for calculation of ground-state properties. The lattice constants are predicted within $\sim 1\,\%$, the bulk modulus, the dissociation energy of molecules, the ionization energy of atoms within $\sim 10\,\%$ of experiment, while the cohesive energy is quite generally overestimated, as a result usually attributed to the predicted under bindings of atoms within LDA. On the other hand the LDA fails in the estimation of the fundamental energy gap for semiconductors and insulator, usually underestimated by 30 - 50 %, although the relative position of the valence band energies for bulk materials agree well with photoemission experiments [70]. The two contributions to E_{xc}, the exchange and the correlation energy respectively within ~10 % and 2 times bigger, tends to compensate and cancel. Thanks to Eq. [2.28] the E_{tot} of Eq. [2.25] can be expressed in this way:

$$E_{tot} = \sum_{i}^{N} \varepsilon_i - \frac{1}{2} \int \frac{n(\mathbf{r})n(\mathbf{r}')}{|\mathbf{r}-\mathbf{r}'|} d\mathbf{r} d\mathbf{r}' + \int n(\mathbf{r}) \Big[\epsilon_{xc}(n(\mathbf{r})) - \mu_{xc}(n(\mathbf{r})) \Big] d\,\mathbf{r} \tag{2.29}$$

where the contribution ϵ_{xc} can be exactly derived taking into account the wavefunction of the homogeneous electron gas as a Slater determinant of plane waves:

$$\epsilon_{xc}(n\mathbf{r}) = \left[\frac{3}{4} \left(\frac{3}{\pi} \right)^{1/3} e^2 \right] n(\mathbf{r})^{1/3} = -\frac{0.458}{r_s} e^2$$

where e^2 is the radius of the sphere containing one electron given by $(4\pi/3)r_s^3 = n^{-1}$. The correlation term, derived by Wigner in 1938,

$$\epsilon_{xc}(n\mathbf{r}) = -\frac{0.44}{r_s + 7.8}$$

was corrected with better precision by David Ceperley and Ben Alder in 1980 [71] through Monte Carlo methods.

As remarked above, the LDA is expected to be useful only for density varying slowly on the scales of the local Fermi wavelength λ_F and Thomas - Fermi wavelength λ_{TF} and, nevertheless, it gives good results for atoms and molecules. The reason lies in the fact that LDA satisfies a sum rule which expresses the normalization of the exchange-correlation hole. This means that with an electron in $\mathbf{r}$, the conditional electron density $n(\mathbf{r}, \mathbf{r}')$ of the other electrons is depleted near $\mathbf{r}$ in comparison with the average density $n(\mathbf{r}')$ by the hole distribution $n_h(\mathbf{r}'; \mathbf{r})$ which integrates to 1. The success of LDA lies then in

- the exchange-correlation energy is well determined by the spherical average of the *exchange-correlation hole*;

- the Local Density Approximation describes with accuracy this kind of spherical average;
- there's a systematic cancellation between the errors as a consequence of the charge conservation in the sum rule;

LDA energy functional suffers for the self-energy interaction: the exchange part of the functional does not cancel exactly the self-energy interaction of the Hartree term. This leads to a wrong asymptotic behaviour of the xc potential for finite systems (it goes exponentially to zero instead as $\frac{1}{r}$) [72]. There have been several attempts to go beyond the LDA approximation [73]: the next class of functionals, in which we can consider the GGA [74], solve some of the problem present in the LDA, but they are just analytical semi-local approaches. The novel meta-GGA include further non-analytical and non local behaviour through the explicitly appearance of the Kohn-Sham wavefunctions, but both GGA and meta-GGA have the wrong asymptotic behaviour.
Another class of energy functionals are the orbital functionals, in the so called optimized effective potential (OEP), or optimized potential method (OPM) [75, 76, 77]. Two example of these orbitals are the exact-exchange (EXX) and the self-interaction corrected SIC-LDA functionals [78, 78, 79]. In the exact exchange method the exchange contribution $E_x[n]$ is treated exactly and also the SIC-LDA cancel the Hartree energy part which contribute to the self-interaction, and vanishes for one-electron systems.

But the "Spin Doctor" says.....

One improvement with respect to the LDA can be achieved with the implementation of polarization in spin, in the so called *Local Spin Density Approximation (LSDA)*, in particular for systems that are subjects to an external magnetic field, or are polarized, or where the relativistic effects are important. The main motivation is due to the fact that the exchange-correlation hole is very different for the electrons with parallel and anti-parallel spins, and that LSD probably gives a better and correct description of the spherically averaged exchange-correlation hole. In this approximation, developed in early seventies from Von Bart and Hedin [80] and then implemented by Gunnarson and Lundqvist [81], the density is now *spin-polarized* with two contributions: $n^{\uparrow}(\mathbf{r})$ and $n^{\downarrow}(\mathbf{r})$. Considering an N-electrons Hamiltonian coupled with the magnetic field $\vec{B}(\mathbf{r})$ and the spin $\hat{\mathbf{s}}$ [79]

$$\hat{H} = \hat{T} + \hat{V}_{ee} + \sum_i v(\mathbf{r_i}) - 2\mu \sum_i \vec{B}(\mathbf{r_i})\hat{\mathbf{s}}^{\mathbf{i}}_{\mathbf{z}} \tag{2.30}$$

the density can be defined now as

$$n_\sigma(\mathbf{r}) = \sum_\sigma f_{\alpha\sigma} \mid \phi_{\alpha\sigma}(\mathbf{r}) \mid^2$$

with $f_{\alpha\sigma}$ occupation number between 0 and 1 and the energy like functionals of the spin polarized densities $n^{\uparrow}(\mathbf{r})$ and $n^{\downarrow}(\mathbf{r})$ such as:

$$\tilde{E} = T[n^{\uparrow}, n^{\downarrow}] + U[n] + E_{xc}[n^{\uparrow}, n^{\downarrow}] + \int d\mathbf{r}\, v(\mathbf{r})\, n(\mathbf{r}) - 2\mu \int d\mathbf{r}\, \vec{B}(\mathbf{r}) \sum_{\sigma} \sigma n_{\sigma}(\mathbf{r})$$

and minimizing the above functional with respect to the density $n_{\sigma}(\mathbf{r})$ through the application of a generalized Hohenberg-Kohn variational principle it's possible to achieve a set of Kohn-Sham like equation that held for the spin polarization:

$$\left\{ -\frac{1}{2}\nabla^2 + v_{eff}^{\sigma}(\mathbf{r}) \right\} \phi_{\alpha\sigma} = \varepsilon_i^{\sigma} \phi_{\alpha\sigma} \tag{2.31}$$

with an effective potential

$$V_{eff}(\mathbf{r}) = v_{ext}(\mathbf{r}) + \frac{1}{2} \int \frac{n(\mathbf{r}')}{|\mathbf{r} - \mathbf{r}'|} d\mathbf{r}' + V_{xc}^{\sigma}(\mathbf{r})$$

where the exchange-correlation potential is

$$V_{xc}^{\sigma}\left(\left[n^{\uparrow}, n^{\downarrow} \right]; \mathbf{r} \right) = \frac{\delta}{\delta n_{\sigma}(\mathbf{r})} E_{xc}\left[n^{\uparrow}, n^{\downarrow} \right] \tag{2.32}$$

and the direct Coulomb potential is

$$u([n]; \mathbf{r}) = \frac{\delta}{\delta\, n(\mathbf{r})} U[n] = \int d\mathbf{r}' \frac{n(\mathbf{r}')}{|\mathbf{r} - \mathbf{r}'|} \tag{2.33}$$

Spin density functional calculation would yield *exact* results of the exact $E_{xc}[n^{\uparrow}, n^{\downarrow}]$ were known and used; in the *local spin density* approximation one recovers

$$E_{xc}^{LSD}[n^{\uparrow}, n^{\downarrow}] = \int d\mathbf{r}\; n(\mathbf{r})\, \epsilon_{xc}\big(n^{\uparrow}(\mathbf{r}), n^{\downarrow}(\mathbf{r})\big) \tag{2.34}$$

where again $\epsilon_{xc}\big(n^{\uparrow}(\mathbf{r}), n^{\downarrow}(\mathbf{r})\big)$ is the exchange-correlation energy per particle of an electron gas with uniform spin densities $n^{\uparrow}$, $n^{\downarrow}$. It has worth underline that this approximation becomes exact when the spin densities vary slowly enough on the scale of the local Fermi wavelength and screening length [79, 80].

One step beyond: Gradient Expansion and GGA

A natural way to go beyond the LDA is to extend the exchange-correlation functional with terms containing the gradients of the density. Through the inclusions of these gradients, variations and changes in the density can be estimated and measured leading to a possible improvement of the results. *The*

Gradient Expansion offers systematic corrections to LSD electron densities that vary slowly over space and might appear to be a natural step beyond LSD. In the original papers of Hohenberg-Kohn and Kohn-Sham [65, 66] is already presented a gradient expansion based on the polarizability of the homogeneous electron gas. For densities $n(\mathbf{r})$ varying slowly over space and having weak variations so $n(\mathbf{r}) = n_0 + \Delta\, n(\mathbf{r})$, it's possible to expand the density around the point $\mathbf{r}$ taken to be the origin:

$$n(\mathbf{r}) = n + \nabla_i\, n(\mathbf{r})\, \mathbf{r}_i + \frac{1}{2} \sum \nabla_{ij}\, n(\mathbf{r})\, \mathbf{r}_i \mathbf{r}_j + \dots \tag{2.35}$$

substituting this expansion in the expression of E_{xc} it leads after some mathematical manipulation to the *gradient expansion*

$$E_{xc} = E_{xc}^{LDA} + \int G_2(n)\, (\nabla n)^2\, d\,\mathbf{r} + \int \left[G_4(n)\, (\nabla^2 n)^2 + \dots \right] d\mathbf{r} + \dots \tag{2.36}$$

where $G_2(n)$ is the universal functional appearing in the Kohn-Sham equations 2.17 defined as $G[n] = E_{xc}[n] + T_s[n]$. The terms of the series above can be resumed as:

$$E_{xc}^{(0)} = \int \epsilon \left(n(\mathbf{r}) \right) n(\mathbf{r})\, d\mathbf{r} \qquad \text{(LDA)} \tag{2.37}$$

$$E_{xc}^{(1)} = \int f^1 \left(n(\mathbf{r}),\, |\nabla n(\mathbf{r})| \right) n(\mathbf{r})\, d\mathbf{r} \qquad \text{(GGA)} \tag{2.38}$$

$$E_{xc}^{(2)} = \int f^2 \left(n(\mathbf{r}),\, |\nabla n(\mathbf{r})| \right) \nabla^2 n(\mathbf{r})\, d\mathbf{r} \tag{2.39}$$

$$\tag{2.40}$$

Here the $E_{xc}^{(0)}$ corresponds to the LDA level and requires the independently one variable calculated function $n(\mathbf{r})$, while the $E_{xc}^{(1)}$ is the so called *Generalized Gradient Approximation (GGA)* which requires the independently calculated *function of two variables*, $n(\mathbf{r})$ and $|\nabla n(\mathbf{r})|$.
According to J.P. Perdew and S. Kurth [82] a first measure of inhomogeneity can be obtained through the *reduce density gradient*

$$s = \frac{|\nabla n|}{2k_F n} = \frac{|\nabla n|}{2\,(3\pi^2)^{1/3}\, n^{4/3}} = \frac{3}{2} \left(\frac{4}{9\pi} \right)^{1/3} |\nabla r_s| \tag{2.41}$$

which measures how fast and how much the density varies on the scale of the local Fermi wavelength $\frac{2\pi}{k_F}$. Then, defining a second kind of length scale, the screening length $1/k_s$[2] and therefore another reduce density gradient

$$t = \frac{|\nabla n|}{2k_s n} = \left(\frac{\pi}{4} \right)^{1/2} \left(\frac{9\pi}{4} \right)^{1/6} \frac{s}{r_s^{1/2}} \tag{2.42}$$

[2] In high-density limit ($r_s \rightarrow 0$) the screening length is the only important length scale for the correlation hole, ($1/k_s \sim \mathbf{r}^{172}$)

it' s possible to write the functional T_s[n], E_x[n] (exchange energy) and E_c[n] (correlation energy) under a uniform density scaling [83] through a gradient expansion

$$T_s[n] = A_s \int d\mathbf{r}\, n^{5/3}\, [1 + \alpha s^2 + \ldots] \tag{2.43}$$

$$E_x[n] = A_x \int d\mathbf{r}\, n^{4/3}\, [1 + \mu s^2 + \ldots] \tag{2.44}$$

$$E_c[n] = A_x \int d\mathbf{r}\, n\, [\epsilon_c^{unif}(n) + \beta(n) t^2 + \ldots] \tag{2.45}$$

neglecting terms of higher order than $|\nabla n|^2$, what comes out is the *second-order gradient expansion* called *Gradient Expansion Approximation* (GEA). The(GEA) scheme assumes that the exchange-correlation functional depends **locally on the density** and on **the density gradient** and in particular even if the form of the expansion is easy to find, harder is to find out the expression for the coefficient that appear in Eq. [2.45]. The GEA is however found to give not so fairly accurate results with respect to the one provided by LDA. The Local Spin Density Approximation to E_{xc} (leading term in the gradient correction) provides good and realistic results for atoms, molecules and solids; but when introducing the second-order correction, which is the next naturally correction in the expansion, the approximation of E_{xc} gets worse. There are two main answer: the former is that the *realistic* electron density is not so close to a *slowly* varying density and the latter is that the GEA does not satisfy many exact constraints, such as for example the exchange-correlation hole sum rule. From this point of view the second-order generalized gradient approximation (GGA) to E_{xc} already defined in Eq. [2.40], can be write in a suitable way in order to correct the improper long-range behaviour of the exchange-correlation hole in GEA and to satisfy the sum rule. The GGA is schematically written

$$E_{xc}^{GGA} = \int f\left(n, |\nabla n|,\, \nabla^2 n\right) n(\mathbf{r})\, d\mathbf{r} \tag{2.46}$$

and with respect to LDA and LSD tends to improve total energies, atomization energies, energy barriers and structural energy differences; GGA also tends to soft bonds sometimes correcting and sometimes overcorrecting the LSD results, but nevertheless GGA gives a better description of density inhomogeneity better than LSD, as depicted in Table 7.3 . The first second-order gradient expansion was derived in 1968 by Ma and Brueckner [84]; then several different and interesting attempts followed in the next years by many contributors, since the 1991 when Perdew and other [85] introduce into the GEA the real space cutoffs $u(\mathbf{r} + \mathbf{u})$ and $u_c(\mathbf{r})$ for the exchange and the correlation that tends to improve GEA upon LSD at small u and tends to correct the spurious large-u values behaviour, providing this way a

Property	LSD	GGA
E_x	5% (not negative enough)	0.5%
E_c	100% (too negative)	5%
bond length	1% (too short)	1% (too long)
structure	overly favors close packing	more correct
energy barrier	100% (too low)	30% (too low)

Table 2.1: Typical errors for atoms, molecules and solids from self-consistent Kohn-Sham calculations within LSD and GGA approximation in the form depicted in this section.

powerful nonempirical scheme to construct GGA. The Perdew-Wang 1991 (PW91) functional an analytical fit to the numerical GGA described in [85] designed to satisfy the exact conditions described above; it is for most purposes equivalent to the "GGA made simple" scheme proposed by Perdew, Burke and Ernzerhof (PBE) [74] in the same year. Ideally the approximate E_{xc} functional should have a non-empirical derivation, be universal to work well at the same time with diverse system and be simple and accurate in order to facilitate its implementation in practical calculations. Since LSD and empirical-GGA have these structures, the aim of PBE was to retain all the correct features of LSD while adding others, such as for example the real-space cutoff scheme of PW91. The correlation energy can be written as

$$E_c^{GGA}[n^{\uparrow}, n^{\downarrow}] = \int d\mathbf{r}\, n \Big[e_c(r_s, \zeta) + H(\mathbf{r}_s, \zeta, t) \Big] \tag{2.47}$$

where e_c is the correlation energy per electron, r_s is the Seitz radius ($n = 3/4\pi {r_s}^3 = {k_F}^3/3\pi^2$) - the radius of a sphere which contains on average one electron, $\zeta = \frac{n^{\uparrow}(\mathbf{r}) - n^{\downarrow}(\mathbf{r})}{n^{\uparrow}(\mathbf{r}) + n^{\downarrow}(\mathbf{r})}$ is the spin polarization factor and $t = \frac{|\nabla n|}{2\phi k_s n}$ is a generalization of reduced density gradient Eq. [2.42] with

$$\phi(\zeta) = \frac{1}{2}\Big[(1+\zeta)^{2/3} + (1-\zeta)^{2/3} \Big]$$

a spin-scaling factor. If $H(\mathbf{r}_s, \zeta, t)$ is supposed to assume the following ansatz

$$H(r_s, \zeta, t) = \left(\frac{e^2}{a_0}\right) \gamma\, \phi^3 \ln \left\{ 1 + \frac{\beta}{\gamma} t^2 \Big[\frac{1 + A\, t^2}{1 + A\, t^2 + A^2\, t^4} \Big] \right\} \tag{2.48}$$

where

$$A = \frac{\beta}{\gamma} \left[exp \left\{ \frac{-\epsilon_c^{unif}}{\gamma\, \phi^3\, e^2/a_0} \right\} - 1 \right]^{-1}$$

the PBE functional will satisfy the properties of

1. *in slowly varying limit ($t \rightarrow 0$) H* tends to second-order gradient expansion
$$H \rightarrow \left(\frac{e^2}{a_0}\right) \beta \, \phi^3 \, t^2$$

2. *in rapidly varying limit ($t \rightarrow \infty$)*
$$H \rightarrow -\epsilon_c^{unif}$$
making the correlation vanish, since the sum rule for the correlation hole density $n_c \int d\mathbf{r} \, n_c(\mathbf{r}, \, \mathbf{r} + \mathbf{u}) = 0$ is satisfied only for $n_c = 0$ [3]

3. *under uniform scaling to high-density*, that means $n(\mathbf{r}) \rightarrow \lambda^3 \, n(\mathbf{r}) for \lambda \rightarrow \infty$ since $r_s \rightarrow 0 \; as \; \lambda^{-1} and \; t \rightarrow \infty \; as \; \lambda^{1/2}$, the correlation energy must scale to a constant cancelling the logarithmic singularity of ϵ_c^{LSD} in the high density limit.

Then the GGA exchange correlation part E_x will be:

$$E_x^{GGA} = \int d\,\mathbf{r} \, n \, \epsilon_x^{unif}(n) \, F_x(s) \tag{2.49}$$

with $\epsilon_x^{unif} = -3e^2 \, k_F \, 4/\pi$ and $F_x(0) = 1$ to recover the correct uniform gas limit. Then, to recover and visualize better the **gradient corrected non locality** behaviour it' s more useful to write

$$E_{xc}^{GGA}[n^{\uparrow}, \, n^{\downarrow}] \approx \int d\,\mathbf{r} \, n(\mathbf{r}) \big(- \frac{c}{r_s} \, F_{xc}(r_s, \zeta, s) \big) \tag{2.50}$$

where $c = (3/4\pi)(9\pi/4)^{1/3}$ and $-c/r_s = \epsilon_x(r_s, \zeta = 0)$ is the exchange energy per electron of a spin-unpolarized uniform electron gas.

Generalized Gradient Approximations generally lead to improved bond angles, lengths and energy; in particular the strengths of hydrogen bonds and other weak ones between closed shell systems are significantly better reproduced than by local density calculations, in particular at a modest additional computational cost. The PBE functional, that remedies to some lack of the PW91, is nowadays the most popular GGA functional; it can be presented as a *first principle* functional since it' s constructed from known limits of the homogeneous electron gas and scaling relations and it doesn't contain any parameters.

[3] For example, in the electron density tail of a finite system, the contribution of the exchange energy density and the potential is bigger than the correlation counterparts in reality, but not in LSD.

2.2.2 The Meaning of Kohn-Sham eigenvalues

Fake plastic Kohn-Sham eigenvalues?

The question arise spontaneously: which meaning have the eigenvalues once resolved the Kohn-Sham single-particle equations? Although the Density Functional formalism has been developed to achieve the *ground-state* properties, in many cases this scheme is also use to get results related to the *excited-state properties* of the systems. This means the possibility to interpret the calculated eigenvalues as excitation energies related to the addition or removal of an electron to the system.

In the Hartree-Fock method the eigenvalues have a physical meaning and are treated exactly as *real excitation energy* through the Koopmans' theorem [86] that proof how eigenvalues can be considered as *addition and/or removal energies*:

$$\epsilon_i^{HF} = E(n_1, \ldots, n_i, \ldots, n_N) - E'(n_1, \ldots, n_i - 1, \ldots, n_N) \tag{2.51}$$

It' s clear from the above relation that the Hartree-Fock eigenvalue ϵ_i^{HF} defined as an energy difference between the total energy of the N-electron system E and the energy of the $N-1$-electron E' ($n_1, \ldots, n_N$ are the electrons occupation numbers), is associated to the energy required to remove an electron from the orbital i. The theorem requires that the orbitals don't relax each time the occupation number n_i is changed; this condition holds in general in systems of non-interacting electron, where the eigenvalues of the one-electron Schrödinger equation describe the energies necessary to remove an electron from the occupied orbitals or to add one to the empty ones. Unfortunately the same doesn't happen in DFT, since there's no analogous to the Koopmans' theorem and due to fact that Kohn-Sham eigenvalues (ϵ_i^{KS}) enter the formalism as *Lagrange multipliers* in Eq. [2.11] to satisfy the request of orthogonality of the $\varphi_i(\mathbf{r})$ orbitals, they don't have any physical meaning. The only KS eigenvalue that has an unambiguous meaning in the *exact DFT* is the energy related to the highest occupied orbital ($HOMO$). The Janak' s theorem [87], in fact, asserts that in the *exact* DF formalism the definition of

$$\epsilon_i(n_1, \ldots\ldots, n_N) = \frac{\partial E}{\partial n_i}$$

and of the total energy difference such as

$$\begin{aligned} E(n_1, \ldots, n_i, \ldots, n_N) \quad - \quad & E(n_1, \ldots, n_i - 1, \ldots, n_N) = \\ = \quad & \int_0^1 d\, n\, \epsilon_i(n_1, \ldots, n_i + n - 1, \ldots, n_N) \end{aligned} \tag{2.52}$$

have formal justification only when refers to the ground-state of the system with N and $N-1$ particles, where $N = \sum n_i$. In this regime ϵ_i^{KS} represents

the *ionization potential* [88, 89, 90, 91], i.e. the energy required to remove the topmost electron. Despite these theoretical limitations, the usage of the Kohn-Sham eigenvalue differences to discuss excitation energies became a common procedure in practice, and they have been demonstrated to represent trends in excitation energies. Solving the KS equations is the most common way to predict electronic Bloch's band structure of real interacting solids: $\epsilon(\mathbf{k})$ would represent the general shape of the excitation energies, but the curves tend to be shifted by an almost $\mathbf{k}$-independent amount respect to the correct values given by experiments.
Trying to calculate it, as a difference between the Kohn-Sham eigenvalues, leads to a seriously underestimation of the fundamental band gap [89, 92, 93, 94, 95, 96].

Mind the gap! - an XC discontinuity issue

Since these one particle KS eigenvalues are used to evaluate the spectra of the solids without any formal justification, several discrepancies have been found between the calculated band gaps within XC functional approximation and the experimental measured gaps. In particular huge differences arise for semiconductors and insulators: the KS energy gap calculated within the Local Density Approximation are underestimated by 30-50% with respect to the band gap observed in the optical spectrum, as shown in Table [2.2]. This failure involves not only LDA but every sort of approximation that go beyond, and as Perdew and Levy have shown [89], an explicit connection between the Kohn-Sham gap ϵ_g^{KS} and the exchange-correlation functional used exists implying therefore the add of some corrections.

	LDA	many-body GW [97]	Expt.
Diamond	3.9	5.6	5.48 [98]
Silicon	0.5	1.19	1.17 [98]
Germanium	< 0	0.75	0.744 [98]
LiCl	6.0	9.1	9.4 [99]

Table 2.2: Results for the fundamental energy gap calculated for different materials in LDA and within the many-body Green function approach compared with the experimental values. All energy in eV.

To better understand the problem, it's worth pointing out that the band gap is defined in term of the *ionization potential (IP)* and *electron affinity*

(EA):

$$IP = -\Big(E_N - E_{N-1}\Big) = \epsilon_v \tag{2.53a}$$

$$EA = -\Big(E_{N+1} - E_N\Big) = \epsilon_c \tag{2.53b}$$

where $IP = \epsilon_v$ is the energy required to remove an electron in the state v from the system, while $EA = \epsilon_c$ is the energy required to add an electron in the state c to the system and E_N is the total energy of the system with N electrons. The band gap is defined as the difference between the largest addition energy and the smallest removal energy of an electron:

$$\begin{aligned} E_{gap} &= IP - EA = \big[E_{N-1} - E_N\big] - \big[E_N - E_{N+1}\big] \\ &= E_{N+1} + E_{N-1} - 2E_N \end{aligned} \tag{2.54}$$

This gap is defined as *quasi-particle gap* E_{qp} while the *optic gap* is defined as

$$E_{opt} = E_{qp} - \Delta\, E_b^{eh} \tag{2.55}$$

since it takes into account the interaction between electron and hole pairs created during the optical excitation process, as it will be discussed in Sec. [3].
The band gap could be also defined as

$$E_{gap} = \varepsilon_{LUMO} - \varepsilon_{HOMO}$$

where the $HOMO$ (Highest Occupied Molecular Orbital) equals $-IP$ and $LUMO$ (Lowest Unoccupied Molecular Orbitals) is $-AE$. In the Hartree-Fock scheme, where the system states are described by single Slater determinants, the energy gap $(\varepsilon_{LUMO} - \varepsilon_{HOMO})$ would yield to the real energy gap in solids; since the single determinant doesn't provide a good description of the energy states (it neglects the effect of polarization related to the addition or removal of an electron), the HF energy gap results inadequate and it tends generally to overestimate the band gaps. In finite system the band gap can be addressed as HOMO-LUMO energy difference, while for extended system this doesn't hold. The above definition of E_{gap} in Eq. [2.54] represents the onset of the continuum of optical transitions in solids where the gap is *direct* (it means that the lowest empty state and he highest occupied state have the same $\mathbf{k}$ vector).

The reason of the inaccuracy of the DFT-LDA in predicting the band gap of several materials arises from the *discontinuity of the XC potential*, a pathological non-analytical behaviour of the xc energy functional that enters directly in the calculation of the energy gap. Since the band gap can be written in terms of the changes in the total ground-state energy of the system after

addition or removal of an electron, via exact DFT-KS eigenvalues, it can be also related to the meaning of *quasi-particle band gap*:

$$E_{gap} = \varepsilon^{KS}_{N+1}(N+1) - \varepsilon^{KS}_{N}(N) \tag{2.56}$$

where $\varepsilon^{KS}_{N+1}(N+1)$ is the energy of the highest occupied KS orbital of the $N+$ 1 electron system, and $\varepsilon^{KS}_{N}(N)$ is the highest level of the N electron system (in *exact* DFT both can be considered as HOMO and formally correct) [88]. For a non interacting system the gap can be obtained directly in terms of difference between orbital energies of the N electron system

$$E^{KS}_{gap} = \varepsilon^{KS}_{N+1}(N) - \varepsilon^{KS}_{N}(N) \tag{2.57}$$

where $\varepsilon^{KS}_{N+1}(N+1)$ it has been replaced by $\varepsilon^{KS}_{N+1}(N)$. It comes out that the quasi-particle gap E_{gap} defined above in Eq. [2.56] differs from the gap E^{KS}_{gap} defined in Eq. [2.60] for the N electron system, by an amount defined as Δ_{xc}:

$$\begin{aligned} E_{gap} - E^{KS}_{gap} &= \varepsilon^{KS}_{N+1}(N+1) - \varepsilon^{KS}_{N}(N) - \varepsilon^{KS}_{N+1}(N) + \varepsilon^{KS}_{N}(N) = \\ &= \varepsilon^{KS}_{N+1}(N+1) - \varepsilon^{KS}_{N+1}(N) = \Delta_{xc} \end{aligned} \tag{2.58}$$

Thus the gap can be defined as

$$E_{gap} = \varepsilon^{KS}_{N+1}(N) - \varepsilon^{KS}_{N}(N) + \left[\varepsilon^{KS}_{N+1}(N+1) - \varepsilon^{KS}_{N+1}(N)\right] = E^{KS}_{gap} + \Delta_{xc} \tag{2.59}$$

where E^{KS}_{gap} is the usually called DFT band gap, that corrected by the amount Δ_{xc} gives the true *quasi-particle* band gap. The Δ_{xc} quantity is related to the difference between the energies of the $(N+1)$-th orbitals of the KS system that correspond to the neutral and ionized electron system. Δ_{xc} is called the *discontinuity* of the exchange-correlation potential and it' s related to the **non analytical** behaviour of the exchange-correlation potential when the number of particles of the system varies, as schematically illustrated in Fig. 2.2, [100, 101]. This discontinuity can be defined in terms of V_{xc} (the exact DFT exchange-correlation potential)

$$\Delta_{xc} = V^{(N+1)}_{xc}(\mathbf{r}) - V^{(N)}_{xc}(\mathbf{r}) \tag{2.60}$$

since V_{xc} is the only part of the DFT potential that can be a non-analytical functional of the charge density when the number of particle is varied. The addition or removal of an electron in a system, infact, causes infinitesimal variations in the density, and the DFT eigenvalues are consistently altered. In a system with $N >> 0$ the chemical potential (Fermi energy or for metallic systems the minimum energy required to add or remove an electron) is given by the DFT eigenvalue of the highest occupied level:

$$\mu_N = \frac{\partial E^{tot}_N}{\partial N} = \varepsilon^{KS}_N(N)$$

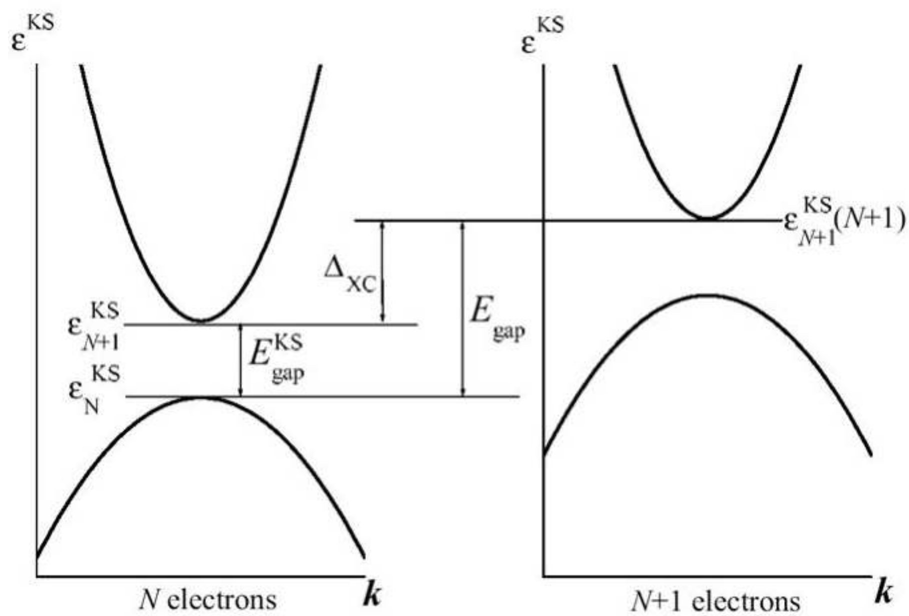

Figure 2.2: Illustration of the significance of Δ_{xc} within a sketch of the Kohn-Sham band structure of a semiconductor. The exact KS DFT one-electron energies are shown in the form of a band structure for the N (left) and $N+1$ (right) particle system. After the addition of an electron into the empty conduction band, the whole band structure shifts up a quantity Δ_{xc}.

In metals $IP = EA = \mu_N = \varepsilon_N^{KS}(N)$, while in semiconductors there' s an energy gap and since $IP \neq EA$, the energy required to remove an electron is not the same needed to add another electron to the system. Following Perdew and Levy [89], the Eq. [2.53b] can be rewritten in terms of the chemical potential of Eq. [2.11] like

$$\begin{aligned} IP &= -\mu_N(N-\delta) \\ EA &= -\mu_N(N+\delta) \end{aligned} \tag{2.61}$$

thus the energy gap become $E_{gap} = IP - EA = \mu_N(N+\delta) - \mu_N(N-\delta)$ where δ represents the change in the number of particle when adding or removing an electron. Through the definition of μ in DFT, (it enters in KS scheme first of all as a Lagrange multiplier, as shown in Eq. [2.11]) it leads to

$$E_{gap} = -\frac{\delta\, E_v[n]}{\delta\, n_-} + \frac{\delta\, E_v[n]}{\delta\, n_+} = \frac{\delta\, T_s}{\delta\, n_+} - \frac{\delta\, T_s}{\delta\, n_-} + \frac{\delta\, E_{xc}}{\delta\, n_+} - \frac{\delta\, E_{xc}}{\delta\, n_-} \tag{2.62}$$

where $n_- = N - \delta$ and $n_+ = N + \delta$ with $\delta \to 0$. For a non-interacting system,

$$E_{gap} = E_{gap}^{KS} = \frac{\delta\, T_s}{\delta\, n_+} - \frac{\delta\, T_s}{\delta\, n_-}$$

while for an interacting one the contribution given by E_{xc} should be included,

$$E_{gap} = E_{gap}^{KS} + \frac{\delta\, E_{xc}}{\delta\, n_+} - \frac{\delta\, E_{xc}}{\delta\, n_-} = E_{gap}^{KS} + \Delta_{xc}$$

To note $\frac{\delta\, E_{xc}}{\delta\, n_+} - \frac{\delta\, E_{xc}}{\delta\, n_-} = C$, where C is a positive constant that represents the discontinuity of the right and left derivatives when the number of electron increases or decreases jumping from $N+\delta$ to $N-\delta$. Then the contribution to the band gap can be divided into two components, the KS gap E_{gap}^{KS} and the Δ_{xc}; an improve in LDA would yield better values for E_{gap}^{KS} and a improved description of the V_{xc} potential will give a better estimation of the amount Δ. In particular if Δ were zero (or very close to zero) the difference between the calculated E_{gap} and the DFT-LDA gap E_{gap}^{LDA} would arise just from limitation in the local density approximation. Nonetheless, LDA has revealed a good approximation when calculating total energies and densities of bulk semiconductors, and improvements upon LDA have been demonstrated to change the KS energy gap only very little. For counterpart, the Δ amount represents a significant part in the correct estimation of the LDA energy gap, up to the 80% fraction of the whole LDA error for semiconductors and insulators, as depicted in Table 2.3 [102].

	Si	GaAs	AlAs	Diamond
Δ_{xc}	0.58	0.67	0.65	1.12
Band Gaps:				
KS-LDA	0.52	0.67	1.37	3.90
G_0W_0	1.24	1.58	2.18	5.33
Expt.	1.17	1.63	2.32	5.48

Table 2.3: The xc discontinuity Δ_{xc} and the calculated and experimental band gap for semiconductors and insulators (all values in eV).

2.3 The Plane Wave Pseudopotential approach

The Density Functional is a very efficiently scheme to calculate the total energy of solids through the iteratively solution of the Kohn-Sham equations. Since the numerical resolution of this procedure is very computational demanding, the Density Functional formalism can be setup into the so called *plane wave pseudopotential approach*, consisting in the expansion of the Hamiltonian $\hat{H}$ into a plane wave (PW) basis set and in the introduction of the pseudopotential approximation to remove the contribution of the core electrons from the calculation in order to render the computation of the total energy easier and less expensive.

Plane wave expansion

The *plane wave* basis set expansion in solids take advantage of the periodicity of the crystal lattice. According to the Bloch's theorem the secular equation with the Hamiltonian operator $\hat{H}^{KS}$ derived from the solution of the Kohn-Sham equation [2.29]

$$\Big(-\frac{\hbar^2}{2m}\nabla^2 + V_{ion}(\mathbf{r}) + V_H(\mathbf{r}) + V_{xc}(\mathbf{r})\Big)\,\psi_{kn} = \epsilon_{kn}\,\psi_{kn}$$

is expanded over a *complete* and *orthogonal* set of plane waves

$$\langle \mathbf{r}\,|\,\mathbf{k}+\mathbf{G}\rangle = \frac{1}{\mathrm{Vol}}\,e^{i(\mathbf{k}+\mathbf{G})\cdot\mathbf{r}}$$

to assume a particularly simple form, where n is the band index, $\mathbf{k}$ Bloch's vector in the Brillouin Zone and $\mathbf{G}$ the reciprocal lattice vectors. Due to the periodicity of the crystal, the Bloch's theorem asserts that also the single particle wavefunction describing the electronic states of the system can be expanded in a discrete set of plane waves at each $\mathbf{k}$-points:

$$\psi_{\mathbf{k}n}(\mathbf{r}) = \sum_{\mathbf{G}} c_{\mathbf{G}}(\mathbf{k}\,n)\,e^{i\mathbf{G}\cdot\mathbf{r}}\,e^{i\mathbf{k}\cdot\mathbf{r}} \tag{2.63}$$

where the coefficient $C_{\mathbf{g}}$ have to be determined through the diagonalization of the KS Hamiltonian in the new basis set:

$$\sum_{\mathbf{G}'} H_{\mathbf{G}\mathbf{G}'}(\mathbf{k})\, c_{\mathbf{G}'}(\mathbf{k}n) = \epsilon_{\mathbf{k}n}\, c_{\mathbf{G}}(\mathbf{k}n) \tag{2.64}$$

where

$$H_{\mathbf{G}\mathbf{G}'}(\mathbf{k}) = \frac{1}{2m} \mid \mathbf{k}{+}\mathbf{G} \mid^2 \delta_{\mathbf{G},\mathbf{G}'} + V_{ion}(\mathbf{k}{+}\mathbf{G}, \mathbf{k}{+}\mathbf{G}') + V_h(\mathbf{G}{-}\mathbf{G}') + V_{xc}(\mathbf{G}{-}\mathbf{G}') \tag{2.65}$$

In this way the kinetic energy is diagonal and the potentials are described in terms of their Fourier transforms, in particular, V_H and V_{xc} are local in space and don't depend explicitly from $\mathbf{k}$ but only from the vectors of the reciprocal lattice through the relation $\mathbf{G} - \mathbf{G}'$. To note that if the crystal has a center of inversion which is chosen as the origin, the secular equation is real, otherwise it's necessary complex.

The Hamiltonian to diagonalize is a matrix whose size is determined by the number of elements, hence by the number of vectors $\mathbf{G}$ included in the expansion, that in principle are infinite when concerning with a periodic crystal. The coefficients $c_{\mathbf{G}}(\mathbf{k}n)$ with small kinetic energy $(\hbar^2/2m)\,|\mathbf{k}+\mathbf{G}|^2$ give a more important contribution in the expansion than those with larger kinetic energy; also in the calculation of the density $n(\mathbf{r}) = \sum_{\mathbf{k}\,n} |\,\psi_{\mathbf{k}\,n}(\mathbf{r})|^2\, f(\varepsilon_{\mathbf{k}\,n})$ only the lowest eigensolutions are needed, converging as the dimension N of the secular equation matrix. Nevertheless, since the diagonalization time increase as N^3, one needs some limitation to the size of the matrix: thus the plane wave basis set can be truncated neglecting the plane waves having kinetic energy greater than the value imposed by some particular *energy cut-off*. This *kinetic energy cutoff*, applied to an infinite basis set, is expressed by

$$\frac{1}{2}|\,\mathbf{k}+\mathbf{G}\,|^2 \;\leq\; E_{\text{kin}}$$

and renders the plane wave expansion finite and discrete, but at the same time, introduce some kind of errors in the final computed total energy. Increasing the cutoff energy the magnitude of the errors will be reduce, improving total energy convergence but slowlying down the computational time. It's worth pointing out that since PWs are extended waves, they can't well reproduce localized functions such as the charge density around the nuclei or even worse the orthogonalization wiggles of inner core states. In order to describe features varying on a length of scale δ, one needs PW components up to $q \sim 2\pi/\delta$, that in a solid means $\sim 4\pi\,(2\pi/\delta)^3/\Omega_{BZ}$ (in Diamond, fcc lattice, PWs $\sim$250,000 are too much for practical use). The number of plane waves N_{pw} scales like

$$N_{pw} \,\propto\, \Omega\,(E_{cutoff})^{3/2}$$

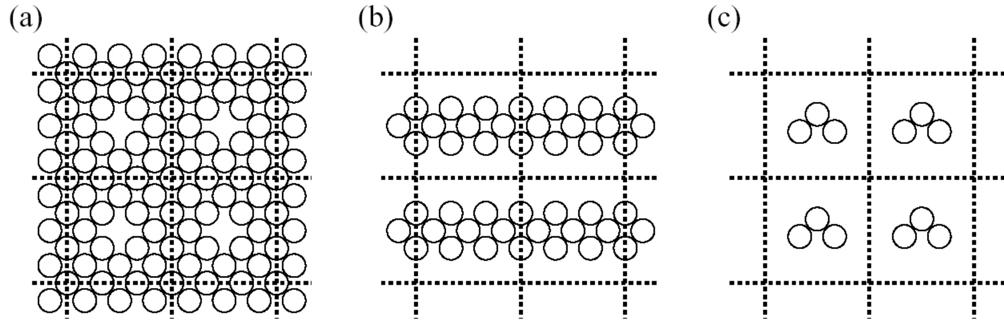

Figure 2.3: Schematic illustration of a supercell geometry (a) for defect vacancy in a bulk crystal, (b) for a surface and (c) for an isolated molecule. The supercell boundaries are depicted by the dotted line.

Periodic Supercells

Since one deals with periodic infinite systems, in which holds the Bloch's theorem, is convenient to simulate the systems with a periodically repeated fictitious *supercell*. Periodic boundary condition are applied to the supercell in order to be reproduced throughout space accordingly to the periodicity of the systems along the three directions. The system cell is now large by construction: the primitive cell of the material is repeated n_i times along the lattice vector $\mathbf{a}_1, \mathbf{a}_2, \mathbf{a}_3$, leading to cell of $n_1 \times n_2 \times n_3 \times N_0$ atoms (where N_0 is the number of atoms in the primitive cell). Accordingly, the Brillouin Zone (BZ) is reduced by a factor of n_i in the respective directions. The cell can be either the primitive unit cell of a crystal or a large supercell containing a sufficient number of independent atoms to mimic locally an amorphous, a liquid, but also a solid with point defect, surfaces or isolated molecules as illustrated in Fig. 2.3. When dealing with such a systems, slabs, isolated molecules or cluster and solids with point defects, is important to make the supercell big enough in order to leave sufficient vacuum space around to avoid interaction between the periodic neighboring replica [103, 104].

Brillouin Zone K-point sampling

Through the plane wave expansion basis set the "sum over the Brillouin zone **k**-points" is mandatory when calculating the charge density $n(\mathbf{r})$ in a periodic system and the related summation is made over an *infinite* number of **k**-points:

$$n(\mathbf{r}) = \sum_{k} \sum_{i} |\, \psi_{\mathbf{k},i}(\mathbf{r})\,|^2$$

When assuming the Born-Von Karman periodic boundary conditions $\psi\,(\mathbf{r} + L\,\mathbf{R}) = \psi(\mathbf{r})$ (where $L = L_1\,L_2\,L_3$ equals the numbers of cells of

the crystal) the discrete sum become an integration over the BZ and the electronic states are allowed only for a set of **k**-points whose density is proportional also to the volume of the solid. Through the Bloch theorem the electronic state to calculated moves from infinite to a finite amount for a infinite number of **k**-points. For insulator and semiconductors it has been shown that the integral can be approximated by a discrete sum over an good number of **k**-points. Symmetries can help to reduce the number of points: only one **k**-point is assigned to represent a so called *star* (the set of **k**-points equivalent by symmetry) with a *weight* w_i proportional to the number of **k**-points in the set. Thus the infinite sum over the BZ is replaced by a discrete sum over a set of points $\{\mathbf{k}_i\}$ and *weights* w_i:

$$\frac{1}{L}\sum_{\mathbf{k}} f_{\mathbf{k}}(\mathbf{r}) \rightarrow \sum_{i} w_i\, f_{k_i}(\mathbf{r})$$

The particular set of **k**-points are called "*special points*" and can be obtained through different methods such as Chadi-Cohen [105] or Monkhorst-Pack [106] that afford to calculate total energy and electronic potential with accuracy over a very small set of **k**-points. For counterpart, metals require more **k**-points for an accurate sampling over the BZ of the Fermi surface; thus one can use the *tetrahedron method* or a *Gaussian broadening* to treat properly fractional occupation of metals.

Ab initio Pseudopotentials

The potential experienced by an electron in condensed aggregate of atoms can be divided into two main terms: the nuclei interaction potential and the electron-electron interaction potential. Moreover also the electrons can be separate into two regions with different characteristics: the region near the nuclei, the *core region*, contains the innermost tightly bound core electrons, which respond very little to the presence of neighboring atoms and do not play a significant role in the chemical bindings of atoms, and the outermost remaining region in the atom containing the *valence electrons* which really determines the chemical bindings of atoms, especially in metals and semiconductors. Thus the *core electrons* can be ignored reducing the atom to a ionic core that interacts via an *effective potential* with the valence electrons: this is the *frozen core approximation.* Thus the KS equation are resolved with a new effective potential interaction where the common all electrons-nuclei interaction is replace by a "fictitious" interaction between valence electrons and ionic core. This interaction that approximate the potential felt by the valence electrons is called **pseudopotential** and was first introduced by Enrico Fermi in the 1934 [107], then developed around the 60-70's through the *empirical pseudopotential* and the *ab initio pseudopotential* formulation by Phillips and Kleinman [108].

The *valence* wavefunction have total energy higher than the *core* states and in the core region the valence electrons are far less likely to be found. However since they experience the same Coulomb potential there and they must therefore have an even higher kinetic energy, the states are here described as *very rapidly oscillating* wavefunctions as a consequence of the strong ionic potential in this region. These oscillations are at the origin of the *orthogonality* between the *core* wavefunctions and the *valence* wavefunctions which is required by the exclusion principle: $\int d\mathbf{r}\, \psi_{c,\mathbf{k}}(\mathbf{r})^* \, \psi_{v,\mathbf{k}}(\mathbf{r}) \; = 0$ (in the core region the oscillations have to interweave in order to give a vanishing integral).

The pseudopotential formalism has grown out of the **Orthogonalized Plane Waves (OPW)** methods developed in 1940 [109] by Herring and in which the valence wave functions are expanded in a set of a plane waves (PW) which are *orthogonalized* to all the core wavefunctions $|\, \psi_c \,\rangle$. In this approach the rapid oscillations of the wavefunction in the core region are compensated via a plane wave expansion in the interstitial regions among the nuclei. Since the core states $|\, \psi_c \,\rangle$ are rapidly oscillating around the nuclei, the valence wavefunctions $|\, \psi_v \,\rangle$ will have strongly oscillations to guarantee the orthogonality with respect the $|\, \psi_c \,\rangle$ core. Then, to describe these rapid oscillations a great number of plane waves are needed with a huge computational effort. However, if the *core* states don't appear in the calculation one can substitute the *valence* wavefunction with some **pseudowavefunctions** identical to the real wavefunction and with no nodes beyond some *cutoff radius* $\mathbf{r_c}$ ($r < r_c$).
Defining the normalized plane wave $|\, \mathbf{k} \,\rangle$ as

$$|\, \mathbf{k} \,\rangle = \frac{1}{\sqrt{\Omega}}\, e^{i\mathbf{kr}}$$

the OPW χ is defined as a plane wave PW to which have been subtracted the core orthogonality wiggles in the core region in order to be orthogonal to all the core wavefunctions ψ_{core}

$$|\, \chi \,\rangle = |\, \mathbf{k} \big\rangle - \sum_{c}^{core} a_c \,|\, \Psi_c(\mathbf{r}) \big\rangle = |\, \mathbf{k} \,\rangle - \sum_{c'} |\, \psi_{c'} \,\big\rangle \big\langle\, \psi_{c'} \,|\, \mathbf{k} \,\rangle = (1 - \hat{\mathbb{P}}) |\, \mathbf{k} \,\big\rangle \quad (2.66)$$

The valence wavefunction can be therefore expanded over the obtained OPW basis set

$$|\, \psi_{\mathbf{k},v} \,\rangle = \sum_{G} a^{v}_{\mathbf{k+G}} \;|\, \chi_{\mathbf{k+G}} \,\rangle \quad (2.67)$$

with the orthogonality condition of the PW with all the *core* states:

$$\begin{aligned}
\langle \Psi_c | \chi \rangle &= \langle \Psi_c | \mathbf{k} \rangle - \sum_{c'}^{core} \langle \Psi_c | \Psi_{c'} \rangle a_{c'} = 0 \\
&\Rightarrow \langle \Psi_c | \mathbf{k} \rangle - \delta_{cc'} \, a_{c'} = 0 \\
&\Rightarrow \langle \Psi_c | \mathbf{k} \rangle = \sum_{c}^{core} a_c
\end{aligned} \tag{2.68}$$

Then substituting the explicit expression of OPW $|\chi\rangle$ in the expansion of *valence* wavefunction one gets

$$|\psi_{\mathbf{k},v}\rangle = \sum_G a^v_{\mathbf{k}+\mathbf{G}} \Big[|\mathbf{k}\rangle - \sum_c |\psi_c\rangle \langle \psi_c | \mathbf{k}+\mathbf{G} \rangle \Big] = (1-\hat{\mathbb{P}}) |\mathbf{k}+\mathbf{G}\rangle \tag{2.69}$$

where $\mathbf{G}$ is the sum over the reciprocal lattice vectors that can be truncated through the introduction of the *cutoff energy.* Defining a **pseudowave-function** $\varphi^{ps}_{\mathbf{k}}$ like

$$|\varphi^{ps}_{\mathbf{k}}\rangle = \sum_{\mathbf{G}} a^v_{\mathbf{k}+\mathbf{G}} |\mathbf{k}+\mathbf{G}\rangle \tag{2.70}$$

we get

$$|\psi_{\mathbf{k},v}\rangle = |\psi_{\mathbf{k},v}\rangle + \sum_c^{core} a^v_c |\psi_c\rangle = (1-\hat{\mathbb{P}}) |\varphi_{\mathbf{k}}\rangle \tag{2.71}$$

One can see that the "real" valence wavefunction can be expressed as the sum of two terms: (i) a smooth function, the **pseudowavefunction** and (ii) an oscillating term that results from the orthogonalization of the *valence* to the inner *core* orbitals. Then, applying $\hat{H}$ to the valence states $\psi_{\mathbf{k},v}$ gives

$$\begin{aligned}
&\hat{H} |\psi_{\mathbf{k},v}\rangle = E_v |\psi_{\mathbf{k},v}\rangle \\
&\hat{H} \, (1-\hat{\mathbb{P}}) |\varphi^{ps}_{\mathbf{k}}\rangle = E_v \, (1-\hat{\mathbb{P}}) |\varphi^{ps}_{\mathbf{k}}\rangle \\
&\hat{H} |\varphi^{ps}_{\mathbf{k}}\rangle - \hat{H} \hat{\mathbb{P}} |\varphi^{ps}_{\mathbf{k}}\rangle = E_v |\varphi^{ps}_{\mathbf{k}}\rangle - E_v \hat{\mathbb{P}} |\varphi^{ps}_{\mathbf{k}}\rangle \\
&\Big[\hat{H} + (E_v - \hat{H}) \hat{\mathbb{P}} \Big] |\varphi^{ps}_{\mathbf{k}}\rangle = E_v |\varphi^{ps}_{\mathbf{k}}\rangle
\end{aligned} \tag{2.72}$$

where defining $\hat{H} + (E_v - \hat{H})\hat{\mathbb{P}} = H^{ps}$ as **pseudohamiltonian** gives

$$\begin{aligned}
\Big[\hat{H} + (E_v - \hat{H}) \hat{\mathbb{P}} \Big] |\varphi^{ps}_{\mathbf{k}}\rangle &= \hat{H} + (E_v - \hat{H}) \sum_c |\psi_c\rangle \langle \psi_c | \varphi^{ps}_{\mathbf{k}}\rangle \\
&= \hat{H} + \sum_c \big[E_v - E_c \big] |\psi_c\rangle \langle \psi_c | \varphi^{ps}_{\mathbf{k}}\rangle
\end{aligned} \tag{2.73}$$

Finally it results

$$\Big[\hat{H} + \sum_c \big[E_v - E_c \big] |\psi_c\rangle \langle \psi_c | \Big] |\varphi^{ps}_{\mathbf{k}}\rangle = E_v |\varphi^{ps}_{\mathbf{k}}\rangle \tag{2.74}$$

from which it can be possible to extract the form of the **pseudopotential** V^{ps}

$$V^{ps} = V + \sum_c \left[E_v - E_c \right] | \psi_c \rangle \langle \psi_c \quad (2.75)$$

The **pseudopotential** described here follows the formulation gives by Phillips and Kleinman [108] and can be view as a in term of with the following main characteristics:

- it is *spatially non local* since it's depends on $\mathbf{r}$ and $\mathbf{r}'$ and it uses different components in relation to different channels ℓ of *angular momentum* and it is *energy dependent* since it depends on the eigenenergy of the state one wishes to find;

- $\left\{ \sum_c \left[E_v - E_c \right] | \psi_c \rangle \langle \psi_c \right\}$ can be considered as a *short-ranged repulsive* correction to the "real" *long-ranged attractive* potential V: near the core both parts completely cancel each other and the whole potential is "well-behaved" and weaker than the true potential near the core according to the *Phillips-Kleinman cancellation theorem*; this implies also that the **pseudowavefunctions** are *smooth* and not oscillate in the core region, as schematically shown in Fig. 2.4 .

- there exists also a normalization problem: although the valence pseudowavefunction $| \varphi_{\mathbf{k}}^{ps} \rangle$ is globally normalized it doesn't reproduce exactly the norm of the real wavefunction outside the core region. From the condition $\langle \psi_v | \psi_v \rangle = 1$ holds

$$\begin{gathered} 1 = \langle \varphi_{\mathbf{k}}^{ps} | \varphi_{\mathbf{k}}^{ps} \rangle - 2 \sum \langle \psi_c | \varphi_{\mathbf{k}}^{ps} \rangle \langle \varphi_{\mathbf{k}}^{ps} | \psi_c \rangle + \sum_c | \langle \psi_c | \varphi_{\mathbf{k}}^{ps} \rangle |^2 \\ \Rightarrow \langle \varphi_{\mathbf{k}}^{ps} | \varphi_{\mathbf{k}}^{ps} \rangle = 1 + \sum_c | \langle \psi_c | \varphi_{\mathbf{k}}^{ps} \rangle |^2 \end{gathered} \quad (2.76)$$

  this difference has to be connected with the so called *orthogonality hole*. The lack of charge density between the valence and the core regions produces this *non* norm-conservation behaviour giving rise to errors and serious problem in the self-consistent calculations.

Since in this thesis work we had used the **norm-conserving** pseudopotential to treat properly the optical features and the **ultrasoft** pseudopotential that allows to manage systems with several hundreds of atoms per unit cell in order to the structural and electronic properties, a brief resume of their main features will follow.

Norm-Conserving pseudopotential

The *norm-conservation* idea was introduce for the first time by Topp and Hopfield [110] in 1974 in the context of empirical pseudopotential and then

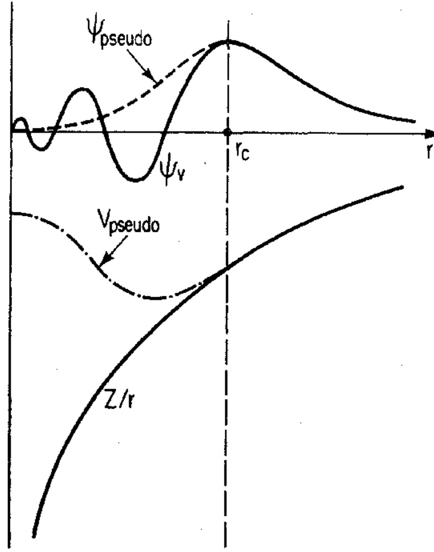

Figure 2.4: How the "pseudo" appears : all-electron wavefunction and potential (solid lines) and pseudopotential and pseudowavefunction (dashed lines). The *cutoff radius* at which the all-electron and pseudo- wavefunction match is labelled by $\mathbf{r}_c$

incorporated into the *ab initio* formulation by Hamman, Schlüter and Chiang [111] in 1979 and then refined by Bachelet, Hamman and Schlüter [112] in 1982. Generically the modern pseudopotentials are obtained inverting the Schrödinger *radial* equation for a given reference configuration applied to the all-electron (AE) wavefunction decomposed into a *radial* R_ℓ and a *spherical* $Y_{\ell,m}$ (spherical harmonic) part and resolved in a self-consistently way:

$$\psi^{AE}(\mathbf{r}) = \sum_{\ell,m} R_\ell^{AE}\, Y_{\ell,m}(\Omega)$$

$$\left(-\frac{\hbar^2}{2m}\frac{d^2}{dr^2} - \frac{l(l+1)}{2mr^2} + V_{KS}^{AE}(r)\right) rR_\ell^{AE}(r) = \epsilon_\ell^{AE}\, r\, R_\ell^{AE}(r) \qquad (2.77)$$

where V_{KS}^{AE} is the KS self-consistent one electron potential containing all the *screening effects* related both to *core* and *valence* electrons

$$V_{KS}^{AE}[n^{AE}](r) = -\frac{Z}{r} + V_{Hartree}(r) + V_{xc}[n^{AE}](r) \qquad (2.78)$$

Then the "pseudization" process can be applied according to the following quite general important conditions:

1. the *valence all-electron* and *pseudopotential* eigenvalues have to be equal for a fixed initial atomic configuration:

$$\epsilon_\ell^{AE} = \epsilon_\ell^{ps} \tag{2.79}$$

2. the all-electron and the pseudo- wavefunction assume the same values beyond a certain critical core *cutoff radius* $r_c(\ell)$, which is strongly dependent by each angular momentum component ℓ:

$$R_\ell^{AE}(r) = R_\ell^{ps}(r) \quad \text{for} \quad r > r_c(\ell) \tag{2.80}$$

   in particular the pseudowavefunctions originating from the solution of the radial Schrödinger equation must be *nodeless* to guarantee smoothness and free of unwanted wiggles;

3. the spatial integrals for the all-electron and pseudo- charge density must give the same value for each radius r beyond $r_c(\ell)$: this means that the pseudowavefunctions are forced to assure the *same norm* as the true real wavefunction. This condition guarantees *norm conservation*, the aim of this kind of pseudopotential.

$$\int_0^r r'^2 \mid R_\ell^{AE}(r') \mid^2 dr' = \int_0^r r'^2 \mid R_\ell(r') \mid^2 dr' \qquad r > r_c(\ell) \tag{2.81}$$

According to these features, through the analytical inversion of the radial Schrödinger equation one obtains the *screened pseudopotential*:

$$w_{scr,\ell}^{ps}(r) = \epsilon_\ell - \frac{\ell(\ell+1)}{2r^2} + \frac{1}{2\,r\,R_\ell^{ps}(r)}\frac{d^2}{d\,r^2}\left[r\,R_\ell^{ps}(r)\right] \tag{2.82}$$

The screened pseudopotential $w_{scr,\ell}^{ps}(r)$ contains the effects due to the valence electrons in $V_{Hartree}$ and V_{xc} that have to be subtracted to yield:

$$w_\ell(r) = w_{scr,\ell}^{ps}(r) - V_{Hartree}[n^{ps}](r) - V_{xc}[n^{ps}](r) \tag{2.83}$$

From the setting of the cutoff radius depends the quality of the pseudopotential. The smallest possible value is determined by the location of the outermost nodal surface of the true all-electron wavefunctions. For cutoff radius close to the minimum, the pseudopotential is realistic and very strong. For large cutoff radius, the pseudopotential is smooth and almost angular momentum independent, but therefore too unrealistic. A smooth potential leads to a fast convergence of plane wave basis calculation.

The main features of the **norm-conserving** pseudopotentials are:

- **transferability**: the needs to describe accurately the behaviour of the valence electrons in several different chemical environments; this holds when the *logarithmic derivative* and the *energy first order derivative* of the all-electron and pseudo- wavefunctions must be equal for each r values beyond $r_c(\ell)$ according to the identity:

$$-2\pi\Big[\big(\,r\,R_\ell(r)\,\big)^2\,\frac{d}{d\epsilon}\frac{d}{dr}\ln\,R_\ell(r)\Big]_r = 4\pi\int_0^r\,[R_\ell(r)\,r]^2\,dr \qquad (2.84)$$

  and it assures that the *scattering* properties of the ionic core are well reproduce like in the true all-electron atoms.

- **non locality**: due to construction there's an explicit dependence on the components of the angular momentum ℓ that can be expressed in terms of projection operator and angular coordinates in real space where *non locality* behaviour is fully revealed:

$$\begin{aligned} V^{ps} &= \sum_{\ell,m} |\,\ell m\,\rangle\,V_\ell^{ps}\,\langle\,\ell m\,| \;=\sum_\ell \hat{\mathbb{P}}_\ell\,V_\ell^{ps} \\ &= \sum_{\ell,m} |\,Y_{\ell\,m}(\Omega)\,\rangle\;V_\ell^{ps}(r)\;\langle\,Y_{\ell m}(\Omega')\,| \end{aligned} \qquad (2.85)$$

  Outside the core radius the potentials V_ℓ are identical for all the angular momentum components of the wavefunction (this means non local). But Kleinman and Bylander found out the definition *semi-local (sl)*, for the pseudopotential V_ℓ which depends on the angular momentum but not on $|\,\mathbf{r}\,|$ and $|\,\mathbf{r}'\,|$ separately;

- **separability**: Kleinman and Bylander (KB) rewrote the *semi-local* potential into a *separable form* in order to reduce the computational cost. First the semi-local potential can be separated into a long-range (local Coulombian tail) and a short-range components:

$$w^{ps}(\mathbf{r}\,\mathbf{r}') \;=\; w_{local}(r) \;+\; \underbrace{\sum_\ell \Delta\,w_\ell(r)\,\sum_{m=-\ell}^{\ell} Y_{\ell m}^*(\mathbf{r}')Y_{\ell m}(\mathbf{r})\delta(\mathbf{r}-\mathbf{r}')}_{nonlocal} \qquad (2.86)$$

$$\text{where}\quad \Delta\,w_{\ell,nl}^{ps}(r) = \,w_\ell^{ps}\;-\;w_{local}^{ps} \qquad (2.87)$$

  and then the KB potential assumes the form:

$$\begin{aligned} w^{KB}(\mathbf{r},\mathbf{r}') &= w_{local}(r) + \sum_\ell \Delta\,w_\ell^{KB}(\mathbf{r},\mathbf{r}') = \\ &= w_{local}(r) + \sum_\ell\sum_{m=-\ell}^{\ell} \frac{\varphi_{\ell m}^{ps}(\mathbf{r})\Delta w_\ell(\mathbf{r})\Delta w_\ell(\mathbf{r}')\varphi_{\ell m}^{ps}(\mathbf{r}')}{\int d^3\mathbf{r}\,\Delta w_\ell(\mathbf{r})\,|\,\varphi_{\ell m}^{ps}(\mathbf{r})\,|^2} \end{aligned} \qquad (2.88)$$

The $w^{ps}_{\ell,nl}(r)$ is the ℓ angular momentum dependent component of any non local pseudopotential, while w_{loc} is a arbitrary component that can be use as a reference to produce accurate and transferable pseudopotentials. The KB potential is a norm-conserving pseudopotential that uses a single basis state for each angular momentum component of the wave function projecting each spherical harmonic component onto a single basis set. The pseudopotential in the form of Eq. [2.85] scales as $N_{pw} \times N_{pw}$ while in the KB separable form of Eq. [2.88]like $16N_{pw} \ln N_{pw}$.

Ultrasoft pseudopotentials

In 1990 David Vanderbilt [113] developed a new class of pseudopotential in order to treat systems, such as transition metals, first-row elements or large-scale electronic structure problems, requiring hard pseudopotentials to ensure transferability and demanding impractically large plane wave basis sets. These new potentials are called *ultrasoft pseudopotentials* since the aim consists in a "relaxation or softening" of the norm-conservation rule and of the standard orthonormality constraint of atomic orbitals, then resulting in a wavefunction which can be expanded using a much smaller plane wave basis set, as shown in Fig. 2.5. The orbitals are allowed to be as soft as possible within the core region, and due to a energy cutoff lower than the common values for the norm-conserving pseudopotentials, this yields to a rapidly converging plane wave expansion due to . Nonetheless, the ultrasoft pseudopotential must recover the same *scattering properties* of the all-electron potential expressed in terms of *transferability* and *logarithmic derivative*. The orthonormality is recovered by introducing a generalized overlap operator which depends on the ionic positions. The all-electron density is obtained by adding to the square modulus of the orbitals an "augmentation charge" localized in the core region.
The first step consists in supplying the "lack of charge density" in the core region through an *augmented charge* Q_{nm}:

$$Q_{nm}(\mathbf{r}) = \psi_n^{\dagger\,AE} \psi_m{}^{AE} - \phi_n^{\dagger\,US} \phi_m{}^{US} \tag{2.89}$$

that corrects the charge density recovering the full valence value in this way:

$$n(\mathbf{r}) = \sum_i \left[|\phi_i^{US}|^2 + \sum_{nm,I} Q^I_{nm}(\mathbf{r}) \langle \phi_i^{US} | \beta^I_n \rangle \langle \beta^I_m | \phi_i^{US} \rangle \right] \tag{2.90}$$

The atomic pseudopotential is separated into a local V_{loc} and a nonlocal V_{nloc} part. The non local potential is written in the separable form, as a

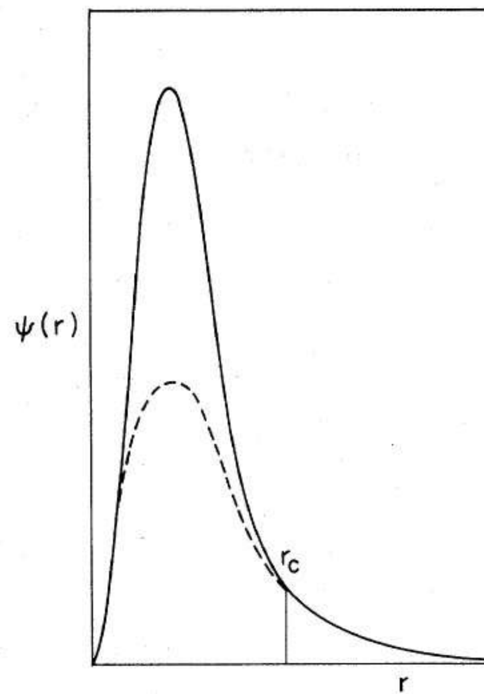

Figure 2.5: "True" pseudowavefunction strongly peaked inside the core region (solid line) and "ultrasoft" pseudowavefunction modified in Vanderbilt's scheme (dashed line).

sum of projectors.

$$
\begin{aligned}
& V^{US}(\mathbf{r}) = V_{loc}(\mathbf{r}) + V_{nloc}(\mathbf{r}) \\
& V^{US}_{nloc} = \sum_{nm} D^{(0)}_{nm} |\, \beta_n\rangle\langle\beta_m \,| \\
\text{with} \quad & |\, \beta_n\rangle = \sum_m \frac{\left[\varepsilon^{AE}_m - (T + V_{loc})\right] \,|\, \phi^{US}_m\rangle}{\langle\phi^{US}_m|\, \left[\varepsilon^{AE}_m - (T + V_{loc})\right] |\phi^{US}_n\rangle}
\end{aligned} \tag{2.91}
$$

$$
\text{and} \quad D^{(0)}_{nm} = \langle\phi^{US}_n|\, [\varepsilon_m - (T + V_{loc})]\, |\phi^{US}_n\rangle + \varepsilon_m Q_{nm} - \int V_{loc}(\mathbf{r}') n(\mathbf{r}') d\mathbf{r} \tag{2.92}
$$

The local part (obtained removing the screening of Hartree and xc) within the core region is smooth, while the non local term is localized within the cutoff radius part since the β-projectors are limited to the core region itself. The orbitals are postulated to obey generalized orthogonality constraints $\langle\psi_n|\, \hat{S}|\psi_n\rangle = \delta$, with the non local overlap operator $\hat{S}$ given by:

$$
\hat{S} = 1 + \sum_{nm} |\beta_n\rangle\langle\beta_m| \tag{2.93}
$$

then the KS equation is generalize in this way $\hat{H}|\phi^{US}_i\rangle = \varepsilon_i \hat{S}|\phi^{US}_i\rangle$ and the hamiltonian becomes

$$
\hat{H} = -\frac{\hbar^2\nabla^2}{2m} + V_{eff}(\mathbf{r}) + \sum_{nm,I} D^I_{nm}|\beta^I_n\rangle\langle\beta^I_m|
$$

where the KS effective potential $V_{eff} = V_{nloc} + V_{loc} + V_{Hartree} + V_{xc}$ contains both the local and the non local part.

2.4 Excited states in DFT

The Hohenberg-Kohn theorem asserts that the ground-state density determines the external potential. In this scheme it's also possible to connect the ground-state density with any excited state, thus considering an excited-state energy as a functional of the ground-state density, allowing in principle DFT to calculate excitation energies. The **ΔSCF** is a method where the ground-state scheme is applied to calculate both excited and ground state as energy differences: practically, it's based on the *energy difference* between two *self-consistent-field (SCF)* calculations. The application of the DF formalism to the excited state can be justified if applied to the lowest-lying state for a given set of quantum numbers [114]. As example, the ionization potential IP and electron affinity AE of a N electron system can be derived through a ΔSCF calculation as difference in total energy between two self-consistent calculations [115], as shown in Sec. [2.2.2]. This method take into account the relaxation effects induced by the removal or addition of an electron to the system. ΔSCF can yield good results when it is possible to simulate the excitations occupying just one-particle orbital; this immediately excludes the possibility to describe those excitations that are not easily described in terms of isolated single particle transitions. Furthermore, this method works in finite systems, but not in infinite ones. This because the main contribution in ΔSCF is the Hartree relaxation, that for extended system is negligible and other contributions, not described in this method, come out.

To describe neutral excitations [116, 117, 118, 118, 119, 120], ΔSCF yields to consider two different electronic configurations γ_i for the system, one for the ground state $\vec{\gamma}_{gs}$ and another one for the excited state $\vec{\gamma}_{exc}$:

- initial state: Ground State

$$\vec{\gamma}_{gs} = \begin{cases} \gamma_i = 1 & i = 1, ..., N \\ \gamma_i = 0 & i > N \end{cases}$$

- final state: Neutral Excited State

$$\vec{\gamma}_{exc} = \begin{cases} \gamma_i = 1 & i = 1, ..., (h-1), (h+1), ..., N \quad \text{and} \quad i = e \ (e > N) \\ \gamma_i = 0 & i = h \quad \text{and} \quad i > N, i \neq e \end{cases}$$

In the last configuration a particle-hole pair is considered in the system promoting an electron from the valence band (i=h) to a conduction band (i=e). For this reason the method is also called *constrained DFT*. The excitation energy of the many-electron system, for which the excited state should be well described by single-orbital transitions, is the difference in total energy, between two self-consistent calculation with the occupations

described above, i.e.:

$$E_{exc} = E_{\vec{\gamma}_{exc}} - E_{\vec{\gamma}_{gs}} \tag{2.94}$$

and this should then give the optical gap since the initial and final states are still neutral.

3

Many Body Perturbation Theory: ”a stairway to heaven”

E questo é il fiore del partigiano,
morto per la libertà.

Bella Ciao, canzone della Resistenza

3.1 Theoretical Spectroscopies

Why the search for *excited state* calculation has become one of the most important and thought challenge of the theoretical solid state research? The answer lies in the aim to developed theoretical instruments, day by day more powerful than the preceding ones, to understand the interaction between the scanning probe sources (electrons, light, X-rays, lasers, and other modern photon sources) and the matter in order to study materials, ranging from solids to atoms, from surface to nanoscale systems. The aim is the simulation through these theoretical tools of the *electronic excitations* and, in general, of the all experimental spectroscopy techniques in order to achieve a complete set of theoretical spectroscopy devices in order to predict with accuracy and to explain the experimental data (ellipsometry, EELS, Raman, IR, NMR, X-Ray, ARPES e ARPIES, STS, I/V transport, etc.).

In general it's not sufficient to calculate ground-state properties in order to interpret or predict results of experiments like photoemission, electron-energy loss, absorption, etc. Direct and inverse photoemission spectroscopies concern the study respectively of the occupied and empty states of the system, evaluating the energy of the photoelectron excited in or out the sample:

this means that the consequent electron excitations leave the initial neutral N-electron system with $N-1$ electron (direct photoemission, in Fig. 3.1(a)) or with $N+1$ electron (inverse photoemission, in Fig. 3.1(b)). This excitations changing the number of electrons from $N \rightarrow N \pm 1$ and leaving the system in a charged state, are called *charged excitations*. On the other side,

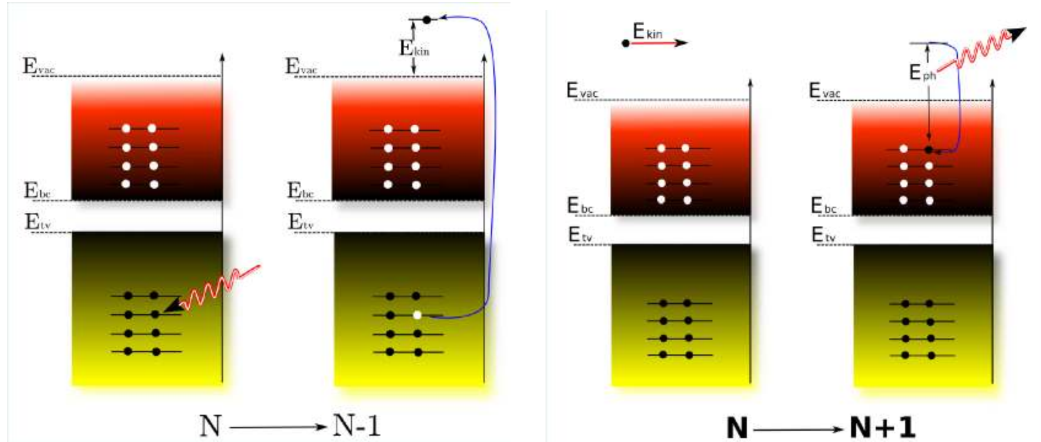

(a) **Direct photoemission**: it offers a way to experimentally investigate the occupied electronic state. A monochromatic radiation ($h\nu$) is absorbed by the sample, and a photoelectron from the valence band is emitted with energy E_k into the vacuum.

(b) **Inverse photoemission**: investigation of empty states. An electron with energy E_k is injected into the system in the conduction band and a photon $h\nu$ is therefore emitted as a consequence of the relaxation of the electron.

Figure 3.1: Charged excitations

spectroscopy techniques based on Optical Absorption (in Fig. 3.2(a)) and on energy loss (such as EELS) (in Fig. 3.2(b)),for example, take advantage of electronic *neutral excitations* which don’t change the number of electrons of the system. This means, in case of optical absorption, that the excited electron is just promoted from the valence to the empty states remaining within the sample, in contrast to what happen for the photoemission, as depicted above. In case of EELS, the electrons are scattered inelastically by the sample and lose their energy with the creation of collective electronic excitations called *plasmon*, longitudinal collective excitation that cannot be excited optically by transverse photons. Electron energy loss spectroscopy can be applied via different electronic microscopes, like TEM or SEM.

3.1.1 External Perturbation and dielectric function

The charged and neutral excitations of a system are related to the response of the system to an external perturbation represented by photons or electrons. From the theoretical point of view the interaction between the electromagnetic field generated by the probe and the matter can be treat as a *weak*

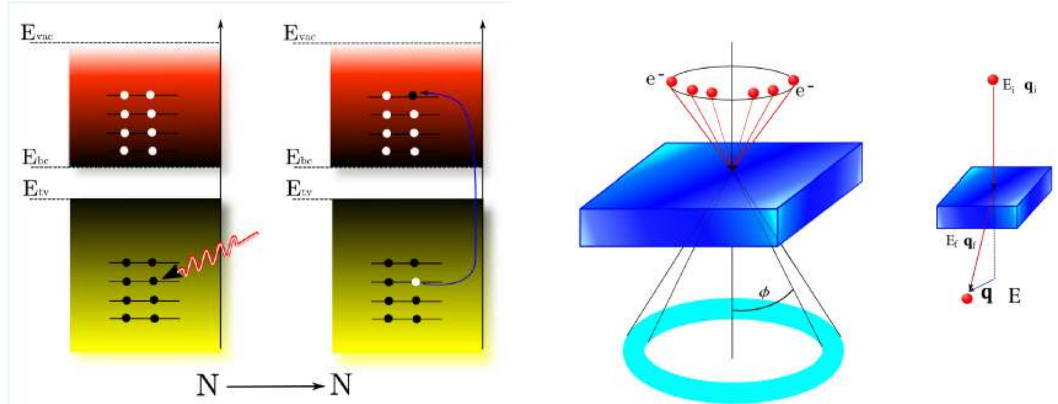

(a) **Optical Absorption**: a photon $h\nu$ absorbed by the sample excite an electron from the valence to the conduction band.

(b) **Electron Energy Loss Spectroscopy:**based on the inelastic scattering of electrons by the system under investigation.

Figure 3.2: Neutral excitations

classical perturbation to the quantum mechanical system. The electromagnetic field described through the vector potential $\mathbf{A}$ and the scalar potential ϕ, enters in the interacting hamiltonian via the change of the *velocity operator* $\hat{\mathbf{p}}$:

$$\sum_i \frac{1}{2}\hat{\mathbf{p}}_\mathbf{i}^\mathbf{2} \rightarrow \sum_\mathbf{i} \frac{\mathbf{1}}{\mathbf{2}}\big(\hat{\mathbf{p}}_\mathbf{i} \cdot \frac{\mathbf{e}}{\mathbf{c}}\mathbf{A}\big)^\mathbf{2} \tag{3.1}$$

and working in the *Coulombian gauge or velocity gauge*$(\nabla \cdot \mathbf{A} = 0)$, setting the scalar potential $\phi = 0$ for no external sources, neglecting the non-linear effects, one gets the interacting hamiltonian

$$\hat{H}_{int} \quad \rightarrow \quad -\frac{e}{c}\sum_i \mathbf{A}(\mathbf{r}_i, t) \cdot \hat{\mathbf{p}}_\mathbf{i} \tag{3.2}$$

that can be treated as a weak perturbation within time-dependent perturbation theory. The vector potential $\mathbf{A}$ can be written through the Fourier transform in a plane wave form:

$$\mathbf{A}(\mathbf{r}, t) = \mathbf{A}_0 e^{i(\mathbf{q}\cdot\mathbf{r} - \omega t)} + c.c. \tag{3.3}$$

where the Coulomb gauge is satisfied if $\mathbf{k} \cdot \mathbf{A}_0(\omega) = 0$, so that $\mathbf{A}_0(\omega)$ is perpendicular to $\mathbf{k}$, and the wave is transverse.

In the time-dependent perturbation theory, the probability per units of time and volume for a transition at frequency ω is, at first order and for weak fields:

$$W(\omega) = 2\pi \sum_{c,v,\mathbf{k},\mathbf{k}'} |\langle c\mathbf{k}'|\frac{1}{c}\mathbf{A} \cdot \hat{\mathbf{p}}|\mathbf{v}\mathbf{k}\rangle \delta(\varepsilon_\mathbf{c}(\mathbf{k}') - \varepsilon_\mathbf{v}(\mathbf{k}) - \omega) \tag{3.4}$$

where $|c\mathbf{k}'\rangle$ and $|v\mathbf{k}\rangle$ denotes the single-particle Bloch states.
In the previous expression we have to calculate the matrix elements of the perturbation between the Bloch states:

$$\hat{\epsilon} \cdot \langle c\mathbf{k}'| e^{i\mathbf{q}\cdot\mathbf{r}} \cdot \hat{\mathbf{p}} |\mathbf{vk}\rangle,$$

where $\mathbf{A} = A_0 \hat{\epsilon}$.
This expression can be simplified in many cases, expanding the exponential $e^{i\mathbf{q}\cdot\mathbf{r}}$ as:

$$e^{i\mathbf{q}\cdot\mathbf{r}} = 1 + (i\mathbf{q}\cdot\mathbf{r}) + \frac{1}{2}(i\mathbf{q}\cdot\mathbf{r})^2 + \ldots$$

Since the wavelength $\mathbf{q}$ of light is small ($\sim 5 \cdot 10^{-2}\ nm^{-1}$) and the wavefunctions have a slowly dependence on $\mathbf{k}$, it is possible to calculate the matrix elements in the dipole approximation, in this way only vertical transitions are taken into account and since $\hat{\mathbf{p}} = \dot{\mathbf{r}} = -\mathbf{i}\nabla$:

$$\hat{\epsilon} \cdot \langle c\mathbf{k}|\hat{\mathbf{p}}|\mathbf{vk}\rangle = -\mathbf{i}\hat{\epsilon} \cdot \langle \mathbf{ck}|\nabla|\mathbf{vk}\rangle = \hat{\epsilon} \cdot \langle \mathbf{ck}|\dot{\mathbf{r}}|\mathbf{vk}\rangle \tag{3.5}$$

Now applying the Heisenberg equation of motion to the variable $\mathbf{r}$, we have:

$$\dot{\mathbf{r}} = (i)^{-1}\left[\mathbf{r}, \hat{H}_0\right] \tag{3.6}$$

where $\hat{H}_0$ is the unperturbed hamiltonian. If only local terms are present in H_0:

$$\langle c\mathbf{k}|\dot{\mathbf{r}}|v\mathbf{k}\rangle = (i)^{-1}\langle c\mathbf{k}|\mathbf{r}\hat{H}_0 - \hat{H}_0\mathbf{r}|v\mathbf{k}\rangle = (i)^{-1}(\varepsilon_v(\mathbf{k}) - \varepsilon_c(\mathbf{k}))\langle c\mathbf{k}|\mathbf{r}|v\mathbf{k}\rangle \tag{3.7}$$

It is possible to derive now the relation between Eq. (3.4) and the optical properties of the system.
Optical properties can be described by the complex macroscopic dielectric function $\varepsilon_M = \varepsilon_1 + i\varepsilon_2$ and the complex refraction index $N = n + ik = \sqrt{\varepsilon}$ where n is the ordinary refraction index and k is known as the extinction coefficient.
Thus the absorption coefficient α of a incident electromagnetic wave in the sample is related with $Im\,\{\varepsilon_M\}$ in this way:

$$\alpha(\omega) = \frac{\omega W(\omega)}{u\frac{c}{n}} = \frac{\omega}{nc}\varepsilon_2(\omega) \tag{3.8}$$

where u is the average energy density defined as $u = \frac{n^2 A_0^2 \omega^2}{2\pi c^2}$ and $\frac{c}{n}$ is the speed of light in the matter.
Then it is possible to obtain for the imaginary part of the macroscopic dielectric function:

$$\varepsilon_2(\omega) = \frac{4\pi^2}{\omega^2}\sum_{c,v,k}|\hat{\epsilon} \cdot \langle c\mathbf{k}|\hat{\mathbf{p}}|\mathbf{vk}\rangle|^{\mathbf{2}}\delta(\varepsilon_{\mathbf{c}}(\mathbf{k}) - \varepsilon_{\mathbf{v}}(\mathbf{k}) - \omega) \tag{3.9}$$

If the one-electron Hamiltonian $\hat{H}_0$ contains non-local terms, in particular when there's a non-local component in the pseudopotential term, additional term must be included in Eq. (3.9) for the calculation of the spectrum:

$$\dot{\mathbf{r}} = \mathbf{v} = \frac{-i\hbar\nabla}{m} + \frac{i}{\hbar}\left[V_{NL}, r\right] \tag{3.10}$$

In this way the *length formula* and the *velocity formula* differs only for the non-local commutator between V_{NL} and $\hat{\mathbf{r}}$ operator [121]. In case of a longitudinal perturbation, the imaginary part of the macroscopic dielectric function is:

$$\varepsilon_2(\omega) = 4\pi^2 \lim_{\mathbf{q}\to 0} \frac{1}{q^2} \sum_{c,v,k} \left| \langle c\mathbf{k}+\mathbf{q}|e^{i\mathbf{q}\cdot\mathbf{r}}\,|\,v\mathbf{k}\rangle \right|^2 \delta(\varepsilon_c(\mathbf{k}+\mathbf{q}) - \varepsilon_v(\mathbf{k}) - \omega) \tag{3.11}$$

which is valid also in the case of non-local pseudopotential. Furthermore the gauge invariance between the two different approaches has been demonstrated [122].

Linear Response of Optical Spectra

When the systems are investigated through spectroscopies the response to the external perturbation used as a probe (being electrons for EELS or photon for optical absorption or photoemission for example) can be described in terms of the *linear response approximation* [123, 124]. The external perturbation potential $V_{ext}(\mathbf{r})$ induces a response of the system in terms variation of charge density and the total potential

$$\delta\rho^{ind}(\mathbf{r},t) = \int d\mathbf{r}'\,dt'\,\chi(\mathbf{r},\mathbf{r}'\,;\,t-t')\,V_{ext}(\mathbf{r}',t')$$

$$V_{tot} = \int d\mathbf{r}'\,\epsilon^{-1}(\mathbf{r}\,\mathbf{r}';t-t')\,V_{ext}(\mathbf{r}') \tag{3.12}$$

The *total potential* is screened because it contains the *external potential* contribution and the potential due to the polarization of the system induced by the external perturbation:

$$V_{tot} = V_{ext} + V_{ind} \tag{3.13}$$

$$\text{where} \quad V_{ind}(\mathbf{r},t) = \int d\mathbf{r}'\,\frac{\rho^{ind}(\mathbf{r}',t)}{|\,\mathbf{r}-\mathbf{r}'\,|} \tag{3.14}$$

The χ function is called *full reducible polarizability* (i.e. the ρ^{ind} is sensible to the bare external potential V_{ext}) and together with the *irreducible polarizability* P are response functions describing how the "polarization cloud" around the particle responds to the external perturbation, as in Fig. 3.3. The *irreducible* polarizability connects the induced charge density with the total potential:

$$\rho^{ind}(\mathbf{r},t) = \int d\mathbf{r}\,dt'\,P(\mathbf{r},\mathbf{r}'\,,t-t')\,V_{tot}(\mathbf{r}',\,t') \tag{3.15}$$

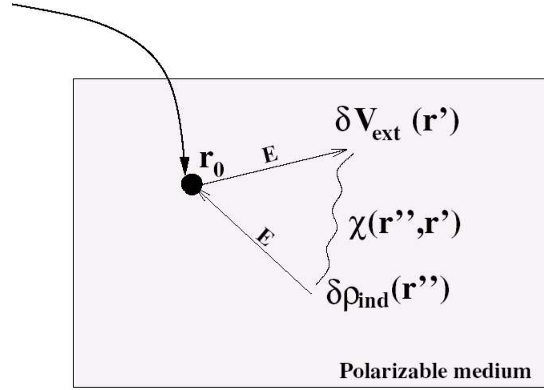

Figure 3.3: The response of a polarizable medium to an external potential: the perturbation acts on the point charge in $\mathbf{r}_0$, inducing a potential δV_{ext} that creates an induced charge $\delta\rho_{ind}$ acting again on the point charge. The wiggle, the polarizability, shows it response function.

Looking at the perturbed system in its ground state, the perturbation implies a redistribution of the charge (read wavefunction), that means depletion of charge (holes) or accumulation of charge (electrons) in some places. This creation of electron-hole pairs, with consequent polarization of the medium, is reflected by the following equations

$$\varepsilon^{-1}(\mathbf{r},\mathbf{r}';\omega) = \delta(\mathbf{r}-\mathbf{r}') + \int d\mathbf{r}''\, v(\mathbf{r}-\mathbf{r}'')\,\chi(\mathbf{r}'',\mathbf{r}';\omega) \tag{3.16}$$

$$\varepsilon^{-1}(\mathbf{r},\mathbf{r}';\omega) = \delta(\mathbf{r}-\mathbf{r}') - \int d\mathbf{r}''\, v(\mathbf{r}-\mathbf{r}'')\,P(\mathbf{r}'',\mathbf{r}';\omega) \tag{3.17}$$

where $v(\mathbf{r}-\mathbf{r}'')$ is a bare Coulomb interaction. When P is zero, the system is not polarizable and hence the total potential is equal to the external one; otherwise P is in general and on the average negative, acting against the external potential. The two polarizability are related in this way, through a Dyson-like equation

$$\chi = P + P\,v\,\chi \tag{3.18}$$

that, introducing the Coulomb modified interaction term $\bar{v}_{\mathbf{G}}(\mathbf{q})$,

$$\bar{v}_{\mathbf{r}}(\mathbf{q}) = \begin{cases} 0 & \mathbf{G}=0 \\ v_{\mathbf{G}}(\mathbf{r}) = \frac{4\pi}{|\mathbf{q}+\mathbf{G}|^2} & \mathbf{G}\neq 0. \end{cases}$$

become

$$\chi_{\mathbf{G},\mathbf{G}'} = P_{\mathbf{G},\mathbf{G}'} + \sum_{\mathbf{G}''} P_{\mathbf{G},\mathbf{G}''}\,\bar{v}_{\mathbf{G}''}\,\chi_{\mathbf{G}'',\mathbf{G}'} + P_{\mathbf{G},0}\,v_0\,\chi_{0,\mathbf{G}'} \tag{3.19}$$

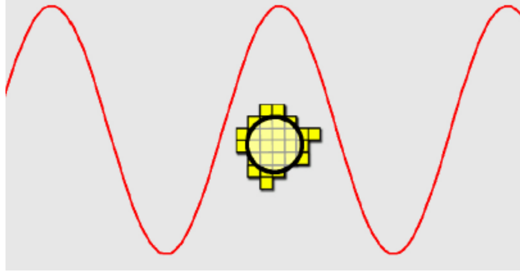

Figure 3.4: Measurable quantities varying on a macroscopic scale. The average is done over distances large compared to the cell diameter but small compared to the wavelength of the external perturbation.

The "real" quantity measured in spectroscopy is a macroscopic average ($\epsilon_M(\omega)$) of the *microscopic dielectric function* $\epsilon_m(\mathbf{r}, \mathbf{r}'\,\omega)$, that appears in the Eq. [3.17]. The microscopic quantities, like total or induced fields, are rapidly varying quantities over the atomic scale and are averaged on a scale that is large with respect to the crystal lattice cell dimension and smaller than the wavelength of the perturbation, see Fig. 3.4. In the case of the dielectric function the correct quantity to average is $\varepsilon^{-1}(\mathbf{r}, \mathbf{r}'; \omega)$ since one is concerned with the total potential $V_{tot} = \epsilon^{-1} V_{ext}$ for a given external potential and not vice versa. According to Adler and Wiser [125, 126], in a periodic system the *macroscopic* dielectric function $\varepsilon_M(\omega)$, in reciprocal space is related to the *zero-th* element of the inverse microscopic dielectric matrix $\varepsilon_{\mathbf{G},\mathbf{G}'}(\mathbf{q}, \omega)$

$$\varepsilon_M(\omega) = \lim_{\mathbf{q}\to 0} \frac{1}{\varepsilon^{-1}_{\mathbf{G}=0,\mathbf{G}'=0}(\mathbf{q}, \omega)}, \tag{3.20}$$

where $\mathbf{q}$ denotes a vanishing wave vector with direction $\hat{q}$ belonging to the first Brillouin zone and $\mathbf{G}$ and $\mathbf{G}'$ represent elements of the reciprocal Bravais lattice of the crystal; the limit $\mathbf{q} \to 0$ correspond to the dipole approximation of Eq. [3.9]. The off-diagonal term in the dielectric matrix $\varepsilon_{\mathbf{G},\mathbf{G}'}(\mathbf{q}, \omega)$ reflects the non-homogeneity of the space and taking into account the off-diagonal terms corresponds to include the so called *local field effects* [127, 128, 129, 130]. All these off-diagonal elements contribute to the 'head' of the inverse dielectric matrix,

$$\varepsilon_{\mathbf{G},\,\mathbf{G}'} = \left(\begin{array}{c|c} \mathbf{G} = \mathbf{G}' = 0 & \mathbf{G} = 0 \\ (head) & (wing) \\ \hline \mathbf{G}' = 0 & \mathbf{G},\ \mathbf{G}' \neq 0 \\ (wing) & (body) \end{array} \right)$$

For homogenous media the microscopic dielectric matrix is a function of $|\,\mathbf{r} - \mathbf{r}'\,|$ and therefore $\varepsilon_{\mathbf{G},\mathbf{G}'}(\mathbf{q}, \omega)$ is *diagonal* in reciprocal space and the

macroscopic dielectric function is calculated directly:

$$\varepsilon_M(\omega) = \lim_{\mathbf{q}\to 0} \varepsilon_{\mathbf{G}=0,\mathbf{G}'=\mathbf{0}}(\mathbf{q},\omega), \tag{3.21}$$

otherwise it depends explicitly on the position $\mathbf{r}$ and $\mathbf{r}'$ and, as said before, the matrix is not diagonal, and $\varepsilon_M(\omega)$ should be calculated through the complete inversion of the microscopic function. In this case all the elements of the matrix contribute to one element of its inverse, reflecting then the effects of local fields arising when there are inhomogeneities in the system at the microscopic scale. Taking into account the local fields implies to consider the realistic situation in which the scanning spectroscopy probe impinging the sample in $\mathbf{r}$ affects the system inducing a perturbation in $\mathbf{r}'$, thus generating differences between what one observes in $\mathbf{r}$ with respect to the same measured in $\mathbf{r}'$. Since the microscopic fields are averaged over a region occupied by the electron, the contribution to this average will be greater from those parts of the unit cell where the electron is more easily polarized. The macroscopic field is obtaining a spatial average of the microscopic quantity over the unit cell, resulting then an unweighed averaged field differ from the local field, which is weighted averaged.

Moreover it is possible to show that another exact formulation of the macroscopic dielectric function [131, 132, 133] is possible, where the inclusion of the local field is done straightforwardly by the insertion of the polarizability $\bar{P}$:

$$\varepsilon_M = 1 - \lim_{\mathbf{q}\to 0} \left[v_0(\mathbf{q}) \bar{P}_{\mathbf{G}=0,\mathbf{G}'=\mathbf{0}}(\mathbf{q},\omega) \right] \tag{3.22}$$

The matrix $\bar{P}_{\mathbf{G},\mathbf{G}'}(\mathbf{q},\omega)$ is the so called modified polarizability, and satisfies the Dyson-like screening equation with the irreducible polarizability P and the modified Coulomb interaction $\bar{v}$ introduced in Eq. [3.1.1]:

$$\bar{P} = P + P\bar{v}\bar{P} \tag{3.23}$$

Through the *modified* polarizability the local fields are included in a straightforward manner in the calculation of ε_M:

$$\varepsilon_M(\omega) = 1 - \lim_{\mathbf{q}\to 0} \left[v_{\mathbf{G}=0}(\mathbf{q}) \left(1 - P_{\mathbf{G}=0,\mathbf{G}'=\mathbf{0}}(\mathbf{q},\omega)\, \bar{v}_{\mathbf{G}=0}(\mathbf{q}) \right)^{-1} P_{\mathbf{G}=0,\mathbf{G}'=\mathbf{0}}(\mathbf{q},\omega) \right] \tag{3.24}$$

Neglecting of local fields in Eq. [3.22] means not considering $\bar{v}_{\mathbf{G}}(\mathbf{q})$ in Eq. [3.23], and is equivalent to set:

$$\varepsilon_M(\omega) = \lim_{\mathbf{q}\to 0} \left[1 - v_{\mathbf{G}=0}(\mathbf{q}) P_{\mathbf{G}=0,\mathbf{G}'=0}(\mathbf{q},\omega) \right] = \lim_{\mathbf{q}\to 0} \varepsilon_{\mathbf{G}=0,\mathbf{G}'=0}(\mathbf{q},\omega) \tag{3.25}$$

The modified polarizability $\bar{P}$ includes a correct inversion of the dielectric matrix and at the same time it gives a formal representation very similar to

that of Eq. [3.25]. Another point we want to stress is that the inclusion of the local field effects is independent of the different levels of approximation that we use to calculate absorption spectra.
The simplest approximation for the polarizability is the *random phase approximation (RPA)*, that consists to consider the *zero-th* order in the expansion of P, that means to put $P = P^0$, where $P^=$ is the polarizability for the non interacting electronic system. The RP approximation implies that the polarization is due only to the creation of an electron-hole pair, propagating independently, thus neglecting excitonic interaction between the two particles. In RPA the electronic transitions in the optical absorption spectra are treated as independent [122]. Moreover, when adding local fields, if the matrix inversion is properly taken into account, the independent transition mix: even if no electron-hole interaction is included in P, there is an effective electron-hole interaction term showing up in ε_M [131].

3.1.2 Electronic Spectra in practice

Within the KS-DFT scheme is possible to achieve a first example of electronic spectra following the recipes give in the section before. The macroscopic quantity measured to evaluate the optical absorption is the *photoabsorption cross section* $\sigma_{ph}(\omega)$:

$$\sigma_{ph}(\omega) = \frac{4\pi\omega}{c} Im\{\alpha(\omega)\} \tag{3.26}$$

Since the dynamical polarizability $\alpha(\omega)$ is defined as

$$\alpha(\omega) = -\int d\mathbf{r}, d\mathbf{r}' \, V_{ext}(\mathbf{r},\omega)\chi^0(\mathbf{r},\mathbf{r}';\omega)\, V_{ext}(\mathbf{r}',\omega) \tag{3.27}$$

then, σ_{ph} is proportional to the imaginary part of χ, polarization function, which is related to the macroscopic averaged dielectric function in this way, $\epsilon_M = 1 - v\chi^0$. The photoabsorption cross section is then directly proportional to the imaginary part of the χ response function and then to the imaginary part of the macroscopic dielectric function

$$\sigma_{ph}(\omega) \propto \lim_{\mathbf{q}\to 0} \frac{\omega}{c} Im\left\{v(\mathbf{q})\,\chi^0(\mathbf{q},\mathbf{q}';\omega)\right\} \tag{3.28}$$

in the long wavelength limit $\mathbf{q} \to 0$. For what concern EELS, when an electron impinges the sample, it loses energy by exciting electron-hole pairs, plasmons etc. The energy loss is given by the imaginary part of the integral of the potential generated by the electron and his induced charge. The external potential V_{ext} due to the scattered electron leads to a momentum transfer $\mathbf{q}$ expressed by the *loss function*

$$L(\omega) \propto -Im\left\{\int d\mathbf{r}\, d\mathbf{r}'\, e^{-i\mathbf{qr}}\,\chi(\mathbf{r},\mathbf{r}';\omega)\, e^{i\mathbf{qr}'}\right\}$$

representing the energy loss by the electron per unit of time during the scattering process and which results in the end proportional to the imaginary part of the inverse of the macroscopic dielectric function ε_M:

$$L(\omega) \propto -\frac{e}{\pi^2}\int d\mathbf{r}\,\frac{1}{\mathbf{q}^2}\,Im\left\{\frac{\omega}{\varepsilon_M(\mathbf{q},\omega)}\right\} \tag{3.29}$$

Considering the Independent Particle RPA framework in which the electronic transition are considered vertical and independent one gets:

$$Abs \propto Im\{\varepsilon\} = Im\left\{1 - v\chi^0\right\} = -v\,Im\left\{\chi^0\right\} \tag{3.30}$$

$$EELS \propto -Im\left\{\varepsilon^{-1}\right\} = -v\,Im\left\{\frac{\chi^0}{1 - v\chi^0}\right\} = \frac{\varepsilon_2}{{\varepsilon_1}^2 + {\varepsilon_2}^2} \tag{3.31}$$

and with χ^0 in the IP-RPA approach defined as

$$\chi^0 = 2\sum_{c,v}\frac{|\langle\phi_c^{KS}|\,e^{-i\,\mathbf{q}\,\mathbf{r}}\,|\phi_v^{KS}\rangle|^2}{\omega\,(\epsilon_c - \epsilon_v) + i\eta} \tag{3.32}$$

3.2 Quasiparticles and Green Functions approach

The excitations of system of strongly interacting particles can often be describe in terms of *quasiparticles*. In solids a "bare" electron repels other electrons via Coulomb potential that can be represented as a "positively charged polarization cloud" surrounding the electron. This screening "cloud" added to the "bare" electron contributes to the *quasiparticle* picture of electrons (as in Fig. 3.5), no more simple particles, but now quasi-particles weakly interacting with the neighbors via a screened Coulomb potential. Quasiparticle has a finite *lifetime* since are only approximate eigenstates of the N-electron Hamiltonian. The energy difference between quasiparticle and the bare particle is usually described by the *self energy* Σ which account for all the exchange and correlation effects beyond the Hartree approximation. The self-energy is a non-local, energy-dependent, and in general non-Hermitian operator. The quasiparticles obeys to a Schroedinger-like equation, named *quasiparticle equation* written as:

$$\left[-\frac{1}{2}\nabla^2 + V_{ext}(\mathbf{r}) + V_H(\mathbf{r})\right]\psi(\mathbf{r},\omega) + \int d\mathbf{r}'\,\Sigma(\mathbf{r},\mathbf{r}',\omega)\,\psi(\mathbf{r}',\omega) = E(\omega)\psi(\mathbf{r},\omega) \tag{3.33}$$

The one-particle Green function is defined as:

$$\begin{aligned} i\,G(1,2) &= \langle N\,|\,\hat{T}\left[\hat{\psi}(\mathbf{x}_1 t_1)\,\hat{\psi}^\dagger(\mathbf{x}_2 t_2)\right]|N\rangle = \\ &= \begin{cases} \langle N\,|\,\hat{\psi}(\mathbf{x}_1 t_1)\,\hat{\psi}^\dagger(\mathbf{x}_2 t_2)\,|\,N\rangle & \text{for } t_1 > t_2 \text{ electron} \\ -\langle N|\hat{\psi}^\dagger(\mathbf{x}_2 t_2)\,\hat{\psi}(\mathbf{x}_1 t_1)\,|\,N\rangle & \text{for } t_2 > t_1 \text{ hole} \end{cases} \end{aligned} \tag{3.34}$$

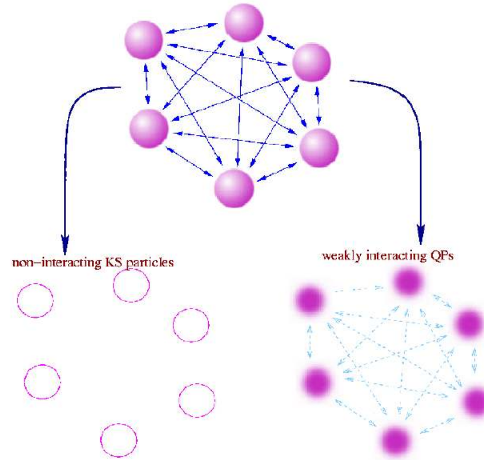

Figure 3.5: A strong-interacting particles system can be mapped onto a KS non-interacting particle system (left side) or onto a weakly-interacting *quasiparticle* system (right side) through a Green functions equation.

where $(\mathbf{x}_1, t_1) = (\mathbf{r}_1, \xi_1, t_1) = 1$ and $(\mathbf{x}_2, t_2) = (\mathbf{r}_2, \xi_2, t) = 2$. $\hat{T}$ is the Dyson time-ordering operator and $\hat{\psi}(x)$ is the field operator in the Heisenberg representation, $|N\rangle$ denotes the ground state of the interacting many-particle system. The one-particle Green's function is called *fermionic propagator* since it describes the propagation of a fermion: for $t_2 > t_1$, gives the probability amplitude that a hole created at $(\mathbf{x}_1, t_1)$ will propagate to $(\mathbf{x}_2, t_2)$ and for $t_1 > t_2$ the probability amplitude that an electron added at $(\mathbf{x}_2, t_2)$ will propagate to $(\mathbf{x}_1, t_1)$. The physical interpretation relates immediately with direct photoemission and inverse photoemission processes, because it describes the propagation of an electron or a hole in a many-electron system. The knowledge of the one-particle Green's function gives observable properties of large interest:

- The expectation value of any single-particle operator in the ground state of the system;

- The ground-state energy of the system;

- The one-electron excitation spectrum of the system:

  * $E_i(N+1) - E(N) = \varepsilon_i^{N+1} \rightarrow$ conduction bands
  * $E(N) - E_i(N-1) = \varepsilon_i^{N-1} \rightarrow$ valence bands

For non interacting systems, the equation of motion, of the one-particle

Green's function $G_0(\mathbf{x}t, \mathbf{x}_1 t_1)$ is:

$$\left[i\frac{\partial}{\partial t} - h(\mathbf{x})\right] G_0(\mathbf{x}t, \mathbf{x}_1 t_1) = \delta(\mathbf{x}-\mathbf{x}_1)\delta(t-t_1). \tag{3.35}$$

In general, the equation of motion for an interacting "two particle" Green function is

$$\left[i\frac{\partial}{\partial t_1} - \left(-\frac{1}{2}\nabla_1^2 + V_{ext}(1) + V_H(1)\right)\right] G(1,2) - \int d3\,\Sigma(1,3)\,G(3,2) = \delta(1,2) \tag{3.36}$$

Then introducing a new *mass operator* M including the whole many-body interaction (self-energy and Hartree potential) that $\Sigma = M - V_H$ one gets

$$\left[i\frac{\partial}{\partial t_1} + \frac{1}{2}\nabla_1^2 - V_{ext}\right] G(1,2) - \int d3\,M(1,3)\,G(3,2) = \delta(1,2) \tag{3.37}$$

where, applying the condition $\Sigma = 0$, comes out the equation for the non-interacting Green function G^0:

$$\left[i\frac{\partial}{\partial t_1} - \left(-\frac{1}{2}\nabla_1^2 + V_{ext}(1) + V_H(1)\right)\right] G^0(1,2) = \delta(1,2) \tag{3.38}$$

The Green function satisfies also a Dyson-like [134, 135] equation that yields combining Eq.s [3.36] and [3.38]:

$$G(1,2) = G^0(1,2) + \int d(34)\,G^0(1,3)\,\Sigma(3,4)\,G(4,2) \tag{3.39}$$

3.2.1 Quasiparticle representation and Spectral Function

Through the "resolvent theory" [136, 137] [1] the Green function can be expressed in terms of the quasiparticle wavefunctions and energies via its spectral function A thus clarifying its physical relevance. The spectral representation of G in the frequency domain is:

$$G(\mathbf{r}, \mathbf{r}', \omega) = \sum_i \frac{\Psi_i(\mathbf{r}, \omega)\Psi_i^*(\mathbf{r}', \omega)}{\omega - \epsilon_i(\omega)} \tag{3.40}$$

where the quasi-particle eigenvalues $\epsilon_i(\omega)$ are in general complex: the *real part* has the physical meaning of the energy required to excite the system, while the *imaginary part* is associated to the dumping of the excited state and therefore to its lifetime. This is strictly related to the imaginary part of the Green function, called *spectral function*:

$$A(\mathbf{r}, \mathbf{r}', \omega) = -\frac{1}{\pi} Im\left\{G(\mathbf{r}.\mathbf{r}', \omega)\right\} \tag{3.41}$$

[1] Given $(z - \mathcal{L})\,|u\rangle = |f\rangle$, with $\mathcal{L}$ differential operator, the Green function is the inverse of the associated homogenous equation, $G(z) = (z - \mathcal{L})^{-1}$

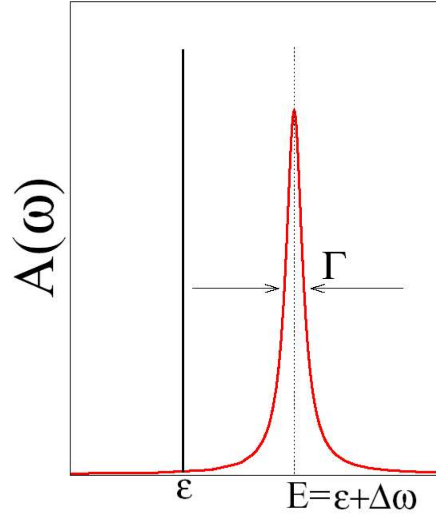

Figure 3.6: Schematic representation of the spectral function A with its Lorentzian broadening, compared with the *delta* of the independent-particle spectral function.

The spectral function A is an important quantity strictly linked with the photoemission experiment; for a non-interacting G^0 green function the spectral function is a series of δ-functions centered at the eigenvalues of the non-interacting electronic Hamiltonian. For a diagonal element of the spectral function of the full G(1,2) we have

$$A(\omega) = \frac{1}{\pi} \sum_i \frac{Im\,[\Sigma(\omega)]}{\mid \omega - \varepsilon_i - Re\,[\Sigma(\omega)] \mid^2 + \mid Im\,[\Sigma(\omega)] \mid^2} \tag{3.42}$$

Evaluating this relation within the quasiparticle approximation, the spectral function results to have Lorentzian shape peaked on the eigenenergy $E = \epsilon_i + Re\,\{\Sigma\} + i\,Im\,\{\Sigma\}$, as in Fig. 3.6, whom physical meaning is the excitation energy $\omega = E = \epsilon + \Delta\omega$:

$$A(\omega) = \frac{\Gamma}{(\omega - \varepsilon - \Delta\omega)^2 + \Gamma^2} = \frac{\Gamma}{(\omega - E)^2 + \Gamma^2} \tag{3.43}$$

The width of the peak (no longer a delta) represents the inverse of the lifetime of the corresponding quasiparticle. Physically the inverse and direct photoemission spectroscopies offer a method to measure experimentally the spectral function which therefore assumes also the meaning of density of states per unit of energy for the empty and occupied bands. [68, 138].

3.2.2 An "alchemic circle": the Hedin's pentagon

In order to solve numerically the problem of an interacting many-electron system, one-particle equations are very often used: for example the Kohn-Sham equations, the Hartree-Fock equations, the quasi-particle equations. The main difference among these lies in the description of the *many-body interaction* which in the Hartree-FocK theory is described through an exchange potential v_x, in DFT through an exchange-correlation potential v_{xc} and in the Green's function approach the self-energy operator Σ contains the information on the electron-electron interaction. The self-energy is a more complicated object with respect to v_{xc} or v_x. In fact it is energy dependent,

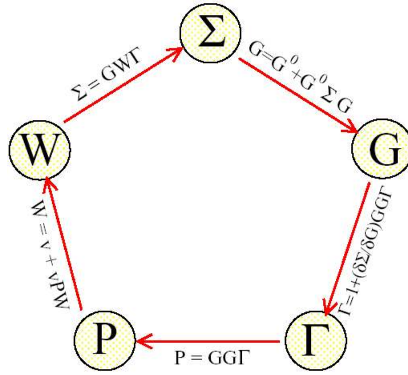

Figure 3.7: Sketch of the coupled integral Hedin equation.

non-local in space and non Hermitian. In 1965, Lars Hedin proposed an expansion of Σ in term of the Coulomb screened potential W, via a scheme of five coupled integral equations (see Fig. 3.7):

- **Vertex function**

$$\Gamma(1,2,3) = \delta(1,2)(2,3) + \int d(4,5,6,7) \frac{\delta\Sigma(1,2)}{\delta G(4,5)} G(4,6)G(7,5)\,\Gamma(6,7,3) \tag{3.44}$$

- **Irreducible polarizability**

$$\tilde{P}(1,2) = -i \int d(3,4)\, G(1,3)\,\Gamma(3,4,2)\, G(4,1^+) \text{ with } 1^+ = (\mathbf{r}_1, \sigma_1, t_1+\delta) \tag{3.45}$$

- **Screened interaction**

$$W(1,2) = v(1,2) + \int d(3,4)\, v(1,3)\, \tilde{P}(3,4)\, W(4,2) \tag{3.46}$$

- **Self energy**

$$\Sigma(1,2) = i\int d(3,4)\, G(1,3^+)\, W(1,4)\, \Gamma(3,2,4) \tag{3.47}$$

- **Dyson equation**

$$G(1,2) = G_0(1,2) + \int d(3,4)\, G_0(1,3)\, \Sigma(3,4) G(4,2) \tag{3.48}$$

At this point we want to obtain from these equations the response functions of the system to the external perturbation. The inverse dielectric function is given as:

$$\epsilon^{-1}(1,2) = \frac{\delta V(1)}{\delta w(2)}, \tag{3.49}$$

$$\epsilon^{-1}(1,2) = \delta(1,2) + \int d\,3 v(1,3) \frac{\delta\rho(3)}{\delta w(2)} \tag{3.50}$$

and we can define the *response function* or *reducible polarizability* as:

$$\chi(1,2) = \frac{\delta\rho(1)}{\delta w(2)} \tag{3.51}$$

which gives the change in the charge density upon a change in the external potential.
The *polarization function* or *irreducible polarizability* is defined instead as the change in the charge density upon a change in the total potential:

$$P(1,2) = \frac{\delta\rho(1)}{\delta V(2)}. \tag{3.52}$$

Then it is possible to write the dielectric matrix and the inverse dielectric matrix as:

$$\epsilon^{-1}(1,2) = \delta(1,2) + \int d\,3 v(1,3)\, \chi(3,2), \tag{3.53}$$

$$\epsilon(1,2) = \delta(1,2) - \int d\,3 v(1,3)\, P(3,2), \tag{3.54}$$

where the relation between the two response functions is:

$$\chi(1,2) = P(1,2) + \int d3\, d4 P(1,3)\, v(3,4)\, \chi(4,2). \tag{3.55}$$

Finally, we show the relation of the screened potential with the irreducible and reducible polarizabilities:

$$\begin{aligned} W(1,2) &= \int d\,3\, \varepsilon^{-1}(1,3) v(3,2) \\ &= v(1,2) + \int d\,3 d\,4 v(1,3) P(3,4) W(4,2) \\ &= v(1,2) + \int d\,3 d\,4 v(1,3) \chi(3,4) v(4,2) \end{aligned} \tag{3.56}$$

3.2.3 The GW Approximation

This approximation (GWA) consists in a shortcut of the Hedin's equations pentagon, avoiding the calculation of the *vertex function* set to unity. Thus the self energy is calculated as the product of the self-consistent single-particle propagator G^0 and the self-consistent dynamically screened interaction W. The GWA corresponds to the first iteration of the Hedin equations, that means to neglect the higher-order vertex corrections, and can be interpreted as the first-order term of the expansion of the self-energy Σ in relation to the screened interaction:

$$\Gamma(1,2,3) = \delta(1,2)\delta(1,3), \tag{3.57}$$

and the polarizability becomes

$$P(1,2) = -iG(1,2^+)G(2,1). \tag{3.58}$$

This is the so called *Random Phase Approximation* (RPA) for P: the polarizability is the product of two one-particle Green's functions. A form for the screened Coulomb potential W can be obtained, finally giving the lowest order contribution in W to the self energy:

$$P^0(1,2) = -iG^0(1,2)G^0(2,1^+) \tag{3.59}$$

$$W^0(1,2) = v(1,2) + \int d(3,4)v(1^+,3)P^0(3,4)W^0(4,2) \tag{3.60}$$

$$\Sigma(1,2) = iG^0(1,2)W^0(1^+,2) \tag{3.61}$$

This self-energy $\Sigma^{GWA} = G^0W^0$ is used to calculate the quasi-particle energies through the quasi-particle equation; in practical calculations the one-particle Green function is calculated as the independent particle Green function G_0 and in the *z*eroth order for Γ it is possible to obtain: P,W and Σ. Starting from the initial KS eigenvalues one gets

$$E_i^{qp} = \varepsilon_i^{KS} + \langle \phi_i^{LDA} \mid \Sigma(E^{qp}) - V_{xc}^{LDA} \mid \phi_i^{LDA} \rangle \tag{3.62}$$

where the E^{qp} appear also as argument of the self-energy itself which expanded in Taylor series, at the first-order term around the ε_i^{KS}

$$\langle \Sigma(E^{qp}) \rangle = \langle \Sigma(\varepsilon^{KS}) \rangle + (E_i^{qp} - \varepsilon_i^{KS}) \langle \frac{\partial \Sigma(\omega)}{\partial \omega} \rangle_{\omega=\varepsilon_i^{KS}} + O\left[(E_i^{qp} - \varepsilon_i^{KS})^2 \right] \tag{3.63}$$

gives the *GW corrections* (at the first-order) with respect to the KS energies:

$$E_i^{qp} - \varepsilon_i^{KS} = \frac{\langle \Sigma(\varepsilon_i) \rangle - \langle V_{xc} \rangle}{1 - \langle \frac{\partial \Sigma(\omega)}{\partial \omega} \rangle_{\omega=\varepsilon_i^{KS}}} = Z_i \left[\langle \Sigma(\varepsilon_i) \rangle - \langle V_{xc} \rangle \right] \tag{3.64}$$

The standard GW approximation represents a valid tool to estimate the Σ obtaining accurate results for excitation energies and quasi-particle band gaps of solids [139, 140, 141, 142]. In order to go beyond, fully or partial self-consistent GW calculation can be performed [143, 144, 145, 146, 147, 148, 149, 150, 151, 142].

3.3 The Bethe-Salpeter approach: an effective Two-Particle Equation

Starting from the Hedin's equation it is possible to obtain a four-point equation for the polarizability and the problem can be reformulate in terms of an eigenvalue problem with an effective Hamiltonian describing the excitonic interaction. For a more detailed derivation of the two-particle Hamiltonian see:[131, 132] .
The starting point is the irreducible polarizability of Eq. (3.45) in GW approximation which contains, through the vertex function, an intrinsic four-point quantity:

$$\frac{\delta\Sigma(1,1,1')}{\delta G(2,2')} = \frac{\delta(iG(1,1')W(1,1'))}{\delta G(2,2')} = \\ = i\frac{\delta G(1,1')}{\delta G(2,2')}W(1,1') + iG(1,1')\frac{\delta W(1,1')}{\delta G(2,2')}, \quad (3.65)$$

where the term $iG(1,1')\frac{\delta W(1,1')}{\delta G(2,2')}$ is usually neglected.
To describe the propagation of an electron-hole pair we need four-point quantities, and so it is convenient to define the four-point screened interaction as:

$$W(1,1';2,2') = W(1,1')\delta(1,2)\delta(1',2'), \quad (3.66)$$

and the four-point independent particle polarizability:

$$P^0(1,1';2,2') = -iG(1',2')G(2,1). \quad (3.67)$$

It is possible to insert Eq (3.65) in the Eq (3.45) and a generalized four-point irreducible polarizability is obtained as:

$$P(1,1',2,2') = P_0(1,1',2,2') + \\ - \int P_0(1,1',3,3')W(3,3',4,4')P(4,4',2,2')\,d3\,d3'\,d4d4', \quad (3.68)$$

where only the attractive screened interaction W appears.
With the same considerations, we can obtain a generalized four-point form for the modified polarizability and for the response function:

$${}^4\chi =^4 P +^4 P^4 v^4\chi,$$

$$^4\bar{P} = ^4 P + ^4 P^4\bar{v}^4\bar{P}.$$

Also the Coulomb potential now is a four-point quantity and the same holds also for the modified Coulomb potential:

$$v(1,1',2,2') = v(1,2)\delta(1,1')\delta(2,2'). \tag{3.69}$$

The explicit form for the response function is:

$$\chi(1,1',2,2') = P_0(1,1',2,2') + \int P_0(1,1',3,3')\times \\ \left[v(3,3',4,4' - W(3,3',4,4')\right] P(4,4',2,2')\, d3\, d3'\, d4d\, 4', \tag{3.70}$$

while the modified polarizability is:

$$\bar{P}(1,1',2,2') = P_0(1,1',2,2') + \int P_0(1,1',3,3')\times \\ \left[\bar{v}(3,3',4,4' - W(3,3',4,4')\right] \bar{P}(4,4',2,2')\, d3\, d3'\, d4d\, 4'. \tag{3.71}$$

The only difference between the Eqs. (3.70) and (3.71) is the long range tail of the Coulomb potential which is responsible for the local-field effects [131]. The macroscopic dielectric function with the inclusion of the electron-hole interaction is:

$$\varepsilon_M(\omega) = 1 - \lim_{\mathbf{q}\to 0}\left[v_{\mathbf{G}=0}(\mathbf{q})\int d\mathbf{r}d\mathbf{r}' e^{-i\mathbf{q}(\mathbf{r}-\mathbf{r}')\,4}\bar{P}(\mathbf{rr},\mathbf{r}'\mathbf{r}';\omega)\right], \tag{3.72}$$

where now $\bar{P}$ has been contracted to a two-point quantity.
Actually the creation and the annihilation of the electron-hole pairs can be considered simultaneous and the interaction instantaneous. Taking into account the translational invariance in time it is possible Fourier transform to the frequency space:

$$\chi(1,1',2,2') = \chi(\mathbf{x}_1 t_1, \mathbf{x}_{1'} t_1^+, \mathbf{x}_2 t_2, \mathbf{x}_{2'} t_2^+) = \chi(\mathbf{x}_1, \mathbf{x}_{1'}, \mathbf{x}_2, \mathbf{x}_{2'}, t_2 - t_1) \\ \to \chi(\mathbf{x}_1, \mathbf{x}_{1'}, \mathbf{x}_2, \mathbf{x}_{2'}, \omega)\delta(\mathbf{x}_1 - \mathbf{x}_{1'})\delta(\mathbf{x}_2 - \mathbf{x}_{2'}).$$

Another approximation commonly used: is the energy dependence of the screened potential is neglected and one assumes $W(\omega) = W(\omega = 0)$ [152].
Equation (3.71) for the modified polarizability has a Dyson-like form, just considering the lowest order of the interaction kernel.
It is possible to invert the polarizability for each frequency ω, but this is very often too demanding. The problem of inverting the matrix can be transformed in an eigenvalue problem, where the electron-hole interaction is described through an effective two-particle Hamiltonian.

The one-particle models can not describe the presence in the experimental spectra of resonance-like structures at low frequency (bound-excitons) and usually may lead too low optical absorption intensities [131]. It is then necessary to include the electron-hole interaction in the calculations. We first assume that the excited state can be obtained by a coherent linear superposition of vertical single-pair excitations plus corrections of higher order:

$$|E\rangle = \sum_{c,v,\mathbf{k}} A_{cv\mathbf{k}} \hat{a}^{\dagger}_{c\mathbf{k}} \hat{a_{v\mathbf{k}}} |0\rangle + |C\rangle. \tag{3.73}$$

$|E\rangle$ is an eigenstate of an "unknown" excitonic Hamiltonian and the excitonic energy Ω can therefore be calulated as:

$$\hat{H}|E\rangle = \Omega|E\rangle. \tag{3.74}$$

Considering only the linear part of $|E\rangle$ in the single-particle transition, it is also possible to write $|E\rangle$ on the basis of single-particle orbitals:

$$\Psi(\mathbf{r}, \mathbf{r}') = \sum_{cv\mathbf{k}} \psi^{qp}_{c\mathbf{k}}(\mathbf{r}) \psi^{qp*}_{v\mathbf{k}}(\mathbf{r}'). \tag{3.75}$$

The excitation energies are the solutions of an eigenvalue problem and it is necessary to find a form of the effective two-particle hamiltonian of Eq. (3.74).
In order to derive the form of the Hamiltonian of the eigenvalue problem of Eq. (3.74) the first step is to change the basis of the quantity we are dealing with and consider as a new basis that of a single-particle eigenfunctions $\phi_n(\mathbf{x})$.
In this basis any four point quantity is:

$$S(\mathbf{x}_1, \mathbf{x}_{1'}, \mathbf{x}_2, \mathbf{x}_{2'}) = \sum_{(n_1,n_1')(n_2,n_2')} \phi^*_{n_1}(\mathbf{x}_1)\phi_{n_1'}(\mathbf{x}_{1'})\phi_{n_2}(\mathbf{x}_2)\phi^*_{n_2'}(\mathbf{x}_{2'}) S_{(n_1,n_1')(n_2,n_2')}, \tag{3.76}$$

the modified polarizability now becomes:

$$\bar{P}_{(n_1,n_1')(n_2,n_2')} = \bar{P}^0_{(n_1,n_1')(n_2,n_2')} + \bar{P}^0_{(n_1,n_1')(n_3,n_3')} \Xi_{(n_3,n_3')(n_4,n_4')} \bar{P}_{(n_4,n_4')(n_2,n_2')}, \tag{3.77}$$

where the interaction kernel is defined as:

$$\Xi_{(n_1,n_1')(n_2,n_2')} = - \int d\mathbf{x}_1 d\mathbf{x}_{1'} \phi_{n_1}(\mathbf{x}_1)\phi^*_{n_1'}(\mathbf{x}_{1'}) W(\mathbf{x}_1, \mathbf{x}_{1'}) \phi^*_{n_2}(\mathbf{x}_1)\phi_{n_2'}(\mathbf{x}_{1'}) + \\ + \int d\mathbf{x}_1 d\mathbf{x}_{1'} \phi_{n_1}(\mathbf{x}_1)\phi^*_{n_1'}(\mathbf{x}_1) v(\mathbf{x}_1, \mathbf{x}_{1'}) \phi^*_{n_2}(\mathbf{x}_{1'})\phi_{n_2'}(\mathbf{x}_{1'}). \tag{3.78}$$

The independent-particle response function polarizability is:

$$\chi_{0\,(n_1,n_1')(n_2,n_2')} = \delta_{(n_1,n_2)(n_1',n_2')} \frac{f_{n_1'} - f_{n_1}}{E_{n_1'} - E_{n_1} - \omega} \tag{3.79}$$

and f_n are the occupation numbers.
The modified polarizability takes the form [131]:

$$\bar{P}_{(n_1,n_1')(n_2,n_2')} = (H^{2p} - I\omega)^{-1}_{(n_1,n_1')(n_2,n_2')}(f_{n_2'} - f_{n_2}) \tag{3.80}$$

where H^{2p} is:

$$H^{2p}_{(n_1,n_1')(n_2,n_2')} = (E_{n_1'} - E_{n_1})\delta_{(n_1,n_2)(n_1',n_2')} + (f_{n_1} - f_{n_1'})\Xi_{(n_1,n_1')(n_2,n_2')}. \tag{3.81}$$

At this point we can apply an identity which holds for a system of eigenvectors and eigenvalues of a general, non hermitian matrix, that is:

$$(H^{2p} - I\omega)^{-1}_{(n_1,n_1')(n_2,n_2')} = \sum_{\mu,\mu'} \frac{A^{(n_1,n_1')}_{\mu} M^{-1}_{\mu,\mu'} A^{*\,(n_1,n_1')}_{\mu'}}{(E_\mu - \omega)}, \tag{3.82}$$

$A^{(n_1,n_1')}_{\mu}$ and E_μ are obtained solving the following eigenvalue problem:

$$\sum_{(n_1,n_1')(n_2,n_2')} H^{exc}_{(n_1,n_1')(n_2,n_2')} A^{\mu}_{(n_2,n_2')} = E^{\mu} A^{\mu}_{(n_1,n_1')}. \tag{3.83}$$

The overlap matrix $M_{\mu,\mu'}$ between the eigenstates (which are in general non orthogonal) can be written as:

$$M_{\mu,\mu'} = \sum_{(n_1,n_1')} A^{(n_1,n_1')}_{\mu} A^{*\,(n_1,n_1')}_{\mu'}. \tag{3.84}$$

The polarizability is obtained solving Eq. (3.83), it is possible to obtain the polarizability and therefore the macroscopic dielectric function.
Considering a two-point contraction of the polarizability in real space and Fourier transforming, the macroscopic dielectric function becomes:

$$\varepsilon_M = 1 - \lim_{\mathbf{q}\to 0} v_0(\mathbf{q}) \sum_{\mu,\mu'} \sum_{(n_1,n_1')} \langle n_1|e^{-i\mathbf{qr}}|n_1'\rangle A^{(n_1,n_1')}_{\mu} \times$$
$$M^{-1}_{\mu,\mu'} \sum_{(n_2,n_2')} \langle n_2'|e^{i\mathbf{qr}'}|n_2\rangle A^{*(n_2,n_2')}_{\mu'} \frac{(f_{n_2'} - f_{n_2})}{(E_\mu - \omega)}. \tag{3.85}$$

This expression can be simplified analyzing the form of the effective Hamiltonian $H^{2p}_{(n_1,n_1')(n_2,n_2')}$.

The index $n_1 = (n, \mathbf{k})$ contains the information of the band (valence or conduction) and of the $\mathbf{k}$ point which labels the corresponding single-particle state, but considering that we are dealing only with vertical transitions, that is $\mathbf{k}$ is fixed, from now on we will omit this index.
In what follows we will use this notation:

- (n_1, n_1'):
  - unoccupied state: v_1,$v_{1'}$
  - occupied state :c_1,$c_{1'}$
- (n_2, n_2'):
  - unoccupied state: v_2,$v_{2'}$
  - occupied state : c_2,$c_{2'}$

the matrix representation of the two-body Hamiltonian $H^{2p}_{(n_1,n_1')(n_2,n_2')}$ is:

$$\left(\begin{array}{c|cccc} & v_2,\, c_2 & c_2,\, v_2 & v_2,\, v_{2'} & c_2,\, c_{2'} \\ \hline v_1,\, c_1 & H^{2p}_{(v_1\, c_1)(v_2\, c_2)} & \Xi_{(v_1\, c_1)(c_2\, v_2)} & \Xi_{(v_1\, c_1)(v_2\, v_{2'})} & \Xi_{(v_1\, c_1)(c_2\, c_{2'})} \\ c_1,\, v_1 & -\Xi_{(c_1\, v_1)(v_2\, c_2)} & -H^{2p}_{(c_1\, v_1)(c_2\, v_2)} & -\Xi_{(c_1\, v_1)(v_2\, v_{2'})} & -\Xi_{(c_1\, v_1)(c_2\, c_{2'})} \\ v_1,\, v_{1'} & 0 & 0 & (E_{v_{1'}} - E_{v_1})\delta_{(v_1,v_2)(v_{1'},v_{2'})} & 0 \\ c_1,\, c_{1'} & 0 & 0 & 0 & (E_{c_{1'}} - E_{c_1})\delta_{(c_1,c_2)(c_{1'},c_{2'})} \end{array}\right)$$

In the definition of $H^{2p}_{(n_1,n_1')(n_2,n_2')}$ there are $\delta_{(n_1,n_2)(n_1',n_2')}$; which is the identity in the transition basis, and $(f_{n_1} - f_{n_1'})$, which is different from zero only for those transitions for which (n_1, n_1')=(occupied,unoccupied) or (n_1, n_1')=(unoccupied,occupied).
Despite the simplifications, the form of the H^{2p} is quite complicated, but it is interesting to note that in the polarizability appears: $(f_{n_2'} - f_{n_2})$.
$(f_{n_2'} - f_{n_2})$ contributes only for the terms corresponding to $(v_2\, c_2)$ and $(c_2\, v_2)$, then we can obtain $H^{exc,2p}_{(n_1,n_1')(n_2,n_2')}$:

$$\left(\begin{array}{cc} H^{2p\ resonant}_{(v_1\, c_1)(v_2\, c_2)} & \Xi^{coupling}_{(v_1\, c_1)(c_2\, v_2)} \\ -\left[\Xi^{coupling}_{(v_1\, c_1)(c_2\, v_2)}\right]^* & -\left[H^{2p\ resonant}_{(v_1\, c_1)(v_2\, c_2)}\right]^* \end{array}\right)$$

The $H^{2p\ resonant}$ is Hermitian and corresponds to positive absorption energy, while $-\left[H^{2p\ resonant}\right]^*$ is the anti-resonant part, and gives the de-excitations energies [152]. In the calculations of optical spectra the coupling part of the

matrix is often neglected (Tamm-Dancoff approximation).
In this approximation the eigenvalue problem can be rewritten as:

$$\sum_{(v_2\,c_2)} H^{exc,2p\ resonant}_{(v_1\,c_1)(v_2\,c_2)} A^{\mu}_{(v_2\,c_2)} = E^{exc}_{\mu} A^{\mu}_{(v_1\,c_1)}, \tag{3.86}$$

and finally Eq. [3.85] can be simplified:

$$\varepsilon_M = 1 - \lim_{\mathbf{q}\to 0} v_0(\mathbf{q}) \sum_{\mu} \sum_{(v_1\,c_1)} \frac{|\langle v_1|e^{-i\mathbf{qr}}|c_1\rangle A^{(v_1\,c_1)}_{\mu}|^2}{E^{exc}_{\mu} - \omega - i\eta} \tag{3.87}$$

4 The Systems

L' Italia é una Repubblica democratica
fondata sul lavoro.
La sovranità appartiene al popolo, che la
esercita nelle forme e nei limiti della
Constituzione

Constituzione Italiana, Art. 1

In this section we will present and comment the results obtained through the computer numerical simulations realized during my three year of PhD fellowship. The numerical simulation have been realized through several *ab initio DFT code* within the plane-wave pseudopotential approach, such as **Pwscf** [153], **VASP** [154, 155] and **Abinit** [156] for what concern the total energy calculation part. On the other side, the optical features of the system have been investigated through different codes, like SELF [157] and EXC [158]. Due to the very huge computational cost of the simulations, the total energy and the many body optical calculations have been performed on supercomputing machines located at the CINECA computing center in Bologna and at CICAIA center in the University of Modena and Reggio Emilia.

4.1 Model System

This chapter is devoted to the description of *0-dimensional Silicon crystal*, commonly called *Silicon nanocrystals (Sinc)*. The Sinc described in this work are spherical nanocrystals isolated in vacuum and doped simultaneously with substitutional impurities of Boron and Phosphorus. Starting point of this study are the undoped Sinc, free-standing nanocrystals built up by considering all the bulk Silicon atoms contained in a sphere centered

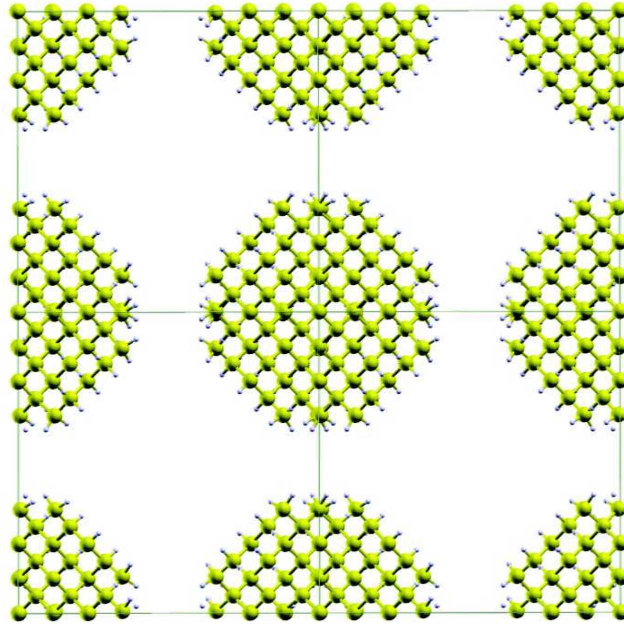

Figure 4.1: Schematic representation of the supercell approach. The supercell is represented by the continuous grey line and the atoms by the spheres (top view). The Sinc into account is the $Si_{147}H_{100}$. As one can see the physical nanocrystal is in the center of the image, while nc appearing in the corners are fictitious replicas introduced by the supercell approach.

on a Si ion; they show an almost spherical shape, the typical tetrahedral coordination of bulk Silicon for the Si-Si bond distances and have T_d point group symmetry of the typical diamond-structured bulk materials.

The present work takes into account different nanocrystals with diameters ranging from 1.1 nm up to 1.79 nm, in order to simulate almost reliable systems through the progressively increasing of dimensions. The undoped Sinc considered, the $Si_{35}H_{36}$ (d=1.10 nm), $Si_{87}H_{76}$ (d=1.5 nm), $Si_{147}H_{100}$ (d=1.79 nm) are passivated at surface with hydrogen to saturate all the possible dangling bonds and to exclude possible effects of surface states and surface reconstruction. The single and codoped Sinc, instead, are obtained from the above nanocrystals with the insertion of one or two impurities, a donor atom (such as Phosphorus) and an acceptor one (like Boron) placed in substitutional site after the removal of the corresponding Si atom. All the Sinc are treated as isolated free standing nanocrystals placed into simple cubic supercells, with side varying from 40 a.u. up to 45 a.u., according to the nc diameter (respectively the former for the $Si_{35}H_{36}$ and the later for the $Si_{87}H_{76}$ and $Si_{147}H_{100}$) in order to leave enough vacuum (at

least 6 Å) around each neighboring nanocrystals to avoid any Coulombian interaction between the periodic replica, as shown in Fig. 4.1. The band folding in the Brillouin Zone and the flattening of the bands into discrete levels without any **k**-dispersion due to the quantum confinement along the 3 coordinate directions, allow to sample the Brillouin Zone only with the single Γ (0,0,0) **k**-point.
The total energy calculation, have been performed using an energy cut-off of 30 Rydberg (Ry), treating the structural relaxation with ultrasoft Vanderbilt pseudopotential in order to manage large supercells with a huge number particles up to 512 atoms, while the optical properties have been calculated via norm-conserving pseudopotential in the formulation of Perdew and Zunger [79]. The application of ultrasoft pseudopotential for optical calculations is problematic both for the relaxation of the norm conservation and also for the presence of the non-local commutator $\hat{p} = \frac{i}{\hbar}\left[\hat{H}, \hat{r}\right]$ that does not permit an accurate and an easy computing description. The XC functional used is GGA in the formulation of Perdew-Burke-Ernzerhof (PBE) [74] very similar to the PW91 pseudopotential (see Section 2.2.1).

4.2 Formation Energy

When defects are present or created in the materials, the systems subdue a perturbation. In our case defects are represented by acceptor and donor impurities, such as Boron (B) and Phosphorous (P) respectively, substitutionally inserted in the hydrogenated Sinc. Our aim is to understand which configuration is more stable when one or two impurities are inserted, and in practice to evaluate what amount of energy is required to sustain the doping process. A theoretical useful tool is the *Formation Energy (FE)* defined, according to the paper of Zhang and Northrup [159], and applied in several others papers [160, 161, 162] with the following formulation:

$$\Delta E_{FE} = E\left(\mathrm{Si}_{n-l-k}\mathrm{B}_k\mathrm{P}_l\mathrm{H}_m\right) - E\left(\mathrm{Si}_n\mathrm{H}_m\right) + (k+l)\,\mu_{\mathrm{Si}} - k\,\mu_{\mathrm{B}} - l\,\mu_{\mathrm{P}}, \quad (4.1)$$

The k and l index can be 0 or 1, thus one has an un-doped, a single B- or P-doped Sinc or a B and P co-doped Sinc. The Formation Energy of neutral B and/or P impurities can be defined as the energy required to insert one B and/or one P atom within the cluster after removing one (or two) Si atoms (depending on single doping or co- doping) which are transferred to the chemical reservoir, assumed to be bulk Si. Here we're calling Formation Energy the amount Δ_{FE} even if this is just an energy difference $\Delta_{\mathrm{FE}} = E_{f_2} - E_{f_1}$, between the formation energy of the pure undoped Sinc

$$E_{f_1} = E\left(\mathrm{Si}_n\mathrm{H}_m\right) - n\,\mu_{Si} - m\,\mu_H \quad (4.2)$$

and the Formation Energy of the doped nanocrystals (with one or two impurities)

$$E_{f_2} = E\left(\mathrm{Si}_{n-l-k}\mathrm{B}_k\mathrm{P}_l\mathrm{H}_m\right) - (k+l)\,\mu_{\mathrm{Si}} - k\,\mu_{\mathrm{B}} - l\,\mu_{\mathrm{P}} - m\,\mu_H \tag{4.3}$$

To evaluate this amount Δ_{FE} one has just to perform total energy calculation of the system energy E (with and without impurities) and of the chemical potentials for each of the atomic species involved in the formula [4.1]: μ_{Si} is the total energy per atom of bulk Si, μ_B the total energy per atom in tetragonal B_{50} for the Boron impurity, as in [163] and μ_P the chemical potential in Orthorhombic Black Phosphorus for P impurity, as in [164]. Since the quantity Δ_{FE} is independent by the number of atoms of the nanocrystals, it can be calculated and compared for several Sinc of different size, giving a measure of the stability of the single and co- doped Sinc with respect to several parameters, such as the dimensions, the number of the chemical species and the relative position of impurities within the nanocrystals.

4.3 What about doping Silicon Nanocrystals?

The semiconductors doping has represented since the 70's a valid and cheap technique to increase the number of carriers of the system. This holds for Silicon in particular because of its intense application in the traditional microelectronics field. Hundreds of papers investigating doping Bulk Silicon are present in the literature, but none of them since last 10 years has concerned the possibility to dope Silicon based nanostructures. In particular, preliminary research works have been presented in international scientific journals by the experimental group of Minoru Fujii since 1998, indicating the way to achieve stimulated emission of visible light from small Silicon nanocrystals single and co doped simultaneously with Boron and Phosphorous [33, 41] embedded in an oxide matrix. From the experimental point of view, these works represent one of the first attempt to investigate the role played by the insertion of III-V impurities in Silicon structure at the nanoscale, in particular focusing the attention on the optical features for possible optoelectronic applications. Others recent attempts to investigate the doping at the nanoscale have been performed on different systems such as CdSe and ZnSe colloidal nanocrystals by Galli [165], Erwin [166], Chelikoswky [161] but only in the early 90's several experimental and theoretical investigations have been performed at the same time about the possibility of inserting impurities in small system, demonstrating that this is possible but nonetheless extremely difficult also for modern techniques. To the best of our knowledge very few theoretical works exist in literature concerning impurity states in Silicon-based systems related to the work made by Fujii. In [167] an empirical LCAO calculation of the activation energies of hydrogenic impurities in nanocrystalline Si is discussed, while quantum confinement in P-doped Sinc

is analyzed in [168] by Melnikov and Chelikowsky, using a real-space *ab initio* pseudopotential density functional method. Very few works exist about doping on Silicon nanostructures but none of them, since now, concerns the codoping [168, 169, 170, 160, 171]. Our investigation focused on the effect of *codoping* of Silicon nanocrystals, results to be innovative and precursor with respect to other theoretical investigations of this research field.

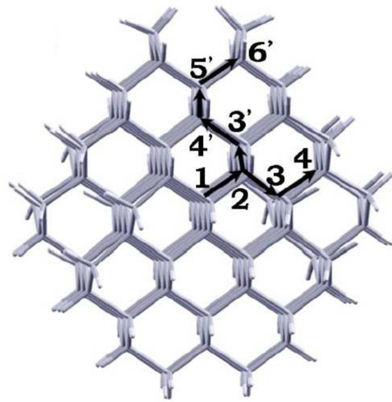

(a) The impurity is moved from the center toward the "subsurface" position within the Sinc.

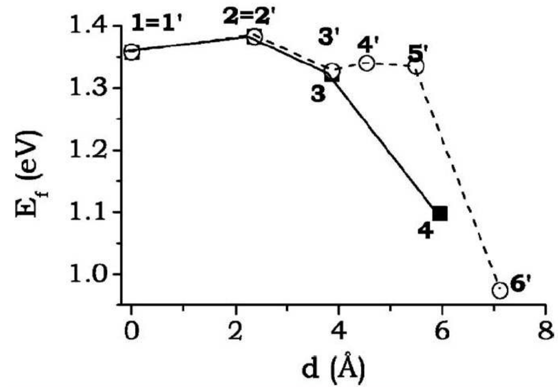

(b) Formation energy for a neutral impurities as a function of the impurity position, labelled from 1 to 6, within the nanocrystals.

Figure 4.2: Formation Energy path for a B- single doped Sinc (from [160]).

The theoretical investigation on the simultaneously doping with Boron and Phosphorous described in this thesis work, takes place by the new and interesting considerations about the single doping reported in their paper by Cantele and Degoli [160]. In their work the authors studied the effects on the Sinc stability after the insertion of single impurities of B, P and Al taking into account several nc with different diameter. The FE for neutral impurity, calculated from Eq. [4.1], has been evaluated as a function of the distance of the impurity from the nanocrystals center. By considering one among the biggest nanocluster studied, the $Si_{146}BH_{100}$, the impurity has been moved from the center toward the surface positions through different substitutional sites, as shown in Fig.4.2(a). It comes out that the FE strongly decreases when the impurity occupies the substitutional sites in the first Silicon layer below the surface (as in Fig.4.2(b)) suggesting that these positions correspond to a stable configuration for the doped Sinc. Moreover the FE decreases with the increasing of the Sinc size, demonstrating that for larger systems the insertion of a substitutional impurity is more convenient and gives rise to an increase of stability. Next, the FE has been calculated with relaxed and unrelaxed bond lengths in order to bring out the effect of the Sinc relaxation on the FE. It comes out that this doesn't really affect

the stability of the system: the FE still decreases with the increasing of dimensions maintaining an almost linear scaling while the relaxation just around the impurity determines a rigid downward shift of FE toward lower energy.

Due to these considerations about the single impurity Formation Energy in the paper by Cantele and Degoli [160], we decide to codope the Sinc inserting simultaneously the Boron and Phosphorous impurities in the first Silicon layer below the surface, as shown in Fig. 4.3. In this configuration the impurities are placed in each Sinc at the largest possible distance according to the diameter of the nanocrystals and to the condition to occupy substitutional site in the first layer below the hydrogenated surface, as depicted from the following resuming Table 4.1:

	Diameter (Å)	D_{BP} (Å)
$Si_{33}BPH_{36}$	11	3.64
$Si_{85}BPH_{76}$	15	10.60
$Si_{145}BPH_{100}$	17.9	13.59

Table 4.1: Diameter and impurity-impurity distance for the codoped Sinc considered in this work.

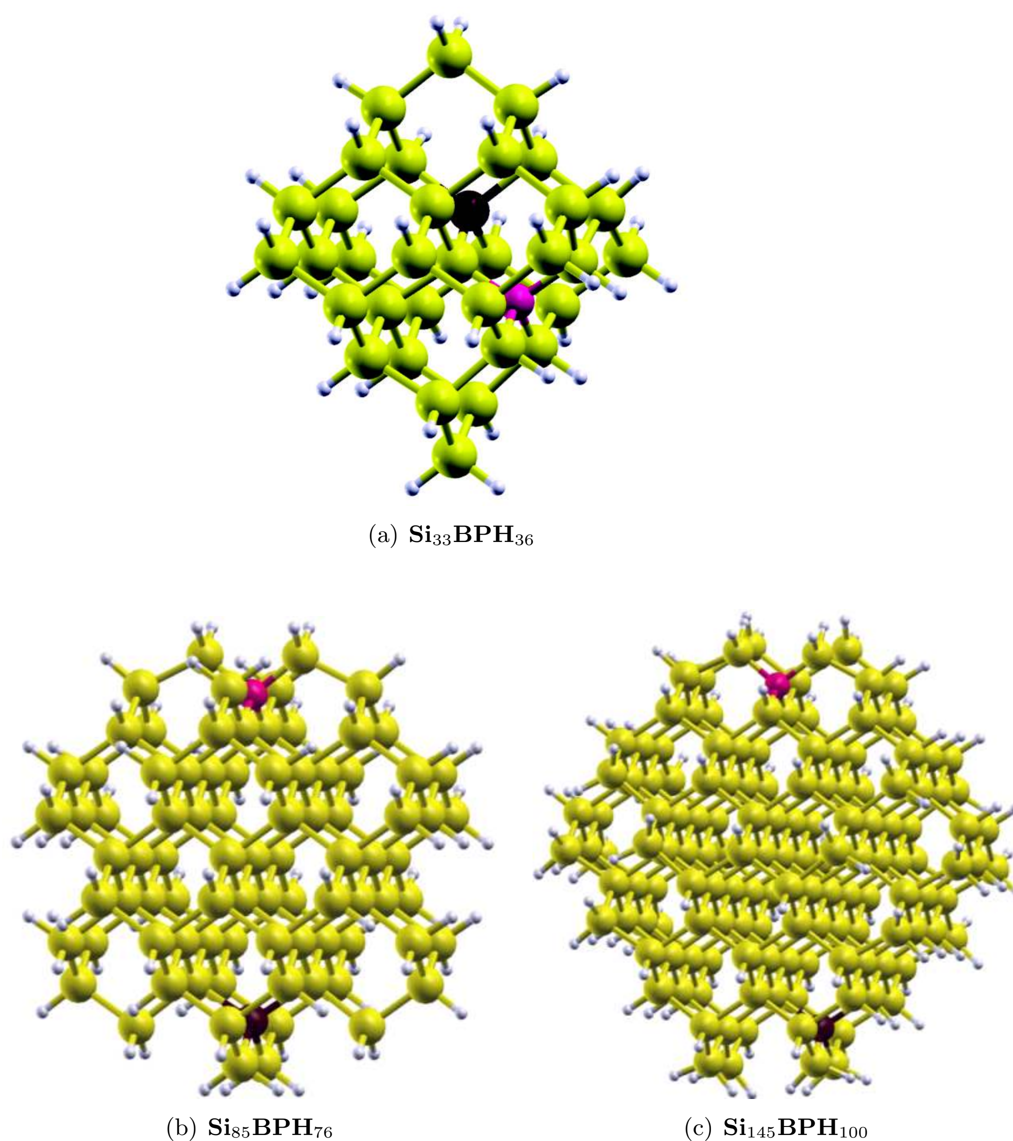

(a) $\mathbf{Si_{33}BPH_{36}}$

(b) $\mathbf{Si_{85}BPH_{76}}$

(c) $\mathbf{Si_{145}BPH_{100}}$

Figure 4.3: Codoped Silicon Nanocrystals. Yellow (gray) balls represent Si atoms, while the white (small grey) balls are the hydrogens used to saturate the dangling bonds. Boron (magenta) and Phosphorus (dark brown) impurities have been located at subsurface position in substitutional sites on opposite sides of the nanocrystals.

4.4 Codoping: Structural Properties

In this section we're going to examine how the structural properties are influenced by the presence of two substitutional impurities with respect to the undoped hydrogenated Sinc and the single doped ones. After the insertion of impurities the Sinc have been relaxed to achieve the most reliable geometric configuration corresponding to the absolute minimum of total energy.

We observe that the insertion of one and/or two impurities gives rise to

Bond	$Si_{87}H_{76}$ Å	Bond	$Si_{86}BH_{76}$ Å	$Si_{86}PH_{76}$ Å	$Si_{85}BPH_{76}$ Å
Si-Si_s	2.355	B-Si_s	2.036		2.021
Si-Si_s	2.355	B-Si_s	2.036		2.021
Si-Si_i	2.363	B-Si_i	2.014		2.034
Si-Si_i	2.363	B-Si_i	2.014		2.034
Si-Si_s	2.355	P-Si_s		2.294	2.295
Si-Si_s	2.355	P-Si_s		2.294	2.295
Si-Si_i	2.363	P-Si_i		2.380	2.331
Si-Si_i	2.363	P-Si_i		2.380	2.331

Table 4.2: Bond lengths around the impurities site for the undoped $Si_{87}H_{76}$ nanocrystals and the single- and codoped ones (diameter 1.50 nm). B and P impurities have been substitutionally located at subsurface positions (see Fig. 4.3(b)). Si_s and Si_i refer to two surface and two inner Si atoms around this site respectively.

variations in the bond lengths focalized in particular around the impurity sites, involving in particular the impurity-Si bonds. In Table 4.2, Table 4.3 and Table 4.4, are reported the relaxed bond lengths around the impurities for each of the Sinc, $Si_{33}BPH_{36}$, $Si_{85}BPH_{76}$, $Si_{145}BPH_{100}$. Comparing the bond lengths of the single doped nc with those of the undoped one, we can see from Table 4.2, that the insertion of one impurity in the singled doped nc, determines an important structural relaxation around the impurity site: the initial T_d symmetry (ref. to Sec. 4.1) of the undoped Sinc turns into the C_{2v} symmetry. More specifically this leads to a local structure with two shorter and two longer Si-impurity distances with respect to the two surface and two inner Si atoms. The more significant relaxation with respect to the undoped nanocrystals is found for the single trivalent atom (B, 2.036 Å and 2.014 Å with respect to 2.355 Å and 2.363 Å) than for the single pentavalent one (P, 2.294 Å and 2.380 Å with respect to 2.355 Å and 2.363 Å). The amount of relaxation around the impurity sites is directly related

Bond	$Si_{35}H_{36}$ Å	Bond	$Si_{34}BH_{36}$ Å	$Si_{34}PH_{36}$ Å	$Si_{33}BPH_{36}$ Å
Si-Si_s	2.300	B-Si_s	2.093		2.035
Si-Si_s	2.300	B-Si_s	2.022		2.026
Si-Si_s	2.300	B-Si_s	2.022		2.026
Si-Si_i	2.361	B-Si_i	2.008		2.007
Si-Si_s	2.300	P-Si_s		2.366	2.303
Si-Si_s	2.300	P-Si_s		2.365	2.302
Si-Si_s	2.300	P-Si_s		2.364	2.297
Si-Si_i	2.361	P-Si_i		2.310	2.334

Table 4.3: Bond lengths around the impurities site for the undoped $Si_{35}H_{36}$ nanocrystals and the single- and codoped ones (diameter d= 1.10 nm). B and P impurities have been substitutionally located at subsurface positions (see Fig. 4.3(a)). Si_s and Si_i refer to three surface and one inner Si atoms around this site respectively.

to the impurity valence.

For what concerns the codoping, instead, one can see from the same tables, that the differences among the four impurity-Si bond lengths are smaller with respect to the single-doped case (the Si-B bonds differ of about 1.08% in the single-doped case and only 0.64% in the co-doped case, whereas this variation in the case of P reduces from 3.61% to 1.54%). Thus, if carriers in the Sinc are perfectly compensated by simultaneously n- and p-type impurities doping, an almost T_d configuration, in which the four impurity-Si bonds are practically the same, is recovered. Moreover looking at Table 4.3 and Table 4.4 where are reported the bond lengths for the $Si_{33}BPH_{36}$ and $Si_{145}BPH_{100}$ respectively, one can see that a lowering of the symmetry with respect to the $Si_{87}H_{76}$ -based nanocrystals occurs for the smaller and larger nanoclusters. In this two cases the impurity-Si bond lengths present a differ trend with respect to the $Si_{85}BPH_{76}$: there are now two shorter bonds with the same value, one longer and one with another little different value. In spite of these light structural modifications occurring around the impurity sites, the possibility to achieve the T_d symmetry for codoped compensated Sinc is achieved also for the smaller and the larger nanocrystals, demonstrating that this behaviour is independent of the Sinc size. The different relaxation trend in the two nanocrystals among the Si-B and Si-P bond lengths, leading to the lowering of symmetry, can be related to the different Silicon neighborhood experienced by the impurities. In the case of $Si_{35}H_{36}$ (blowup in Fig. 4.4) and $Si_{145}BPH_{100}$ (blowup in Fig. 4.5), the im-

Bond	$Si_{147}H_{100}$ Å	Bond	$Si_{146}BH_{100}$ Å	$Si_{146}PH_{100}$ Å	$Si_{145}BPH_{100}$ Å
Si-Si$_s$	2.356	B-Si$_s$	2.029		2.016
Si-Si$_s$	2.356	B-Si$_s$	2.029		2.016
Si-Si$_s$	2.356	B-Si$_s$	2.063		2.018
Si-Si$_i$	2.369	B-Si$_i$	2.009		2.022
Si-Si$_s$	2.356	P-Si$_s$		2.310	2.306
Si-Si$_s$	2.356	P-Si$_s$		2.310	2.306
Si-Si$_s$	2.356	P-Si$_s$		2.372	2.338
Si-Si$_i$	2.369	P-Si$_i$		2.321	2.321

Table 4.4: Bond lengths around the impurities site for the undoped $Si_{147}H_{100}$ nanocrystals and the single- and codoped ones (diameter d = 1.79 nm). B and P impurities have been substitutionally located at subsurface positions (see Fig. 4.3(c)). Si$_s$ and Si$_i$ refer to three surface and one inner Si atoms around this site respectively.

purities in the first layer below the surface are bonded to one inner Si atom and to three surface Si atoms passivated with one and two hydrogen while in $Si_{85}BPH_{76}$ the impurities have two surface Si atoms and two inner core Si neighbors (see blowup in Fig. 4.5): to that the impurity sites experience a different relaxation, with a different amount of bond softening.

After the investigation on the effect of dimension and chemistry on the structural relaxation, we focus the attention on the effect played by the impurity-impurity distance on the structural modification when two impurities are simultaneously present in the same nanocluster, comparing the impurity-Si distances to the corresponding Si-Si ones for the undoped nc. We consider the biggest nanocrystals reported here, the $Si_{147}H_{100}$, and by keeping fixed the Boron in a subsurface position, we moved the Phosphorus through substitutional sites all along the first subsurface Silicon layer, as schematically depicted in Fig. 4.6. For each of the impurity sites occupied by the Phosphorous and labelled by position by II, III, V-a, V-b, VI-a, VI-b, VIII-a, VIII-b, IX-a, IX-b and X, where the roman number refers simply to the positions evidenced in Fig. 4.6, a different configuration has been achieved and for each of them energy and structural minimization have been performed through *ab initio* calculations. Then, for each minimized configuration, the relaxed B-P and the corresponding Si-Si distances have been calculated. These values are reported in Fig.4.7 where are also compared with the corresponding relaxed Si-Si distances of a $6 \times 6 \times 6$ supercell bulk

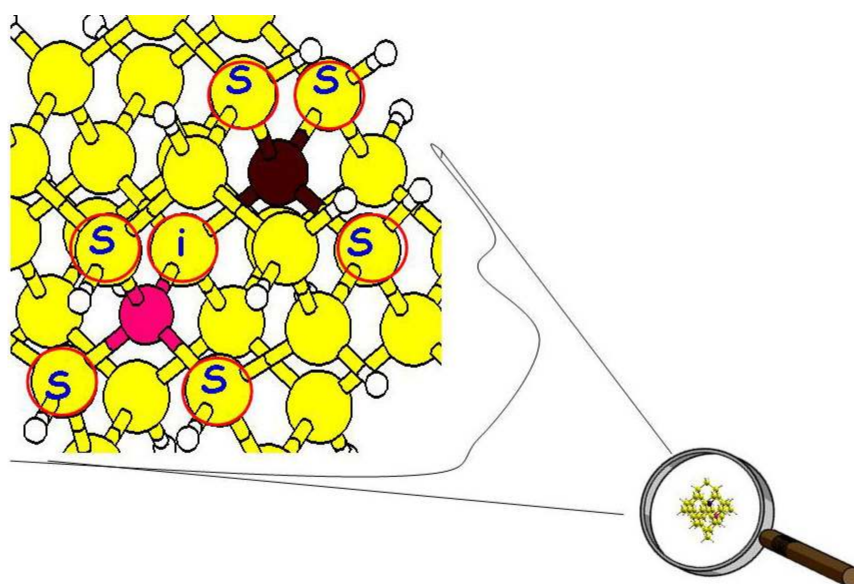

Figure 4.4: Blow up of the bond lengths around the impurity sites in codoped $Si_{33}BPH_{36}$. The "S" label indicates surface Silicon atoms bonded to the impurity, while the "i" refers to the inner Si atoms. In yellow are Si atoms, in white the H ones at surface.

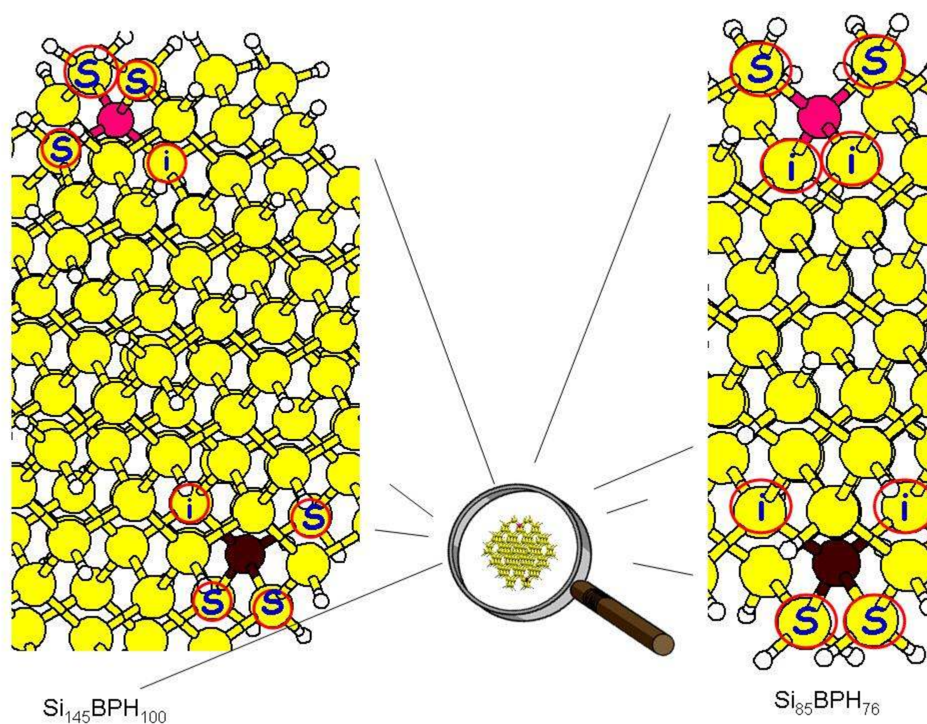

Figure 4.5: Blow up of the bond lengths around the impurity sites in codoped $Si_{145}BPH_{100}$ (left side) and $Si_{85}BPH_{76}$ (right side). The "S" label indicates surface Silicon atoms bonded to the impurity, while the "i" refers to the inner Si atoms. In yellow are Si atoms, in white the H ones at surface.

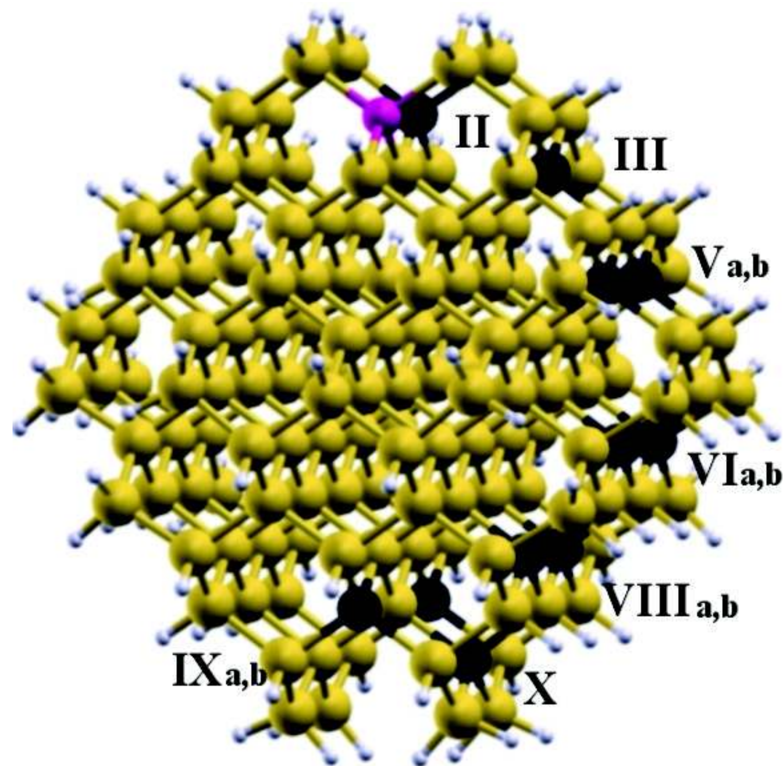

Figure 4.6: "Phosphorus impurity path" in $Si_{145}BPH_{100}$. Phosphorus atom (dark brown) exploring several substitutional sites (labelled by number) while Boron atom (magenta) fixed: both atoms are in first Si layer below the surface shell.

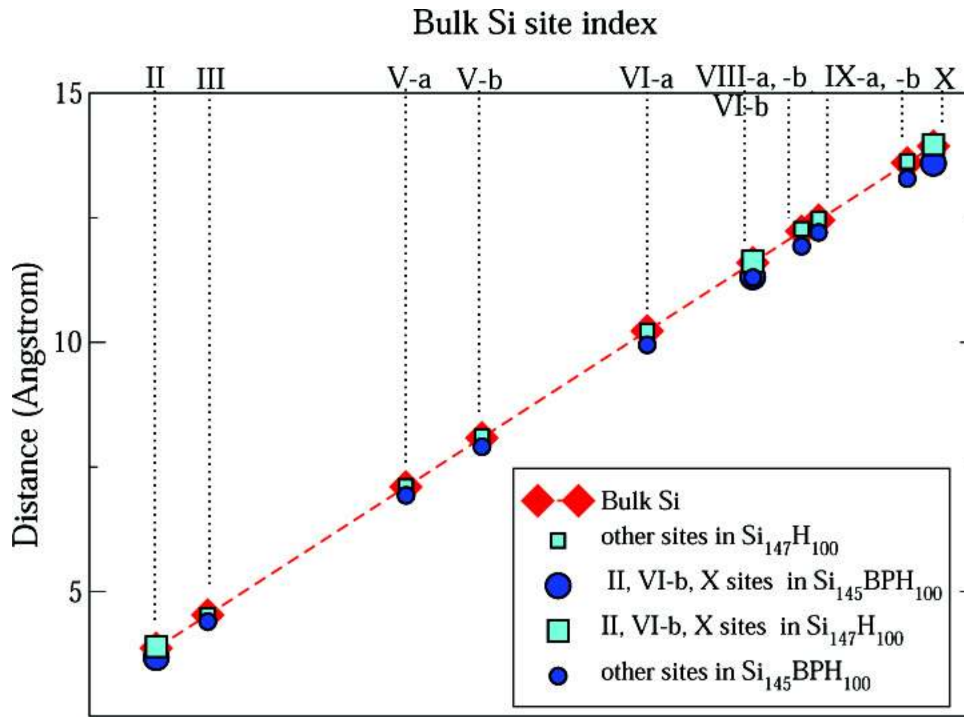

Figure 4.7: Boron-Phosphorus substitutional site distances in the $Si_{145}BPH_{100}$ nanocrystal (blue circles) and the corresponding Si-Si distances in the undoped $Si_{147}H_{100}$ nanocrystal (cyan squares) compared to the bulk Silicon corresponding distances (red diamonds).

Silicon. Since the bulk Silicon distances are considered as reference, values above the dashed line correspond to an increase of the B-P distance, while values below correspond to a reduction. Thus, since the displacement of the B-P distance values with respect to this line is really small, one can conclude that only weak modification occur in the codoped distances with respect to the bulk. On going from the undoped nanocrystals, where the distances are practically the same as in bulk Silicon, to the codoped ones we note a very small shrinkage of the impurity-impurity distances with respect to the previous Si-Si distances. This shows, once again, that if carriers in the Sinc are perfectly compensated by simultaneous doping, the starting undoped Sinc undergoes practically no geometry distortion. In Table 4.5 are resumed the relaxed B-P distances for the codoped Sinc of different dimensions considered here.

Cluster	B-P Distance (Å)	Neighbors index
$Si_{33}BPH_{36}$		
B,P @I shell	3.5646	2nd
$Si_{85}BPH_{76}$		
- B,P @ I shell (1)	10.5940	VIII
$Si_{145}BPH_{100}$		
B,P @I shell		
	13,594	X
	13.286	IX_b
	12,2022	IX_a
	11,9254	$VIII_b$
	11,3159	VI_b
	11,2973	$VIII_a$
	9,9503	VI_a
	7,9056	V_b
	6,9328	V_a
	4,3970	III
	3.68	II

Table 4.5: Relaxed B-P distances for codoped Sinc.

4.5 Codoping: Formation Energy

The structural modifications introduced by the presence of one or two impurities discussed in the previous section, affect also the stability of the system and have to be carefully taken into account when dealing with different kind of single and co- doped Silicon nanocrystals. The stability of doped systems has been evaluated through the calculation of the *Formation Energy (FE)*, defined in Sec. 4.2, as the energy required to insert neutral impurities of B or/and P substitutionally within the hydrogenated Silicon nanocrystals Si_nH_m [44] by removing an equivalent number of Si atoms, and depicted in Eq. [4.1]. In order to clarify which are the parameters that play a crucial role in the determination of the Formation Energy, we have performed a series of total energy calculations considering: i) single-doped and codoped nanocrystals, ii) nanocrystals of different sizes, iii) impurities located in different sites and iv) variable impurity-impurity distance within the same nanocrystal. First of all our aim is to understand which kind of doping is more easier to realize, by comparing in Fig.4.8 FE for B and P single and co- doped Sinc, for each size of Sinc considered here. To note that in this figure the B and P impurities have been placed in the Sinc as second neighbors, since this choice

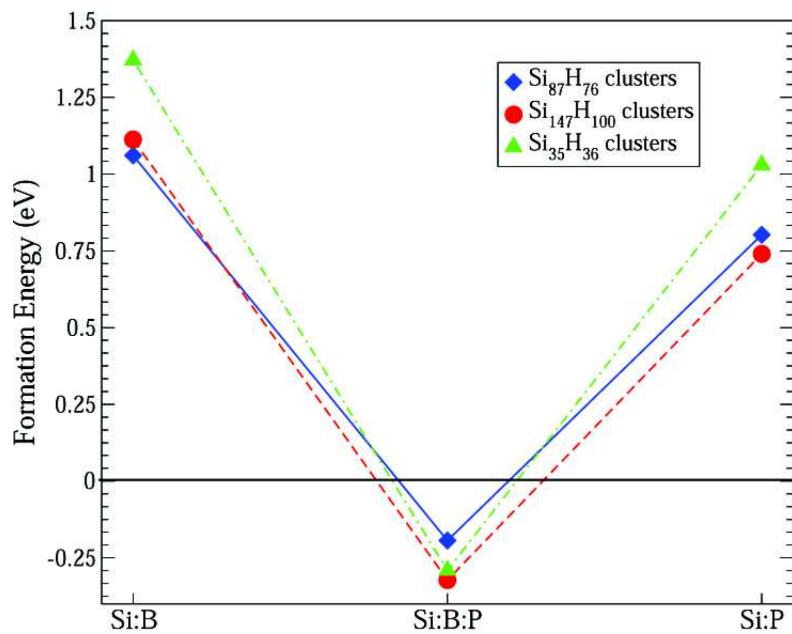

Figure 4.8: Formation energy for single-doped and codoped Si-nanocrystals. In the codoped nanocrystals the impurities are placed as second neighbors in the first subsurface shell (see text). B and P single-doped and B-P codoped nanocrystals are considered. Green triangles are related to $Si_{35}H_{36}$, blue diamonds to $Si_{87}H_{76}$ and red circles to $Si_{147}H_{100}$ based nanocrystals. The lines are a guide for eyes.

corresponds to the nearest possible distance between the two impurities for the $Si_{33}BPH_{36}$-nc in Fig. 4.3(a), and the $Si_{145}BPH_{100}$-nc (see the position labelled II in Fig. 4.6). After geometry relaxation the distances between B and P impurities are D_{BP} = 3.56 Å, D_{BP} = 3.64 Å and D_{BP} = 3.68 Å for the $Si_{33}BPH_{36}$, $Si_{85}BPH_{76}$ and $Si_{145}BPH_{100}$ nanocrystals, respectively, as shown in Table 4.5.
From Fig. 4.8 it is clear that simultaneous B and P doping strongly reduces (of about 1 eV) the Formation Energy with respect to both B or P single-doped cases and that this reduction is similar for Sinc of different size. Thus while B or P single doping is very costly (in particular, the formation energy increases with decreasing nanocrystals size, in agreement with previous calculations [168, 160]) B and P codoping results much easier to obtain and almost independent on the nanocrystals size. The important point here is that Sinc can be more easily simultaneously doped than single-doped; this is due to both the charge compensation and the minor structural deformation subdue by the Sinc.
Moreover we performed more calculations exploring different configuration of codoped impurities, in order to investigate in details the dependence of FE on the distance between impurities and on the Sinc dimension. In Fig. 4.9 has been compared the FE for the single and co- doped $Si_{87}H_{76}$ and $Si_{147}H_{100}$ nanocrystals with impurities placed at two different distances: first the impurities are second neighbors in both the nc (as in previous Fig. 4.8), the minimum possible distance considering only substitutional subsurface position (relaxed D_{BP}=3.64 Å and 3.68 Å respectively) and then the impurities are placed at the largest possible distance according to the dimension of the Sinc, that means after the relaxation, D_{BP}=10.60 Å for $Si_{85}BPH_{76}$ and D_{BP}=13.29 Å for $Si_{145}BPH_{100}$ respectively. It's worth pointing out that for both the nanocrystals considered when the impurity-impurity distance is reduced, the Formation Energy decreases of 0.2-0.3 eV and assumes negative values. This fact demonstrates that a stronger interaction between n- and p- type impurities leads to a strong reduction in the Formation Energy, so that codoping results easier to realize when the dopants are closer each other. The amount of Formation Energy reduction is about the same for each considered nanocrystals, and thus, as shown in Fig. 4.8, it's almost independent by the nanocrystals size. Since the FE used here is calculated as a difference between the total energies of the nanocrystals with and without impurities (see Eq.[4.1], negative values of FE obtained for the codoped Sinc in Fig. 4.9 means that the calculated total energies of the codoped nanocrystals are bigger in absolute value than the total energies of the single doped nc. More negative are these FE values, more the codoped nanocrystals are likely to be obtained during the formation process with respect the single doped ones under the same growth conditions.

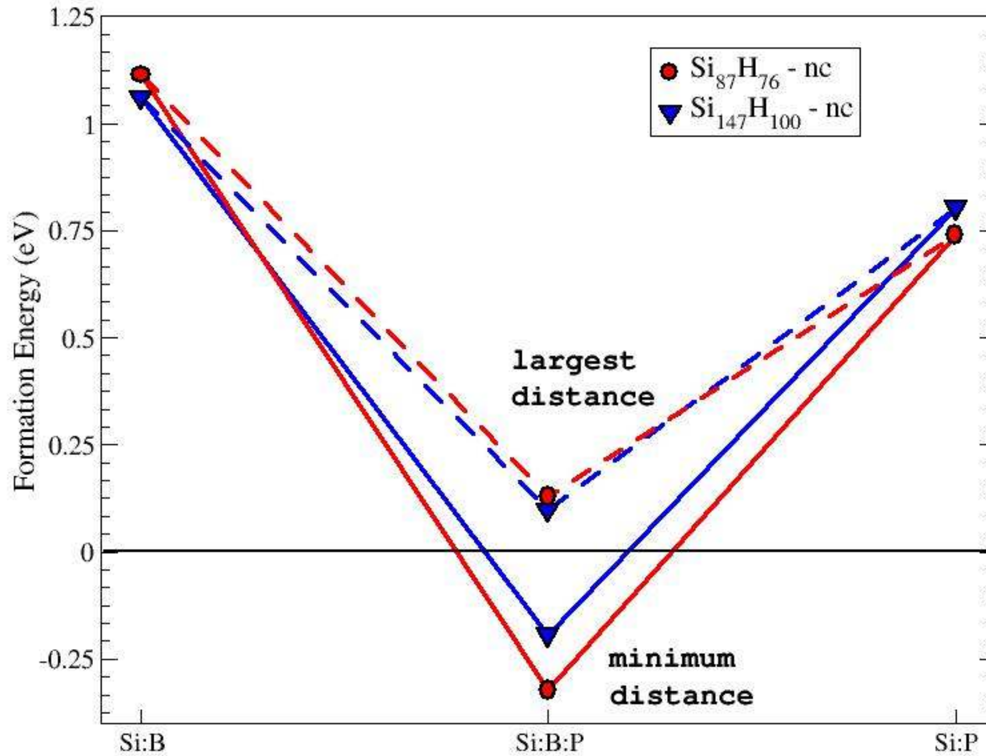

Figure 4.9: Formation Energy of $Si_{87}H_{76}$ and $Si_{147}H_{100}$ single-doped and codoped nanocrystals, with impurities placed within the codoped nanocrystals at two different distances: a large (dashed lines) and a small one (solid lines) (see text). Red circles refer to $Si_{87}H_{76}$-nc and blue squares to $Si_{147}H_{100}$-nc. The lines are a guide for eyes.

Nonetheless, regarding again Fig. 4.8, it comes out that the smallest B- and P- single doped nc, the $Si_{34}PH_{36}$ and $Si_{34}BH_{36}$, present the greater positive FE values with respect to the other single doped cases. This suggests that the single doping in small clusters results to be more difficult to realize and more unfavorable than in other cases. This aspect is in good accord with the conclusion asserted by Dalpian and Chelikowsky [161]: the increase in the formation energies of these impurities with the decrease of the nc size is a clear evidence that single doping small nanocrystals is more difficult compared to single doping bigger systems, such as bulk for example. Dalpian and Chelikowsky define *self-purification* a possible intrinsic property of nanocrystals, consisting in the exclusion of dopants from small nanocrystals, that follows the increase of Formation Energy. This confirms the fact that substitutional impurities are more stable in subsurface position just below

the surface, contributing then to shed more light on the most preferred position of single dopants within the nanocrystals. From the experimental works, the doped and codoped Sinc are described such as embedded in an glass Boron and/or Phospho- silicate glass matrix. One possible hypothesis one the location of impurities is that the dopants could prefer to migrate at the interface between the nanocrystals and the silica matrix, according to the intrinsic difficulty of impurities to diffuse into small Sinc, that therefore constrains the impurities to be relegate in the interface region. The nanocrystals dimensions can be an important parameter to manage with the doping process like the structural modifications which can also affect the stability of the system as demonstrated by the work of Ramos et al. [169, 170] where the FE of single doped impurities strongly varies by moving from spherical to faceted Sinc.
Nevertheless, our investigation on the codoping Sinc, demonstrates how the simultaneous insertion of donor and acceptor impurities within Sinc is more suitable than single doping, and that the amount of reduction of FE is practically size independent; although only spherical Sinc are here considered, we can think concerning the codoping that the faceted Sinc present a similar behaviour in which the size and shape have assume reduce importance with respect to the singled doped cases studied in [170].
Then, in order to investigate more in details the dependence of the Formation Energy on the impurity-impurity distance, we focus our attention on the biggest codoped $Si_{145}BPH_{100}$, trying to trace a "Formation Energy path" by progressively increasing the B-P distance. To do this we kept fixed the B atom in a subsurface position and moved the P atom through different substitutional site along the first subsurface shell, as schematic shown in Fig. 4.6 and already explained in the previous Section 4.4. For each different configuration, we performed total energy DFT calculation in order to evaluate opto-electronic properties and Formation Energy as a function of the B-P distance within the nanocrystal.

The results of these calculations are shown in Fig. 4.10 and Fig. 4.11 where two interesting effects are evidenced. From Fig. 4.10 we observe an augmentation in FE with the increase of the Boron-Phosphorus distance within the nanocrystal, as depicted in Fig. 4.10, where is reported the FE for each of the different impurity configuration as a function of the B-P distance in terms of the distance (in Angstrom) and of the neighbors site index labelled in Roman numbers. Some interesting consideration could be done.
The first is that FE assumes negative values for impurity between the site II (3.68 Å) and site VI (9.95 Å) while going up with the distance, FE becomes bigger and positive. This change from negative to positive values, can lead to the definition of a "critical impurity distance": below such value, the interaction between Boron and Phosphorus is stronger and it gives rise to a reduction of FE meaning that codoping results more favorable and increase

the stability of Sinc, while, above this value, the Coulomb interaction tends to be more screened and therefore to be quenched leading to a minor influence on the FE then reducing the stability of the impurity complex within the nanocrystals.

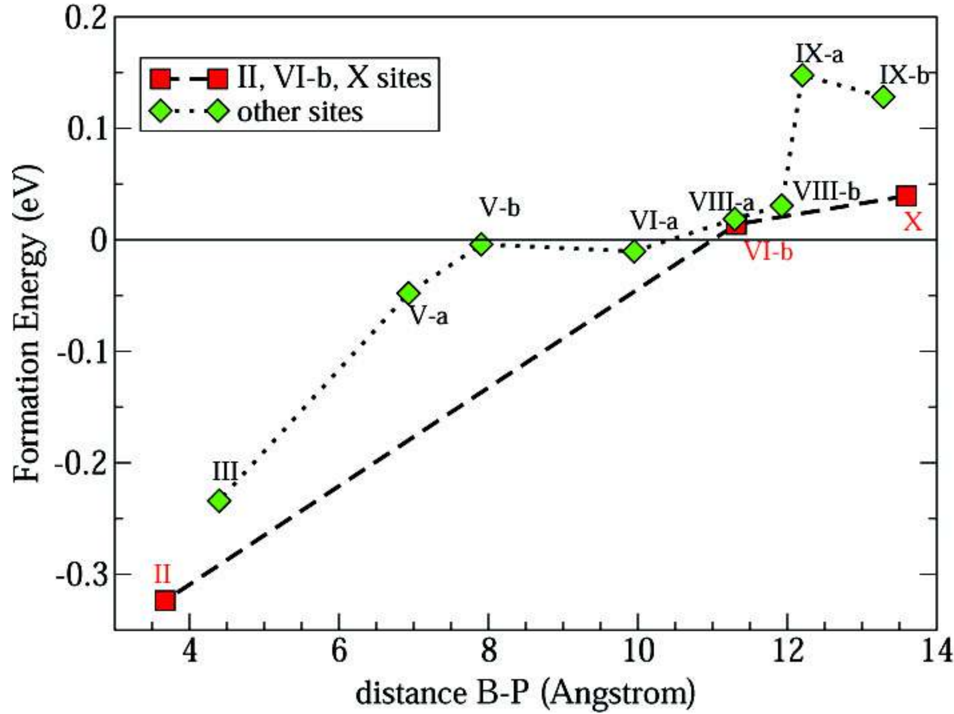

Figure 4.10: Formation Energy as a function of the Boron-Phosphorus distance. Roman numbers refer to the positions of the P atom (see Fig. 4.6). The dotted and dashed lines connect two categories of impurity sites, where the surrounding surface Si atoms are bounded to the same number of passivating H atoms.

These outcomes are supported also by Fig. 4.11, in which we report the values of the Formation Energy for three nanocrystals different in size and with impurities located in the subsurface shells at different distances. As before, it appears clear that the distance between impurities plays a fundamental role on the decrease of the Formation Energy. Below a given impurity-impurity distance the Formation Energy assumes negative values for each nc size. Moreover we see that the Formation Energy shows the minimum value when the impurities are located at the minimum possible distance in each codoped Sinc apart from the different diameter size. Indeed the impurity-impurity distance seems to play a major role on the FE with respect to the nanocrystals size, since the Formation Energy values are similar for similar impurity-impurity distances independently of the nanocrystals dimension. The small difference between the $Si_{85}BPH_{76}$, the $Si_{33}BPH_{36}$ and the $Si_{145}BPH_{100}$ is due to the different neighborhood

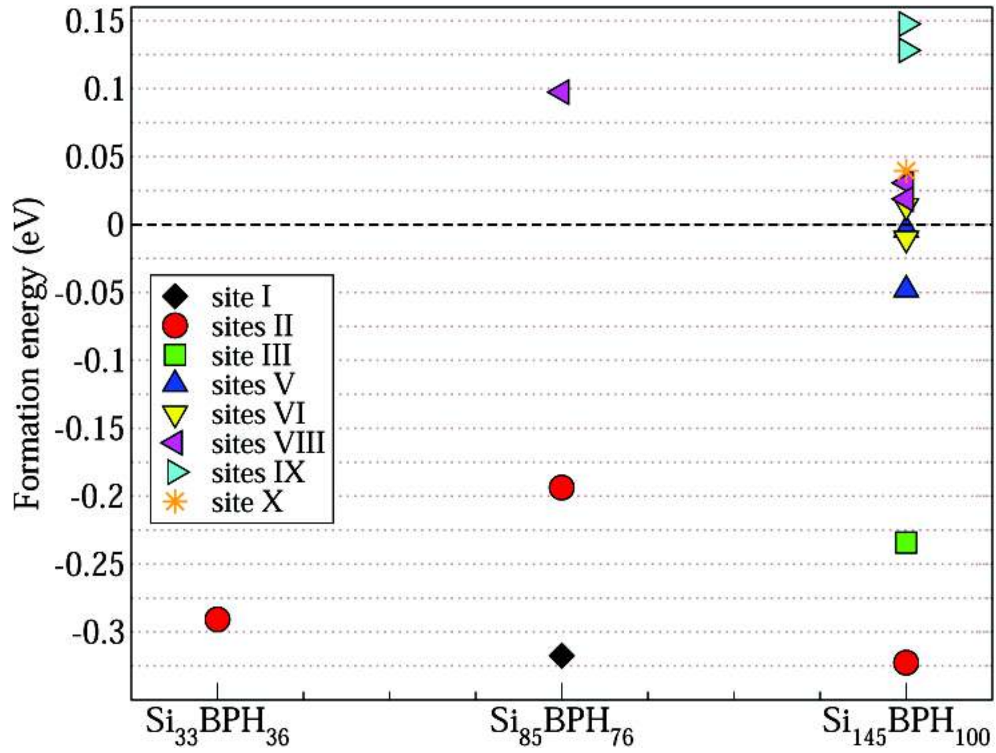

Figure 4.11: Formation Energy as a function of Sinc size and impurity-impurity distance. For the three different considered Sinc one has the following nc diameters (d) and impurity-impurity distances (D_{BP}): $Si_{33}BPH_{36}$ d= 1.10 nm and D_{BP} = 3.56 Å (site II); $Si_{85}BPH_{76}$ d= 1.50 nm and D_{BP} = 2.00 Å (site I), D_{BP} = 3.64 Å (site II), D_{BP} = 10.60 Å (site VIII); $Si_{145}BPH_{100}$ d= 1.79 nm and D_{BP} = 3.68 Å (site II), D_{BP} = 4.40 Å (site III), D_{BP} = 6.93 Å (site V-a), D_{BP} = 7.91 Å (site V-b), D_{BP} = 9.95 Å (site VI-a), D_{BP} = 11.32 Å (site VI-b), D_{BP} = 11.30 Å (site VIII-a), D_{BP} = 11.93 Å (site VIII-b), D_{BP} = 12.20 Å (site IX-a),D_{BP} = 13.29 Å (site IX-b), D_{BP} = 13.59 Å (site X).

experienced by the impurities in the three cases (see Tables I, II and III).

The second other relevant point is the possibility to identify two distinct trends for the Formation Energy depicted in Fig. 4.10, that can be related to the type of Silicon cage surrounding the P dopant site. One can group (dotted line) together the cases in which the P impurity is located in the positions labelled II, VI-b and X with respect to the B impurity (see Fig. 4.6). In these positions two of the surface Si atoms bounded to the P impurity present two passivating H atoms instead of one, the situation that actually dominates in all other configurations; it's thus possible to say that a different number of capping H atoms influences the Formation Energy.

Many other calculations has been done on the biggest $Si_{145}BPH_{100}$ codoped nanocrystals with impurities located at the center of the nanocrystals in order to shed more lights on the most favorable dopants sites. Different B and P impurity configurations have been investigated taking into account cases with impurities placed like near neighbors and second neighbors at the center of the nc. It comes out that the inner substitutional sites are not among the most stable positions for impurities, since they give rise to positive Formation Energy values: near neighbors B-P impurities give a FE equals to 0.18 eV, while when B and P are second neighbors the FE decreases a little bit but still remaining positive around 0.08 eV. Moreover when the P is located at the center of the nc while the B is substituted in the first subsurface layer the FE diminishes again at the value of 0.018 eV, close to zero but positive, confirming once again that the most favorite positions for both Boron and Phosphorus are the subsurface sites.

5 Back to the future: OptoElectronics

> Son morto con altri cento,
> son morto ch'ero bambino
> passato per il camino,
> e adesso sono nel vento.
>
> *Auschwitz*, Francesco Guccini

In this new section we present the calculated optoelectronic features of the B and P codoped Silicon nanocrystals. The aim is to understand the role played by the simultaneously presence of substitutional acceptor and donor impurities such as Boron and Phosphorous , on the electronic structure of the nanocrystals and to investigate how this features can be manipulated and engineered by simply handling with impurity position within the system. As already depicted in the Introduction, the main goal of this research would be the full comprehension of the mechanism that rule the emission and the tuning of visible light from the doped and codoped Sinc, yet experimentally observed by the group of Minoru Fujii. From the theoretical point of view this will contribute enormously to the research on Silicon nanocrystals for photonic applications.

5.1 Electronic Properties

Here, as the title preventively suggests, are described the electronic properties of the single and co- doped Sinc. The semiconductors doping is nowadays a well established technique used to inject and manage the numbers of carriers in semiconductors systems, or to shift insulator system into semiconductors through the insertion of donor and/or acceptor impurities. It

has been proof that when impurities are present or later inserted in semiconductors, new *discrete* electronic levels arise due to the impurities within the band gap [172]. The dopants are classified by their chemical valence. In particular, in the tetrahedral elemental semiconductor, impurities with valence charge greater than four are considered as *donors* (like elements from V group, P, As, N) while impurities with valence lower than four are called *acceptors*, such as the elements from III group like B, Al. This is what happens also in Silicon, the most popular semiconductor among the tetravalent ones, as depicted by Fig. 5.1. The donors dopants posses an extra electron which doesn't participate to the chemical tetravalent bonding and it's relatively free to move throughout the crystal. On the other hand, the acceptors atoms, need an extra electron to complete the tetravalent coordinate bonding of the elemental crystalline environment; thus the unsaturated bond may migrate throughout the crystal and in this way it can be depicted as an hole. The semiconductors with an insignificant number of

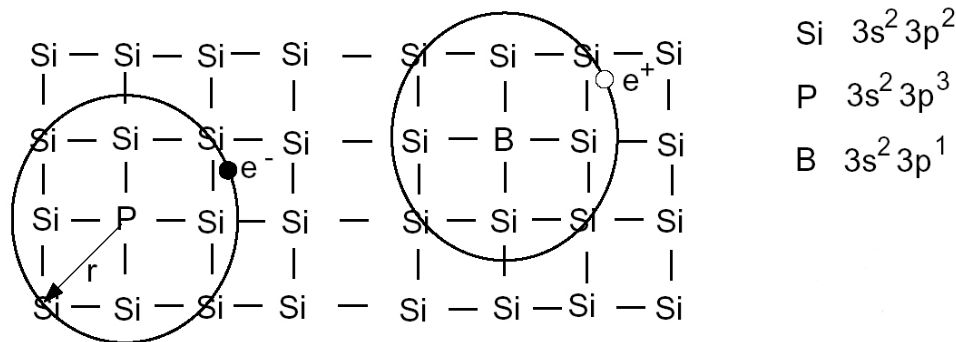

Figure 5.1: Chemical valence of the dopants inserted into a tetrahedral semiconductor, here bulk Silicon. Atoms from III group like Boron become *acceptors* while atoms from V group, such as Phosphorus, are defined as *donors*.

carriers can be consider almost *pure* and are called *intrinsic*. The number of charge carriers is therefore determined by the properties of the material itself instead of the amount of impurities; moreover in intrinsic semiconductors the number of electrons and the number of holes are equal. Instead, when an amount of dopants impurities is inserted into a semiconductor, which results to be doped, the semiconductor is called *extrinsic*. The electron and hole carrier concentrations of the semiconductor at thermal equilibrium are then changed. Dominant carrier concentrations in an extrinsic semiconductor classify it as either an n-type or p-type semiconductor. The electrical properties of extrinsic semiconductors make them essential components of many electronic devices. The donor and acceptor impurities considered here are called *shallow* since they give rise to discrete energy level close to the

conduction and valence band edge respectively as shown in Fig. 5.2.

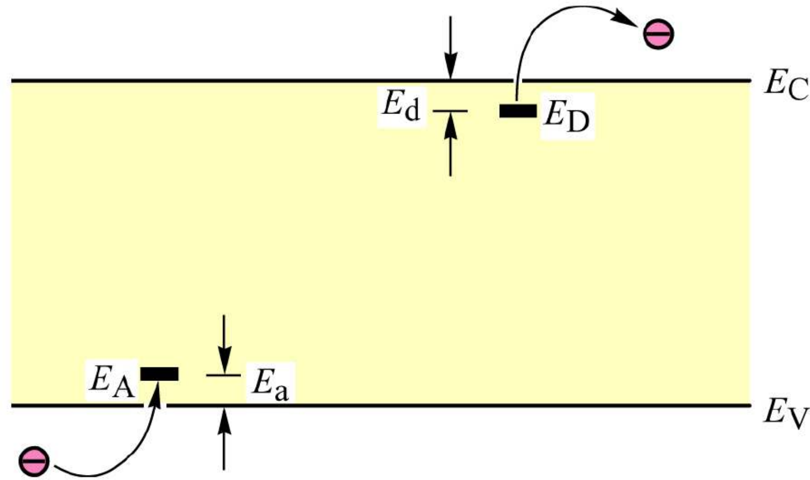

Figure 5.2: Energy levels of acceptors and donors in the semiconductor band diagram, placed near the conduction E_C and valence E_V band edge. The shallow donor energy level E_D and the acceptor energy level E_A have respectively ionization energies E_d and E_a.

The main idea behind this work is to demonstrate from a theoretical point of view but supported by the experimental evidences (see Fujii[41, 33, 36, 40, 32, 38]) that the traditional doping of bulk semiconductor can be also applied to nanostructured system in order to control not only electrical properties but especially the optical features of these innovative systems. The possibility to achieve visible light and to tune its spectrum just playing with the doping of the Sinc represents a new and groundbreaking combination of a traditional well established technique with one of the newest class of nanosized system which should be still deeply investigate at all.

Free standing *undoped* hydrogenated Silicon nanocrystals show an electronic structure constituted by discrete energy levels as a consequence of the quantum confinement effect, as demonstrated by numerous works realized in the last 15 years [51, 173, 117, 174, 47, 44]. The undoped Sinc have a semiconductor-like band gap that varies according to the variations of the dimensions of the nanocrystals. The introduction of dopant atoms within the Silicon nanocrystals has been demonstrated to produce a behaviour similar to the doping bulk semiconductor, with the creation of discrete impurity states near the conduction and valence band edge.

B, P Single doped Nanocrystals

All the data regarding the electronic structures calculated are obtained, as for the geometric structure, using Vanderbilt ultrasoft pseudopotential with GGA exchange-correlation functional.
First of all we're going to resume what happens when only one impurity (Boron or Phosphorous) is present within the Sinc. In Fig. 5.3 and in Fig 5.4 are reported the energy levels calculated at Γ for the two different size of Sinc; only the levels corresponding to the highest occupied molecular orbital (HOMO), the lowest unoccupied molecular orbital (LUMO), the HOMO-1 and LUMO+1 states are shown. According to the previous considerations about the formation energy and thus on the more preferred impurity position within the Sinc, here the impurities are single doped in the first layer below the surface, as one can see from Fig.5.5 where the localization of HOMO and LUMO states is shown. As for bulk Silicon, the impurities inserted give rise to new *shallow* electronic levels near the band edge. The Boron dopant gives rise to an impurity level close the valence edge, while the Phosphorous atom gives rise to a level localize just below the conduction band edge. As reported in Fig. 5.3 and Fig. 5.4 these Kohn-Sham impurity levels become more shallow as the size of Sinc increase, thus when the quantum confinement is reduced and the dimensions tend to the bulk limit. The HOMO (Highest Occupied Molecular Orbital) level of

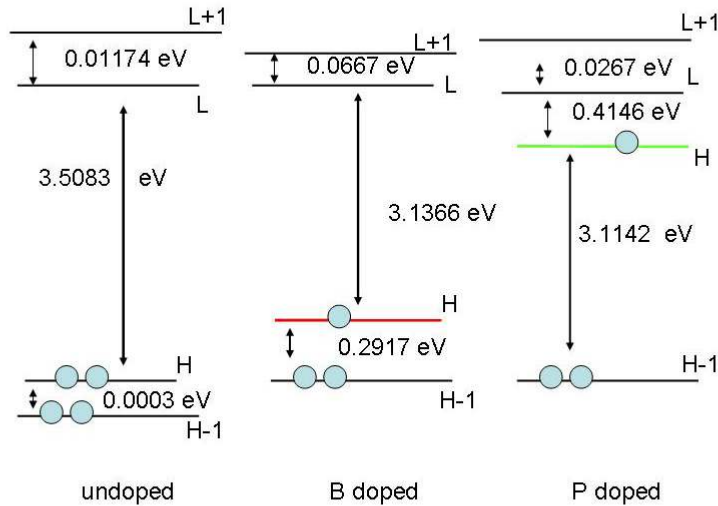

Figure 5.3: Calculated energy levels at the Γ point for the $Si_{35}H_{36}$, the $Si_{34}BH_{36}$ and $Si_{34}PH_{36}$ single doped Sinc. The alignment has been performed locating at the same energy the fully occupied levels with the same type of localization.

single doped nanocrystals contains only one electron and the Kohn-Sham

energy gap is defined for the single doped nc as the energy difference between the highest occupied level (HOMO) that is partially filled and the lowest unoccupied one (LUMO) which is empty. The presence of donor or acceptor states lowers the above defined energy gap (E_G) with respect the corresponding undoped Sinc and the changes in the electronic structure are directly related to the impurity valence. Since the impurity level is semi-occupied it leads the single doped Sinc to have an odd numbers of electrons with respect the undoped ones and to become a metallic system. Performing spin-polarized calculations it has been demonstrated that the impurity level with the lower energy is always occupied by the unpaired electron (spin-up or spin-down) while the level with higher energy is not occupied [170]. Some

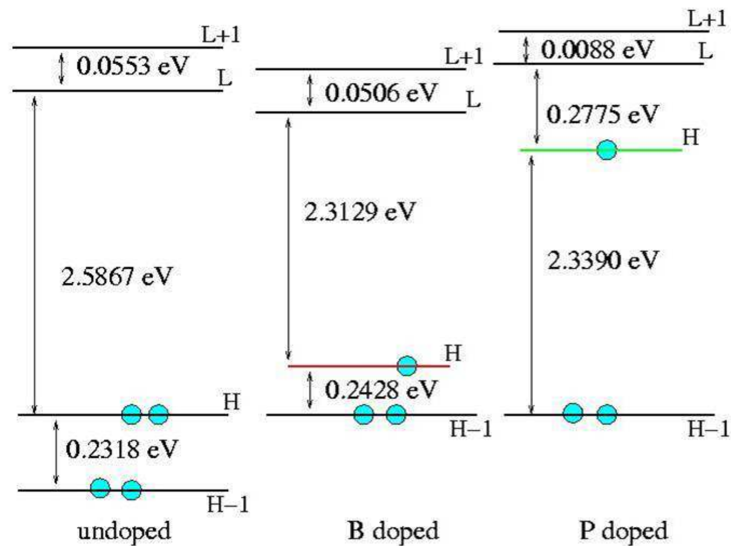

Figure 5.4: Calculated energy levels at the Γ point for the $Si_{87}H_{76}$, the $Si_{86}BH_{76}$ and $Si_{86}PH_{76}$ single doped Sinc. The alignment has been performed locating at the same energy the fully occupied levels with the same type of localization

light differences arise between spin-up and spin-down energy calculations, and in particular the amount of discrepancy between spin-up and spin-down states depends slightly by the Sinc size: for small nc the splitting is more pronounced while for bigger the differences tend to become negligible [170]. Nonetheless the actual calculations on the B and P singled doped Sinc are in fair good agreement with other similar investigation on the single doping Sinc made by Zhou and Brus [171, 175].

The insertion of a single impurity into the nc perturbs then not only the electronic structure, but also the localization of the HOMO and LUMO orbitals of the Sinc, with respect to the undoped counterpart, as depicted

in Fig. 5.5. The HOMO and LUMO orbitals of the undoped Sinc are spread all over the entire cluster, as confirmed by previous work on hydrogenated nanocrystals[44]; in the single doped cases, instead, the HOMO is strongly focused on the Boron and Phosphorous impurity sites, while the LUMO is delocalized over the all Silicon inner core of the nc, thus recovering the typical behaviour of the undoped hydrogenated Sinc. Due to the strong localization of the impurity level, for example, in the case of $Si_{86}BH_{76}$ the defect level is located just 0.28 eV above the valence band reducing the above defined energy gap from 2.59 eV (the value for the undoped Sinc) to 2.31 eV. In $Si_{86}PH_{76}$ the defect level is located just 0.28 eV below the conduction band so that the energy gap is only 0.28 eV. It is interesting to note that the experimental substitutional donor binding energy for P in bulk Si is about 33 meV, while the experimental acceptor energy for B in Si is 45 meV,[176] showing how, in the case of nanocrystals, the combined effects of both quantum confinement and weak screening tend to "transform" shallow impurities in "deep" centers [168, 160, 177].

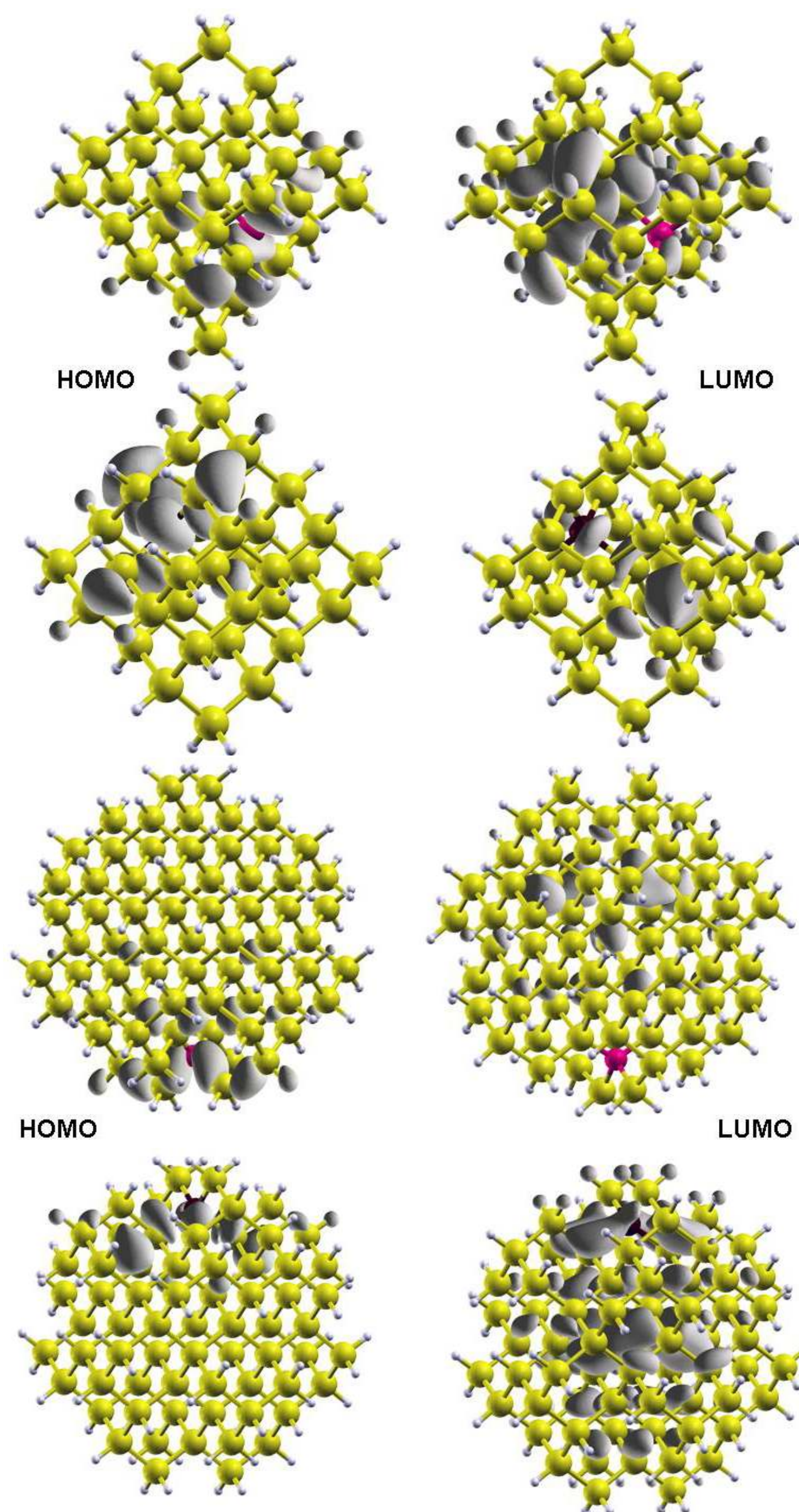

Figure 5.5: The HOMO (left column) and LUMO (right column) square modulus contour plots calculated for the B and P single doped $Si_{35}H_{36}$- (upper panel) and $Si_{87}H_{76}$- (lower panel) based nc.The isosurfaces correspond to 10% of the maximum value.

B and P Codoped Nanocrystals

When the Boron and Phosphorous dopant atoms are simultaneously inserted within the Sinc, the single perturbations related to the presence of an acceptor and a donor impurity sum and the system recover a semiconductor character. It means that new electronic levels due to the simultaneous codoping and related to the different character of the III and V group dopants, arise into the energy gap of the Sinc which is fully occupied. This can be clarified from Fig. 5.6 where we show the electronic levels for

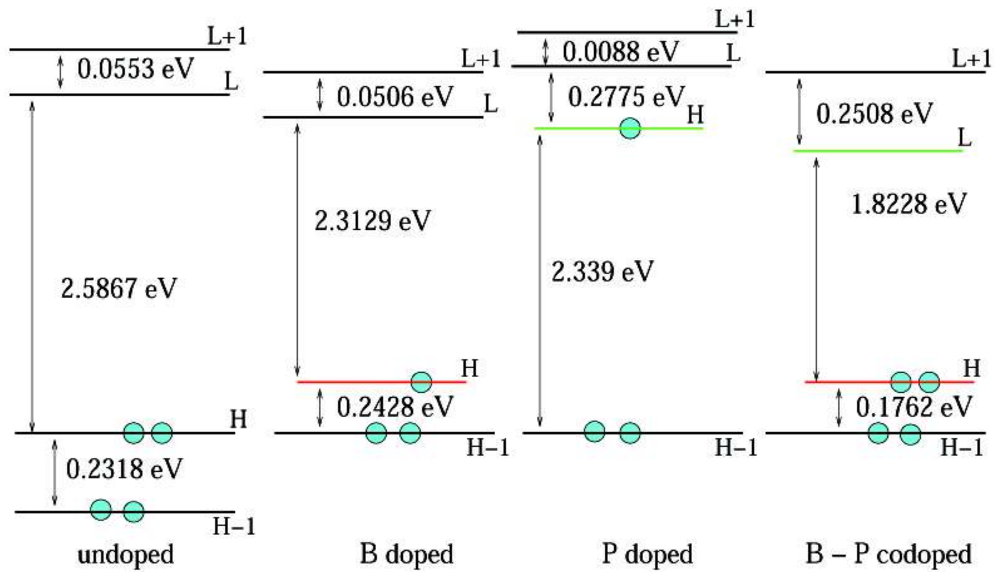

Figure 5.6: Calculated energy levels at the Γ point for the $Si_{87}H_{76}$, $Si_{86}BH_{76}$, $Si_{86}PH_{76}$ and $Si_{85}BPH_{76}$ nc. The alignment has been performed locating at the same energy the fully occupied levels with the same type of localization.

the $Si_{87}H_{76}$- based nc, the single doped (as in the previous section) and the codoped $Si_{85}BPH_{76}$. Again only the HOMO, LUMO, HOMO-1 and LUMO+1 orbital states are reported (see Fig. 5.7) and the alignment has been realized locating at the same energy the states with the same kind of electronic occupations and with the same type of localization. It comes out that now on going from the pure to the codoped nc, the HOMO and LUMO states tend progressively to localize around the two impurity sites (bottom panel of Fig. 5.7): thus the HOMO is mainly focused around the Boron impurity, the acceptor, while the LUMO is centered around the Phosphorus impurity, the donor site. Thus we can associate HOMO and LUMO states to the new impurity levels, and we have to remember that the codoped nc we're dealing is compensated by the presence of a donor and an acceptor

at the same time, with valence levels completely double occupied. The new HOMO and LUMO impurity states arise within the energy gap, determining a strong reduction from 2.5867 eV (undoped Sinc) to 1.8228 eV (codoped Sinc).

The same trend is realized for the codoped $Si_{33}BPH_{36}$ with respect to the $Si_{35}H_{36}$, where the energy gap of the codoped Sinc is strongly reduced by an amount of about 1 eV as depicted in Fig. 5.8 where energy levels at Γ are depicted for the smallest single and codoped nc.

It worth pointing out how the distance between the two impurities within the Sinc could influence the electronic structure. Thus on going from the smallest to the biggest nanocrystals we decide to investigate the electronic properties as a function of the impurity-impurity distance. Several configurations of codoped nc with coupled impurities inserted in the first Silicon layer below the surface (following the consideration on the FE of the previous section) with different distance between the Boron and the Phosphorous atoms have been investigate. To better understand how the B-P distance could really influence the electronic properties, we take into account one of the biggest Sinc, the $Si_{145}BPH_{100}$ codoped with the impurities placed one time at the largest possible distance in the first subsurface Silicon layer (D_BP=13.29 Å) and the second time at the lowest possible distance such as second neighbors just below the surface (D_BP=3.69 Å) and then we calculate the corresponding electronic structures as shown in Fig. 5.9. From the figure it comes out that when the two impurities are at the larger distance (corresponding to site X) the energy gap E_G is strongly lowered with respect to the undoped $Si_{147}H_{100}$ moving from 2.30 eV to 1.63 eV; moreover when the impurities are closer each other, thus second neighbors (configuration labelled by site II), the E_G enlarges to 2.03 eV, keeping always lower than the value of the undoped Sinc. A possible explanation is that when impurities are brought closer each other, the Coulomb interaction becomes stronger so that the energy gap becomes larger. Boron and Phosphorus feel each other like a B-P complexes with a gap opening recalling the DFT-LDA calculated gaps for the Boron Phosphide bulk system: direct gap ($\Gamma \rightarrow \Gamma$) 3.3 eV, indirect gaps ($\Gamma \rightarrow X$) 2.2 eV, and ($\Gamma \rightarrow \Delta$) 1.2 eV, as described in [178]. These behaviors are corroborated by the calculated HOMO and LUMO wave functions. Fig. 5.10 shows the square modulus contour plots of the HOMO and LUMO states of the two $Si_{145}BPH_{100}$ nanocrystals with different B-P distances. The top panel shows the contour when the impurities are at a large distance while the bottom panel is that with the impurities at short distance. It clearly appears from these contours that on going from the case with well separated impurities to the that with close impurities, the overlap between the HOMO, strongly centered on the Boron atom, and the LUMO, mainly localized on the Phosphorus atom, strongly increases.

Moreover, the detailed influence played by the mutual B-P distance on the electronic structure of codoped Sinc, has been carried out by looking at

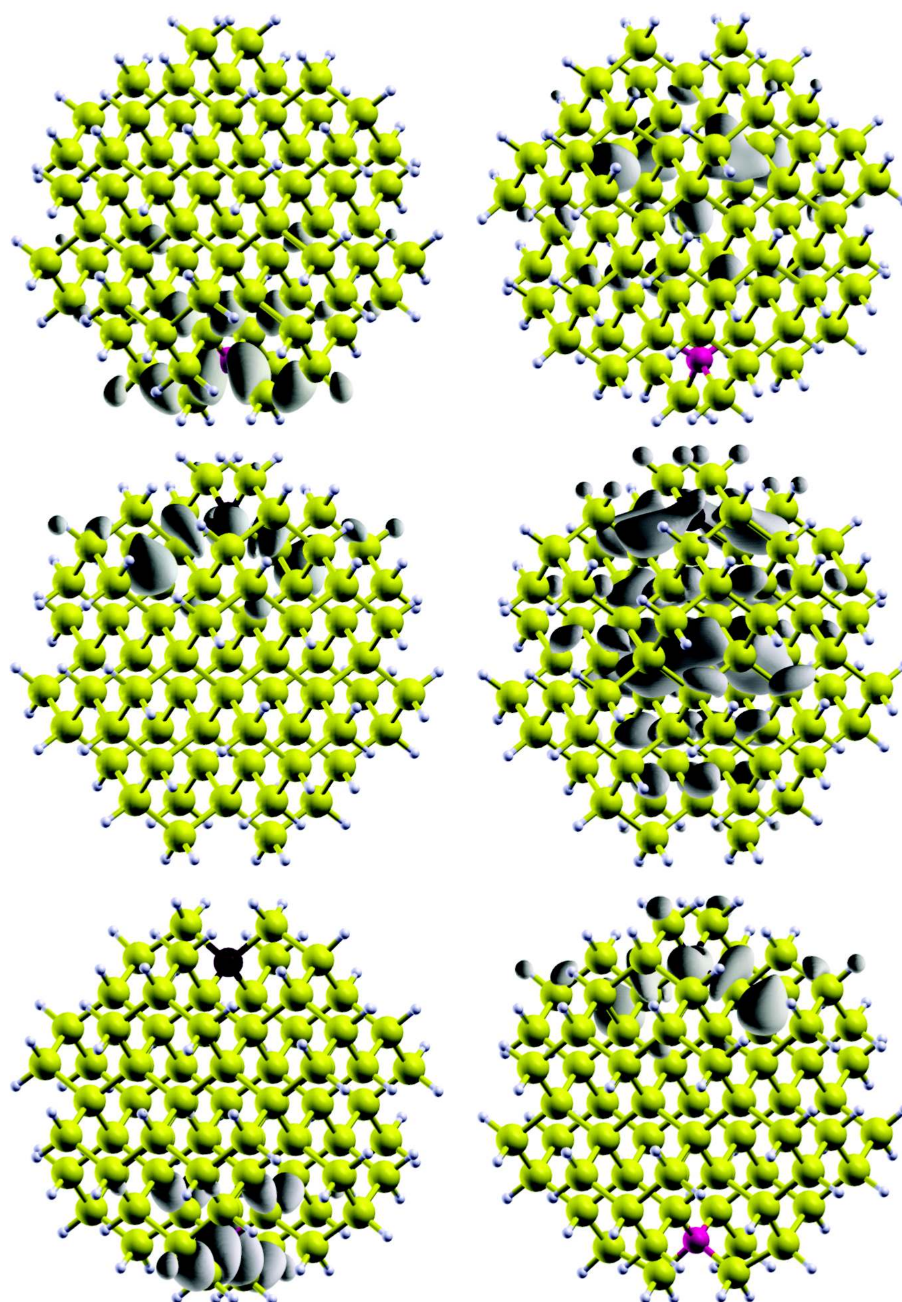

Figure 5.7: The HOMO (left column) and LUMO (right column) square modulus contour plots calculated for the $Si_{86}BH_{76}$ (top panel), $Si_{86}PH_{76}$ (middle panel) and $Si_{85}BPH_{76}$ (bottom panel). The isosurfaces correspond to 10% of the maximum value

the changes in the electronic levels for each of the impurities configurations

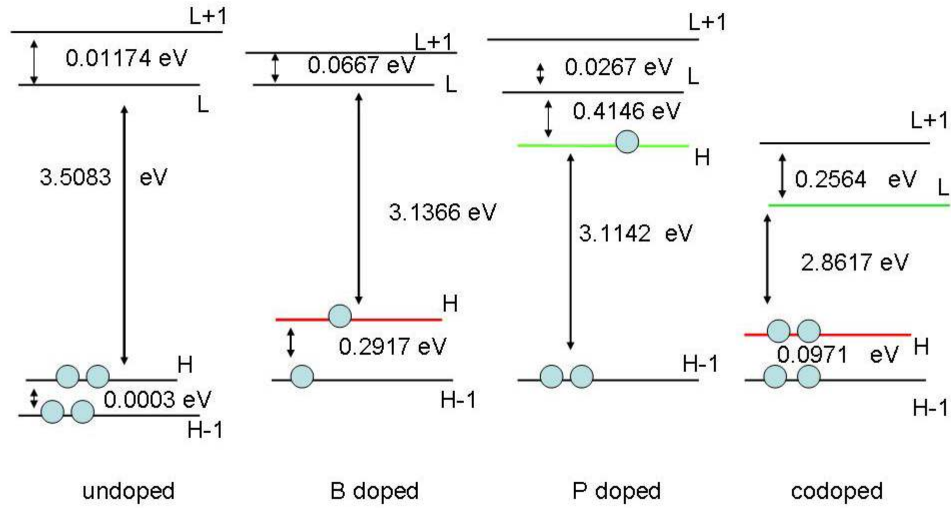

Figure 5.8: Calculated energy levels at the Γ point for the $Si_{33}BPH_{36}$, $Si_{34}BH_{36}$, $Si_{34}PH_{36}$ and $Si_{35}H_{36}$ nc. The alignment has been performed locating at the same energy the fully occupied levels with the same type of localization.

within the $Si_{145}BPH_{100}$ nanocrystal (see Fig. 4.6) as done before for the formation energy. In Fig. 5.11, the trend of the HOMO-LUMO energy gap with respect to distance between impurities within the $Si_{145}BPH_{100}$ is reported. What comes out is that the mutual impurity distance deeply affects not only the formation energy (as in Sec. 4.2) but also the energy gap of the semiconductor nanocrystals. As one can see, the E_G strongly decreases almost linearly with the increase of the impurity distance; moreover, also in this case we can figure out the presence of two different trends related to the different surface region experienced by the P atom in the sites II, VI-b and X, with respect to the other ones (see also Fig. 4.10 and related discussion). Fig. 5.11 points out how, at least in principle, it is possible to tune E_G as a function of the impurity-impurity distance. It is easy to predict that for Sinc larger than those considered here it would be possible by codoping to obtain a energy gap even smaller than whose of bulk Si.

Moreover, by keeping constant the impurity-impurity distance between B and P for each dimension of the Sinc considered, it's possible to see how the energy gap depends by the Sinc size. By placing the B and P impurities like second neighbors in substitutional subsurface position in all the different Sinc, it come out how its in principle possible to tune and modulate the electronic gap by moving from the undoped to the codoped Sinc. From Fig. 5.12 it can be see how the undoped E_G is strongly reduced in the presence of codoping. In particular also looking at the numerical values in Table 5.1,

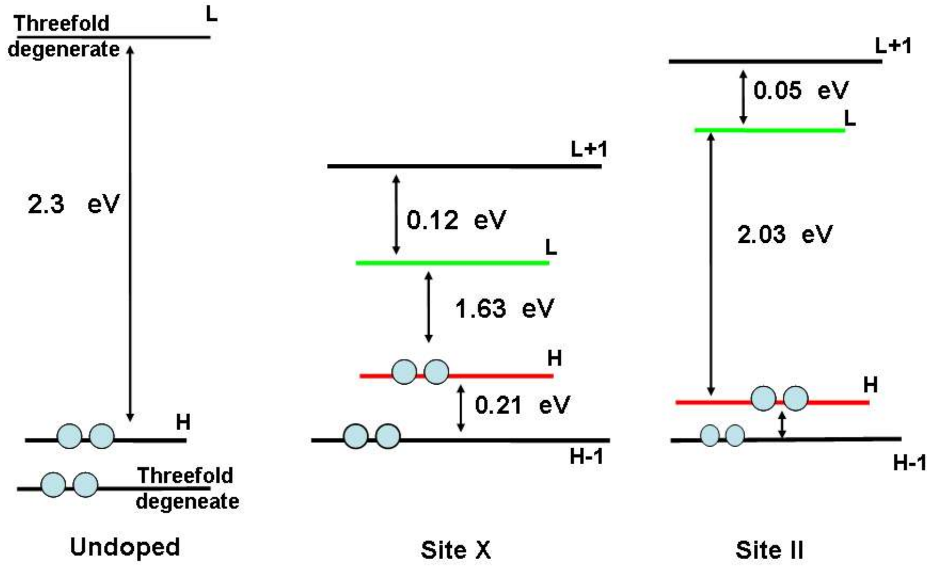

Figure 5.9: Calculated energy levels of the undoped $Si_{147}H_{100}$ (left panel), codoped $Si_{145}BPH_{100}$ with an impurity-impurity distance D_{BP} = 13.29 Å (central panel), codoped $Si_{145}BPH_{100}$ with an impurity-impurity distance D_{BP} = 3.68 Å (right panel). The alignment has been done locating at the same energy the fully occupied levels with the same type of localization. Site X and Site II are referred to Fig. 4.6. H stands for HOMO, L for LUMO.

the E_G of the codoped Sinc appear to be shifted toward lower values with respect to the corresponding undoped ones. The amount of shift is stronger for smaller nanocrystals, 0.65 eV for $Si_{33}BPH_{36}$, 0.30 eV for $Si_{85}BPH_{76}$ and 0.27 eV for $Si_{145}BPH_{100}$, but it tends to saturate when the diameter of the Sinc exceeds some threshold value (here the $Si_{87}H_{76}$diameter). The same quantum confinement effect trend (i.e. larger gap for smaller nanocrystals) is observed for both the undoped and the codoped cases. The energy gap trend depicted in Fig. 5.11 and Fig. 5.12 can be directly connected with the experimental outcomes by Fujii and coworkers [38, 36, 37] who found photoluminescence peaks centered in the 0.9-1.3 eV energy region: we can therefore argue that Sinc playing a role in the experiment should have dimensions of the order of few nanometers, as shown from the E_G decreasing trend in Fig. 5.11. This foregone conclusion is consistent with the experimental outcomes [38, 36, 37] that indicates an average nanocrystals diameter of about 5 nm. The possibility to modulate and control at pleasure the electronic structure, in particular the possibility to tune the energy gap of the Sinc just by the modulation of codoping, discloses several new routes for electronic and optoelectronic applications.

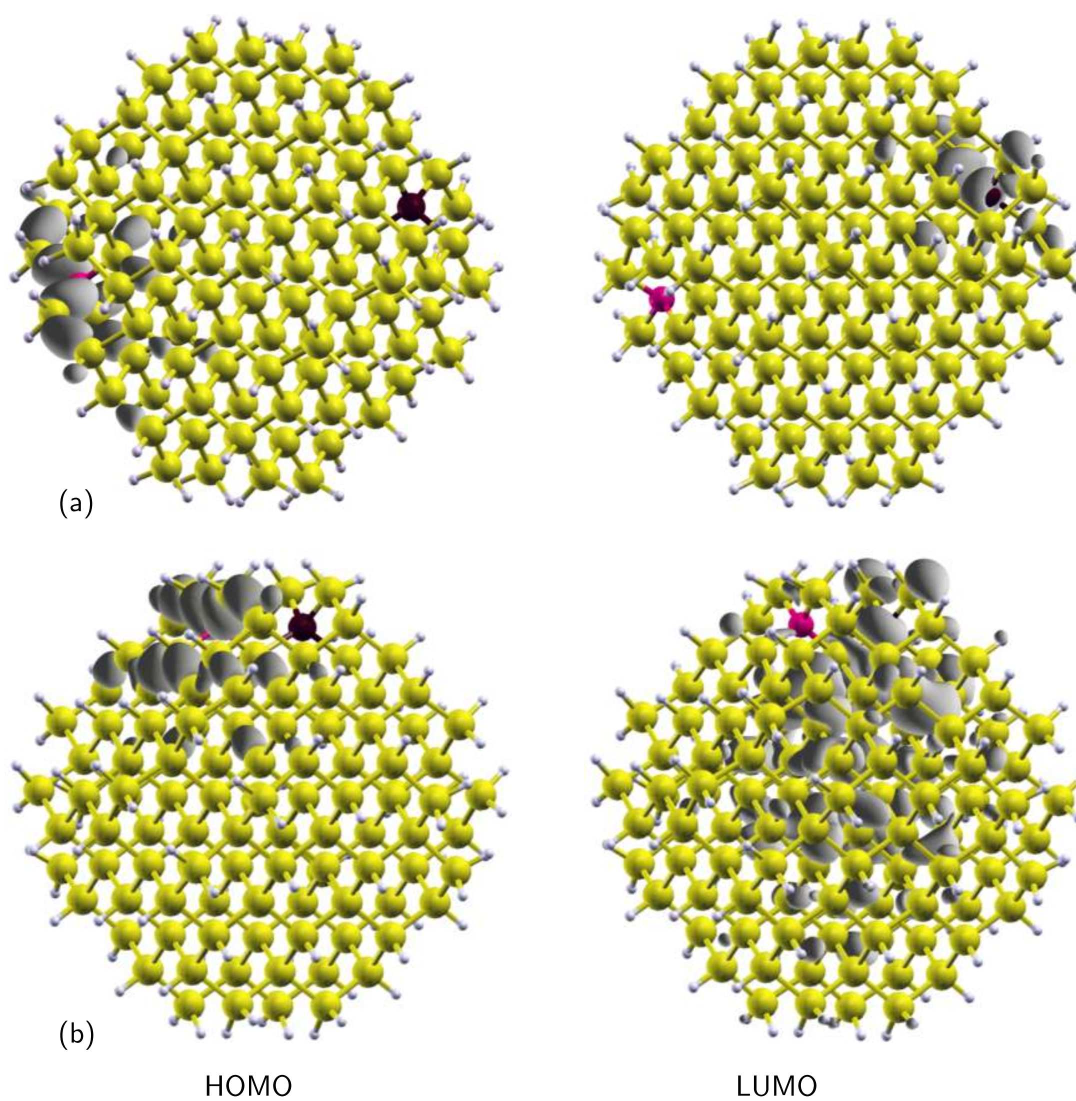

Figure 5.10: From the top to the bottom: the HOMO (left) and LUMO (right) square modulus contour plots calculated for $Si_{145}BPH_{100}$ (atom colors same as in Fig. 4.3). The impurities are located on opposite sides of the nanocrystal, at distance $D_{BP} = 13.29$ Å (a) or as second neighbors, with an impurity-impurity distance $D_{BP} = 3.68$ Å(b). The isosurfaces correspond to 10% of the maximum value.

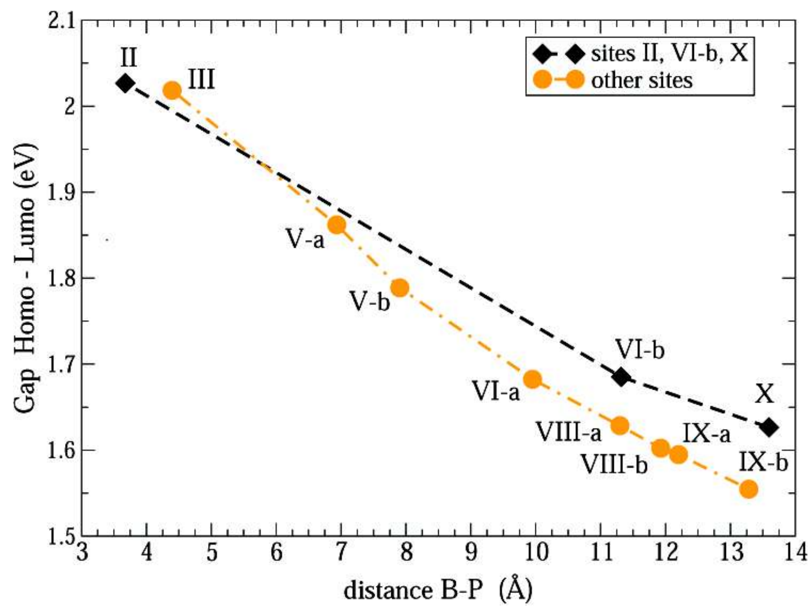

Figure 5.11: The HOMO-LUMO energy gap as a function of the distance between the B and P impurities within the $Si_{145}BPH_{100}$ nc. Roman numbers refer to the positions of the P atom (see Fig. 4.6). The dashed and dash-dotted lines connect the two subsets of impurity sites in which the surrounding surface Si atoms are bonded to the same number of passivating H atoms.

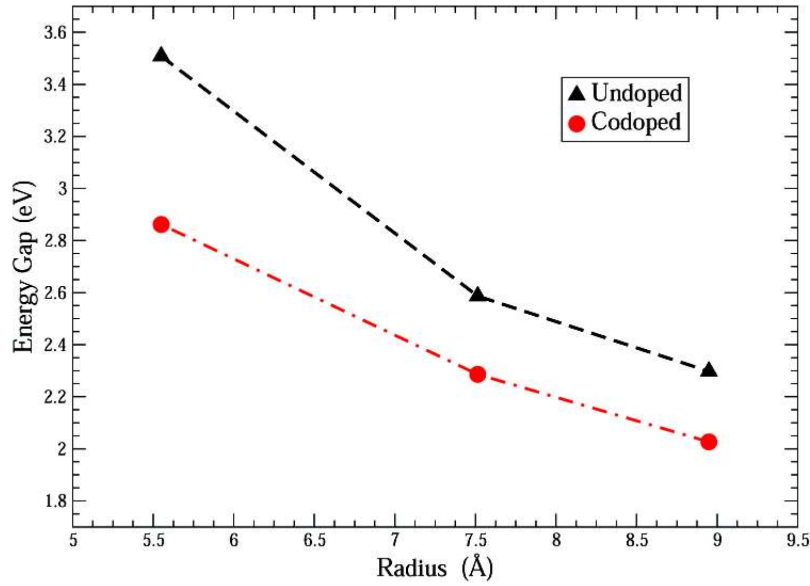

Figure 5.12: Comparison between energy gaps of the undoped (black triangles) and the codoped (red circles) nanocrystals as a function of the nanocrystal radius. Impurities are located in the first shell below the surface, as second neighbors. The impurity-impurity distances are 3.56 Å, 3.64 Å, and 3.68 Å for $Si_{33}BPH_{36}$, $Si_{85}BPH_{76}$, $Si_{145}BPH_{100}$ respectively. The lines are a guide for the eye.

Starting nc	d (nm)	E_G undoped (eV)	E_G codoped (eV)
$Si_{35}H_{36}$	1.10	3.51	2.86
$Si_{87}H_{76}$	1.50	2.59	2.29
$Si_{147}H_{100}$	1.79	2.30	2.03

Table 5.1: HOMO-LUMO gap (E_G) for $Si_{35}H_{36}$, $Si_{87}H_{76}$, $Si_{147}H_{100}$ and the corresponding codoped $Si_{33}BPH_{36}$, $Si_{85}BPH_{76}$, and $Si_{145}BPH_{100}$. Impurities are second neighbors. The impurity-impurity distances are 3.56 Å, 3.64 Å, and 3.68 Å, for $Si_{33}BPH_{36}$, $Si_{85}BPH_{76}$, and $Si_{145}BPH_{100}$ respectively. d is the nanocrystal diameter.

5.2 Optical Properties

The optical features of these codoped Sinc will be examined in this section by investigating how the absorption and the emission spectra can be affected and modulated by the codoping. In particular optical spectra performed

first in the Independent Particle Random Phase Approximation (IP-RPA) and next in the Many Body Perturbation Theory approach(GW-BSE) (see Sec.3) will be compared in order to bring out the effect of local field and many body correction. In the RPA approach the absorption has been calculated as the imaginary part of the dielectric function $\epsilon_2(\omega)$ expressed through the "classical" *Fermi golden rule* [179]. To understand the role of dimensionality and impurity distance and to show the importance of including many-body effects in the optical spectra, we are going to present first the result of a IP-RPA optical response for various codoped nanocrystals different in dimensions and in impurity location (see Sec. 5.2.2), and next, we will present a complete study of a codoped Sinc where we go beyond the single-particle approach within the GW-BSE framework (see Sec. 5.2.4).

5.2.1 Computational details

For all the calculations performed *norm-conserving pseudopotentials* have been used, without the inclusion of the *non local commutator* $[V_{NL}, r]$. Since it has been demonstrated that this term affects only the intensity of the absorption peaks in the spectrum without changing their positions, the commutator can be therefore neglected without loosing physical information. All the calculations performed are not spin-polarized. However it should be noted that single-particle calculations for undoped Sinc done by Franceschetti and Pantelides [116] within the local spin-density approximation, show that the singlet-triplet splitting is significantly smaller than the Stokes shift [170].

The nanocrystals optical response is evaluated for both the ground and the excited state relaxed geometries computing the imaginary part of the dielectric function ($\epsilon_2(\omega)$) through the well known *Fermi golden rule*, as expressed in Eq.[3.11]. To the best of our knowledge, the present work is the first up to now which takes care to study and understand the mechanisms that govern not only the absorption but in particular the emission process from codoped Sinc. As remarked in the Introduction, the control of emission of light from Silicon nanostructures is important to realize photonic devices integrated with the traditional electronic dispositive. Therefore, the study of emission process leads to the knowledge of *excited states* both for extended or confined system; in particular the theoretical framework that permits to treat and to manage with the excited states is still under debate and upgrading. Approaches within the Many Body Perturbation Theory that permit to treat the many body effects by calculating the self energy correction via the GW approximation and to evaluate the role of local field and exciton effect through the solution of Bethe-Salpeter equation, are still very computing demanding and supported by huge calculation.

In this work we decide to go beyond the GS calculation and to simulate also the excited state of our systems combining together two well known approaches in order to carry out a first estimation of the emission process without dealing for the moment with calculations based on Green Functions. The combination of a *Constrain DFT (ΔSCF)* approach with the calculation of the imaginary part of the dielectric function $\epsilon_2(\omega)$ with also the inclusion of the many body effects, has led to an almost reliable and physical treatment of the excited state [44, 47, 119, 117]. The emission spectra have been calculated using the **relaxed atomic positions of the excited state** combined with the **electronic occupation of the ground state**. The excited state is characterized by an electronic configuration in which the highest occupied single-particle state (HOMO) contains a hole (h), while the lowest unoccupied single-particle state (LUMO) contains the corresponding electron (e), thus simulating the creation of a electron-hole pair under excitation, as shown in Fig. 5.13(b), according

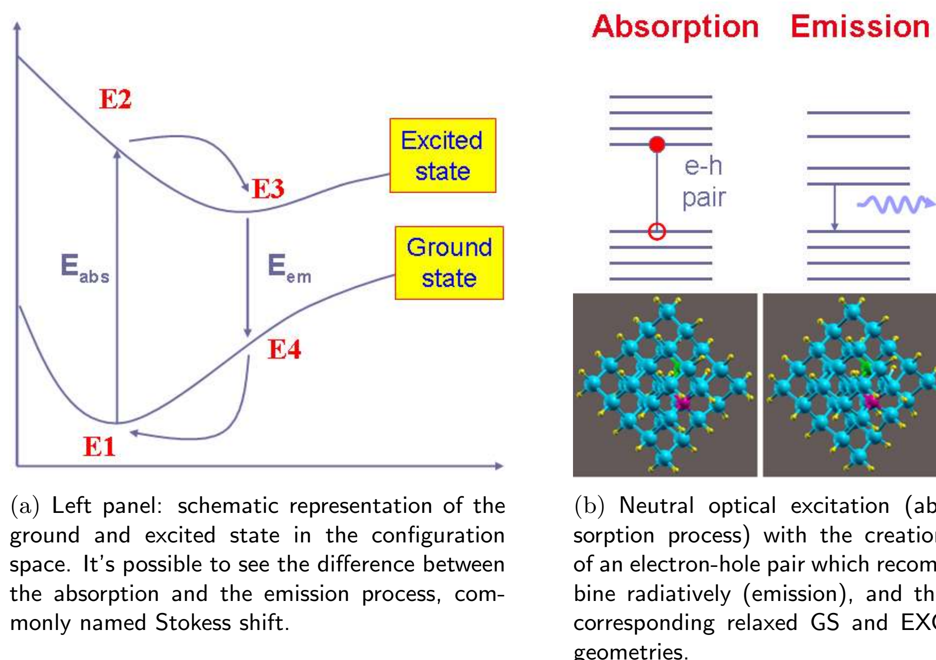

(a) Left panel: schematic representation of the ground and excited state in the configuration space. It's possible to see the difference between the absorption and the emission process, commonly named Stokess shift.

(b) Neutral optical excitation (absorption process) with the creation of an electron-hole pair which recombine radiatively (emission), and the corresponding relaxed GS and EXC geometries.

Figure 5.13: Schematic representation of the one-particle excitation process in a codoped Sinc.

to the Constrained-DFT approach (ΔSCF) [114]. After excitation, due to the change in the charge density and in presence of the electron-hole pair, relaxation occurs until the atoms reach a new minimum energy configuration called *relaxed geometry of the excited state*. The new atomic positions modify the electronic spectrum, implying that the levels involved

in the emission process change. This model assumes that the relaxation under excitation is faster than the electron-hole recombination. The difference between the absorption and emission energies due to the different atomic positions represents the nanocrystals Stokes shift [116, 57], that is schematically depicted in Fig. 5.13(a).

It's worth pointing out that now the *emission* spectrum can be expressed as an *absorption spectrum* calculated in new structural geometry, that means to calculate the emission exactly as the imaginary part of dielectric function ($\epsilon_2(\omega)$), thus like an absorption, but with the electronic occupation of the ground state and the relaxed structural geometry of the excited state. It should be noted that although $\epsilon_2(\omega)$ should only be used for calculating the nanocrystals absorption coefficient, it can also be used to get a first approximation for the emission spectra, simply because the emission can be viewed as the time reversal of the absorption, whose main features are also those of the emission spectra as one can see from the Fermi golden rule [179]. To note that for the first time, the electron-hole interaction is here considered in the emission geometry via a ΔSCF scheme, while since now excitation of nanoclusters has been studied calculating pair-excitation energies [115, 119, 117]. It is worth mentioning that the photoluminescence spectra can be derived using the well known Van Roosbroeck and Shockley [180] relation which, again, involves the imaginary part of the dielectric function, $\epsilon_2(\omega)$. However, such a calculation requires the knowledge of the electron and hole populations, at the working temperature, in the LUMO and HOMO states respectively. The populations, in turn, depends on the actual dynamics in the excitation and emission processes, including the non radiative electron-hole recombination. In this work, nevertheless, we have not considered any particular dynamics so that our emission spectra contains only the information related to both the transition energies and the oscillator strengths.

In the second part of the section, we have gone beyond the single-particle approach including in the calculation of the optical response of the system the many body effects, through the computation of the GW self energy correction and the application of the Bethe-Salpeter equation in order to treat properly the two body electron-hole interaction (see Sec. 3). Since the inclusion of the self energy correction, the local field effects and excitonic interaction makes the calculation very tough and very computationally demanding, we take into account these many body effects (for the moment) only for the $Si_{33}BPH_{36}$ the smallest Sinc considered here.
We have included the self-energy corrections by means of the GW approximation [181]. In a successive step, excitonic effects are include solving the Bethe-Salpeter equation [131]. A further advantage of this procedure is that the inhomogeneity of the system is taken into account by properly includ-

ing local fields effects [182, 183] This approach, in which many-body effects are combined with a study of the structural distortion due to the impurity atoms in the excited state, allows a precise determination of the Stokes shift between absorption and emission spectra [57].

5.2.2 Absorption and Emission: RPA results

The modifications induced in the electronic levels of the Sinc when adding donor and acceptor impurities are reflected also in the optical features of single and co- doped nanocrystals. What we expect is that with the arising of new impurity states within the energy gap, new interesting transitions could be originated.

"To dope or to codope?"

What is the best solution between the doping and codoping to obtain interesting and new optical features?
With reference to the electronic structure of the doped and codoped Sinc based on the $Si_{87}H_{76}$-reference cluster, in Fig. 5.14 are reported the IP-RPA absorption spectra of the B and P singled doped cluster, $Si_{86}BH_{76}$ and $Si_{86}PH_{76}$, compared with the corresponding spectra of the undoped $Si_{87}H_{76}$ reference nc. With respect to the undoped nc, the presence of a single impurity within the nanocrystals determines new optical transitions arising in the lower part of the energy spectrum, both in the case of B- or P- single doping as in Fig. 5.14. New strong peaks appear in the infra-red region below the absorption onset of the undoped Sinc due to the interband and also intraband transitions that involve the B and P impurity states and the Si energy levels. These new optical features in the absorption spectrum can be important for the possible applications in the field of infrared or also in Raman lasers technology [184]. Unfortunately this kind of single doped Silicon Nanocrystals are very inefficient for the emission properties since, due to the breakdown of the **k**-conservation rule in Si nanocrystals makes Auger processes significantly more efficient than in the bulk: a kinematic temperature dependent threshold for the Auger process known for bulk is absent in nanocrystals. Therefore, the branching ratio between rates of radiative and non-radiative Auger processes can significantly exceed the bulk value: the crystallites containing a shallow impurity are *dark* as reported by Kovalev et al. [39].

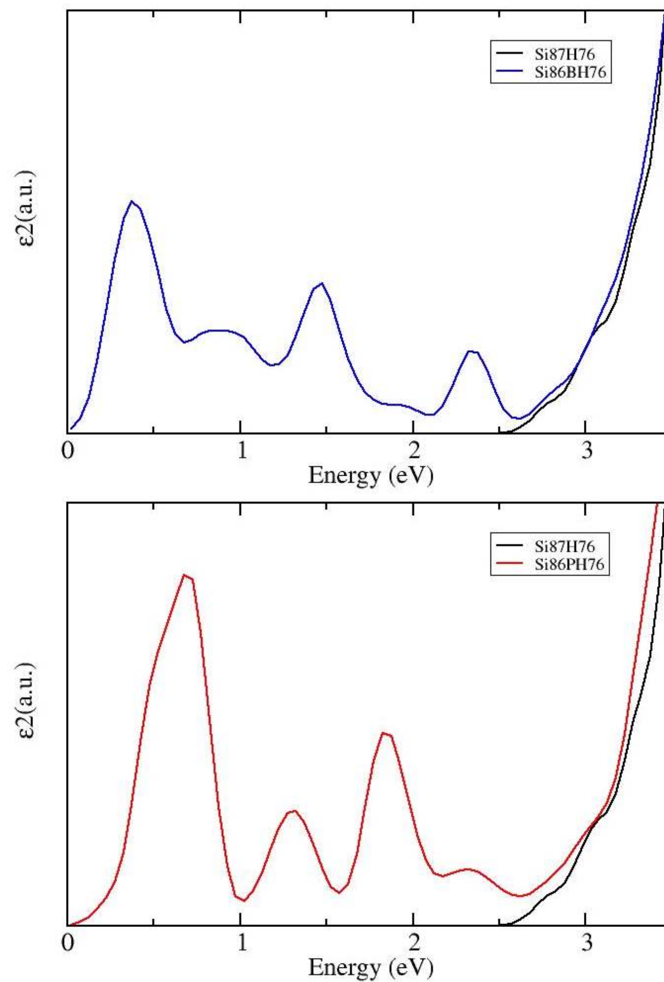

Figure 5.14: Calculated imaginary part of the dielectric function ($\epsilon_2(\omega)$) for the single doped $Si_{86}BH_{76}$ (blue line) and $Si_{86}PH_{76}$ (red line) compared with the undoped $Si_{87}H_{76}$ (black line) case. A Gaussian broadening of 0.1 eV has been applied.

The simultaneously insertion of two impurities thus render the Sinc compensated: since no semi-occupied energy level now exist, the shallow impurity energy levels arising within the gap will be then shown to be responsible of new interesting optical features. In Fig. 5.15 we can see

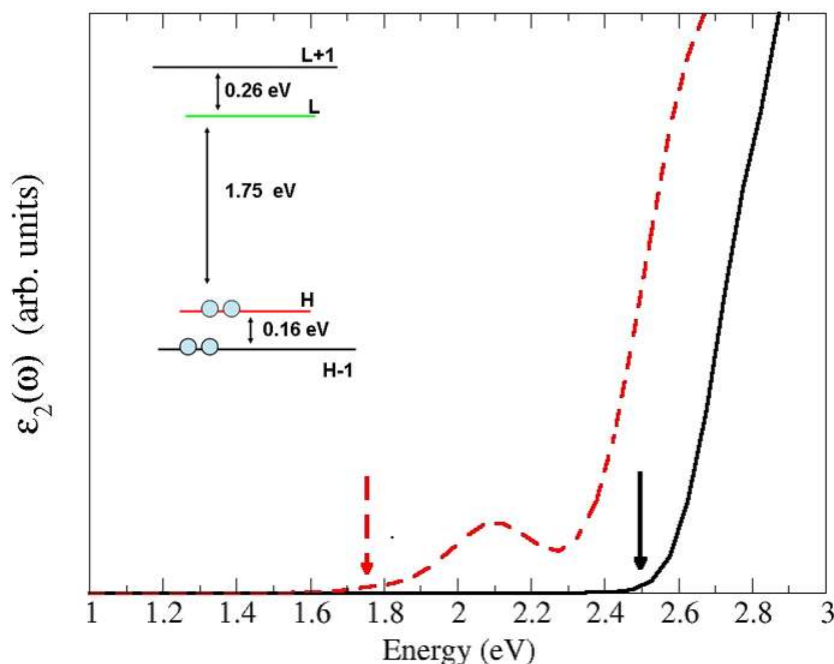

Figure 5.15: Comparison between the undoped $Si_{87}H_{76}$ (solid line) and the codoped $Si_{85}BPH_{76}$ (dashed line) single-particle absorption spectra. The impurities are at a distance of 10.60 Å. Arrows indicate the energy gaps. The calculated energy levels for the codoped nanocrystal are shown in the inset. A Gaussian broadening of 0.1 eV has been applied. H stands for HOMO, L for LUMO.

the comparison between the IP-RPA absorption spectrum of the undoped $Si_{87}H_{76}$ and the codoped $Si_{85}BPH_{76}$ with impurities placed at a distance of 10.60 Å. With respect to the single doped cases before, one can see that now several optical transitions arise below the absorption onset of the undoped nanocrystal. In particular due to the presence of both n- and p- type impurities, the overall valence electrons result to be compensated. The absorption onset of the codoped Sinc is shifted toward lower energies, with a consequent enhancement of the intensity of the transitions around the 2.0 eV. These new transitions are due to the presence of new HOMO and LUMO states localized on the impurities, as described in Sec. 5.1 (see for example Fig. 5.10). The inset of Fig. 5.15 clarifies how the peak located in the 2.0-2.2 eV energy region is related to contributions that involve the

HOMO-1, HOMO to LUMO, LUMO + 1 transitions; it should be noted that for all these levels the wavefunctions are predominantly localized on the impurities. If we compare these results with those of a single-doped Sinc [185], we note that the simultaneous presence of both impurities naturally suppresses all the absorption energy structures present in the infrared region (below 1 eV) of the single-doped spectra, thus giving new chance for an efficient emission of light in the visible range as confirmed by the experimental outcomes by Minoru Fujii [37, 36, 33, 41].

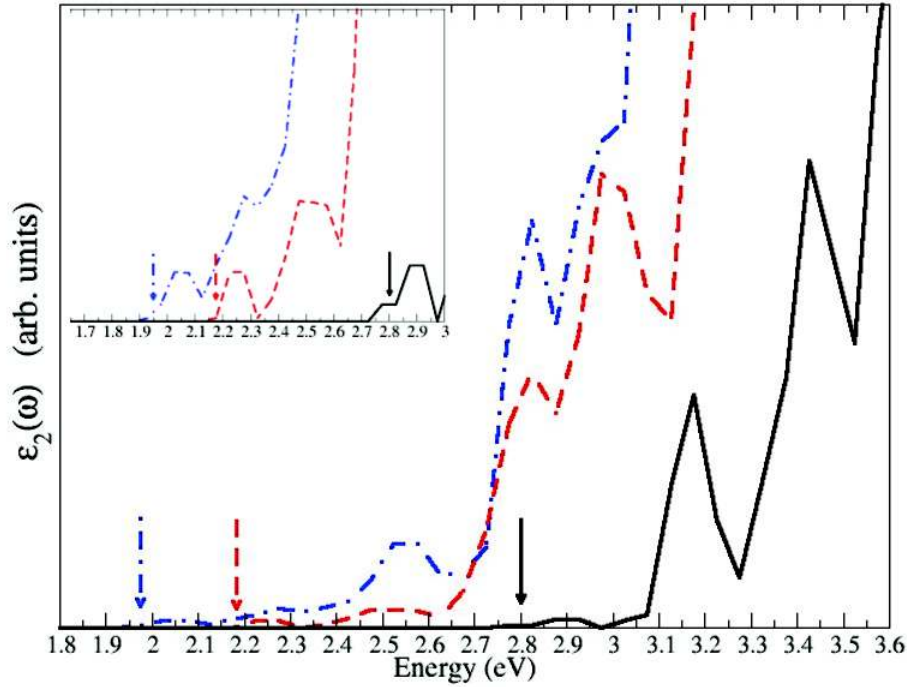

Figure 5.16: Single-particle absorption spectra of $Si_{33}BPH_{36}$ (black solid line), $Si_{85}BPH_{76}$ (red dashed line), and $Si_{145}BPH_{100}$ (dash-dotted blue line). In all cases the impurities are second neighbors. The impurity-impurity distances are 3.56 Å, 3.64 Å, and 3.68 Å for $Si_{33}BPH_{36}$, $Si_{85}BPH_{76}$, $Si_{145}BPH_{100}$ respectively. Arrows indicate the energy gaps. In the inset a zoomed view of the spectra onset. No Gaussian broadening has been applied.

Role of dimension and B-P distance

After this outcomes about the different effects between single doping and codoping, our aim will be the investigation of the role played by the dimensions and by the impurity distance on the optical features, in analogy to what has been done for the electronic properties. The role of the Sinc dimensions on the absorption spectrum is shown in Fig. 5.16 where is reported the absorption onset for the three different nanocrystals size with impurities located at the same distance. The $Si_{33}BPH_{36}$, $Si_{85}BPH_{76}$ and $Si_{145}BPH_{100}$, with diameters of 1.10 nm, 1.50 nm and 1.79 nm respectively, present substitutional impurities located as second neighbors with corresponding distances of 3.56 Å, 3.64 Å and 3.68 Å. Looking at the figure two main aspects emerge:

- on increasing the nanocrystals size the absorption gap is strongly reduced (see arrows in Fig. 5.16). This trend well agrees with the quan-

tum confinement effect of the Sinc already highlighted in several work on hydrogenated Sinc (see for example [44]): the energy gap and the absorption one decrease as the dimension of the Sinc increase, since they coincide for the biggest nc, toward the bulk limit. This is trend also confirms the experimental results of Fujii, according to them, the average dimension of codoped Sinc that contributes to emit light in the visible range is around 5 nm;

- an increase of the Sinc diameter (i.e. a decrease of the impurity weight with respect to the total number of atoms, thus we can say a lowering of "concentration") results in a lowering of the intensity for the transitions that involve the impurities. This can probably be related to the quenching of the effect that spatial confinement on the localization in real space of the impurity wavefunction involved in the transition; in smaller Sinc due to the better overlap between the electron and hole envelop function, it should be expected infact strong enhancement of e-h interaction.

Going on, another interesting investigation has been the comprehension of the role played by the impurity-impurity distance on the absorption spectrum, done following the same approach used adopted for the electronic properties. The absorption spectrum of the $Si_{145}BPH_{100}$ has been calculated by varying the distance between impurities, placing the P atom on sites II, III, IX, and X respectively (see for comparison Fig. 4.6). The IP-RPA absorption spectrum at issue are reported in Fig. 5.17 where in particular the attention is focused on the onset in order to the shape of the peaks change near the absorption edge. Here a shift of the absorption gap to lower energy on increasing the distance between the impurities is observed (see arrows in Fig. 5.17). Moreover, also the intensity is affected by the impurity distance. The intensity gets lower when the impurities are at a larger distances, whereas stronger transitions arise when the impurities are closer due to the increased overlap between HOMO and LUMO states which are mainly localized on the impurity site (as demonstrated previously). Nonetheless the optical transitions near the band edge (indicated by arrows in Fig. 5.17) exhibit weaker oscillator strengths, as sign that to these transitions contribute also states around the energy gap, such as HOMO-1 and LUMO+1.

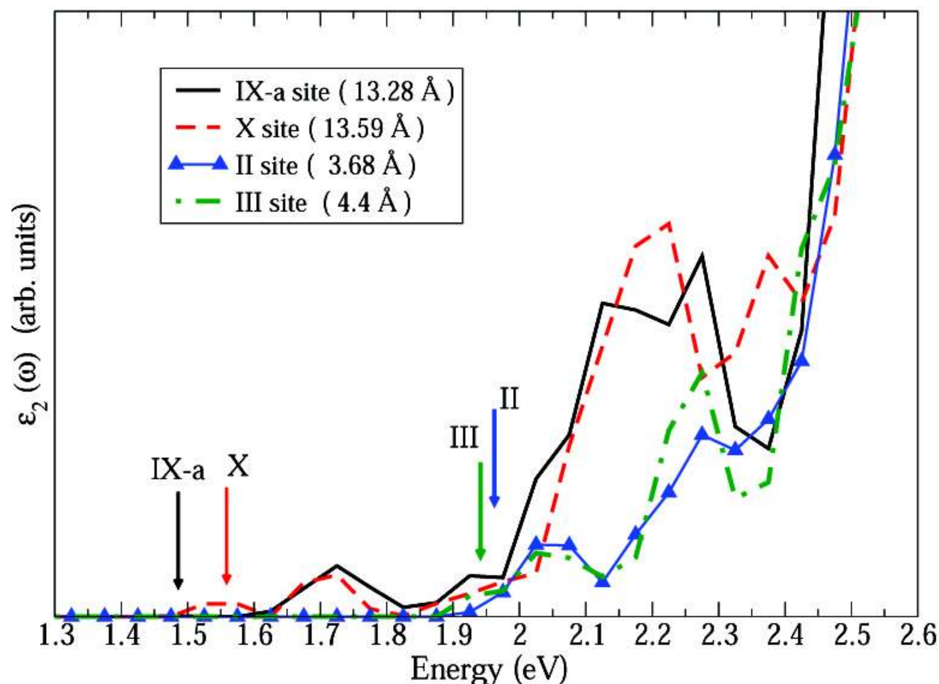

Figure 5.17: Single-particle absorption spectra of $Si_{145}BPH_{100}$ Sinc with impurities placed at different distances (see the inset). Arrows indicate the energy gaps. Roman numbers refer to the sites occupied by the P atom with respect to the B one (see Fig. 4.6). No Gaussian broadening has been applied.

5.2.3 Absorption, Emission and Stokes Shift: IP-RPA results

Here are presented and discussed the results for both absorption and emission spectra and the consequent Stokes Shift calculated for two codoped Sinc. The Stokes shift, as already defined, represents the difference between the absorption and the emission gap. As already depicted in Fig. 5.13(a), we report here in Fig. 5.18 a more detailed scheme of a Stokes shift relaxation.

The quantity ϵ_{ex}^{A} and ϵ_{ex}^{B} represent respectively the *Absorption* and the *Emission* gap as defined via a Constrain DFT-ΔSCF approach used in preceding work [44, 119, 117, 116, 186] to estimate with success these quantities without using the Green Function approach. In these papers it has been demonstrated that treating the HOMO-LUMO gap for the ground and the excited state as the proper absorption and the emission energies respectively leads to wrong results, in particular for smaller nanocrystals, since in particular the GS HOMO-LUMO gap tends to be always smaller than the absorption energy while the EXC HOMO-LUMO gap tends to assumes larger values than the emission energy.

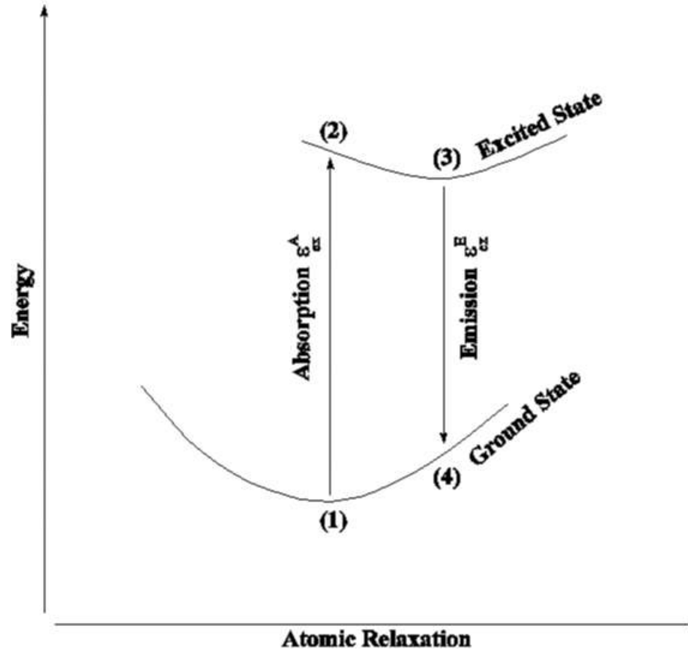

Figure 5.18: Schematic representation of a Stokes shift relaxation. In position (1), the cluster is in its electronic ground state, and the atomic geometry is relaxed to its lowest energy configuration. On absorption of a photon, the nanocluster undergoes a vertical electronic excitation from (1) to (2). Once in the excited electronic state, the atomic geometry of the cluster relaxes to a lower energy configuration [from (2) to (3)]. Finally, the excited electron and hole recombine via another vertical transition, (3) to (4). The Stokes shift is defined as $\epsilon_{ex}^{A} - \epsilon_{ex}^{B}$.

Nevertheless in this work we will refer to the HOMO-LUMO gap of the Ground and Excited State as the "absorption and emission gap". Since the computation of the absorption and emission energies $\{\epsilon_{ex}^{A}$ and $\epsilon_{ex}^{B}\}$ are very time consuming and computationally demanding. We decided for sake of simplicity to used the HOMO-LUMO gaps amounts to indicate absorption and emission energies, being aware of the discrepancies but considering also, as shown in [44], that the error made tends to reduce as the dimensions of the Sinc increase, thus leading our values close to the "correct ΔSCF" absorption and emission energies.

The calculations have been performed for two Sinc of different sizes, taking, in the larger Sinc, the impurities located at different distances. In the $Si_{33}BPH_{36}$-nc, the impurities are placed like second neighbors, as the possible largest distance within the Sinc (D_{BP}=3.56 Å), while in the $Si_{85}BPH_{76}$ the impurities are at the minima (D_{BP}=2.00 Å) and largest dis-

	$Si_{33}BPH_{36}$	$Si_{85}BPH_{76}$	
d (nm)	1.10	1.50	
D_{BP} (Å)	3.56	2.00	10.60
Abs. (eV)	2.77	2.32	1.75
Ems. (eV)	1.78	2.20	1.36
Δ (eV)	0.99	0.12	0.39

Table 5.2: Absorption and emission energy gaps (and their difference, 5th row) calculated as HOMO-LUMO differences in the ground and the excited relaxed geometries configuration, respectively. The results are obtained within the DFT single-particle approach. d is the nanocrystal diameter, D_{BP} is the distance between impurities and Δ the calculated Stokes shift between absorption and emission energy gaps.

tance (D_{BP}=10.6 Å) within the Sinc, in order to point out the effect on the emission spectra in particular. As shown in Table 5.2, both the absorption and emission HOMO-LUMO energies are affected by nc dimensions and impurity-impurity distance. With regard to the first parameter, we note that the Stokes shift strongly depends on the size showing a strong decrease on increasing the diameter of the Sinc. This is due to the fact that for larger nanocrystals the excitation determines a minor distortion of the geometry. Concerning the second parameter, we see that the Stokes shift tends to slightly increase with B-P distance although this effect is small if compared with the lowering due to the increase of the Sinc dimensions. The comparison between these results and the ones previously obtained for undoped clusters (0.92 eV for the $Si_{35}H_{36}$-nc [44] and 0.22 eV for the $Si_{87}H_{76}$-nc [117]) confirm that the Stokes shifts is mainly determined by the nanocrystals size, but that nevertheless it depend slightly on the presence of the impurities and also on their mutual distance. This trend is corroborated by Fig. 5.19 in which the absorption and emission onset for the $Si_{85}BPH_{76}$ nc are shown for the two different kind of impurity configuration.

The HOMO-LUMO transition (absorption gap) in $Si_{85}BPH_{76}$ (1.75 eV, bottom panel) is almost dark when the two impurities are far apart and becomes instead allowed (2.32 eV, top panel) when their distance decreases. As discussed before, this oscillator strength enhancement in the absorption spectrum is a consequence of the character of the HOMO and LUMO states in the two cases, both highly localized on impurity sites, but subjected to a different overlap.

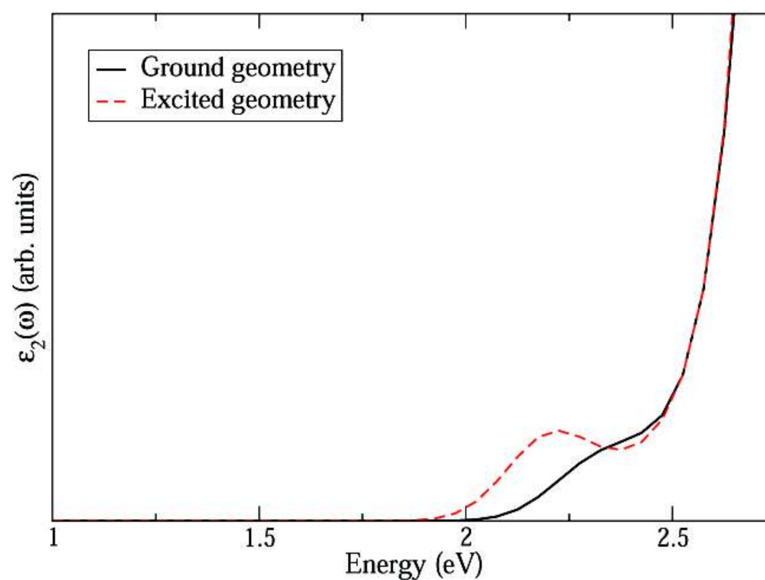

(a) B and P atoms are at the smallest possible distance, D_{BP}=2.00 Å.

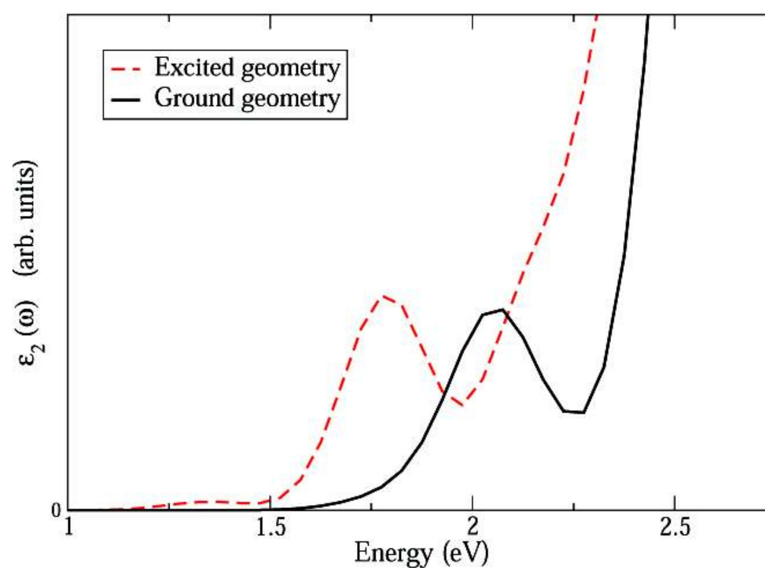

(b) B and P atoms are at the largest possible distance D_{BP}=10.60 Å.

Figure 5.19: Single-particle imaginary part of the dielectric function for the codoped $Si_{85}BPH_{76}$ nanocrystal in the ground (black-solid line) and in the excited (red-dashed line) geometries. A Gaussian broadening of 0.1 eV has been applied.

The emission (red-dashed lines in Fig. 5.19) spectra is red shifted with respect to the absorption (black-solid lines in Fig. 5.19) toward lower energy values. This red shift is a consequence of the geometry relaxation in the excited state due to the excess energy necessary for promoting of an electron in the LUMO level. The amount of Stokes shift is strongly influenced by the size and the B-P distance. Increasing the dimension of the Sinc, the Stokes shift decreases according to the same trend figured out for the undoped hydrogenated Sinc[44]. At the same time, looking at Fig. 5.19, the Stokes shift strongly decrease when impurity are brought closer (D_{BP}=2.0 Å), since in this case the emission gap become more similar to the absorption energy. Nonetheless in both cases the presence of two Boron and Phosphorous impurities determines in emission an intensity enhancement of the HOMO-LUMO transition, whose peak position moves in energy spectrum according to the distance at which the impurities are placed: increasing the B-P distance leads to a more strong shift of the emission peak toward lower energies. This result fits very well the experimental results of the work of Minoru Fujii, which shows that introducing shallow $n-$ and $p-$ type impurities within the Sinc, it's possible to tune the photoluminescence (PL) of the nc, in particular below the Silicon bulk-band-gap PL value [38].
It's worth pointing out that only with a "simple" single-particle RPA approach the results presented here are in really fair agreement with the experimental outcomes of Minoru Fujii [38, 37, 36]. The shift of the emission peak toward lower energies well represents the analogous shift of the PL peak below the bulk band gap limit obtained by the experimental setup of Fujii and coworkers. In particular we recover the real possibility to control and tune the emission by playing with dimensions of Sinc, and most important with the distance and the position of impurities inside the nanoclusters.

5.2.4 Absorption, Emission and Stokes shift: Many-Body results

In order to give a complete description, within the many-body framework, of the codoped Sinc response to an optical excitation, we consider both the self-energy corrections by means of the GW method to obtain the quasiparticle energies and the excitonic effects through the solution of the Bethe-Salpeter equation. The effect of local fields is also included, to take into account the inhomogeneity of the systems.

The heavy GW-BSE calculation is made considering a 50 a.u. lattice parameter large FCC supercell in order to reduce the number of plane waves. For the GW calculation have used the non self-consistent G_0W_0 approach within the RPA plasmon pole approximation. through a planewave-frequency space code. The correlation part of the self-energy Σ_c has been calculated using 10081 plane waves, while 49805 plane waves have been used for the exchange part Σ_x. Then, the full excitonic Hamiltonian has been diagonalized considering more than 8000 transitions using the EXC code [158]. The complete matrix calculation $W_{\mathbf{G},\mathbf{G}'}(\mathbf{q};\omega)$ have been diagonalized by using 4573 **G** vectors while the calculation without coupling has been performed using a 6975 plane wave basis set.

Since the GW-BSE calculation [158] are very computing demanding, we have only considered the smaller codoped nanocrystal $Si_{33}BPH_{36}$ (see Fig. 4.3(a)). In this particular cluster, we found that Local fields effects are, although not negligible, of minor importance with respect to GW and excitonic effects. It is anyway essential to include *all* of them (LF and many-body) in order to get the final converged spectrum shown in Fig. 5.20. In order to carry out emission spectra calculations, we use the excited state geometry and the ground state electronic configuration. As already noted before, in this case $\epsilon_2(\omega)$ corresponds to an absorption spectrum in a new structural geometry. In other words, we consider the emission as the time reversal of the absorption.[**?**, 57] Thus, the electron-hole interaction is here considered also in the emission geometry.

Fig. 5.20 shows the calculated absorption and emission spectra fully including the many-body effects. The electron-hole interaction yields significant variations with respect to the single-particle spectra (see for a comparison Fig. 5.19), with an important transfer of the oscillator strength to the low energy side. Moreover, in the emission spectrum the rich structure of states characterized, in the low energy side, by the presence of excitons with largely different oscillator strengths, determines excitonic gaps well below the optical absorption onset. Thus the calculated emission spectrum results

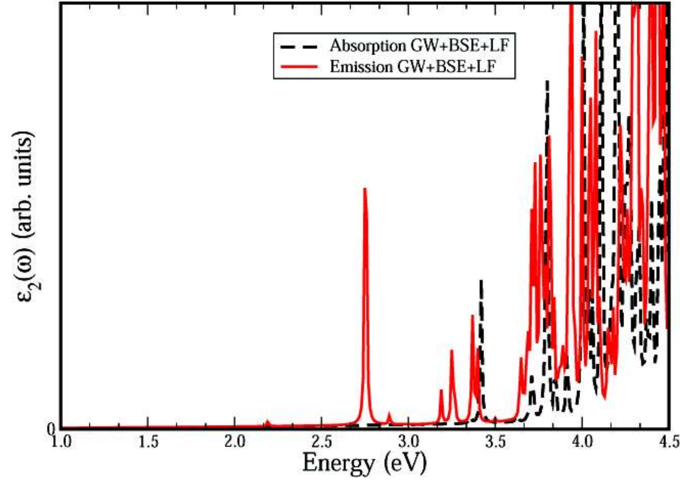

Figure 5.20: Absorption (black-dashed line) and emission (red -solid line) many-body spectra of $Si_{33}BPH_{36}$.

to be red shifted to lower energy with respect to the absorption one. This energy difference between emission and absorption, the Stokes shift, can be lead back to the relaxation of the Sinc after the excitation process.

The new important features that appear in the emission many-body spectra are related to the presence of both B and P impurities as showed by Fig. 5.21, which gives the real-space probability distribution $|\psi_{exc}(r_e, r_h)|^2$ for the bound exciton as a function of the electron position r_e when the hole is fixed in a given r_h position. In this case the hole is fixed on the Boron atom (labelled by the white X) and we see that the bound exciton is mainly localized around the Phosphorus atom.

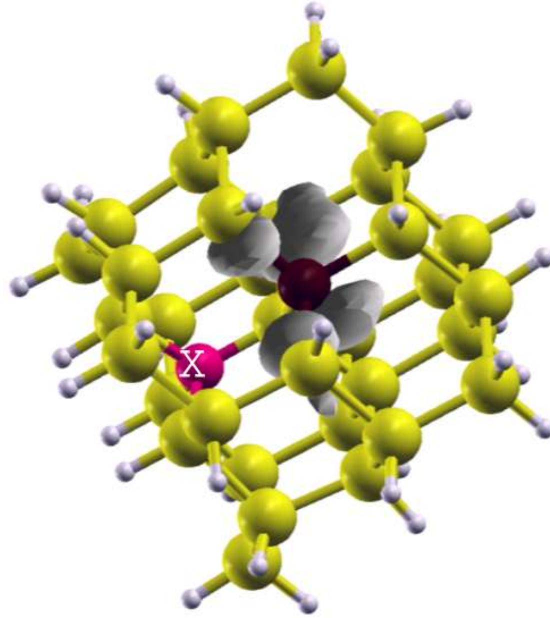

Figure 5.21: Excitonic wave function of $Si_{33}BPH_{36}$ (atom colors as in Fig. 4.3(a)). The grey isosurface represents the probability distribution $|\psi_{exc}(r_e, r_h)|^2$ of the electron with the hole fixed on the B impurity.

This confirms the consideration pointed out in the experiments: the compensated doping helps to localize the carriers further and to increase the probability of a quasi-direct electron-hole radiative recombination with intense emission of light, such as represented by the strong excitonic peak in emission spectrum of Fig. 5.20. From Table 5.3, it can be seen that the single-particle DFT results strongly underestimate the absorption and emission edge with respect to the GW+BSE calculation, in which the excitonic effect are taken exactly into account. This means that, in this case, the cancellation between GW gap opening (which gives the electronic gap) and BSE gap shrinking (which originates the excitonic gap) is only partial [187].

The difference between the GW electronic gap and the GW+BSE optical excitonic gap gives the exciton binding energy E_b. We note the presence of exciton binding energies as big as 2.2 eV, which are very large if compared with bulk Si ($\sim$ 15 meV) or with carbon nanotubes[188, 189] where $E_b \sim 1$ eV, but similar to those calculated for undoped Sinc [57] of similar size and for Si and Ge small nanowires [190, 191].

The differences between full many-body calculations and single-particle results are of 0.55 eV and 0.41 eV for absorption and emission energy gaps respectively, and of 0.14 eV between the two Stokes shifts. It is interesting to note that the HOMO-LUMO transition in the emission spectrum at 2.20 eV

$Si_{33}BPH_{36}$	DFT	GW	GW+BSE
Abs. (eV)	2.80	5.52	3.35
Ems. (eV)	1.79	4.37	2.20
Δ (eV)	1.01	1.15	1.15

Table 5.3: Absorption and Emission energies calculated as HOMO-LUMO energy difference within the single-particle DFT, the many-body GW and the GW+BSE approaches. Δ is the calculated Stokes shift between absorption and emission energy gap. The 2.20 eV energy corresponds to an almost dark transition.

is almost dark while an important excitonic peak is evident at about 2.75 eV (see Fig. 5.20), again red-shifted with respect to the first absorption peak. As expected, what comes out is the importance of fully taking into account the many-body aspect of the problem in order to overcome the limits of the single-particle approach.

To resume, the main effort of the work presented since now is to shed more light on the possibility to tune the electronic properties of the Sinc playing with the codoped impurities to achieve a well defined technique that permits to engineer at the end the absorption and the emission of radiation of these nanocrystals. The doping technique, commonly used to modify the electronic properties to achieve better conductivity and high performing transport features, has been here converted into a method to improved and speed up the possibility to engineer the optical features instead, in particular to tune the emission of light from Silicon-based nanostructures which can be used for technological innovative application, in optoelectronic and telecommunications.

6

Multidoping... is better

Vagar mi fai co' miei pensieri su l'orme
Che vanno al nulla eterno; e intanto fugge,
questo reo tempo, e van con lui le torme
delle cure onde meco egli si strugge;
e mentre io guardo la tua pace, dorme
quello spirto guerrier ch'entro mi rugge.

Alla Sera, Ugo Foscolo

In this section we'll investigate how the formation energy, the electronic and optical features of the Silicon nanocrystals can be influenced by the insertion of **more** impurities, in the specific by adding one, two or three more impurities with respect the initial codoped nanocrystal.

6.1 The systems

We called this insertion of several impurities *multidoping*. This procedure tends to simulate a *heavy doping* with compensated B and P impurities and it's similar to what is done in the bulk Silicon wafers in traditional microelectronics to improve or tune transport and optical properties [192, 193, 194, 195]. Now the *multidoping* has been realized on Silicon nanocrystals in order to investigate the role played by heavy doping with B and P and also the effect of a variation of impurity concentration on the stability and on the electronic and optical feature of the Sic. The starting codoped nc configuration is the most stable one found in the previous section, where the B and P impurities are placed like second neighbors at a distance of D_{BP}=3.68 Å, in site II with reference to Fig. 4.6. Then more dopant atoms have been added to the yet codoped Sinc in order to achieve a Sinc with

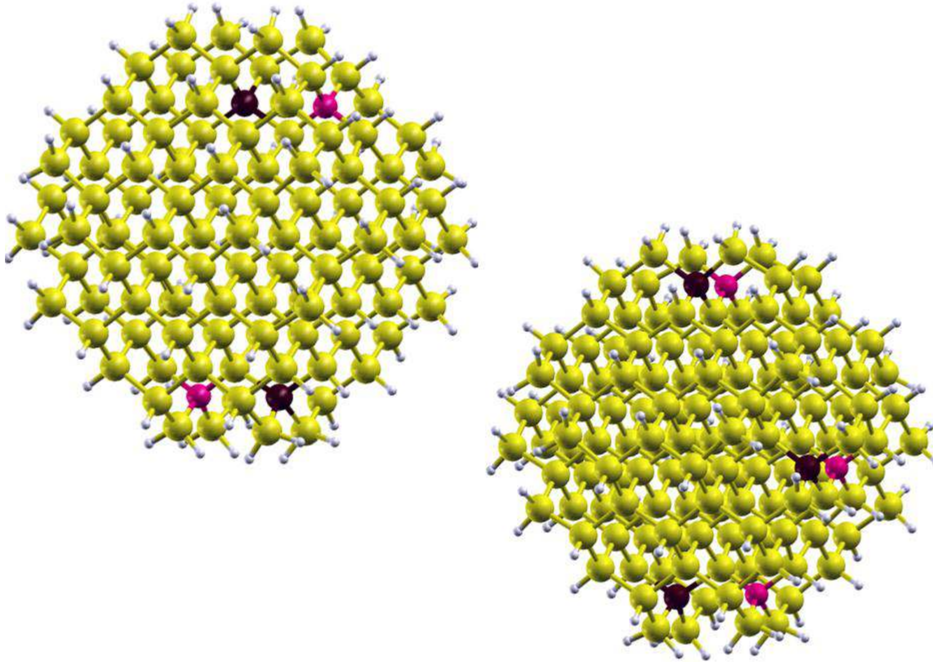

Figure 6.1: Some compensated multidoped nc with an even number of impurities: $Si_{143}H_{100}$:BBPP-nc (left side) and $Si_{143}H_{100}$:BBBPPP-nc (right side). Yellow balls represent Si atoms, while the white balls are the H atoms used to saturate the dangling bonds. P atoms are dark brown and B atoms are magenta.

three impurities as in Fig. 6.2 or four or six impurities such as depicted in Fig. 6.1.

Then one single impurity has been added in order to produce an excess of dopants for each species: an excess of Boron with two B atoms and one P atom in the $Si_{144}BBPH_{100}$ or an excess of Phosphorus with two P atoms an one B atom in the $Si_{144}BPPH_{100}$. In the end we obtain the $Si_{143}BBPPH_{100}$ and the $Si_{141}3B3PH_{100}$ by adding respectively two B and two P atoms, in the former case and three B and three P dopants in the later one. These Sinc containing two and three pairs of $n-$ and $p-$ type impurities are compensated as the $Si_{145}BPH_{100}$. For what concern this last Sinc, one configuration with the two B-P pairs are placed within the nc at a distance of D_{pairs}=12.11 Å, and the other one in which the two pairs are found at a distance of D_{pairs}=13.59 Åin order to understand which effect the mutual position can bring about.

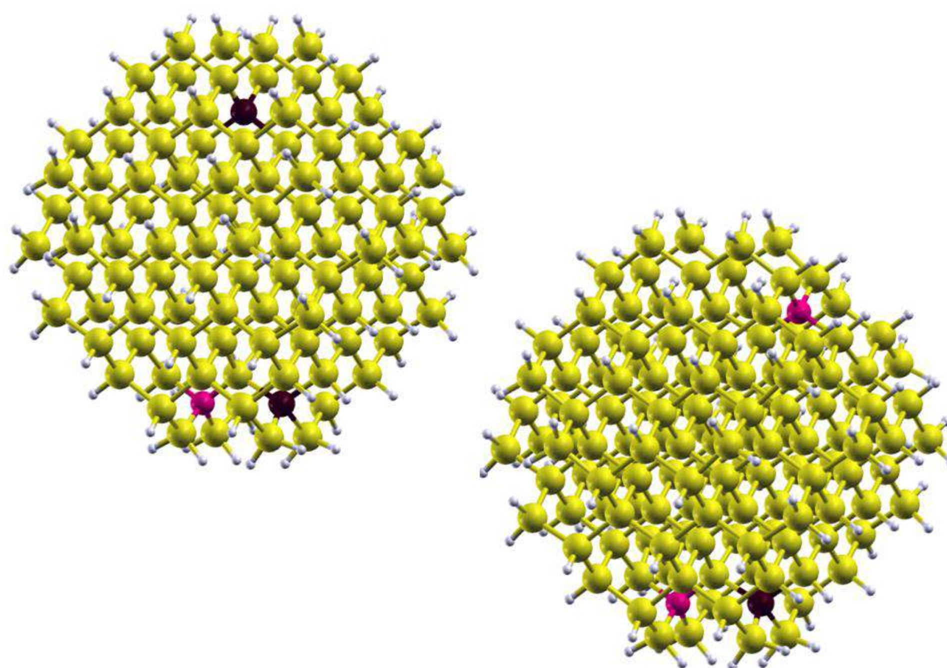

Figure 6.2: The uncompensated multidoped nc with an odd number of impurities: $Si_{144}H_{100}$:BPP-nc (left side) and $Si_{144}H_{100}$:BBP-nc (right side). Yellow balls represent Si atoms, while the white balls are the H atoms used to saturate the dangling bonds. P atoms are dark brown and B atoms are magenta.

6.2 Structural properties and Formation Energy

The insertion of one or more impurities in the already codoped Sinc determines no relevant modification in the geometry of the nanocrystal. Adding one or two more impurities within the codoped Sinc, it results in a general lowering of the Formation Energy, both for nanocrystal with an even and odd number of dopants atoms as shown in Fig. 6.3 where the FE of the single doped, codoped and multidoped $Si_{147}H_{100}$-based nanocrystal are reported for comparison. It can be seen that the nanocrystal with an **odd** number of impurities (one or three) have always the highest positive FE values with respect to the Sinc with an **even** number of dopants shared in equal part of $n-$ and $p-$ type impurities. In particular the uncompensated Sinc with impurities, $Si_{144}BBPH_{100}$ and the $Si_{144}BPPH_{100}$, presents FE values lower with respect the uncompensated single doped nc. Thus, although the doping with one or three impurities results to be less favorite and preferred with respect the doping with an even number of compensated impurities, it seems more easier to produce an excess of Boron or Phosphorous in an already

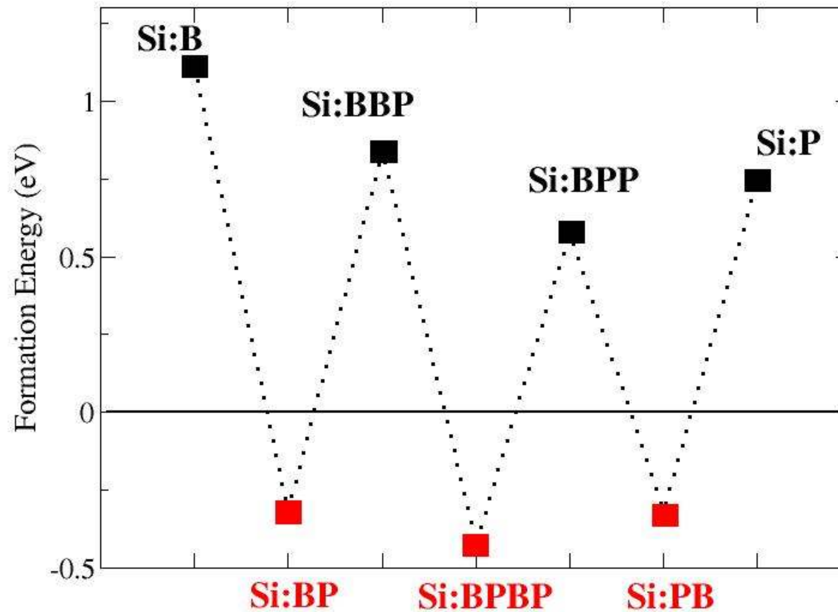

Figure 6.3: Formation Energies for single, co- doped and multidoped Si nanocrystals. In red are reported the FE for compensated Sinc (with an even number of impurities), in black are shown the FE for Sinc with an odd number of impurities.

doped Sinc, than in a undoped hydrogenated Silicon nanocrystal.

As shown from Table 6.1 it is evident that the Sinc with an even number of impurities infact assume lower values then the others. The FE becomes more negative as the number of $n-$ and $p-$ type dopant pairs increase: the $Si_{141}3B3PH_{100}$ infact presents the smallest negative Formation Energy value among all the cases take into account. This suggests that by augmenting the impurity concentration, or better, increasing the number of compensated donor-acceptor B-P pairs in the nanocrystal, it should more easier to *multidope* the nanocrystals. Moreover also the distance between the B-P impurity pairs influence the Sinc stability: increasing the distance between the B-P pairs the FE values decrease, assuming more negative values. As confirmed by the numerical values in Table 6.1, as in the case of simple codoping, multidoping is much easier to realize when the impurity are in even number inside the nanocrystal, in order to have same number of donor and acceptor dopant atoms; furthermore, increasing the stability of the doped nc by adding more impurities, cancel out also the possible depen-

Cluster	Formation Energy (eV)	Energy Gap (eV)
$Si_{146}BH_{100}$	1.11	2.08
$Si_{146}PH_{100}$	0.74	0.13
$Si_{145}BPH_{100}$	-0.32	2.03
$Si_{145}BPH_{100}$	0.15	1.59
$Si_{144}BBPH_{100}$	0.84	2.02
$Si_{144}BPPH_{100}$	0.58	0.15
$Si_{143}BBPPH_{100}$		
$D_{BPpairs}$=12.11 Å	-0.42	1.97
$D_{BPpairs}$=13.59 Å	-065	2.01
$Si_{141}3B3PH_{100}$	-0.97	1.92

Table 6.1: Formation Energy and Energy Gap (see text) for the Single Doped, Codoped and the Multidoped Silicon nanocrystals.

dence of the Formation Energy on the impurity position within the Silicon layers of the nc. By mapping through an atom-probe tomography the concentration of heavily doped Boron atoms within Si nanostructures volumes [196], it results that B atoms in great excess tend to segregate to the grain boundaries, also producing small impurity clusters; this confirms our finding on the decreasing of FE when more impurities are close each other, in particular the values found for the $Si_{141}3B3PH_{100}$-nc. The gain in stability of the Sinc with the increase of the number of impurities inserted, reflects also a permanent difficulty in the control and estimation of the real number of impurities inside the nc during all the experimental steps of doping process.

6.3 Electronic structure

Here we investigate how the electronic levels are influenced by adding one or two more impurities to the yet codoped $Si_{145}BPH_{100}$-nc. Looking at the electronic structure in Fig. 6.4, the two Si-nc with three impurities, present a similar behavior to those corresponding to B or P single-doped Si-nc, depicted in the previous section of the thesis. Every new dopant inserted gives raise to a new impurity level, which is half occupied. From theoretical and experimental works in literature, it is well known that large concentrations of donors and acceptors in a semiconductor cause a reduction of the forbidden gap [?] and the so-called "band tailing" effect due to the random impurity distribution of donors and acceptors that forms a broad band near the energy gap edge [195, 194].

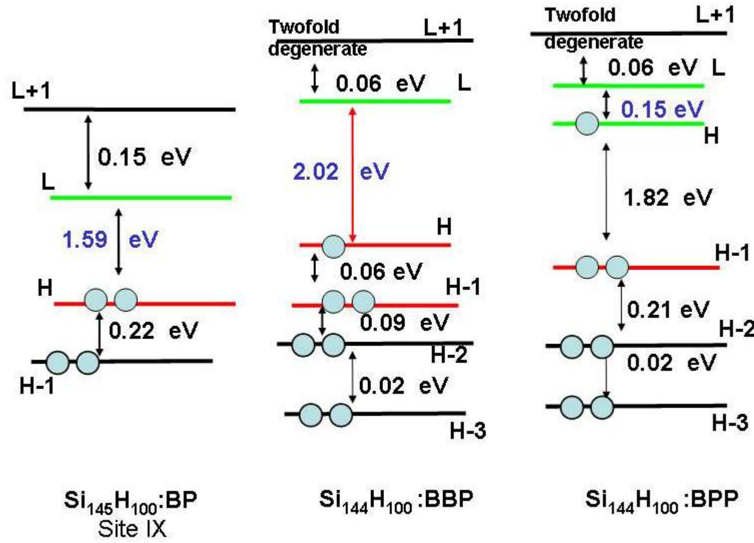

Figure 6.4: Comparison between the electronic levels the Γ point for the codoped Sinc and the uncompensated multidoped nc with an odd number of impurities. Left: $Si_{145}BPH_{100}$-nc (D_{BP}=13.28 Å). Middle: $Si_{144}BBPH_{100}$-nc. Right: $Si_{144}BPPH_{100}$-nc. Alignment has been performed locating at the same energy the fully occupied levels with the same type of localization.

Thus looking at Table 7.3 we see that the HOMO-LUMO energy difference for the nanoclusters with an odd number of impurity atoms are very similar: 2.02 eV for the $Si_{144}BBPH_{100}$-nc with respect to 2.08 eV for the B single doped case ($Si_{146}BH_{100}$), and 0.15 eV for the $Si_{144}BPPH_{100}$-nc with respect to 0.13 eV for the P single doped case ($Si_{146}PH_{100}$) respectively. Besides, another time, when the impurities are compensated, as in the case of $Si_{143}BBPPH_{100}$-nc, the system becomes semiconductor: now the

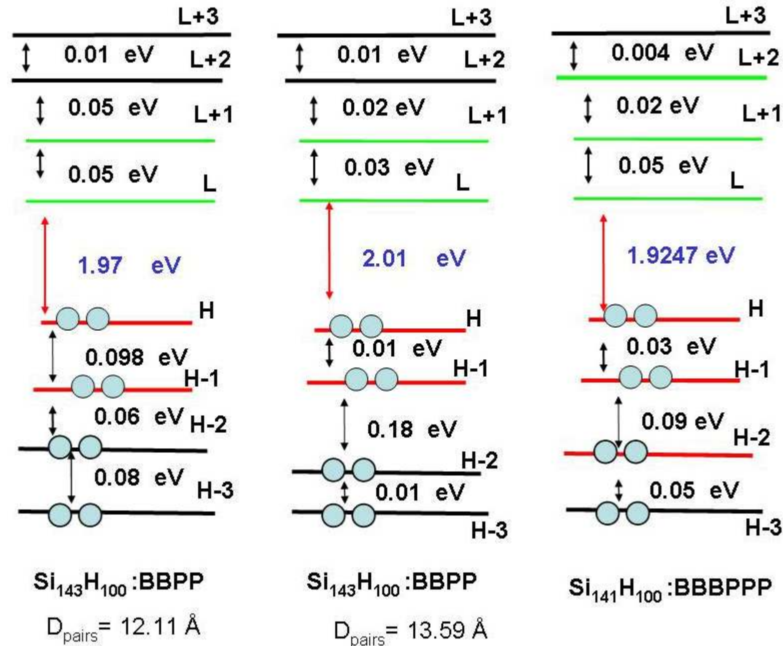

Figure 6.5: Comparison between the electronic levels the Γ point for the compensated multidoped nc with an even number of impurities. Left: $Si_{143}BBPPH_{100}$-nc (D_{pairs}=12.11 Å). Middle: $Si_{143}BBPPH_{100}$-nc (D_{pairs}=13.59 Å). Right: $Si_{141}BBBPPPH_{100}$-nc. Alignment has been performed locating at the same energy the fully occupied levels with the same type of localization.

HOMO contains again two electrons, and the value of the energy gap (1.97 eV) is between the two E_G values associate to the two opposite codoped configuration for the $Si_{145}BPH_{100}$ with impurities located at different distance (2.03 eV for impurities closer each other and 1.59 eV for impurities at the opposite side of the Si-nc). Furthermore regarding Fig. 6.5, where are compared the multidoped Sinc with an even number of impurities, with two or three B-P impurity pairs, one can see that the energy gap remains practically constant with respect to the distance between the B-P impurity pairs (in the $Si_{143}BBPPH_{100}$) and also with respect to the increasing of the number of compensated B-P impurity pairs.

In from Fig. 6.6 are reported the HOMO and LUMO states square modulus for the compensated multidoped Sinc. Once again it is confirmed the trend already depicted in the case of codoped compensated Sinc: the HOMO state is mainly localized on the Boron impurity site, while the LUMO states is principally centered around the Phosphorus atom. Nonetheless there are

some differences due to the excess of impurities. It comes out that when impurities of the same valence kind are coupled along the nanocrystal diameter the impurity wavefunctions tend to be localized on the two impurity sites. This is what happen in the $Si_{143}BBPPH_{100}$-nc ($D_{BPpairs}$=13.59) (middle panel) where due to this sort of particular "coupling" of the B and P atoms of the two pairs, the HOMO states is spread along the B-B direction, while the LUMO state is delocalized along the direction linking the two P atoms. On the opposite case, where two dopants with different valance charge are on the same linking diameter, the two wavefunction interferes destructively leaving the HOMO and LUMO mainly focused respectively on the B and P atom of the two pairs, as shown in the first panel of Fig. 6.6. This particular behaviour is confirmed by the localization of orbitals in the $Si_{141}3B3PH_{100}$-nc where due to the constructive overlapping among the impurity states related to the P atoms, the LUMO state is spread all over the three impurity sites within the nc.

6.4 Optical Absorption

The calculated optical absorption spectrum of $Si_{143}BBPPH_{100}$nc has been compared in Fig. 6.7 with the corresponding spectra of the $Si_{145}BPH_{100}$ codoped with impurities placed at two different distances within the nanocrystal, at site II and site IX with reference to the "$Si_{145}BPH_{100}$ impurity path" of Fig. 4.6. For what concern the two codoped Si-nc we observe a shift of the absorption onset toward lower energy on increasing the distance between impurities. It is worth pointing out that when impurities are at larger distance the transition intensities near the band edges become weaker due to a small oscillator strengths. When, instead, impurities are closer each other due to the strong localization of HOMO and LUMO on the impurity sites, the transitions near the band edge are more intense and involve in particular the Homo-1, Homo, Lumo and Lumo+1 levels. The multidoped $Si_{143}BBPPH_{100}$-nc shows an onset which is intermediate in energy between the two codoped cases, now the stronger optical transitions are far from the HOMO-LUMO gap and peaked in the 2.0-2.2 eV energy region, thus involving transitions between levels within the valence and the conduction band. The particular localization of HOMO and LUMO states depicted in the section before can offer a possible explanation. Due to the low overlap between the HOMO and LUMO state due to the interference among the impurity states, the optical transitions result almost dark and unfavored. We can think that when the dopant atoms with same charge valence couple an enhancement of the collective impurity state arise, leading as in the two cases of Fig. 6.6 to a better overlap of HOMO and LUMO states and thus to an increase of oscillator strength of transitions that involves levels around the band edge.

Moreover, as explained in [195], in heavily compensated doped Silicon the relative decrease in intensity of direct transitions can be due to the screening of the electron-dopants interaction by the compensating impurities and charge carriers; this screening can partially block the momentum transfer to the impurities thus leading to a quenching of the intensity of the direct nophonon mediated optical transition involving the impurity levels, as infact appear also in the spectrum in Fig. 6.7.

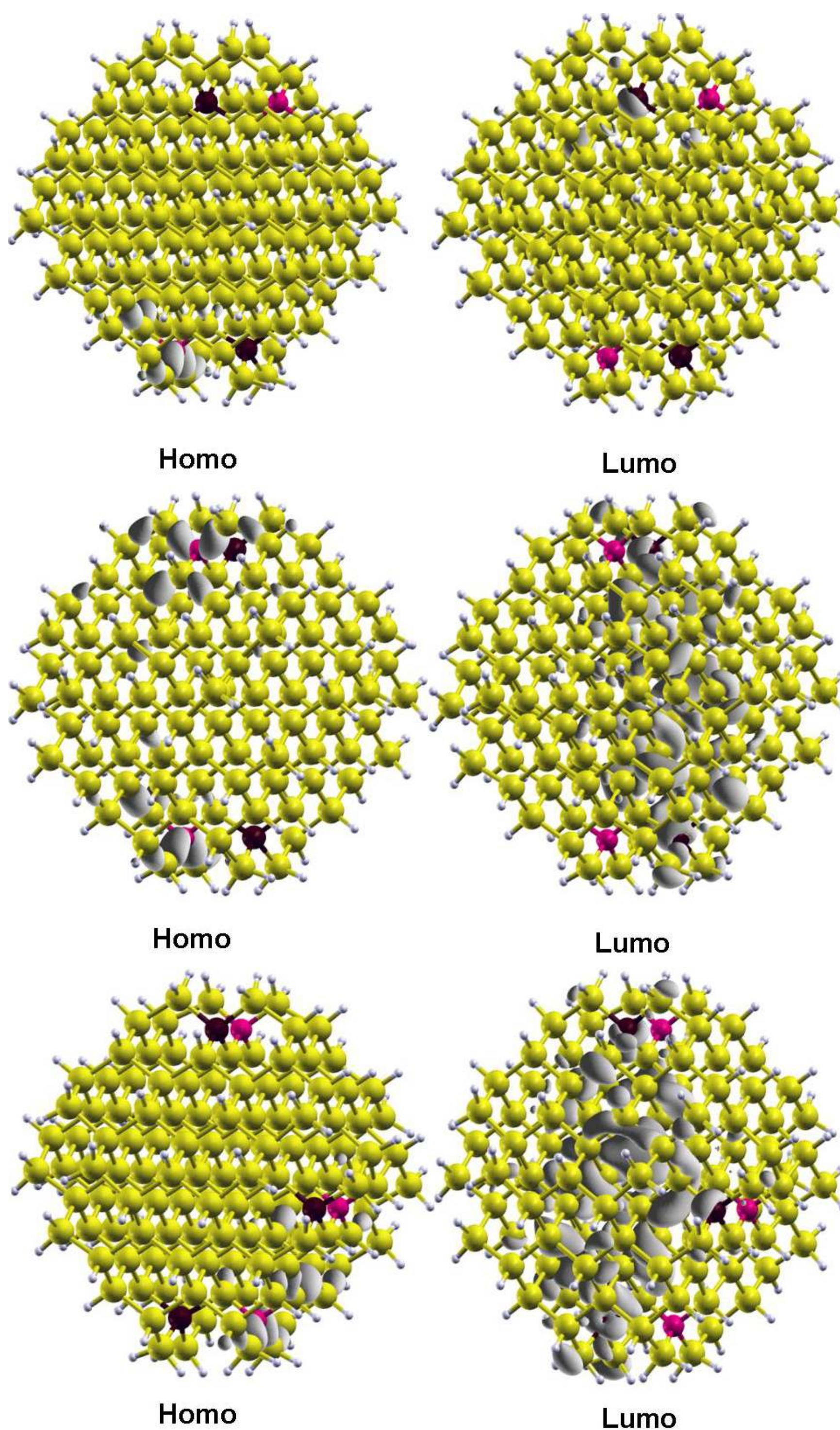

Figure 6.6: HOMO and LUMO square modulus contour plots calculated for the compensated multidoped Sinc. Upper panel: $Si_{143}BBPPH_{100}$-nc ($D_{BPpairs}$=12.11). Middle panel: $Si_{143}BBPPH_{100}$-nc ($D_{BPpairs}$=13.59). Lower panel: $Si_{141}3B3PH_{100}$-nc. The isosurfaces correspond to 20% of the maximum value.

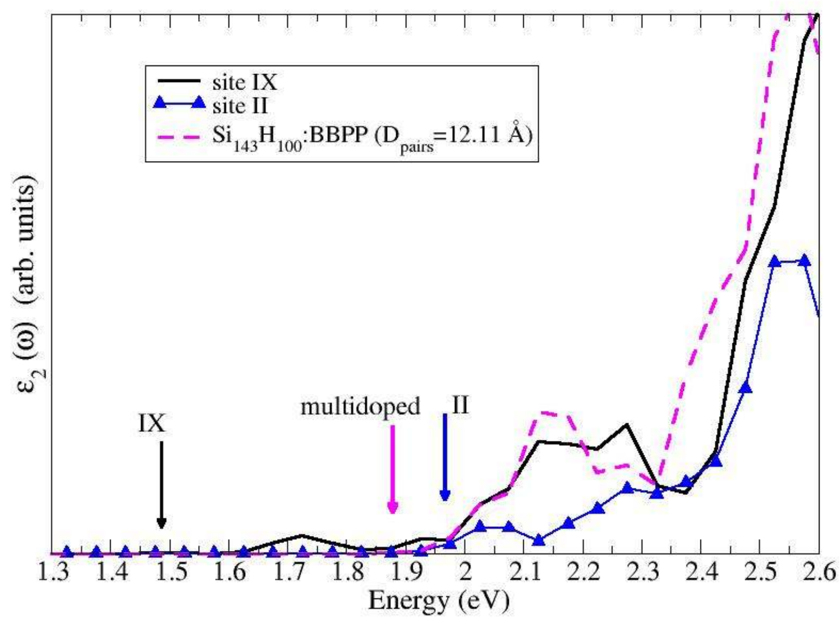

Figure 6.7: The imaginary part of the dielectric function $\epsilon_2(\omega)$ for the $Si_{145}BPH_{100}$ Si-nc with impurities placed at different distances and for the multidoped $Si_{143}BBPPH_{100}$-nc (see the inset). Arrows indicate the HOMO-LUMO energy gaps. The roman number refer to the site occupied by the P atom with respect to the B one (see Fig. 4.6). The arrows indicate the absorption thresholds.

7 Codoped Silicon Nanowires

Ramble on,
And now's the time,
the time is now
To sing my song.

Ramble on, LED ZEPPELIN

The Silicon Nanowires (Sinw) are semiconducting one-dimensional (1D) nanostructures which are attracting in the last years increasing interest for potential nanoelectronic and nanophotonic applications. Among all the one-dimensional nanostructures, such as the carbon nanotubes or nanowires, the Silicon nanowires offer the biggest advantage to be compatible with the existing silicon-based microelectronics. Moreover the possibility to tailor their electronic properties by changing thickness, orientation, surface morphology and doping is another important point in their favor [34, 35]. Several ab-initio studies on Si-nw are present in the literature. They are mainly concentrated on H-passivated or pristine Si-nw and demonstrate the dependence of the energy band gap from the wire diameter and from the surface morphology [12, 197, 198, 199, 200, 191]. Instead, few investigations have been dedicated to the influence of the electronic and transport properties from doping [201, 43]. In particular, due to the application in electronic devices, the main efforts have been devoted to the study of B and P single doped Si-nw, while only one ab-initio study has investigated the BP codoping [43]. For this reason, in complete analogy with the Si-nc, here is resumed the systematic analysis performed on the effect of the Boron and Phosphorous codoping on Sinw, concentrating not only on the structural properties but also on how doping influences the electronic and optical properties.

7.1 The systems

The Silicon Nanowires considered here are isolated wires passivated at surface with hydrogen in analogy with the nanocrystals and oriented along the [110] direction. Their geometrical structure is the same used by M. Bruno and coworkers [191, 190] in their study of the electronic and optical properties of undoped Silicon and Germanium nanowires. The same nanowires structures have been previously described in the work by Filonov et al. [202]. It comes out that there are two main parameters defining the structure of a nanowire:

- **linear cross section *l***: the maximum linear distance between two bulk atoms belonging to the same plane; as depicted in Fig. 7.1 is then possible to characterize wires grown along different directions with the same parameter l.

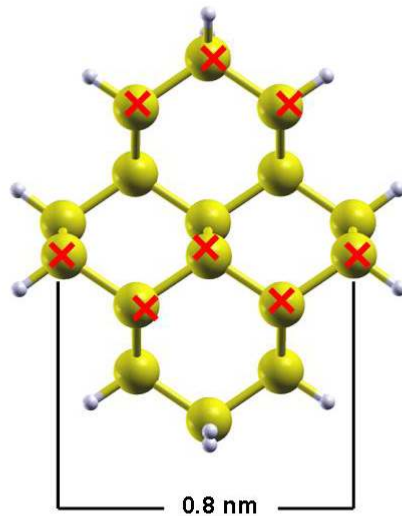

Figure 7.1: Unit cell projections onto the basis plane of the [110] oriented nanowire. Yellow ball are Silicon atoms, the white one the hydrogens. Si atoms labelled with the red X belong to the same atomic plane. As described in [202], the value of the linear cross section reported is l=0.8 nm.

- **effective diameter *d***:

$$d = 2\sqrt{\frac{A}{\pi}}$$

  where A is the cross section of the wire. One point of investigation infact will deal with the scaling of the electronic and optical features with respect the effective diameter of the nanowire and with the comparison with experimental evidence.

Here Silicon nanowires with two different values of linear cross section take into account: one with l=0.8 nm, as depicted in Fig. 7.2, and the other a little bit bigger with l=1.2 nm, as in Fig. 7.4, in order to investigate also the dependence on the dimensions and therefore on the increasing of the number of atoms. All the Sinw are passivated at the surface with hydrogen as done previously with the silicon nanocrystals and as free standing nanowires, are stuck within large supercell with a sufficiently portion of vacuum interposed between the period replicas.

- **Silicon Nanowire (l=0.8 nm) - $Si_{16}H_{12}$** The $Si_{16}H_{12}$ nanowire is constituted by 16 Si atoms and 12 H atoms in the unit cell and a linear cross section of l=0.8 nm . The direction of growth is along the [110] as one can see in Fig. 7.3
- **Silicon Nanowire (l=1.2 nm) - $Si_{30}H_{16}$** The $Si_{30}H_{16}$ nanowire has a larger cross section with 30 Si atoms and 16 H atoms in unit cell, as in Fig. 7.4. The [110] growth direction is shown in Fig. 7.5.

For what concern the computational details, the DFT-total energy calculations have been performed through the Quantum Espresso package [?], while the many-body calculations have been carried out using this time the optic code SELF [157] developed in Rome in Tor Vergata. In table 7.1 are shown the details of the total energy calculations for the two kind of nanowires.

	$Si_{16}H_{12}$	$Si_{30}H_{16}$
diameter	8 Å	12 Å
unit cell (Bohr)	$7.19 \times 40.68 \times 40.68$	$7.19 \times 50 \times 50$
Energy cutoff	30 Ry	30 Ry
k-point mesh	$16 \times 1 \times 1$	$8 \times 2 \times 2$
shift k	0.5 1 1	0.5 1 1

Table 7.1: Technical details of the ground state calculations performed on the nanowires.

In this work we moved from the previous outcomes by Bruno, Palummo, Ossicini et al. [191, 190] related to the study of electronic and optical features of undoped Silicon and Germanium nanowires, and we add one or two simultaneously impurities of Boron and/or Phosphorous in substitutional sites within the nanowires.

To the best of our knowledge the majority of works combining impurities and Silicon nanowires have been related since now to modify the conductivity features for transport applications, like recent studies conduct by Fernandez-Serra and Xavier Blase [201, 42], Riccardo Rurali [199] and coworkers and

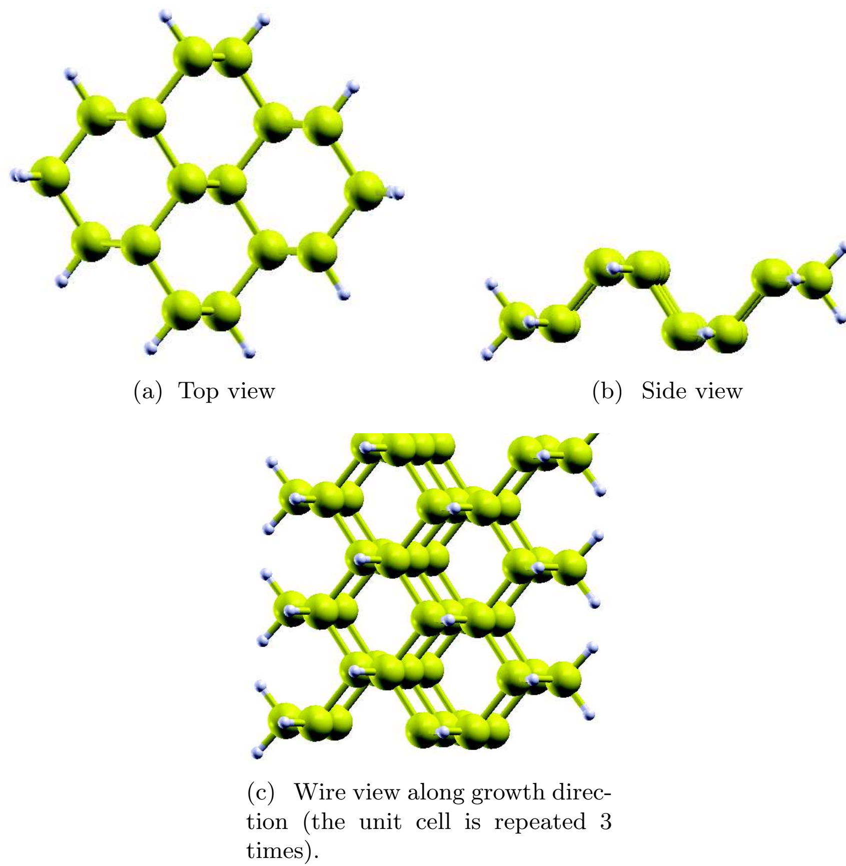

(a) Top view

(b) Side view

(c) Wire view along growth direction (the unit cell is repeated 3 times).

Figure 7.2: Undoped Hydrogenated Silicon Nanowire structure with l=0.8 nm and one single unit cell considered. The yellow balls are Si atoms, while the white are the surface Hydrogens.

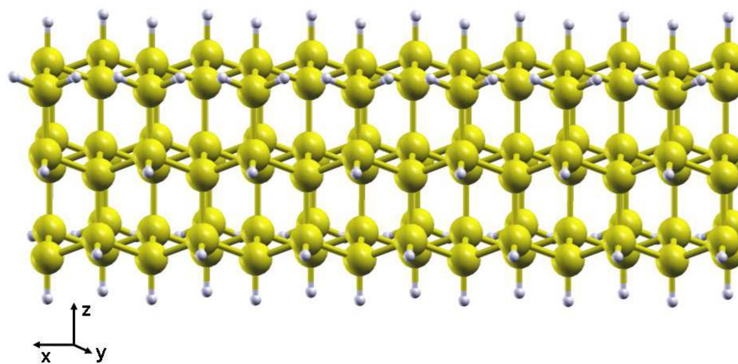

Figure 7.3: Growth direction along the [110] direction of the $Si_{16}H_{12}$ nanowire.

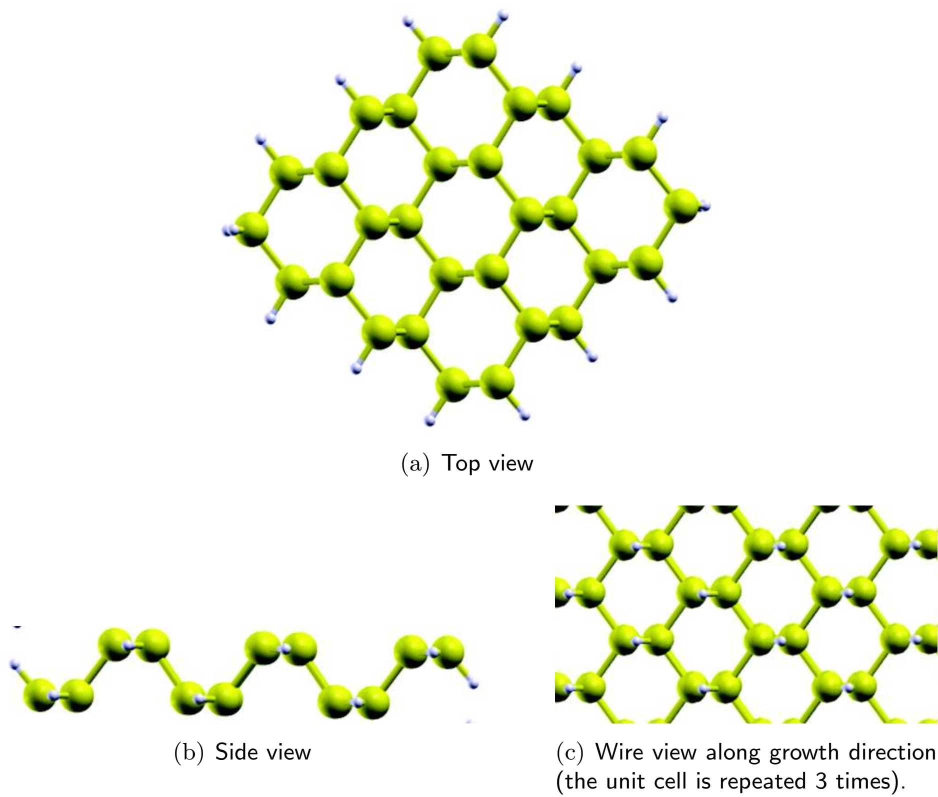

(a) Top view

(b) Side view

(c) Wire view along growth direction (the unit cell is repeated 3 times).

Figure 7.4: Undoped Hydrogenated Silicon Nanowire structure with l=1.2 nm and one single unit cell considered. The yellow balls are Si atoms, while the white are the surface Hydrogens.

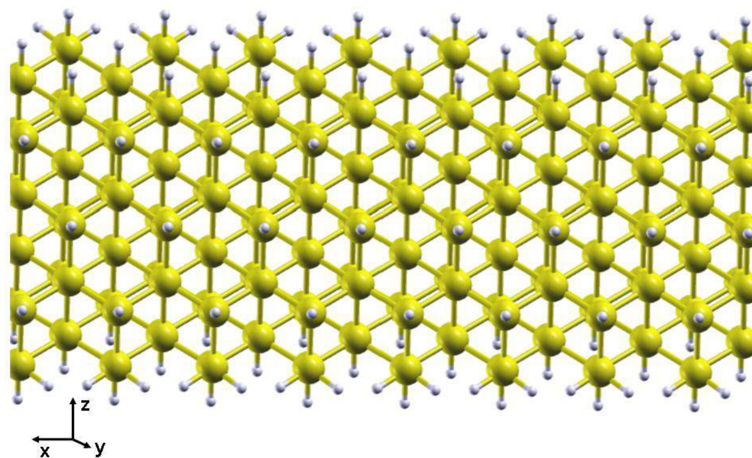

Figure 7.5: Growth direction along the [110] direction of the $Si_{30}H_{16}$ nanowire.

other theoretical and experimental groups [203, 204] demonstrate; in particular all these works concern the single doping with Boron or in alternative Phosphorous inserted in several substitutional sites within these Sinws. Aim of this work is otherwise the investigation of how the insertion of one or two impurities within the Sinw could be functional to engineer new characteristics such as optical features and emission light for optical and photonic devices, a domain almost forbidden for bulk silicon.

Among the many paper concerning the role played by single B or P doping on Sinws and although the major of them have been published in the last years [205, 206, 203, 199, 204, 201, 42] none of them deal with the B and P codoping. Since now to the best of our knowledge the only work dealing with the B and P codoping nanowires has been realized by the Belgian group from Antwerpen: this group through an *ab initio* DFT approach has investigated the possibility to insert simultaneously n- and p- type impurities in substitutional sites within Silicon [43] and Germanium nanowires [207], evaluating Formation Energy and electronic properties of codoped Sinw with two different cross section, l=1.2 nm and l=1.6 nm.

7.2 Formation Energy

We evaluate the stability of codoped Sinw by moving from the previous considerations made for codoping the Silicon nanocrystals, and moreover motivated by the analysis work made by Peelaers and Peeters [43] in which they evaluate what impurity substitutional sites lower the formation energy of the wire, increasing thus the stability of the codoped Sinw.

The fact that the more stable impurity position concerning the B and P codoped nanocrystals, are substitutional sites in the first Silicon layer below the surface, also holds for the Silicon nanowires as demonstrated by Peelaers et al. [43] in Fig. 7.6. To calculate the Formation Energy they have exactly followed the same approach used in the present thesis work, calculating the FE via Eq.[4.1], and as one can see from Fig. 7.6(a) the nanowires have the same orientation but bigger diameter with respect the corresponding described here. What comes out from this analysis confirm our previous findings, that both single or codoped the impurities are more stable in substitutionally sites in the first layer below the surface; moreover, from Fig. 7.6(b) it comes out that the stability of singled doped Sinw increase not only when they are below the surface, but also when the nanowire unit cell is increased by two or even better three times with respect the single one, thus determining a strong lowering of the FE with respect the previous situations as a consequence of minor interaction between the impurities.

Due to these last observations, we focus our attention on exploring different possible combination of B and P substitutional impurities for the smallest nanowire considered here, l=0.8 nm. By moving from the more

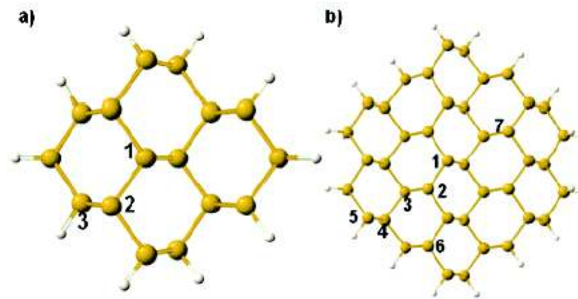

(a) Single unit cell of Sinw by Peelaers and Peeters. (a) the 1.2 nm wire (16 Si atoms and 12 H atoms) corresponds to the 0.8 nm Sinw described in the present work. (b) the 1.6 nm wire consists of 4 Si atoms and 20 H atoms.

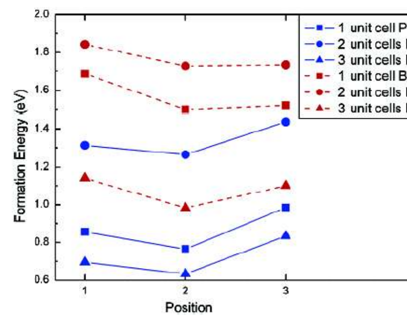

(b) Formation Energy as a function of the position of impurity with reference to Fig. 7.6(a). Single doped cases for the biggest 1.2 nm Sinw.

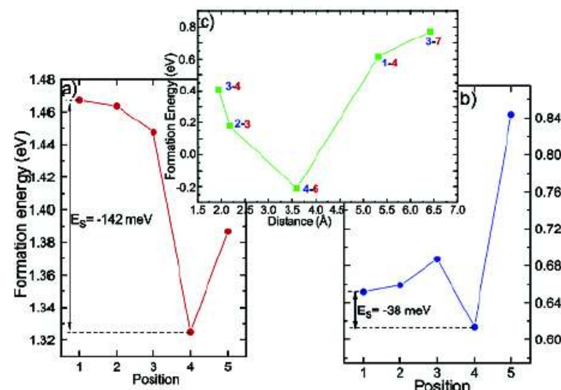

(c) Formation Energy as a function of the position of impurity with reference to Fig. 7.6(a). Codoped cases for the biggest 1.2 nm Sinw.

Figure 7.6: Figures illustrating the data on the Formation Energies explained in the work by Peelaers, Peeters et al.[43] on B-P codoping Silicon Nanowire.

stable impurity sites for the single doped cases corresponding to the substitutional sites just below the surface and illustrated in Fig. 7.7 we decide

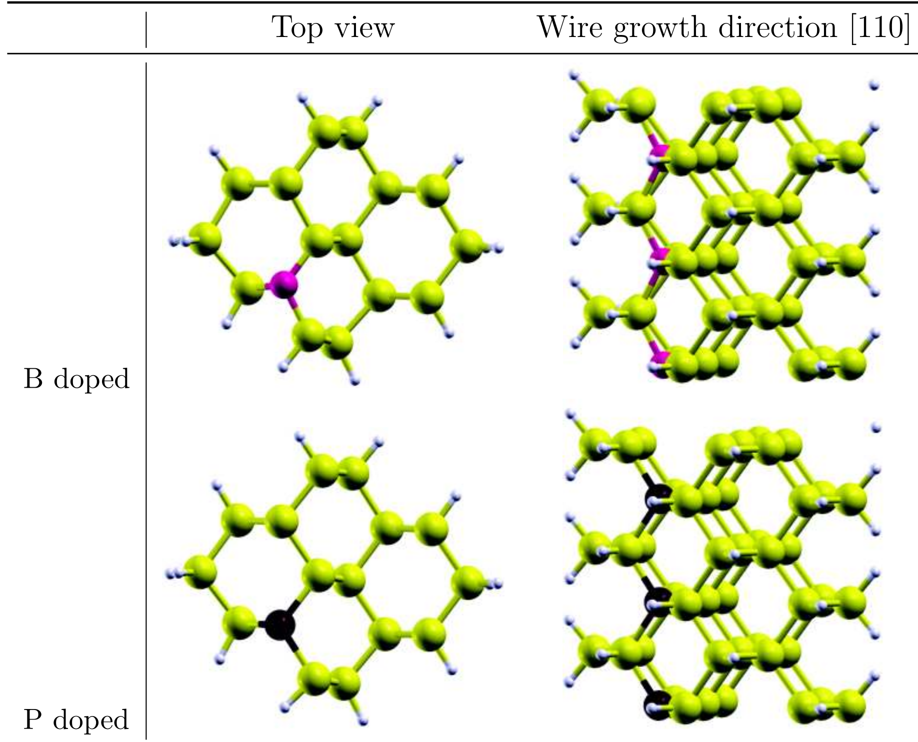

Figure 7.7: One unit cell single doped Sinw (l=0.8 nm) with B and P impurities in substitutional sites in the first layer below the surface. On the left column is reported the nanowire cross section while on the right column the nanowire is oriented along the [110] growth direction; magenta atom is Boron, dark-brown is Phosphorus.

how to codoped the nanowires. Several impurity configuration have been explored in order to bring out how the mutual position of the two simultaneous impurities in the first layer below the surface affects the stability and then the electronic structure of the nanowires. In Fig. 7.8 are reported four different type of configuration for the codoped l=0.8 nm Sinw.

In the first panel the B and P are both subsurface like second neighbors (D_{BP}=4.29 Å) while in the second and third panels the impurities are placed like near neighbors keeping the B fixed in the subsurface layer and putting the P atom one time in the center of the Sinw (D_{BP}=1.95 Å) and the other one in a surface substitutional site (D_{BP}=2.17 Å). In the fourth panel the B is in a substitutional site at the surface, the P instead in a subsurface site like near neighbors as before, and maintaining the same mutual distance as the previous case (D_{BP}=2.17 Å).

Thus, from Table 7.2 where the Formation Energy and the energy gap

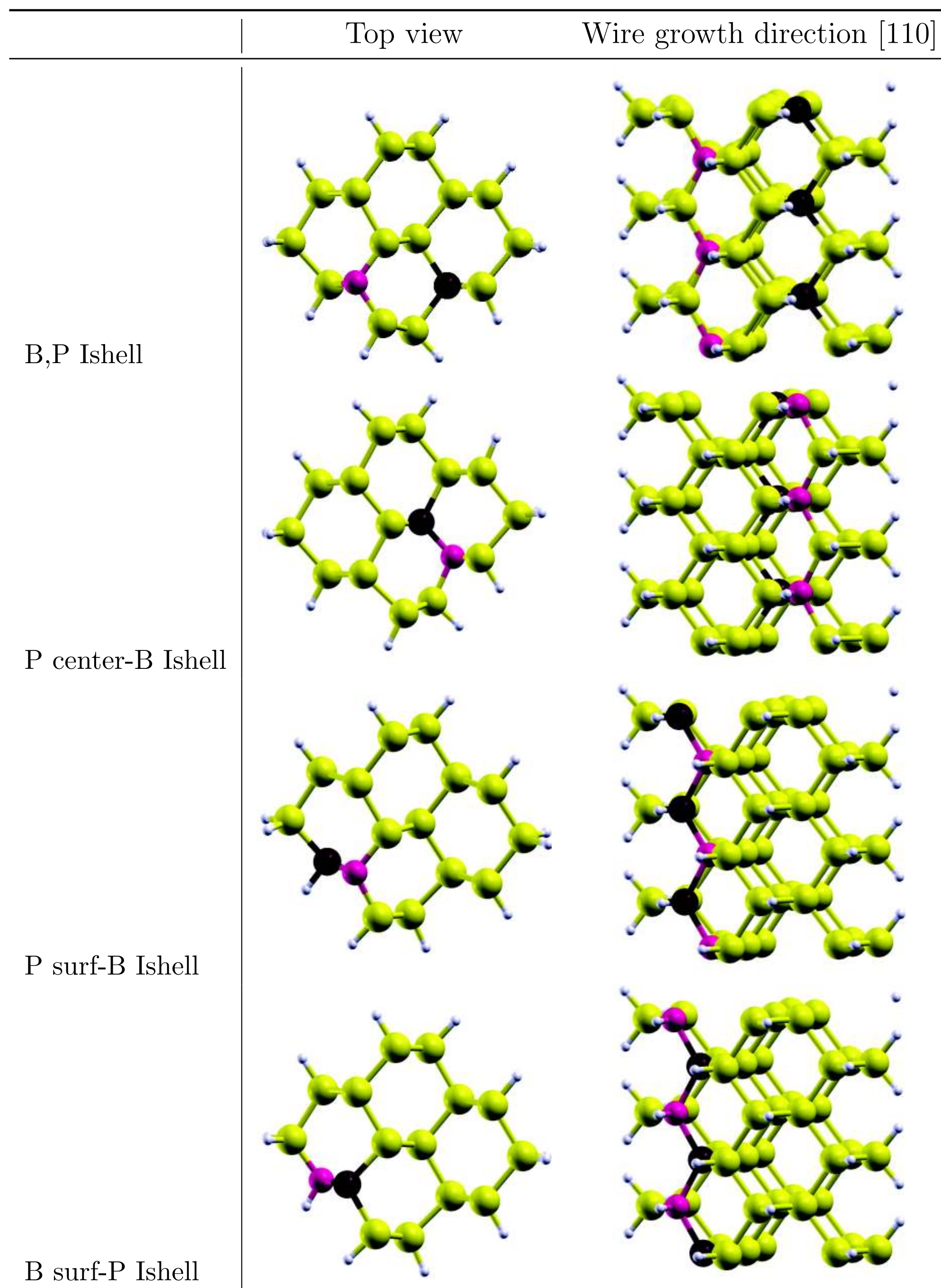

Figure 7.8: One unit cell B-P codoped Sinw (l=0.8 nm): several impurity configuration are explored (see text for details).

Nanowire (l=0.8 nm)	D_{BP} (Å)	Formation Energy (eV)	Direct Energy Gap (eV)
$Si_{15}BH_{12}$		1.13	1.4
$Si_{15}PH_{12}$		0.66	
$Si_{14}BPH_{12}$			
B and P subsurface	4.3	0.41	0.08
P center, B subsurface	1.95	0.10	0.63
P surface, B subsurface	2.17	-0.05	0.97
B surface, P subsurface	2.17	-0.28	1.24

Table 7.2: Formation Energy and Energy Gap (see text) for the single doped and the codoped (see Fig. 7.8 nanowires (l=0.8 nm)).

for single and codoped Sinw are reported, one can see that as for the Sinc, the single doping is less favored than the codoping, in good agreement with the previously theoretical prediction in [43]. Nonetheless, what's result to be new and interesting with respect the work [43], is that for the smallest Sinw we considered here (l=0.8 nm) the most stable sites for B and P impurities were not the subsurface positions. In this cases, infact, the FE is strongly lowered with respect the case in which the two impurities are simultaneously in substitutional sites below the surface, where it is 0.41 eV. As from the numerical values of Table 7.2 and as sketched in Fig. 7.9, the FE moves from a small positive value (0.1 eV) when the P atom occupies a Si core substitutional site (in Fig. 7.9 position label by 1) to a negative one (-0.05 eV) when the P impurity is substitutionally placed surface site and passivated by hydrogen (position 1). Furthermore, with respect to this last configuration, when the mutual position of B and P are exchanged (last panel of Fig. 7.8), FE becomes again more negative assuming the smallest value (-0.28 eV) since now.

Some observations could be done. There's no linear dependence between the strong decrease of FE from 0.41 eV to -0.28 eV and the B-P impurity distance, but nevertheless when the mutual distance decreases under a certain value, the stability of the codoped nanowires increases, thus demonstrating once again that more closed are the n- and p- type dopants more the wire gains stability form the formation of a B-P impurity complex. It's also worth mentioning that the negative FE values found when a P or B atom is passivated at surface with hydrogen are corroborated by the experimental evidence by the work of Fukata [206, 205] which demonstrate how the impurities tend to be substitutionally doped in the Si core of the nanowires where they can be activated, but also that when the doped Sinw are passivated with hydrogen impurities, Boron in

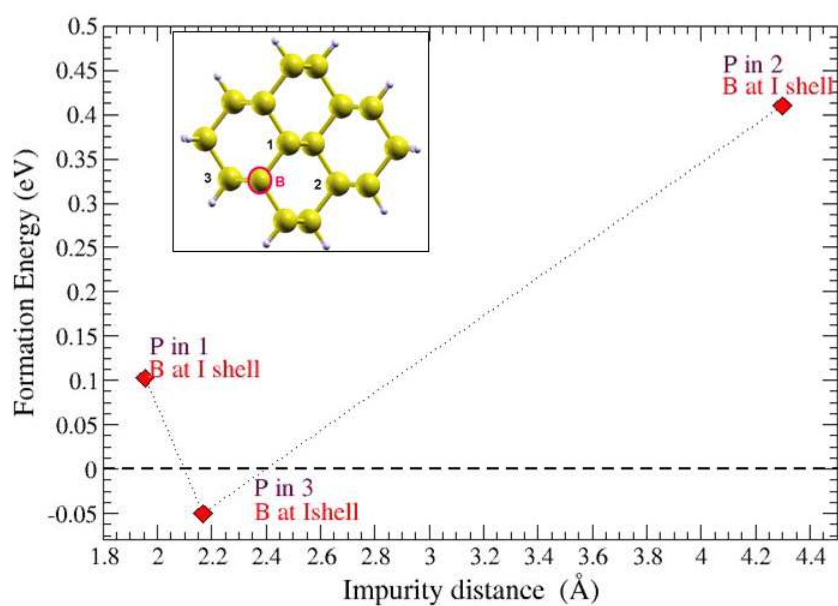

Figure 7.9: Formation Energy for BP codoped l=0.8 nm Sinw as a function of the distance between the two impurities. The FE is calculated for each step of the "*Phosphorus impurity path*": the B impurity (magenta) is frozen in a subsurface site, while the P atom occupies different substitutional sites labelled each time by 1, 2 or 3. The lines are guide for eyes.

particular, tend to form strong complexes with H, called passivation centers. Moreover, the experimental work [205] confirm that B preferentially segregate at the edge boundary region of the Sinw, rather than in the Si core sites.

Moreover the discrepancy between the positive FE value and the one found in the other paper [43] for the codoped Sinw with impurities in the first layer below the surface depends on the different dimension of Sinw considered in the two cases: here the FE energy has been calculated for the l=0.8 nm Sinw, while in the other work the Sinw take into account has a larger diameter of 1.2 nm. Taking into account the larger Sinw with cross section l=1.2 nm codoped with B and P in subsurface position at a distance of 3.65 Å the corresponding FE results to be -0.28 eV, thus confirming an increase in stability when the nanowire cross section increase in well agreement with the theoretical prediction by Peelaers et al. and moreover demonstrating that small nanowires are more difficult to codoped than the bigger one, such as for the Silicon nanocrystals. Supported by the reduction of FE for bigger wire diameter, we can say that codoping impurity in the first layer below the surface, as done here, borders more a sort of *shell-doping* [204] than a traditional doping to insert impurities within the nanowires.

The possibility that the FE of codoped Sinw with subsurface BP decreases with the augmentation of the nanowires dimension, could be guess by taking a nanowire unit cell two, three and four times bigger than the one unit cell considered in this cases, as shown in Table 7.10. In Table 7.3 are collected the FE values for this bigger unit cell nanowires (l=0.8 nm) with BP impurities kept almost at the same distance in the first subsurface layer for each situation. As depicted in Fig. 7.10 where bigger unit cell are reported,

Nanowire (l=0.8 nm)	D_{BP} (Å)	Formation Energy (eV)	Direct Energy Gap (eV)
$Si_{14}BPH_{12}$ 1 unit cell	4.3	0.41	0.08
$Si_{30}BPH_{24}$ 2 unit cell	4.35	-0.15	1.1
$Si_{46}BPH_{36}$ 3 unit cell	4.2	-0.6	1.43
$Si_{62}BPH_{48}$ 4 unit cell	4.35	-0.64	1.51

Table 7.3: Formation energy and energy gap codoped nanowires (l=0.8 nm) with two, three and four times bigger than the single unit.

increasing the unit cell corresponds to increase the overall number of atoms within the cell and, furthermore, this translates for the codoped Sinw to a decrease of the concentration of the impurity number with respect the total number of the Silicon atoms within the wire. Thus what comes out is that first codoping big nanowires is easier than codoping smaller one and that a lowering of the impurity concentration results in a gain of stability for the

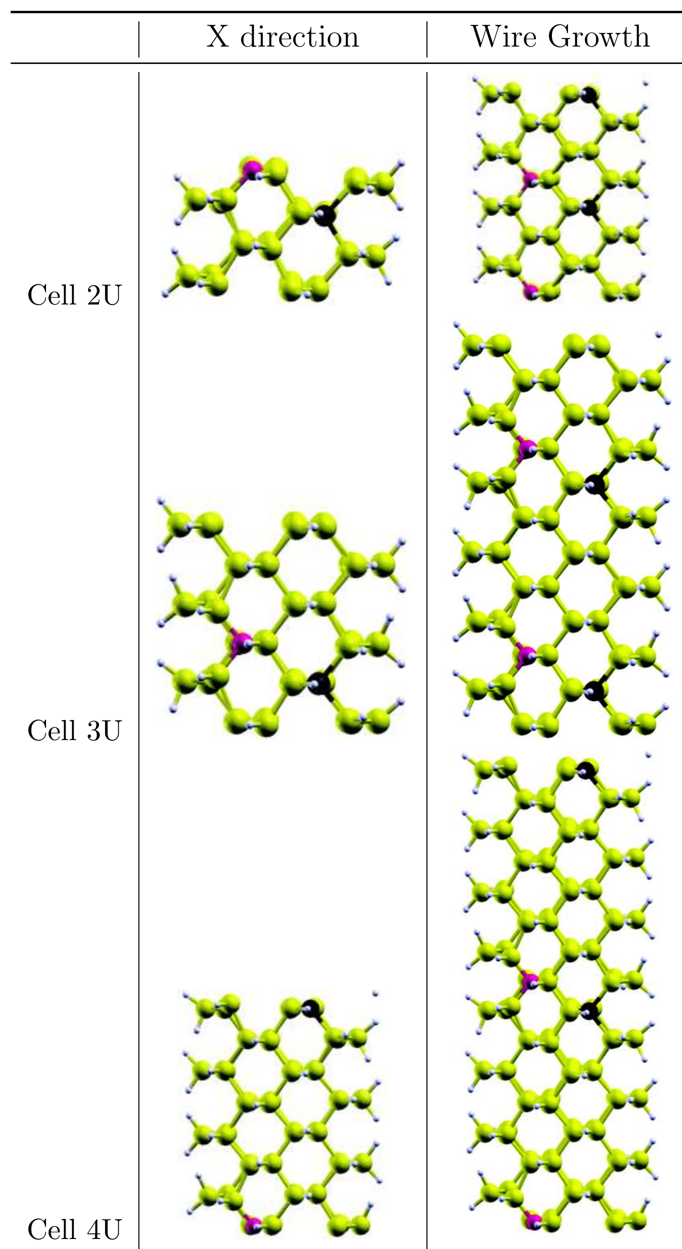

Figure 7.10: Bigger unit cell nanowires. Cell 2U: double unit cell. Cell 3U: three times unit cell. Cell 4U: four time unit cell.

codoped Sinw.

7.3 Electronic Properties

The insertion of n- and p- type impurities tends to drastically change the features of the electronic structure of the Silicon nanowires, in a much more pronounced way with respect the Silicon nanocrystals counterpart. The dopants within the Sinw act as shallow impurities and, as already described for the nanocrystals, new electronic states whose character is directly related to the valence of the impurity, arise near the band edge. In several previous works, theoretical and experimental, has been shown and established that undoped pure Silicon nanowires are semiconductors systems, with a *direct* band gap at the zone center with respect Germanium nanowires and also bulk Silicon which have indirect gaps. This is due to a quantum confinement effect of the charge carriers, as for the nanocrystals, but now in the plane orthogonal to the wire axis, determining an opening of the band gap. With respect to the nanocrystals, the Sinw present energy band and not discrete energy levels, due to a quantum confinement effect along only two direction. The particularity of the band energy gap E_G of the Silicon nanowires (such as for the Genw) are two:

- the energy gap decreases monotonically with the increasing of the wire's diameter;

- the band gap depends strongly on the orientation of the wires: in particular the [110] orientation gives rise to the smallest energy gap among all the other, probably because the quantum confinement effects are much more stronger in [100]- and [111]- oriented wires [190, 191].

The undoped [110] $Si_{16}H_{12}$ (l=0.8 nm) considered here presents a direct band gap at the Γ as shown by Fig. 7.11: the DFT-GGA gap is 1.66 eV bigger than the corresponding Si bulk value, but in really good agreement with other E_G from the literature for the same wire diameter and orientation.

As said, the simultaneously insertion of B and P dopants leads to a clear band gap reduction although it retains a minimum gap at Γ like in the pure Sinw as depicted in Fig. 7.12. The DFT-GGA band gap of the codoped Sinw result to be at Γ 0.08 eV in perfect agreement with the value found in the work by Peelaers [43].

Moreover taking into account the "*Phosphorus impurity path*" depicted above in Fig. 7.9, it's interesting to note that as the formation energy tends to decrease the direct band gap enlarge from 0.08 eV (in the case with the highest positive FE value) to 0.97 eV (the most stable one) as shown graphically from the band structures plots in Fig. 7.13. From Table 7.2 the direct band gap increases by an amount of 0.9 eV undergoing from the codoped BP in subsurface sites, to the nanowire with B subsurface and P at surface.

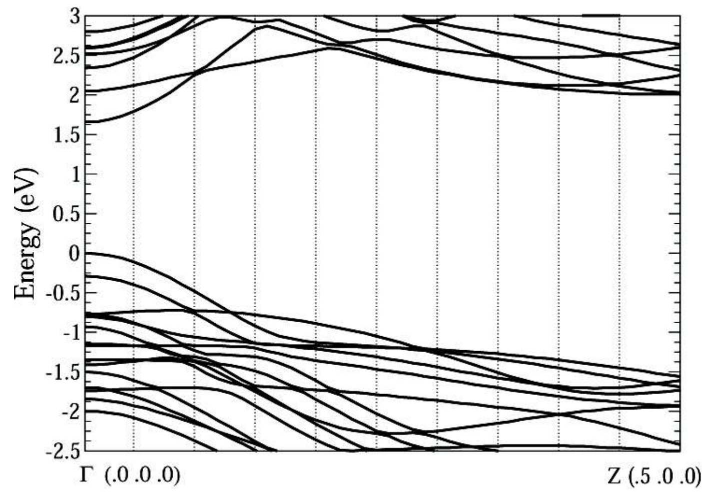

Figure 7.11: Electronic band Structure of the undoped 0.8 nm diameter [110] $Si_{16}H_{12}$ nanowire in one-dimensional Brillouin zone along the wire axis. The band gap is direct at the Γ $\mathbf{k}$-point.

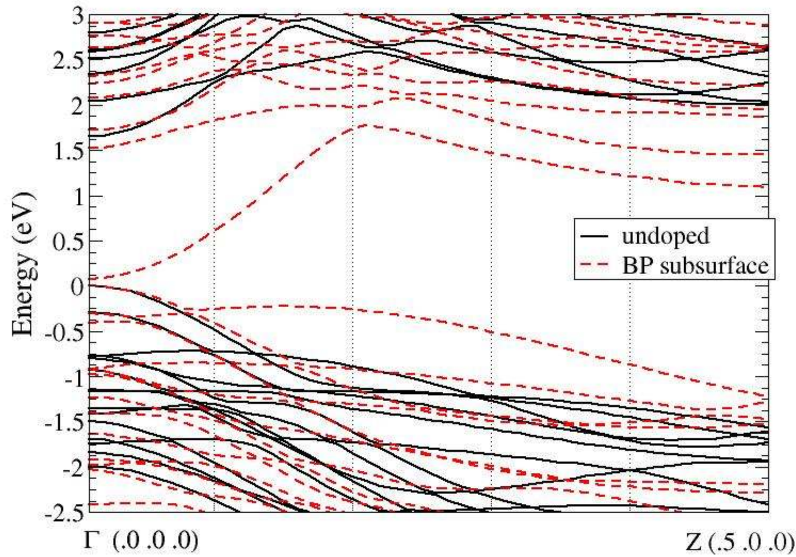

Figure 7.12: Electronic band Structure of the 0.8 nm diameter Si[110] nanowires in one-dimensional Brillouin zone along the wire axis. The black (dashed)line is related to the undoped wire, the red (solid) line refers to the codoped wire. In the figure the 0 refers to the Fermi Level of the considered wires. Impurities are in subsurface position (D_{BP}=4.29 Å).

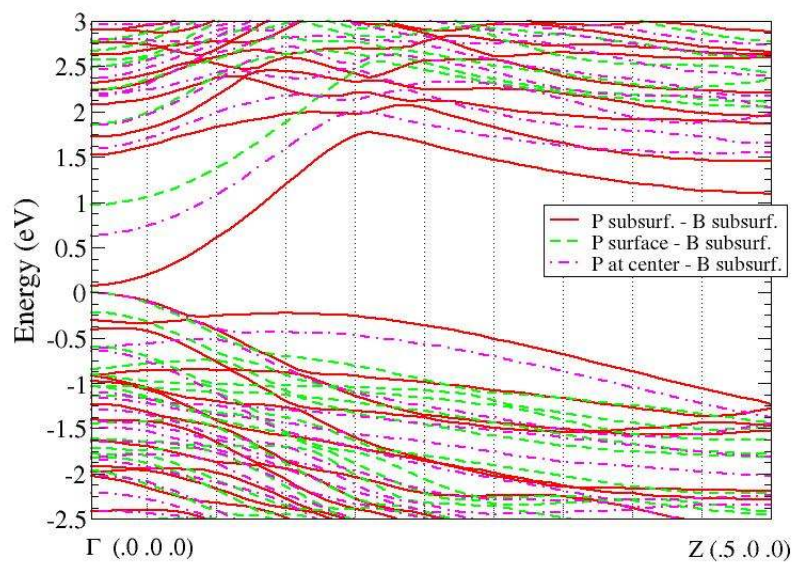

Figure 7.13: Phosphorous path: electronic band Structure of the codoped 0.8 nm diameter Si[110]nanowire with B subsurface and P atom occupying different sites: P subsurface position, D_{BP}=4.3 Å, (red solid line); P at surface D_{BP}=2.17 Å(green dash-dotted line); P at center D_{BP}=1.95 Å(magenta dashed line). In the figure the 0 refers to the Fermi Level of the considered wires.

The band gap behaviour can be understood by looking at the spatial localization at the Γ **k**-point of the Highest Occupied Molecular Orbital (HOMO) and the Lowest Unoccupied Molecular Orbitals (LUMO) within the nanowires. In Fig. 7.14, 7.15, 7.16 are shown the square modulus contour plots, with isosurface corresponding to 20% of the maximun value, for the codoped 0.8 nm codoped wire considered before.

From Fig. 7.14 we can see that the HOMO and LUMO orbitals of undoped and B or P single doped Sinw present the same features which came out for the Sinc. Thus HOMO and LUMO are spread all over the Silicon core cross section of the wire, while, for the single doped Sinw, HOMO is mainly centered on the impurity site, whereas LUMO maintains the same kind of localization of the pure hydrogenated Sinw; this respects the trend highlighted in the theoretical work by Singh et al. [203] where it's depicted the localization of the charge density in n- and p- type single doped Sinw for different diameters and different surface morphologies, thus confirming an universal orbital localization behaviour in presence of single impurities. When, instead,the B and P impurities are simultaneously inserted in the first silicon layer subsurface, see first column of Fig. 7.15, HOMO and LUMO are localized on the two dopants site respectively, determining as a consequence the strong reduction of the band gap at the Brillouin zone center. Nonetheless the localization of the wavefunction square modulus can change in the codoped Sinw according to whose substitutional sites are occupied by the dopants atoms. In Fig. 7.16 and in the right column of Fig. 7.15 this variation of orbital localization is shown for different substitutional site occupied by the Phosphorous atom. When the two impurities are no more contemporary in subsurface substitutional sites, it changes the spatial localization of HOMO orbital, which results now centered on the Silicon core of the wire apart from the sites occupied by the P dopant. Furthermore, from Fig. **??** when the two impurities are near neighbors, the LUMO is focused on the B-P complex formed. This behavior can be at the origin of the strong reduction in Formation Energy, as a sort of *modulation doping* or a Boron-Phosphorus linear chain "decorating" the wire and deeply altering the peculiar electronic and thermodynamic features of the undoped Si wire. Thus playing with impurity positions can be a way to modulate, to tune the electronic structure of the Silicon nanowire. Another way to do that and here a little bit investigated is what happen when are increased the dimensions of the wire by augmenting the unitary cell. As already reported by numerical values in Table 7.3 as the dimension of the wire unit cell increase, the band gap at Γ of the BP codoped wires tends to increase. This monotonic increasing trend is represented in Fig. 7.17, where the direct band energy gap is plotted with respect to the different unit cell, that means with respect to the total number of atoms within each unit cell. The increasing of two, three, fourth times the unit cell correspond physically to reduce the fraction of impurities with respect to the overall number of Silicon atoms,

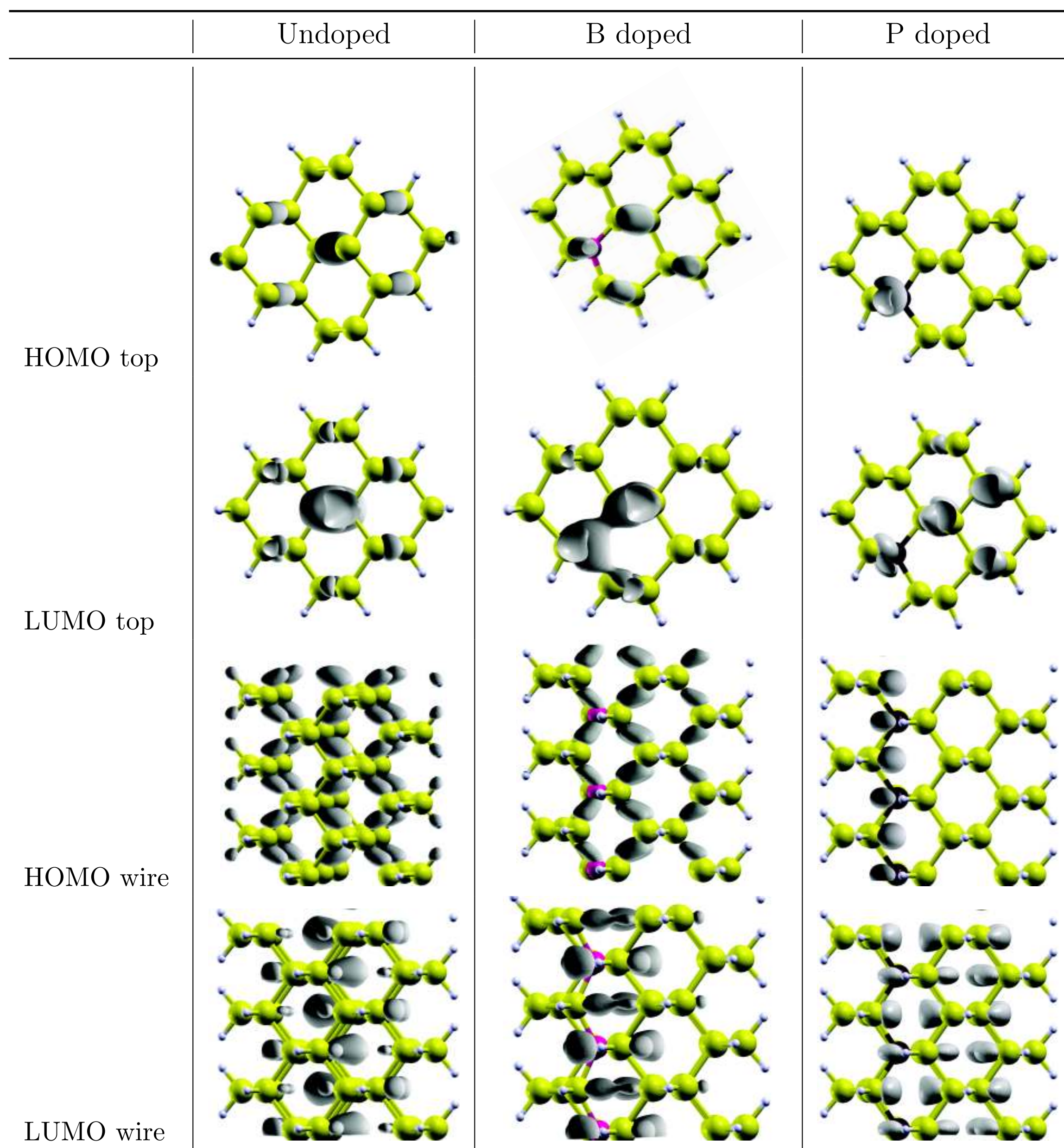

Figure 7.14: HOMO and LUMO square modulus contour plots calculated for undoped and single doped Sinw (l=0.8 nm). Columns: undoped (left); B subsurface (middle); P subsurface (right). Horizontal: the [110] top view (first two panels) and the [110] direction view (last two panels) of the HOMO and LUMO orbitals respectively.

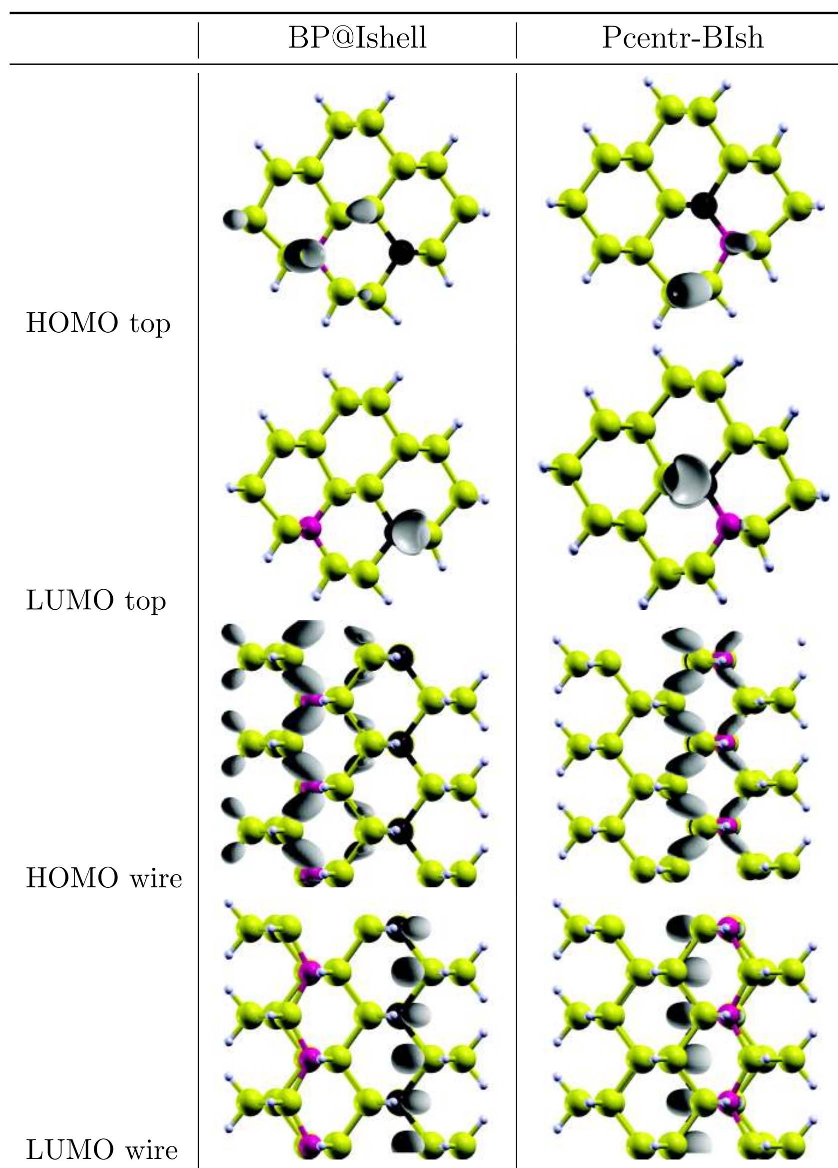

Figure 7.15: HOMO and LUMO square modulus contour plots calculated for codoped Sinw (l=0.8 nm). Columns: BP subsurface (left); P at center, B subsurface (right). Horizontal: the [110] top view (first two panels) and the [110] direction view (last two panels) of the HOMO and LUMO orbitals respectively.

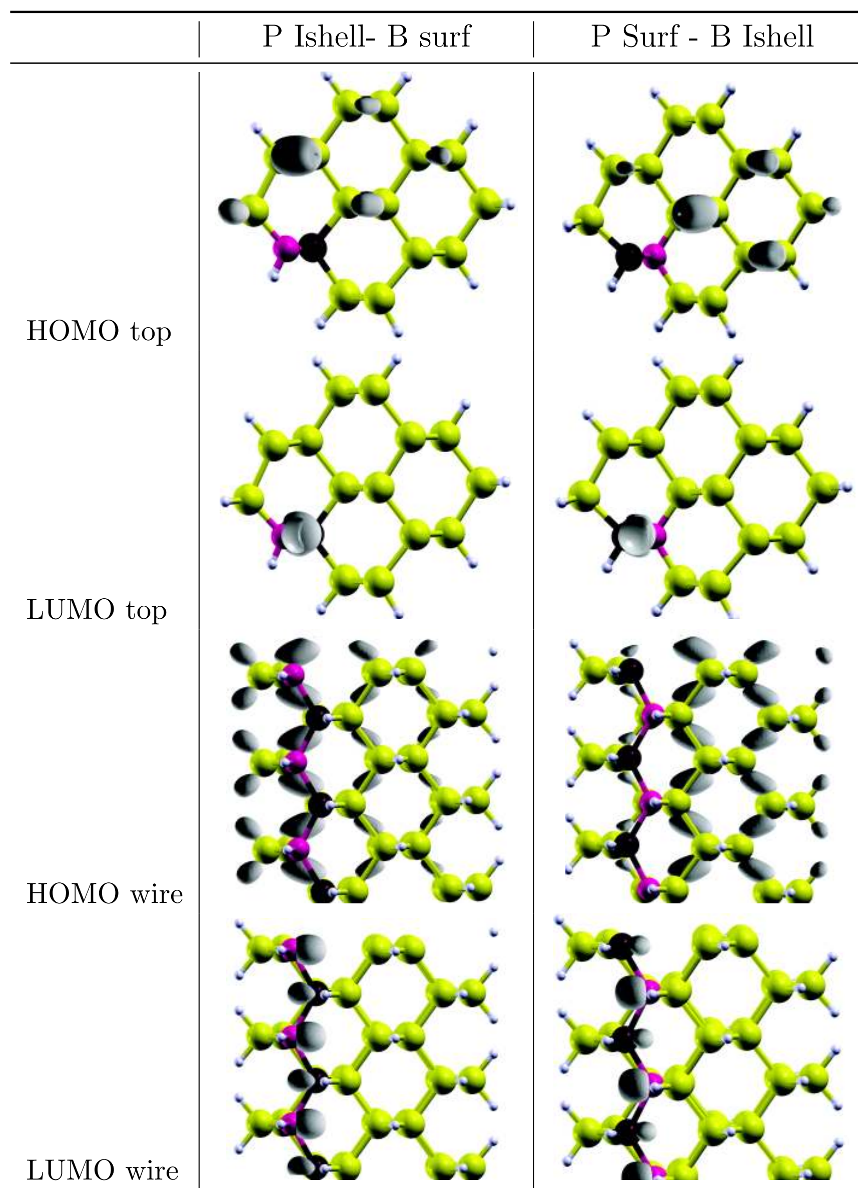

Figure 7.16: HOMO and LUMO square modulus contour plots calculated for codoped Sinw (l=0.8 nm). Columns: P subsurface , B at surface (left); P at surface, B subsurface (right). Horizontal: the [110] top (first two panels) and the [110] direction view (last two panels) of the HOMO and LUMO orbitals respectively.

thus to a reduction of impurity concentration. Thus from Fig. 7.17 it can be seen that the band gap increases with the augmentation of the unit cell, thus with the lowering of impurity concentration within the cell, approaching asymptotically to the undoped band gap limit represented by the dashed black line placed at 1.67 eV. Thus we can see that there are many way to induce with the codoping a modification of the electronic structure of the Silicon nanowire.

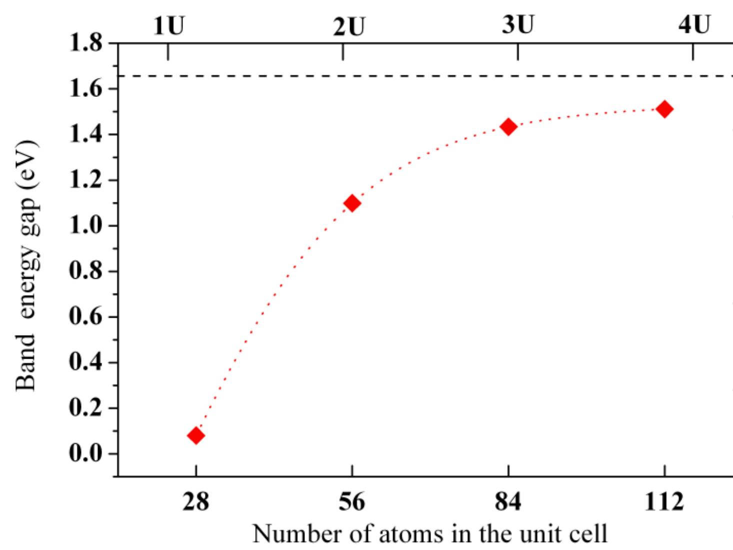

Figure 7.17: DFT-GGA direct band gap calculated at the Γ point with respect Single Unit cell, double unit cell, third unit cell and fourth unit cell nanowire (l=0.8 nm). The red dotted line is a guide for eyes. The black dashed line is the undoped band energy gap (E_G=1.67 eV), constant for each unit cell considered.

7.4 Optical Features

Here we take into account the main results achieved for the optical features of the codoped Sinw. We considered the 0.8 nm wire with the four different unit cell size and 1.2 nm wire with single unit cell. The absorption spectra have been calculated with the Independent-Particle RPA approach applying the simple Fermi Golden rule to estimate the Imaginary part of the dielectric function, $\varepsilon_2(\omega)$, as already describe in Section 3 by the Eq.[3.11]. In Fig 7.18 is reported the optical absorption spectrum for the 0.8 nm undoped and codoped (B and P subsurface) nanowires for a single unit cell, obtained within the single-particle RPA approach. Due to the depolarization effect which makes the wire almost transparent in the visible region for light polarized perpendicularly to the wire axis [190, 191], only the spectrum for light polarized along the wire axis is shown, together with the spectrum obtained for the corresponding pure Si-nw. The indirect character of the high-valence and low-conduction energies states is confirmed here for the pure Si-nw. The codoped Sinw, instead, shows an intense absorption peak in correspondence of the absorption edge at 0.08 eV, due to the high overlap between the HOMO and LUMO orbitals which are strongly localized on the Boron and Phosphorous impurity states respectively. The effect of the impurity states affects deeply the absorption spectrum of the codoped Sinw, revealing a quasi-continuous absorption behaviour typical of a metallic system; in particular an absorption edge is lower than the related undoped one and also than the bulk Silicon band gap limit.

Furthermore, the absorption spectra of the other codoped 0.8 nm Sinw here discussed, reveal a different behaviour.

In Fig. 7.19 and Fig. 7.20 are reported the absorption spectra of the other single unit cell codoped Sinw (0.8 nm) which are more stable due to lower and negative formation energy values. In Fig. 7.19 are reported the absorption spectra of codoped Sinw where P impurity is moved from the center toward surface and subsurface position, while the B atom is kept fixed in a subsurface site. When P impurity occupies substitutional sites at the center or at the surface, the absorption thresholds are very close each other located at higher values with respect the B-P at Ishell codoped case. Unfortunately there are any interesting and appreciable absorption peaks near the absorption edge, indicating that the main absorption features here resemble the indirect character of the undoped Sinw and that in particular the presence of impurity states do not change so much the spectrum. The same happen when one of the two impurities is in a substitutional site at the surface of the nanowire: in Fig.7.20 again there aren't any intense absorption structures around the two absorption edge (blue and cyan line). Thus Phosphorous or Boron in a surface site gives rise to the same effect, very similar to a depletion of intense and significative optical transitions in the region below 1.75 eV. This effect can be related to the presence of surface states due to the

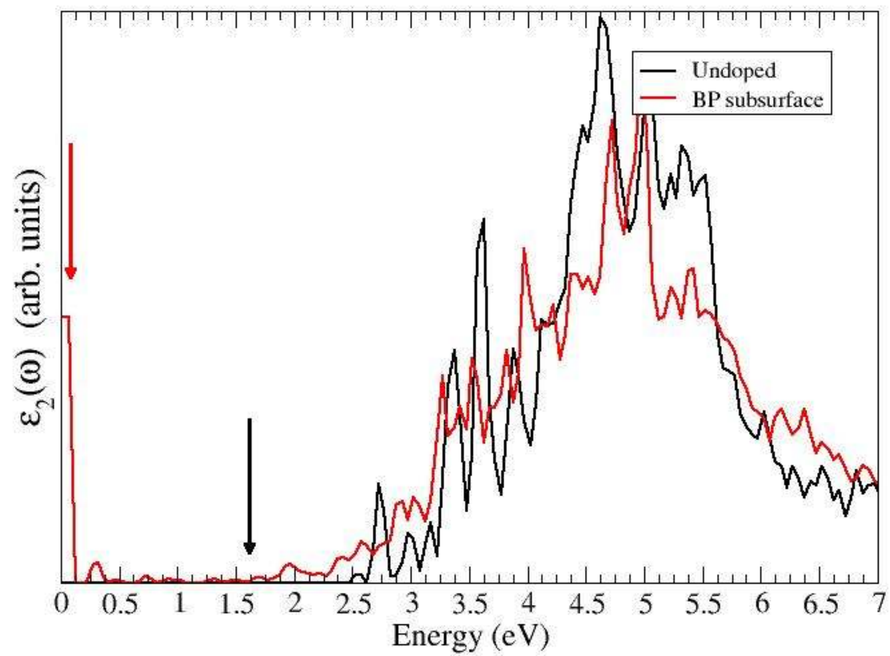

Figure 7.18: The imaginary part of the dielectric function $\epsilon_2(\omega)$ for the [110] oriented Si nanowires (l=0.8 nm). The black solid line is related to the undoped wire, the red solid line refers to the codoped wire, with impurities in the first layer below the surface (D_{BP}=4.3 Å). The arrows indicate the absorption thresholds.

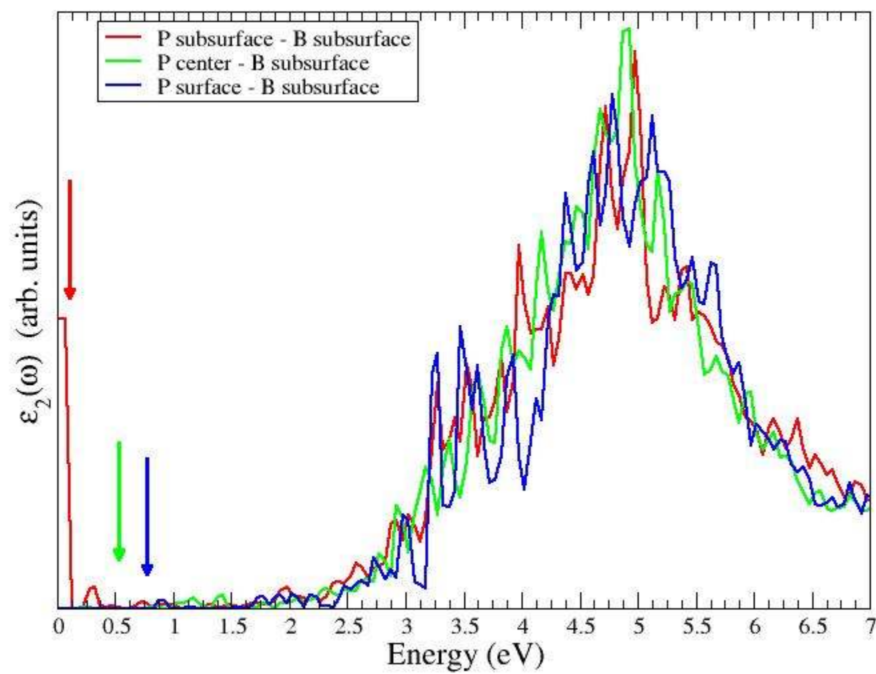

Figure 7.19: The imaginary part of the dielectric function $\epsilon_2(\omega)$ for the [110] oriented Si nanowires (l=0.8 nm). Red solid line: B and P in subsurface position (D_{BP}=4.3 Å). Green solid line: P at center, B subsurface (D_{BP}=1.95 Å). Blue solid line: P at surface, B subsurface (D_{BP}=2.17 Å). The arrows indicate the absorption thresholds.

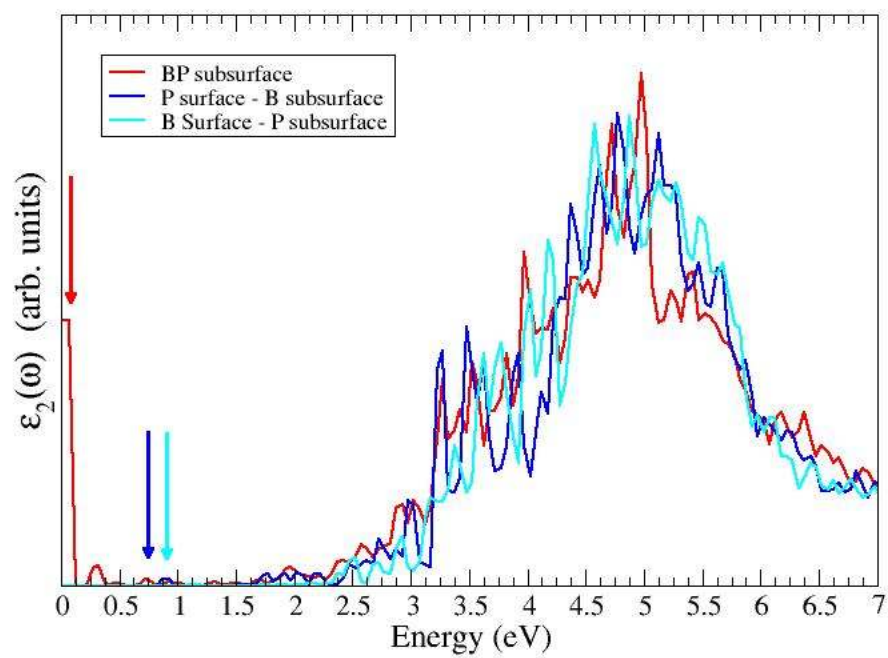

Figure 7.20: The imaginary part of the dielectric function $\epsilon_2(\omega)$ for the [110] oriented Si nanowires (l=0.8 nm). Red solid line: B and P in subsurface position (D_{BP}=4.3 Å). Blue solid line: P at surface, B subsurface (D_{BP}=2.17 Å). Cyan solid line: P subsurface, B at surface (D_{BP}=2.17Å). The arrows indicate the absorption thresholds.

presence of a surface impurity that renders the low-energy transition dark and unfavorable.

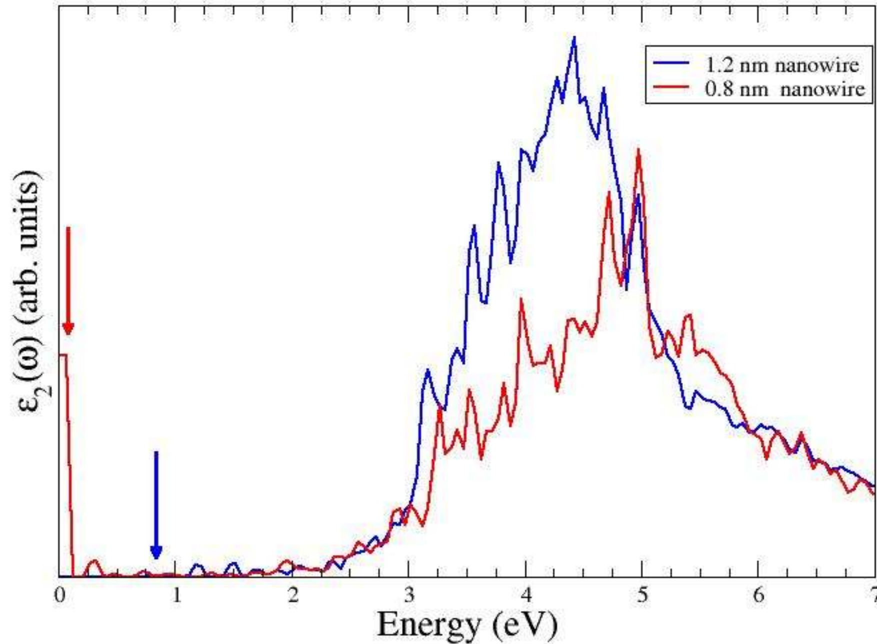

Figure 7.21: The imaginary part of the dielectric function $\epsilon_2(\omega)$ for the [110] oriented codoped Si nanowires with l=0.8 nm (D_{BP}=4.3 AA) and l=1.2 nm (D_{BP}=3.64 AA) . The impurities are both in the first layer below the surface. The arrows indicate the absorption thresholds.

In Fig. 7.21 is shown the comparison between the 0.8 nm codoped nanowire and the 1.2 nm codoped one with impurities in the first layer below the surface. It can be seen that the impurities states, due to B and P dopants, presents within the gap, have a slight influence of the optical spectrum that shows very small peaks in the optical region below 2.5 eV and no more the intense peak at 0.08 eV in the codoped 0.8 nm wire; moreover the absorption spectrum of the codoped wire, above 2.5 eV, remains similar to the corresponding spectrum of the undoped wire, showing the main absorption peak at about 4.5 eV.

Increasing the size unit cell for the 0.8 nm wire, it comes out, as depicted in Fig. 7.22, that increasing the size of the wire unit cell the absorption threshold don't change so much. By considering a unit cell two, three and

four times bigger along the wire growth direction [110], the absorption edge tends to be blue shifted towards higher energy with respect to the codoped single unit cell nanowire. As before, no intense transition peaks can be recognized for the bigger cell wire below 2 eV. A possible explanation can be related by considering the variation dopants concentration in each Sinw unit cell: when the unit cell enlarges, the concentration of impurities decrease thus producing an optical response of the codoped Sinw more similar to the response of an undoped Sinw.

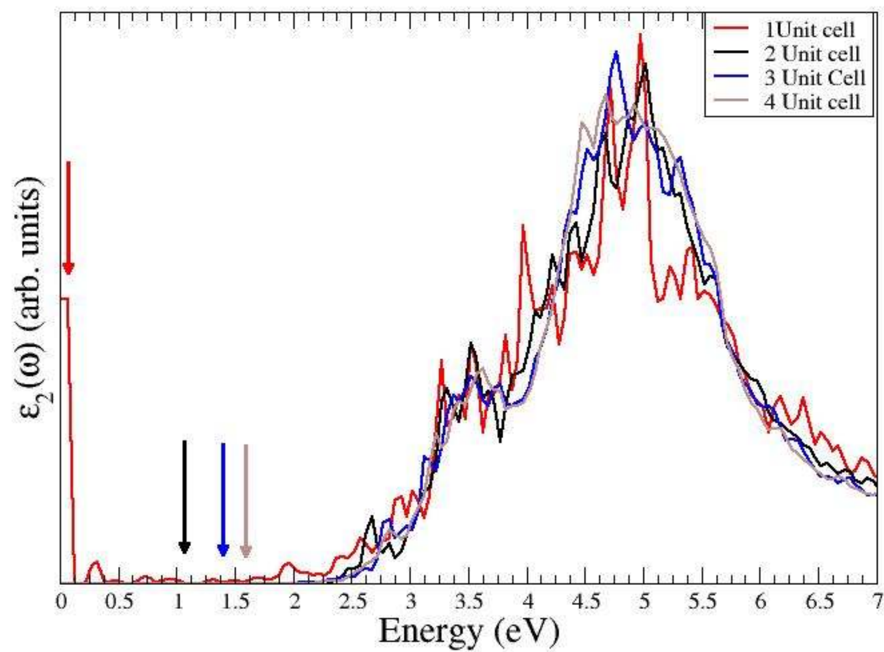

Figure 7.22: Increasing unit cell size: imaginary part of the dielectric function $\epsilon_2(\omega)$ for the [110] oriented codoped Si nanowires (l=0.8 nm) with B and P in the first layer below the surface. The arrows indicate the absorption thresholds.

7.4.1 Many Body Absorption Spectra

Here the absorption spectrum of the codoped 0.8 nm wire with B and P in subsurface substitutional position (see top panel in Fig. 7.8) has been calculated with the introduction of the many body effects, namely the self-energy and the excitonic effects [131]. In order to overcome the well known underestimation of the DFT-GGA band gap (in any local or semilocal approximation for the exchange-correlation potential) with respect to the experiments, the self energy corrections have been calculated within the standard G_0W_0 approach, leading thus to a better definition of the band gap in terms of quasi-particle energy:

$$E_g^{QP} = E_g^{DFT} + \Delta E_g^{GW}$$

As has been discussed in the literature (see for instance [208]), the use of a truncated Coulomb potential in the many-body calculations, when dealing with isolated systems in the supercell approach, is really an important point to reach a good accuracy in the final results. In fact, in the case of low-dimensional non periodic nanostructures, such as the wires, it prevents the interaction between the replica and allows the use of one-dimensional k-point samplings. The converged parameters of present GW calculations, performed in a simulation cell with a vacuum region of about $18\mathring{A}$, are the following: a uniform one-dimensional grid of 16 k-points, a kinetic-energy cut-off of 5 Ry and a sum over the unoccupied states up to about 20 eV above E_F in the correlation part of the self-energy, Σ_c, while a kinetic-energy cut-off of 10 Ry in the calculation of exchange part of the self-energy Σ_x.

Before to carry out the calculation for the codoped Si nanowire, we performed it in the corresponding undoped nanowire. In this way the GW correction to the minimum direct band-gap results to be 1.8 eV. This value is in a reasonable good agrement with previous self-energy calculations on the same pure hydrogenated Si-NW [200, 191]. As a general comment, it is important to point out here, that this quasi-particle correction is bigger than the corresponding value in bulk silicon (about 0.7 eV). Moreover it is nowadays clear that the self-energy corrections tend to decrease toward the bulk value, as the wire diameter is enlarged.
Afterwards we performed the same calculation for the codoped Sinw. in this case the minimum direct gap opens of 1.6 eV with respect to the DFT value, showing, at least in the studied case, a slight dependence from the doping. *GW* calculations (in the same simulation cell) without the use of a truncated coulomb potential take to quasi-particle gaps 0.3 smaller, both for the pure and for the codoped wire. This difference is clearly due to the long-range replica interactions which persist when the cylindrical cut-off is not used, but in any case confirms their slight dependence from the doping.

When the quasi-particles states are known, absorption spectrum can be calculated by including also the excitonic effects that take into account the interaction between an electron and hole pair by resolving the Bethe-Salpeter equation and including only the resonant part of the excitonic hamiltonian. The diagonalization of the excitonic hamiltonian has been performed using 1000 $\mathbf{G}$ vectors for the screened interaction W, 5000 $\mathbf{G}$ for $\bar{v}$ on 40 bands (half occupied, half empty). In Fig. 7.23 is reported comparison between the imaginary part of the dielectric function of the BP codoped [110] oriented Sinw (l=0.8 nm) calculated in the GW quasiparticle approximation without

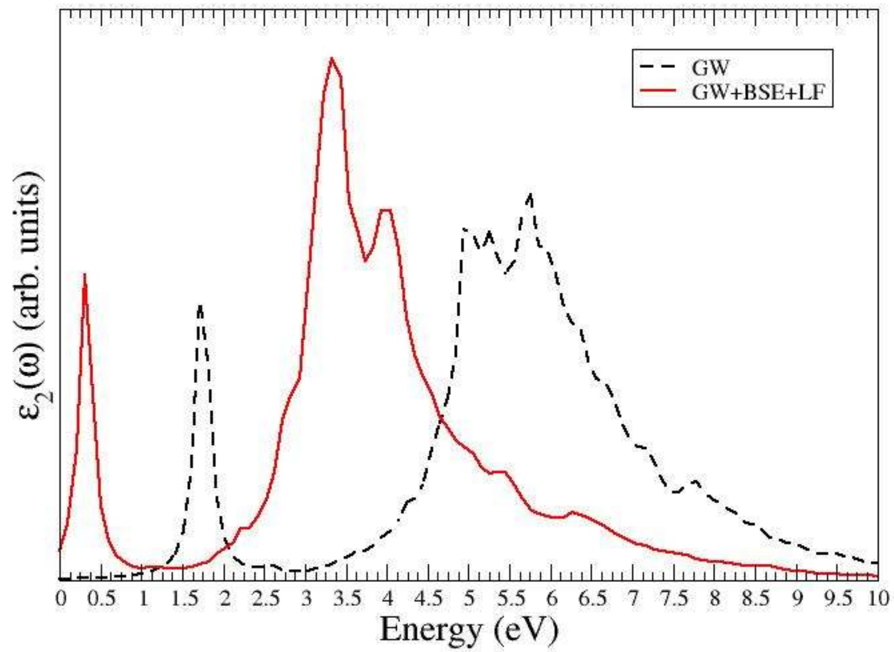

Figure 7.23: Optical Absorption spectra of [110] oriented codoped Si nanowires (l=0.8 nm) with B and P in the first layer below the surface. Black dashed line quasiparticle (GW) absorption spectrum and red solid line quasiparticle + excitonic effect (BSE+LF) spectrum.

the inclusion of excitonic effects (black dashed line) and by including e-h interaction and local field effects by solving the BSE equation (red solid line), with the inclusion also of the cut-off on the Coulombian potential. The quasiparticle effect is the opening of the gap that shift toward higher energies at 1.70 eV the main peak centered around the band edge in the previous IP-

RPA spectrum of Fig. 7.18. When instead excitonic effects are included the electron-hole interaction tends to close the gap again: the excitonic effect tends again to compensate the GW correction and to cancel partially the quasiparticle effect, thus recovering almost the same peak position around the band gap, now located at 0.28 eV. For this kind of small diameter (0.8 nm) wire, the binding energy of the exciton is of the order of 1.3 eV much bigger then the value for bulk Ge and Si, which is around 60 meV and of the same order of magnitude of the binding energies of the corresponding undoped wire, which is 1÷2 eV.

Conclusions

> Il sogno di una persona sola rimane un sogno... quello di tante persone insieme é la realtà che comincia.
>
> SUBCOMANDANTE MARCOS

The theoretical study performed through *ab initio* calculations and illustrated in this thesis work represents the summary of my research activity achieved during the last three year of PhD fellowship in Modena. The research illustrated is a first study on the effect play by the codoping with donor and acceptor impurities on Silicon Nanocrystals and Nanowires and it is part of a bigger field of study on the electronic and optical properties of the Silicon Nanostructures with different kind of passivation and surface termination that aim to carry out more information on the possibility to achieve light and stimulated amplified emission from these nanosized Silicon based systems.

This basic research thesis work, conduced under the smart and careful supervision of Stefano Ossicini and Elena Degoli, is proud to illustrate from a theoretical point of view and for the first time, how the insertion of compensated impurities into small Silicon nanostructures can drastically modifies their properties contributing thus to shed some more know-how on the possibility to realize sustainable emission of light from Silicon nanostructures for optoelectronic applications. To that, briefly are resumed what we have understand about the doping and the codoping in nanosized Silicon:

- **Doping nanostructures is not easy to achieve, but possible**. The insertion of impurities in Silicon nanostructures in both nanocrystals and nanowires is difficult. In particular the Formation Energy

(FE) (Sec. 4.2) carries the information that **codoping** is easier to realize with respect to single doping; when two impurities are simultaneously present, due to the charge compensation between the B and P dopants, in both nanocrystals and nanowires the FE assumes negative values that means an increase in the stability of the codoped system. Single doping depends strongly by the systems dimensions since the FE decrease with the size, thus is more difficult to single dope small nanostructure than the bigger one. Moreover, the most favorable positions for the two impurities (here Boron and Phosphorus) have been demonstrated to be the substitutional sites in the first Silicon layer below the surface, both for the nanocrystals and the nanowires.

- **Silicon nanocrystals**: due to the charge compensation the codoping reveals to be almost independent by the nanocrystals size; moreover the stability increases when the impurities are closer each other such as second neighbors, in order to increase their Coulomb interaction;
- **multi-doped nanocrystals**: inserting more impurities, thus augmenting the concentration of dopants within the same nanocrystal lowers more the FE, thus increasing the stability of the multi-doped nanocrystals. This should be related to a variation in the screening between the embedded dopants that can increase their mutual interaction. In particular an even number of doped compensated impurities leads always to the minor and more negative value of FE.

- **Electronic Properties can be tuned from the corresponding undoped structures counterparts.** The simultaneously insertion of compensated donor and acceptor impurities such as Boron and Phosphorus gives rise to the formation of new bound electronic impurity states near the band edge, both in nanocrystals than in nanowires which deeply alter the overall electronic structure with respect the corresponding undoped system.

  - the energy gap is direct at the Γ k-point and it is strongly reduced by the new impurity levels. The energy gap can be tuned just playing with the distance between impurities: in same the biggest nanocrystals it shrinks as the B-P distance augments, also below the undoped nc value and the bulk Si band gap.
  - the energy gap of codoped nanocrystals and nanowires is rigid shifted toward lower energies with respect to the undoped counterparts; nevertheless, it maintain a decreasing trend with the enlarging of the size, approaching to the bulk limit.
  - both in nanocrystals and nanowires, there is a strong localization of HOMO and LUMO orbitals on the impurity sites: HOMO is

focused on the Boron site, while the LUMO is centered on the Phosphorus site.

- in nanowires, the simultaneously insertion of B and P in smaller nanowires considered, gives rise to a strong reduction of the direct band gap and to an almost flattening of the band structure around the Γ point;
- in the multi-doped nanocrystals, the addition of more impurities determines as in codoped nc new impurity states around the valence and the conduction edge, with a reduction of the energy gap. Nonetheless as the number of inserted impurities increase the amount of gap shrinking tends almost to saturate toward a constant value.;

- **Promising new optical features close to the experimental outcomes.** The insertion of single impurities gives rise to new intense optical transitions in low energy range, below the absorption edge of the undoped nanocrystals and also below the bulk Silicon band gap limit. Nevertheless these transitions in single doped nanostructures have been demonstrated to be almost dark. Indeed, when two simultaneously compensated impurities are inserted within nanocrystals and nanowires, new "radiative" not-forbidden transition arise in the absorption and emission spectra.

  - Absorption spectra: the IP-RPA calculations show that the absorption edge is strongly lowered with respect to the undoped absorption spectrum both for nanocrystals and nanowires; in particular increasing the size of the system shifts the absorption onset toward lower energies, in particular in the visible energy range. Several states around the gap edge are involved in these transitions. The many body calculations (performed on the smallest nanocrystal and nanowire among the all considered in the study) confirm this trend also with the inclusion of the local field contribution.
  - Emission spectra: it has been proposed an efficient scheme to calculate the emission spectra combining a Constrain DFT approximation with the Green function approach (GW+BSE). For the first time in the emission spectrum is take into account also the electron-hole interaction, thus leading to treat in a rough but realistic way the emission spectrum as an estimation of the photoluminescence. To that the calculation show an intense Stokes shift between emission and absorption: several intense excitonic peaks appear in the low energy part of the emission spectra in the visible range, in really good agreement with the experimen-

tal outcomes of Fujii [36, 37], thus confirming the possibility to achieve light emission by codoping Silicon nanocrystals.

Future Perspective

Considering the conclusions achieved an important preliminary basic step for a deeper investigation on the role of doping to engineer the electronic and optical features of Silicon Nanocrystals and Nanowire, here on the following I present my main expectations for future research outcomes, on many of which theoretical investigation within our group is still begun:

1. to study **radiative and non-radiative lifetime** of the electron-hole pair recombination in codoped Silicon nanocrystals and nanowires from first principle, including also the many-body effects in terms of excitonic hamiltonian and self-energy corrections;

2. to investigate from a first principle approach **gain and stimulated emission** in Silicon nanostructures. For the first time a simple " four level" model will give the possibility to expand book-learning knowledge about the microscopic origin of optical gain in Silicon Nanocrystal, expanding the investigation also to nanowires and to codoped Si-based nanostructures;

3. to study **codoped Silicon nanostructures embedded in a Silicon Dioxide** (SiO_2) matrix, thus approaching the simulation to the experimental systems setup;

4. to include in the study of codoped Silicon nanowire the **effects of the wire-wire interaction** as yet done for undoped Si nanowire, in order to better simulate the interconnected structure of nanowires by which the Porous Silicon is made up and that contain impurities introduced during the hydrofluoric acid etching process.

Federico Iori
Modena, 6 Novembre 2007

EUROPEAN CURRICULUM VITAE FORMAT

PERSONAL INFORMATION

Name	**FEDERICO IORI**
Address	**VIA IMOLA N° 33 – 41100 MODENA- ITALY**
Telephone	**+39 059 2055283 office - +39 059 302274 home**
Fax	**+39 059 374794 office**
E-mail	**iori.federico@unimore.it**
Nationality	ITALIAN
Date of birth	29 / 10/ 1979

EDUCATION AND TRAINING

• From January 2005 Up tp December 2007	**PhD student**
• Name and type of organisation providing education and training	Departement of Physics – INFM –CNR and National Center on nanoStructures and bioSystem at Surface S3 - University of Modena and Reggio Emilia
• Principal subjects	PhD thesis on electronic and optical properties of doped Silicon Nanostructures. Advisor: Prof. Stefano Ossicini

For more information go to
www.cedefop.eu.int/transparency
www.europa.eu.int/comm/education/index_en.html
www.eurescv-search.com

• July 2004 — **Degree in Physics**

• Name and type of organisation providing education and training: University of Modena and Reggio Emilia

• Principal subjects: Degree thesis title:
"Ab initio calculations of ground and excited states of silicon nanocrystals"

Advisor Prof. Stefano Ossicini

• July 1998 — **High School Scientific Diploma**

• Name and type of organisation providing education and training: Scientific Lycee "Alessandro Tassoni"
Modena

• Principal subjects: Maths, physics, natural science, chemistry, latin, Italian and English litterature

PERSONAL SKILLS AND COMPETENCES

MOTHER TONGUE: **ITALIAN**

OTHER LANGUAGES

ENGLISH

• Reading skills: GOOD
• Writing skills: GOOD
• Verbal skills: GOOD

FRENCH

• Reading skills: GOOD
• Writing skills: ELEMENTARY – NEED A PROPER COURSE
• Verbal skills: GOOD

For more information go to
www.cedefop.eu.int/transparency
www.europa.eu.int/comm/education/index_en.html
www.eurescv-search.com

PHD COMPETENCES

I work on *ab initio* simulations of isolated systems like silicon nanocrystals and nanowires at the nanoscale. Aim of my research is to understand which mechanisms govern the absorption and the emission of light from these nanostructures leading to the possibility to achieve visible amplified light from them for optoelectronic applications. The main idea is to study the role play by simultaneously doping with boron and phosphorus on the electronic structure and on absorption and emission features of the nanocrystals and nanowires. The theoretical investigation on the electronic and ground state properties has been realized within the Density Functional Theory scheme, using ab initio plane wave pseudopotential codes. Moreover to evaluate the optical response of the systems I've taken the advantage of numerical codes that permits to calculate absorption and emission spectra going beyond the single particle approach using a many body framework thus taking into account interaction between electrons and holes at the same time.

Knowledge of different *Plane wave pseudopotential abinitio codes:*

- Espresso Quantum package (PWscf)
- Abinit
- VASP

Knowledge of code for theoretical spectroscopy:

- SELF code
- DP code
- EXC code

Knowledge of Fortran 90 – Latex - Linux main scientific tools

For more information go to
www.cedefop.eu.int/transparency
www.europa.eu.int/comm/education/index_en.html
www.eurescv-search.com

PHD TRAINING PROGRAMM

Courses from 2005 – 2007

a. Strong Correlated Paradigm of Electronic Levels in Solids (Dr. Rontani)

b. Electronic properties of Solids (Dott. Guido Goldoni)

c. Conduct and Misconduct in Sciences (Prof. Stefano Ossicini)

d. Many Body Theory course (Prof. Franca Manghi)

e. Introduction to Montecarlo Theory (Prof. Carlo Jacoboni)

f. Focus group on:

- Nanofriction and tribology (Dr. Andrea Vanossi)
- Scanning probe microscopy (Prof. M. Affronte- A. Alessandrini)
- Many body theory (GW approximation, TDDFT) (Dr. E. Chang – Dr. C.A. Rozzi)
- Electronic and Optoelectronic properties of solids (Prof. Lorenzo Pavesi)
- X-rays Photoemission Spectroscopies (Prof. Petra Rudolf)

TEACHING EXPERIENCE

Teaching assistant on Mathematical Methods for Physicist class exercises – 2005-2007

For more information go to
www.cedefop.eu.int/transparency
www.europa.eu.int/comm/education/index_en.html
www.eurescv-search.com

SCHOOLS

- Electronic excitations and spectroscopies : Theory and Codes Laboratoire des Solides Irradies – Ecole Ploytechnique Palaiseau – Paris Cedex, March 2006
- Summer School on Parallel Calculation, High Performance Computation division, CINECA, -Bologna (Italy) , September 5-16, 2005
- Summer School on Computational Materials Science, Materials and Computation Center, University of Illinois, Urbana-Champaign (US) June 13–23, 2005.

CONFERENCES

Poster presentation:

- Nanoquanta Young Researchers' Meeting (Donostia, May 15-18 2007)
"Novel Optoelectronic Properties of Simultaneously n- and p- doped Silicon Nanostructures"

- 13th Total Energy Workshop (Trieste, January 10-13, 2007)
"Optical spectra of Doped Silicon Nanocrystals"

Oral presentation:

- The E-MRS 2007 Spring Meeting (Strasbourg, May 28 - June 1, 2007)
"Novel Optoelectronic Properties of Simultaneously n- and p- doped Silicon Nanostructures"

- 11th NanoQuanta WorkShop Meeting (Houffalize, September 18-24, 2006)
"Optical spectra of doped Silicon Nanocrystals"

- NanoQuanta Young Researchers' Meeting (Rome, May 3-8, 2006)
"The Nano Doped: Electronic and optical properties of Single and Codoped Silicon Nanocrystals"

VISITS AND EXCHANGE

1) Marie Curie Fellowship
from January 2006 to April 2006:

Laboratoire des Solides Irradies - Ecole Polytechnique (Palaiseau) advisor Lucia Reining and Christine Giorgetti - abinitio studies of the electronic and optical properties of graphite;

2) Galileo Programm for Cooperation between Italy and France
Visiting period June 2007:

Laboratoire des Solides Irradies - Ecole Polytechnique (Palaiseau) advisor Lucia Reining and Christine Giorgetti - theoretical spectroscopy of graphite and graphite-like systems with different interplanar stacking;

For more information go to
www.cedefop.eu.int/transparency
www.europa.eu.int/comm/education/index_en.html
www.eurescv-search.com

Full list of publications

1. Federico Iori, Elena Degoli Maurizia Palummo and Stefano Ossicini, *Novel Optoelectronic Properties of Simultaneously n- and p- doped Silicon Nanostructures*, Superlattices and Microstructures (2007) - in press

2. R. Magri, E. Degoli, Federico Iori, E. Luppi, O. Pulci, S. Ossicini, G. Cantele, F. Trani, D. Ninno, *Role of surface passivation and doping in Silicon Nanocrystals*, Journal of Computational Methods in Science and Engineering (2007) - to be published

3. Federico Iori, Elena Degoli, Rita Magri, Ivan Marri, G. Cantele, D. Ninno, F. Trani, O. Pulci, Stefano Ossicini, *Engineering Silicon Nanocrystals: Effect of Codoping with Boron and Phosphorus*, Physical Review B **76**, 085302 (2007)

4. Luppi Eleonora, Iori Federico, Magri Rita, Pulci Olivia Ossicini Stefano, Degoli Elena, Olevano Valerio, *Excitons in silicon nanocrystallites: The nature of luminescence*, Physical Review B **75**, 033303 (2007)

5. Stefano Ossicini, E. Degoli, Federico Iori, O. Pulci, G. Cantele, R. Magri, O. Bisi, F. Trani, D. Ninno, *Doping in Silicon Nanocryslals*, Surface Science **601**, 2724-2729 (2007)

6. Stefano Ossicini, O. Bisi, Elena Degoli, I. Marri, Federico Iori, Eleonora Luppi, Rita Magri, Raffaele Poli, G. Cantele, D. Ninno, F. Trani, M . Marsili, O. Pulci, M. Gatti, K. Gaal-Nagy, A. Incze, G. Onida, V. Olevano, *First Principle Study of Silicon Nanocrystals: Structural and Electronic Properties, Abosprtion, Emission and Doping*, Journal of Nanoscience and Nanotechnology **10**, 1-14 (2007)

7. Federico Iori, Stefano Ossicini, E. Degoli, E. Luppi, R. Poli, R. Magri, G. Cantele, F. Trani, D. Ninno, *Doping in Silicon nanostructures*, physica status solidi (a) **204** No. 5, 1312-1317 (2007)

8. Federico Iori, Elena Degoli, Eleonora Luppi, Rita Magri, Ivan Marri, G. Cantele, D. Ninno, F. Trani, and Stefano Ossicini, *Doping in Silicon nanocrystals: an ab-initio study of the structural, electronic and optical properties*, Journal of Luminescence **121**, 335-339 (2006)

9. Stefano Ossicini, Federico Iori, Elena Degoli, Eleonora Luppi, Rita Magri, G. Cantele, F. Trani, and D. Ninno, *Understanding Doping in Silicon Nanostructures* Journal of Selected Topics in Quantum Electronics **12** No 6, 1585 (2006)

10. Stefano Ossicini, Federico Iori, E. Degoli, E. Luppi, R. Magri, G. Cantele, F. Trani, D. Ninno *Simultaneously B- and P-doped Silicon Nanoclusters: Formation Energies and Electronic Properties* Applied Physics Letters **87**, 173120 (2005)

11. S. Ossicini, Federico Iori, E. Degoli, E. Luppi, R. Magri, G. Cantele, F. Trani, and D. Ninno, *P and B single- and co-doped Silicon Nanocrystals: Formation and Activation Energies, Electronic and Optical Properties*, IEEE (Catalog Number 05EX1053) Group IV Photonics, P3 (2005) 1-3.

12. Stefano Ossicini, O. Bisi, G. Cantele, E. Degoli, R. Del Sole, M. Gatti, A. Incze, Federico Iori, E. Luppi, R. Magri, D. Ninno, G.Onida,O.Pulci, *Ab-initio Calculations Of The Electronic Properties of Hydrogenated and Oxidized Silicon Nanocrystals: Ground and Excited States*, Proceedings del XVII Congresso AIV-17, 277-282 (2005).

13. S.Ossicini, E. Degoli, E. Luppi, R. Magri, Federico Iori, G. Cantele, D. Ninno, *The structural, electronic and optical properties of silicon nanoclusters: effect of size, doping and surface passivation*, Science and Supercomputing at Cineca - Report 2005 ISBN 88-86037-16-3 Editors: Marco Voli, Patrizia Coluccia CINECA Printed by: Monograf s.r.l

Bibliography

Bibliography

[1] *Semiconductor Silicon: The Extraodindary Made Ordinary*, volume 22 of *MRS Bulletin*, MRS Bulletin, 1997.

[2] R. Kirchain and L. Kimerling, A roadmap for nanophotonics, Nat Photon **1**(6), 303–305 (2007).

[3] L. Kimerling, Silicon Microphotonics, App. Surf. Science **159-160**, 8–13 (200).

[4] A. Irace, G. Coppola, G. Breglio, and A. Cutolo, Fast silicon-on-silicon optoelectronic router based on a BMFET device, Selected Topics in Quantum Electronics, IEEE Journal of **6**, 14 (2000).

[5] B. Li, Z. Jiang, X. Zhang, X. Wang, J. Wan, G. Li, and E. Liu, SiGe/Si Mach–Zehnder interferometer modulator based on the plasma dispersion effect, Applied Physics Letters **74**(15), 2108–2109 (1999).

[6] S. M. Cstak, J. D. Schaub, W. E. Wu, and J. C. Campbell, High-speed monolithically integrated silicon optical receiver.

[7] G. Masini, L. Colace, and G. Assanto, Si based optoelectronics for communications.

[8] S. Winnerl, D. Buca, S. Lenk, C. Buchal, S. Mantl, and D.-X. Xu, MBE grown Si/SiGe undulating layer superlattices for infrared light detection.

[9] S. Ossicini, L. Pavesi, and F. Priolo, *Light Emitting Silicon for Microphotonics*, volume 194 of *Monograph Springer Tracts in Modern Physics*, Springer-Berlin, 2003.

[10] *Silicon Photonics*, Springer Tracts in Modern Physics, Springer Verlag, New York, 2004, 2003.

[11] L. T. Canham, Silicon quantum wire array fabrication by electrochemical and chemical dissolution of wafer, Appl. Phys. Lett. **57**, 1045–1048 (1990).

[12] O. Bisi, S. Ossicini, and L. Pavesi, Porous silicon: a quantum sponge structure for silicon based optoelectronics, Surf. Sci. Rep. (Netherlands) **38**, 1–126 (2000).

[13] A. G. Cullis and L. T. Canham, Visible light emission due to quantum size effects in highly porous crystalline silicon, Nature **353**(6342), 335–338 (1991).

[14] P. D. J. Calcott, K. J. Nash, L. T. Canham, M. J. Kane, and D. Brumhead, Identifications of radiative transitions in highly porous silicon, J. Phys. Condens. Matter. **5**, L91–L98 (1993).

[15] L. Pavesi, L. D. Negro, C. Mazzoleni, G. Franzò, and F. Priolo, Optical gain in silicon nanocrystals, Nature (London) **408**, 440–444 (Nov. 2000).

[16] C. Garcia, B. Garrido, P. Pellegrino, R. Ferre, J. A. Moreno, J. R. Morante, L. Pavesi, and M. Cazzanelli, Size dependence of lifetime and absorption cross section of Si nanocrystals embedded in SiO_2, Appl. Phys. Lett. **82**(10), 1595–1597 (Mar. 2003).

[17] L. D. Negro, M. Cazzanelli, L. Pavesi, S. Ossicini, D. Pacifici, G. Franzò, F. Priolo, and F. Iacona, Dynamics of stimulated emission in silicon nanocrystals, Appl. Phys. Lett. **82**(26), 4636–4638 (June 2003).

[18] *Towards the first silicon laser*, NATO Science Series, Kluwer Academic Publishers, Dordrecht 2003, 2003.

[19] Y. Kanemitsu, K. Suzuki, H. Uto, Y. Masumoto, T. Matsumoto, S. Kyushin, K. Higuchi, and H. Matsumoto, Visible photoluminescence of silicon-based nanostructures: Porous silicon and small silicon-based clusters, Appl. Phys. Lett. **61**(20), 2446–2448 (Nov. 1992).

[20] G. Allan, C. Delerue, and M. Lannoo, Theory of optical properties of polysilanes:Comparison with porous silicon, Phys. Rev. B **48**(11), 7951–7959 (Sept. 1993).

[21] W. Wilson, P. F. Szajowski, and L. E. Brus, Quantum confinement in size-selected, surface-oxidized silicon nanocrystals, Science **262**(5137), 1242–1244 (Nov. 1993).

[22] Z. H. Lu, D. J. Lockwood, and J. Baribeau, Quantum confinement and light emission in SiO_2/Si superlattices, Nature (London) **378**, 258–260 (1996).

[23] J. Ruan, P. M. Fauchet, L. D. Negro, M. Cazzanelli, and L. Pavesi, Stimulated emission in nanocrystalline silicon superlattice, Appl. Phys. Lett. **83**(26), 5479–5481 (Dec. 2003).

[24] A. G. Nassiopoulos, S. Grigoropoulos, and D. Papadimitriou, Electroluminescent device based on silicon nanopillars, Appl. Phys. Lett. **69**(15), 2267–2269 (1996).

[25] J. Johnson, H. Yan, R. Schaller, L. Haber, R. Saykally, and P. Yang, Single Nanowire Lasers, Journal of Physical Chemistry B **105**(46), 11387–11390 (2001).

[26] X. D. Cui, A. Primak, X. Zarate, J. Tomfohr, O. F. Sankey, A. L. Moore, T. A. Moore, D. Gust, G. Harris, and S. M. Lindsay, Reproducible Measurement of Single-Molecule Conductivity, Science **294**(5542), 571–574 (Oct. 2001).

[27] Y. Cui, Z. Zhong, D. Wang, W. Wang, and C. Lieber, High Performance Silicon Nanowire Field Effect Transistors, Nano Letters **3**(2), 149–152 (2003).

[28] C. Delerue, G. Allan, and M. Lannoo, Electron-phonon coupling and optical transitions for indirect-gap semiconductor nanocrystals, Phys. Rev. B **64**(19), 193402 (Oct 2001).

[29] S. Ossicini, O. Bisi, G. Cantele, E. Degoli, R. D. Sole, M. Gatti, A. Incze, F. Iori, E. Luppi, R. Magri, D. Ninno, G. Onida, and O.Pulci, Ab-initio Calculations Of The Electronic Properties of Hydrogenated and Oxidized Silicon Nanocrystrals: Ground and Excited States, in *Proceedings del XVII Congresso AIV-17*, pages 277–282, 2005.

[30] C. Delerue, G. Allan, and M. Lannoo, Dimensionality-Dependent Self-Energy Corrections and Exchange-Correlation Potential in Semiconductor Nanostructures, Phys. Rev. Lett. **90**(7), 076803 (Feb. 2003).

[31] J. C. Vial, A. Bsiesy, F. Gaspard, R. Hérino, M. Ligeon, F. Muller, R. Romestain, and R. M. Macfarlane, Mechanisms of visible-light emission from electro-oxidized porous silicon, Phys. Rev. B **45**(24), 14171–14176 (Jun 1992).

[32] S. Takeoka, M. Fujii, S. Hayashi, K. Yamamoto, and K. Toshikiyo, Control of photoluminescence energy of Si nanocrystals by Ge doping, Journal of Luminescence **87-89**, 350–352 (May 2000).

[33] M. Fujii, S. Hayashi, and K. Yamamoto, Photoluminescence from B-doped Si nanocrystals, Journal of Applied Physics **83**(12), 7953–7957 (1998).

[34] Y. Cui and C. M. Lieber, Functional Nanoscale Electronic Devices Assembled Using Silicon Nanowire Building Blocks, Science **291**(5505), 851–853 (2001).

[35] D. D. D. Ma, C. S. Lee, F. C. K. Au, S. Y. Tong, and S. T. Lee, Small-Diameter Silicon Nanowire Surfaces, Science **299**(5614), 1874–1877 (2003).

[36] M. Fujii, Y. Yamaguchi, Y. T. K. Ninomiya, and S. Hayashi, Control of photoluminescence properties of Si nanocrystals by simultaneously doping n- and p-type impurities, Appl. Phys. Lett. **85**(7), 1158–1160 (2004).

[37] M. Fujii, Y. Yamaguchi, Y. Takase, K. Ninomiya, and S. Hayashi, Photoluminescence from impurity codoped and compensated Si nanocrystals, Applied Physics Letters **87**(21), 211919 (2005).

[38] M. Fujii, K. Toshikiyo, Y. Takase, Y. Yamaguchi, and S. Hayashi, Below bulk-band-gap photoluminescence at room temperature from heavily P- and B-doped Si nanocrystals, Journal of Applied Physics **94**(3), 1990–1995 (2003).

[39] D. Kovalev, H. Heckler, G. Polisski, and F. Koch, Optical Properties of Si Nanocrystals, Phys. Status Solidi B **215**, 871–932 (1999).

[40] M. Fujii, A. Mimura, S. Hayashi, and K. Yamamoto, Photoluminescence from Si nanocrystals dispersed in phosphosilicate glass thin films: Improvement of photoluminescence efficiency, Applied Physics Letters **75**(2), 184–186 (1999).

[41] A. Mimura, M. Fujii, S. Hayashi, D. Kovalev, and F. Koch, Photoluminescence and free-electron absorption in heavily phosphorus-doped Si nanocrystals, Phys. Rev. B **62**(19), 12625–12627 (Nov 2000).

[42] M.-V. Fernandez-Serra, C. Adessi, and X. Blase, Conductance, Surface Traps, and Passivation in Doped Silicon Nanowires, Nano Letters **6**(12), 2674–2678 (2006).

[43] H. Peelaers, B. Partoens, and F. Peeters, Formation and Segregation Energies of B and P Doped and BP Codoped Silicon Nanowires, Nano Letters **6**(12), 2781–2784 (2006).

[44] E. Degoli, G. Cantele, E. Luppi, R. Magri, D. Ninno, O. Bisi, and S. Ossicini, Ab initio structural and electronic properties of hydrogenated silicon nanoclusters in the ground and excited state, Physical Review B (Condensed Matter and Materials Physics) **69**(15), 155411 (2004).

[45] L. E. Ramos, J. Furthmüller, and F. Bechstedt, Reduce influence of defects on oxidized Si nanocrystallites, Phys. Rev. B **71**(3), 035328 (Jan. 2005).

[46] H.-C. Weissker, J. Furthmüller, and F. Bechstedt, Calculation of optical properties and density of states for systems with huge unit cells, Phys. Rev. B **64**(3), 035105 (July 2001).

[47] H.-C. Weissker, J. Furthmüller, and F. Bechstedt, Structural relaxation in Si and Ge nanocrystallites: Influence on the electronic and optical properties, Phys. Rev. B **67**(24), 245304 (2003).

[48] A. J. Williamson, J. C. Grossman, R. Q. Hood, A. Puzder, and G. Galli, Quantum Monte Carlo Calculations of Nanostructure Optical Gaps: Applications to Silicon Quantum Dots, Phys. Rev. Lett. **89**(19), 196803 (Nov. 2002).

[49] J. R. Chelikowsky, L. Kronik, and I. Vasiliev, Time-dependent dentity-functional calculations for the optical spectra of molecules,clusters, and nanocrystals, J. Phys. Condens. Matter. **15**, R1517–R1547 (Aug. 2003).

[50] D. V. Melnikov and J. R. Chelikowsky, Electron affinities and ionization energies in Si and Ge nanocrystals, Phys. Rev. B **69**(11), 113305 (Mar. 2004).

[51] S. Öğüt, J. R. Chelikowsky, and S. G. Louie, Quantum Confinement and Optical Gaps in Si Nanocrystals, Phys. Rev. Lett. **79**(9), 1770–1773 (Sept. 1997).

[52] G. Allan, C. Delerue, and M. Lannoo, Nature of Luminescent Surface States of Semiconductor Nanocrystallites, Phys. Rev. Lett. **76**(16), 2961–2964 (Apr. 1996).

[53] J. P. Proot, C. Delerue, and G. Allan, Electronic structure and optical properties of silicon crystallites: application to porous silicon, Appl. Phys. Lett. **61**(16), 1948–1950 (Appl. Phys. Lett.).

[54] C. Delerue, G. Allan, and M. Lannoo, Theoretical aspects of the luminescence of porous silicon, Phys. Rev. B **48**(15), 11024–11036 (Oct. 1993).

[55] N. Daldosso, M. Luppi, G. Dalba, L. Pavesi, F. Rocca, F. Priolo, G. Franzò, F. Iacona, E. Degoli, R. Magri, and S. Ossicini, Experimental and Theoretical Joint Study on the Electronic and Structural Properties of Silicon Nanocrystals Embedded in SiO_2: Active Role of the Interface Region, in *Optoelectronics of Group-IV-Based Materials*, edited by T.Gregorkiewicz, R. G. Elliman, P. M. Fauchet, and J. A. Hutchby, volume 770 of *Mat. Res. Soc. Symp. Proc.*, pages I6.1.1–I6.1.5, MRS, 2003.

[56] N. Daldosso, M. Luppi, S. Ossicini, E. Degoli, R. Magri, G. Dalba, P. Fornasini, R. Grisenti, F. Rocca, L. Pavesi, S. Boninelli, F. Priolo, C. Spinella, and F. Iacona, Role of the interace region on the optoelectronic properties of silicon nanocrystals embedded in SiO_2, Phys. Rev. B **68**(8), 085327 (Aug. 2003).

[57] E. Luppi, F. Iori, R. Magri, O. Pulci, S. Ossicini, E. Degoli, and V. Olevano, Excitons in silicon nanocrystallites: The nature of luminescence, Physical Review B (Condensed Matter and Materials Physics) **75**(3), 033303 (2007).

[58] M. Born and J.M. Oppenheimer, *Ann. Physik* 84, 457 (1927).

[59] D. R. Hartree, *Proc. Cambridge Philos.* 24, 89 (1928).

[60] V. Fock, *Z. Phys.* 61, 126 (1930).

[61] G. D. Mahan, *Many-particle physics*, Plenum, New York, 1981.

[62] L.H. Thomas, *Proc. Cambridge Philos.* 23, 542 (1927).

[63] E. Fermi, *Z. Phys.* 48, 73 (1928).

[64] P. A. M. Dirac, *Proc. Cambridge Philos.* 26, 376 (1930).

[65] P. Hohenberg and W. Kohn, Inhomogeneus Electron Gas, Phys. Rev. **136**(3B), B864–B871 (Nov. 1964).

[66] W. Kohn and L. J. Sham, Self-Consistent Equations Including Exchange and Correlation Effects, Phys. Rev. **140**(4A), A1133–A1138 (Nov. 1965).

[67] R. M. Dreizler and E. K. U. Gross, *Density Functional Theory: An Approach to the Quantum Many-Body Problem*, Springer, 1990.

[68] A. L. Fetter and J. D. Walecka, *Quantum theory of many-particle systems*, McGraw-Hill, New York, 1971.

[69] R. W. Godby and P. García-González, Density Functional Theories and Self-energy Approaches, in *A Primer in Density Functional Theory*, edited by C. Fiolhais, F. Nogueira, and M. Marques, Lecture Notes in Physics, Springer-Verlag, 2003.

[70] W. Kohn, Nobel Lecture: Electronic structure of matterwave functions and density functionals, Rev. Mod. Phys. **71**(5), 1253–1266 (Oct. 1999).

[71] D. M. Ceperley and B. J. Alder, Ground State of the Electron Gas by a Stochastic Method, Phys. Rev. Lett. **45**(7), 566–569 (Aug 1980).

[72] J. Jung, P. Garcia-Gonzalez, J. E. Alvarellos, and R. W. Godby, Assessment of density-functional approximations: Long-range correlations and self-interaction effects, Phys. Rev. A **69**(5), 052501 (May 2004).

[73] S. Ossicini and C. M. Bertoni, Density-functional calculation of atomic structure with nonlocal exchange and correlation, Phys. Rev. A **31**(6), 3550–3556 (Jun 1985).

[74] J. P. Perdew, K. Burke, and M. Ernzerhof, Generalized Gradient Approximation Made Simple, Phys. Rev. Lett. **77**(18), 3865–3868 (Oct. 1996).

[75] C. A. Ullrich, U. J. Gossmann, and E. K. U. Gross, Time-dependent optimized effective potential, Phys. Rev. Lett. **74**(6), 872–875 (Feb. 1995).

[76] E. Engel, Orbital-Dependent Functionals for the Exchange-Correlation Energy: A Third Generation of Density Functionals, in *A Primer in Density Functional Theory*, edited by C. Fiolhais, F. Nogueira, and M. Marques, Lecture Notes in Physics, Springer-Verlag, 2003.

[77] G. E. Engel, Linear Response and the Exchange-Correlation Hole within a Screened-Exchange Density Functional Theory, Phys. Rev. Lett. **78**(18), 3515–3518 (Aug. 1997).

[78] S. Kummel and J. P. Perdew, Simple Iterative Construction of the Optimized Effective Potential for Orbital Functionals, Including Exact Exchange, Phys. Rev. Lett. **90**(4), 043004 (Jan. 2003).

[79] J. P. Perdew and A. Zunger, Self-interaction correction to density-functional approximations for many-electron systems, Phys. Rev. B **23**(10), 5048–5079 (May 1981).

[80] U. von Barth and L. Hedin, A local exchange-correlation potential for the spin polarized case. i, Journal of Physics C: Solid State Physics **5**(13), 1629–1642 (1972).

[81] O. Gunnarsson and B. I. Lundqvist, Exchange and correlation in atoms, molecules, and solids by the spin-density-functional formalism, Phys. Rev. B **13**(10), 4274–4298 (May 1976).

[82] J. P. Perdew and S. Kurth, Density Functionals for Non-relativistic Coulomb Systems in the New Century, in *A Primer in Density Functional Theory*, edited by C. Fiolhais, F. Nogueira, and M. Marques, Lecture Notes in Physics, Springer-Verlag, 2003.

[83] M. Levy and J. P. Perdew, Hellmann-Feynman, virial, and scaling requisites for the exact universal density functionals. Shape of the correlation potential and diamagnetic susceptibility for atoms, Phys. Rev. A **32**(4), 2010–2021 (Oct 1985).

[84] S.-K. Ma and K. A. Brueckner, Correlation Energy of an Electron Gas with a Slowly Varying High Density, Phys. Rev. **165**(1), 18–31 (Jan 1968).

[85] J. P. Perdew, K. Burke, and Y. Wang, Generalized gradient approximation for the exchange-correlation hole of a many-electron system, Phys. Rev. B **54**(23), 16533–16539 (Dec 1996).

[86] T. Koopmans, *Physica* 1, 104 (1933).

[87] J. F. Janak, *Phys. Rev. B* 18, 7165 (1978).

[88] C.-O.Almbladth and U. von Barth, Exact results for the charge and spin densities, exchange-correlations potentials, and density-functional eigenvalues, Phys. Rev. B **31**(6), 3231–3244 (1985).

[89] J. P. Perdew and M. Levy, Physical Content of the Exact Kohn-Sham Orbital Energies: Band Gap and Derivative Discontinuities, Phys. Rev. Lett. **51**(20), 1884–1887 (1983).

[90] L. S. Sham and M. Schlüter, Density Functional Theory of the Energy Gap, Phys. Rev. Lett. **51**(20), 1888–1891 (Nov. 1983).

[91] J. P. Perdew, R. G. Parr, M. Levy, and J. L. Balduz, Density-functional theory for fractional particle number: derivative discontinuities of the energy, Phys. Rev. B **49**(23), 1691–1694 (Dec. 1982).

[92] L. J. Sham and M. Schlüter, Density-functional theory for the band gap, Phys. Rev. B **32**(6), 3883–3889 (Sept. 1985).

[93] M. S. Hybertsen and S. G. Louie, First-Principles Theory of Quasiparticles: Calculation of Band Gaps in Semiconductor and Insulators, Phys. Rev. Lett. **55**(13), 1418–1421 (Sept. 1985).

[94] M. S. Hybertsen and S. G. Louie, Electron correlation and the band gap in ionic crystals, Phys. Rev. B **32**(10), 7005–7008 (Nov. 1985).

[95] M. S. Hybertsen and S. G. Louie, Erratum: Electron correlation and the band gap in ionic crystals, Phys. Rev. B **35**(17), 9308 (June 1987).

[96] W. Ku and A. G. Eguiluz, Band-Gap Problem in Semiconductors Revisited: Effects of Core States and Many-Body Self-Consistency, Phys. Rev. Lett. **89**(12), 126401 (Sept. 2002).

[97] M. S. Hybertsen and S. G. Louie, Electron correlation in semiconductors and insulators: Band gaps and quasiparticle energies, Phys. Rev. B **34**(8), 5390–5413 (Oct. 1986).

[98] Landolt and Bornstein, *Zahlenwerte und Funktionen aus Naturwissenschaften und Technik, in Vol. III of Landolt-Bornstein*, Springer, New York, 1982.

[99] B. B. G. Baldini, Optical Properties of Na and Li Halide Crystals at 55° K, Phys. Status Solidi B **38**(1), 325.

[100] R. W. Godby, M. Schlüter, and L. J. Sham, Accurate Exchange-Correlation Potential for Silicon and Its Discontinuity on Addition of an Electron, Phys. Rev. Lett. **56**(22), 2415–2418 (June 1986).

[101] R. W. Godby, M. Schlüter, and L. J. Sham, Self-energy operators and exchange-correlation potentials in semiconductors, Phys. Rev. B **37**(17), 10159–10175 (June 1988).

[102] R. W. Godby, M. Schlüter, and L. J. Sham, Quasiparticle energies in GaAs and AlAs, Phys. Rev. B **35**(8), 4170–4171 (Mar 1987).

[103] M. C. Payne, M. P. Teter, D. C. Allan, T. A. Arias, and J. D. Joannopoulos, Iterative minimization techniques for ab initio total-energy calculations: molecular dynamics and conjucate gradients, Rev. Mod. Phys. **64**(4), 1045–1097 (Oct. 1992).

[104] W. E. Pickett, Pseudopotential Methods in Condensed Matter Applications, Comp. Phys. Rep. **9**, 115.

[105] D. J. Chadi and M. L. Cohen, Special Points in the Brillouin Zone, Phys. Rev. B **8**(12), 5747–5753 (Dec 1973).

[106] H. J. Monkhorst and J. D. Pack, Special points for Brillouin-zone integrations, Phys. Rev. B **13**(12), 5188–5192 (June 1976).

[107] E. Fermi, *Il Nuovo Cimento*11, 157 (1934).

[108] J. C. Phillips and L. Kleinman, New Method for Calculating Wave Functions in Crystals and Molecules, Phys. Rev. **116**(2), 287–294 (Oct 1959).

[109] C. Herring, A New Method for Calculating Wave Functions in Crystals, Phys. Rev. **57**(12), 1169–1177 (Jun 1940).

[110] W. C. Topp and J. J. Hopfield, Chemically Motivated Pseudopotential for Sodium, Phys. Rev. B **7**(4), 1295–1303 (Feb 1973).

[111] D. R. Hamann, M. Schlüter, and C. Chiang, Norm-Conserving Pseudopotentials, Phys. Rev. Lett. **43**(20), 1494–1497 (Nov 1979).

[112] G. B. Bachelet, D. R. Hamann, and M. Schluter, Pseudopotentials that work: From H to Pu, Phys. Rev. B **26**(8), 4199–4228 (Oct. 1982).

[113] D. Vanderbilt, Soft self-consistent pseudopotentials in a generalized eigenvalue formalism, Phys. Rev. B **41**(11), R7892–R7895 (Apr. 1990).

[114] R. O. Jones and O. Gunnarsson, The density functional formalism, its applications and prospects, Rev. Mod. Phys. **61**(3), 689–746 (July 1989).

[115] R. W. Godby and I. D. White, Density-Relaxation Part of the Self-Energy, Phys. Rev. Lett. **80**(14), 3161–3161 (Apr. 1998).

[116] A. Franceschetti and S. T. Pantelides, Excited-state relaxations and Frank-Condon shift in Si quantum dots, Phys. Rev. B **68**(03), 033313 (July 2003).

[117] A. Puzder, A. J. Williamson, J. C. Grossman, and G. Galli, Computational Studies of the Optical Emission of Silicon Nanocrystals, J. Am. Chem. Soc. **125**, 2786–2791 (2003).

[118] F. Mauri and R. Car, Firts-Principles Study of Excitonic Self-Trapping in Diamond, Phys. Rev. Lett. **75**(17), 3166–3169 (1995).

[119] H.-C. Weissker, J. Furthmüller, and F. Bechstedt, Excitation Energies and Radiative Lifetimes of $Ge_{1-x}Si_x$ Nanocrystals: Alloying Versus Confinement Effects, Phys. Rev. Lett. **90**(8), 085501 (Feb 2003).

[120] F. Iori, E. Degoli, R. Magri, I. Marri, G. Cantele, D. Ninno, F. Trani, O. Pulci, and S. Ossicini, Engineering silicon nanocrystals: Theoretical study of the effect of codoping with boron and phosphorus, Physical Review B (Condensed Matter and Materials Physics) **76**(8), 085302 (2007).

[121] A. F. Starace, Length and Velocity Formulas in Approximate Oscillator-Strength Calculations, Phys. Rev. A **3**(4), 1242–1245 (Apr. 1971).

[122] R. D. Sole and R. Girlanda, Optical properties of semiconductors within the indipendent-quasiparticle approximation, Phys. Rev. B **48**(16), 11789–11795 (1993).

[123] J. Tauc, editor, *The Optical Properties of Solids*, 1966.

[124] N. H. R. Kubo, M. Toda, *Statistical Physics II*, volume 31 of *Springer Series in Solid-State Sciences*, Springer-Verlag, 1978.

[125] S. L. Adler, Quantum Theory of the Dielectric Constant in Real Solids, Phys. Rev. **126**(2), 413–420 (Apr. 1962).

[126] N. Wiser, Dielectric Constant with Local Field Effects Included, Phys. Rev. **129**(1), 62–69 (Jan. 1963).

[127] S. Baroni and R. Resta, *A*b Initio calculation of the macroscopic dielectric constant, Phys. Rev. B **33**(10), 7017–7021 (May 1986).

[128] N. E. Brener, Random-phase-approximation dielectric function for diamond, with local field effects included, Phys. Rev. B **12**(4), 1487–1492 (Aug. 1975).

[129] M. S. Hybertsen and S. G. Louie, *Ab initio* static dielectric matrices from the density-functional approach. I. Formulation and application to semiconductors and insulators, Phys. Rev. B **35**(11), 5585–5601 (Apr. 1987).

[130] M. S. Hybertsen and S. G. Louie, *Ab initio* static dielectric matrices from the density-functional approach. II. Calculation of the screening response in diamond, Si, Ge, and LiCl, Phys. Rev. B **35**(11), 5602–5610 (Apr. 1987).

[131] G. Onida, L. Reining, and A. Rubio, Electronic excitations: density-functional versus many-body Green's-function approaches, Rev. Mod. Phys. **74**(2), 601–659 (Apr. 2002).

[132] G. Bussi, Effects of the Electron-Hole Interaction on the Optical Properties of Materials: the Bethe-Salpeter Equation, Phys. Scr. **T109**, 141–151 (2004).

[133] O. V. Dolgov, D. A. Kirzhnits, and E. G. Maksimov, On an admissible sign of the static dielectric function of matter, Rev. Mod. Phys. **53**(1), 81–93 (1981).

[134] F. J. Dyson, The Radiation Theories of Tomonaga, Schwinger, and Feynman, Phys. Rev. **75**(3), 486–502 (Feb 1949).

[135] F. J. Dyson, The S Matrix in Quantum Electrodynamics, Phys. Rev. **75**(11), 1736–1755 (Jun 1949).

[136] G. F. Roach, *Green's Functions. Introductory Theory with Applications*, Van Nostrand Reinhold Co. - London, 1970.

[137] A. E. Taylor and D. C. Clay, *Introduction to Functional Analysis*, Krieger Publ. Co. Malabar - Florida, 1986.

[138] A. S. Kheifets, V. A. Sashin, M. Vos, E. Weigold, and F. Aryasetiawan, Spectral properties of quasiparticles in silicon: A test of many-body theory, Phys. Rev. B **68**(23), 233205 (Dec. 2003).

[139] M. S. Hybertsen and S. G. Louie, Spin-orbit splitting in semiconductors and insulators from the *ab initio* pseudopotential, Phys. Rev. B **34**(4), 2920–2922 (Aug. 1986).

[140] M. M. Rieger and R. W. Godby, Charge density of semiconductors in the GW approximation, Phys. Rev. B **58**(3), 1343–1348 (July 1998).

[141] P. Bokes and R. W. Godby, Conductance and polarization in quantum junctions, Phys. Rev. B **69**(24), 245420 (2004).

[142] P. García-González and R. W. Godby, GW self-energy calculations for surfaces and interfaces, Comput. Phys. Commun. **137**(1), 108–122 (June 2001).

[143] U. von Barth and B. Holm, Self-consistent GW_0 results for the electron gas: Fixed screened potential W_0 within the random-phase approximation, Phys. Rev. B **54**(12), 8411–8419 (Sept. 1996).

[144] B. Holm and U. von Barth, Fully self-consistent GW self-energy of the electron gas, Phys. Rev. B **57**(4), 2108–2117 (jan 1998).

[145] E. L. Shirley, Optimal basis sets for detailed Brillouin-zone integrations, Phys. Rev. B **54**(23), 16464–16469 (Dec. 1996).

[146] E. L. Shirley, Many-body effects on bandwidths in ionic, noble gas, and molecular solids, Phys. Rev. B **58**(15), 9579–9583 (Oct. 1998).

[147] W.-D. Schöne and A. G. Eguiluz, Self-Consistent Calculations of Quasiparticle States in Metals and Semiconductors, Phys. Rev. Lett. **81**(8), 1662–1665 (Aug. 1998).

[148] D. Tamme, R. Schepe, and K. Henneberger, Comment on "Self-Consistent Calculations of Quasiparticle States in Metals and Semiconductors", Phys. Rev. Lett. **83**(1), 241 (July 1999).

[149] A. G. Eguiluz, Eguiluz Replies, Phys. Rev. Lett. **83**(1), 242 (July 1999).

[150] B. Holm, Total Energies from GW Calculations, Phys. Rev. Lett. **83**(4), 788–791 (July 1999).

[151] P. García-González and R. W. Godby, Self-consistent calculation of total energies of the electron gas using many-body perturbation theory, Phys. Rev. B **63**(7), 075112 (2001).

[152] M. Rohlfing and S. G. Louie, Electron-hole excitations and optical spectra from first principles, Phys. Rev. B **62**(8), 4927–4944 (Aug. 2000).

[153] S. Baroni, A. Dal Corso, S. de Gironcoli, and P. Giannozzi, 2001, `http://www.pwscf.org`.

[154] G. Kresse and J. Furthmüller, Efficient iterative schemes for ab initio total-energy calculations using a plane-wave basis set, Phys. Rev. B **54**(16), 11169–11186 (Oct 1996), `http://cms.mpi.univie.ac.at/vasp/`.

[155] G. Kresse and J. Furthmüller, Efficiency of ab-initio total energy calculations for metals and semiconductors using a plane-wave basis set, Comp. Mat. Sci. **6**(15) (1996).

[156] X. G. et al., First-principles computation of material properties: the ABINIT software project, Comp. Mat. Sci. **25** (2002), `http://www.abinit.org/`.

[157] SELF code, Andrea Marini, `http://www.fisica.uniroma2.it/~self/`.

[158] EXC code, Valerio Olevano, `http://www.bethe-salpeter.org/`.

[159] S. B. Zhang and J. E. Northrup, Chemical potential dependence of defect formation energies in GaAs: Application to Ga self-diffusion, Phys. Rev. Lett. **67**(17), 2339–2342 (Oct 1991).

[160] G. Cantele, E. Degoli, E. Luppi, R. Magri, D. Ninno, G. Iadonisi, and S. Ossicini, First-principles study of n- and p-doped silicon nanoclusters, Physical Review B (Condensed Matter and Materials Physics) **72**(11), 113303 (2005).

[161] G. M. Dalpian and J. R. Chelikowsky, Self-Purification in Semiconductor Nanocrystals, Physical Review Letters **96**(22), 226802 (2006).

[162] Q. Xu, J.-W. Luo, S.-S. Li, J.-B. Xia, J. Li, and S.-H. Wei, Chemical trends of defect formation in Si quantum dots: The case of group-III and group-V dopants, Physical Review B (Condensed Matter and Materials Physics) **75**(23), 235304 (2007).

[163] X. Luo, S. B. Zhang, and S.-H. Wei, Understanding Ultrahigh Doping: The Case of Boron in Silicon, Phys. Rev. Lett. **90**(2), 026103 (Jan 2003).

[164] L. G. Wang and A. Zunger, Phosphorus and sulphur doping of diamond, Phys. Rev. B **66**(16), 161202 (Oct 2002).

[165] G. Galli, Solid-state physics: Doping the undopable, Nature **436**, 32 (2005).

[166] C. Erwin Steven, Z. Lijun, I. Haftel Michael, L. Efros Alexander, A. Kennedy Thomas, and J. Norris David, Doping semiconductor nanocrystals, Nature **436**, 91 (2005).

[167] M. Lannoo, C. Delerue, and G. Allan, Screening in Semiconductor Nanocrystallites and Its Consequence for Porous Silicon, Phys. Rev. Lett. **74**(17), 3415–3418 (Apr. 1995).

[168] D. V. Melnikov and J. R. Chelikowsky, Quantum Confinements in Phosphorus-Doped Silicon Nanocrystals, Phys. Rev. Lett. **92**(4), 046802 (Jan. 2004).

[169] L. E. Ramos, E. Degoli, G. Cantele, S. Ossicini, D. Ninno, J. Furthmüller, and F. Bechstedt, Optical properties of doped Si nanocrystallites, Physical Review B, accepted (2007).

[170] L. E. Ramos, E. Degoli, G. Cantele, S. Ossicini, D. Ninno, J. Furthmüller, and F. Bechstedt, Structural features and electronic properties of group-III-, group-IV-, and group-V-doped Si nanocrystallites, Journal of Physics: Condensed Matter **19**(46), 466211 (12pp) (2007).

[171] Z. Zhou, M. L. Steigerwald, R. A. Friesner, and L. Brus, Structural and chemical trends in doped silicon nanocrystals: First-principles calculations, Phys. Rev. B **71**(24), 245308 (2005).

[172] B. I. Shklovskii and A. L. Efros, *Electron Properties of Doped Semiconductors*, Springer-Verlag, 1984.

[173] S. Ossicini, R. Magri, E. Degoli, M. Luppi, and E. Luppi, Surface and confinement effects on the optical and structural properties of silicon nanocrystals, SPIE Proc. **5222**, 1–11 (2003).

[174] I. Vasiliev, S. Ogut, and J. R. Chelikowsky, Ab Initio Absorption Spectra and Optical Gaps in Nanocrystalline Silicon, Phys. Rev. Lett. **86**(9), 1813–1816 (2001).

[175] Z. Zhou, R. Friesner, and L. Brus, Electronic Structure of 1 to 2 nm Diameter Silicon Core/Shell Nanocrystals: Surface Chemistry, Optical Spectra, Charge Transfer, and Doping, Journal of the American Chemical Society **125**(50), 15599–15607 (2003).

[176] P. Y. Yu and M. Cardona, *Fundamentals of Semiconductors*, Springer-Berlin, 2001.

[177] F. Trani, D. Ninno, G. Cantele, G. Iadonisi, K. Hameeuw, E. Degoli, and S. Ossicini, Screening in semiconductor nanocrystals: Ab initio results and Thomas-Fermi theory, Physical Review B (Condensed Matter and Materials Physics) **73**(24), 245430 (2006).

[178] R. M. Wentzcovitch, K. J. Chang, and M. L. Cohen, Electronic and structural properties of BN and BP, Phys. Rev. B **34**(2), 1071–1079 (Jul 1986).

[179] F. Bassani and G. P. Parravicini, *Electronic States and Optical Transitions in Solids*, Pergamon Press, New York, 1975.

[180] W. van Roosbroeck and W. Shockley, Photon-Radiative Recombination of Electrons and Holes in Germanium, Phys. Rev. **94**(6), 1558–1560 (Jun 1954).

[181] L. Hedin, New method for calculating the one-particle Green's function with application to the electron gas problem, Phys. Rev. **139**(3A), A796–A823 (Aug. 1965).

[182] F. Trani, D. Ninno, and G. Iadonisi, Role of local fields in the optical properties of silicon nanocrystals using the tight binding approach, Physical Review B (Condensed Matter and Materials Physics) **75**(3), 033312 (2007).

[183] F. Trani, D. Ninno, and G. Iadonisi, Tight-binding formulation of the dielectric response in semiconductor nanocrystals, Physical Review B (Condensed Matter and Materials Physics) **76**(8), 085326 (2007).

[184] O. Boyraz and B. Jalali, Demonstration of a silicon Raman laser, Opt. Express **12**(21), 5269–5273 (2004).

[185] F. Iori, E. Degoli, E. Luppi, R. Magri, I. Marri, G. Cantele, D. Ninno, F. Trani, and S. Ossicini, Doping in silicon nanocrystals: An ab initio study of the structural, electronic and optical properties, J. Lumin. **121**, 335–339 (Sept 2006).

[186] M. Hirao, in *Microcrystalline and Nanocrystalline Semiconductors*, edited by L. Brus, M. Hirose, R. W. Collins, F. Koch, and C. C. Tsai, volume 358 of *Mat. Res. Soc. Symp. Proc.*, MRS, 1995.

[187] C. Delerue, M. Lannoo, and G. Allan, Excitonic and Quasi Particle Gaps in Si Nanocrystals, Phys. Rev. Lett. **84**(11), 2457–2460 (Mar. 2000).

[188] C. Spataru, S. Ismail-Beigi, L. Benedict, and S. Louie, Quasiparticle energies, excitonic effects and optical absorption spectra of small-diameter single-walled carbon nanotubes, Appl. Phys. A **78**(8), 1129–1136 (May 2004).

[189] E. Chang, G. Bussi, A. Ruini, and E. Molinari, Excitons in Carbon Nanotubes: An *Ab Initio* Symmetry-Based Approach, Phys. Rev. Lett. **92**(19), 196401 (May 2004).

[190] M. Bruno, M. Palummo, A. Marini, R. D. Sole, V. Olevano, A. N. Kholod, and S. Ossicini, Excitons in germanium nanowires: Quantum confinement, orientation, and anisotropy effects within a first-principles approach, Phys. Rev. B **72**(15), 153310 (2005).

[191] M. Bruno, M. Palummo, A. Marini, R. D. Sole, and S. Ossicini, From Si Nanowires to Porous Silicon: The Role of Excitonic Effects, Phys. Rev. Lett. **98**, 036807 (jan 2007).

[192] L. Vina and M. Cardona, Effect of heavy doping on the optical properties and the band structure of silicon, Phys. Rev. B **29**, 6739–6751 (Jun 1984).

[193] A. Selloni and S. T. Pantelides, Electronic Structure and Spectra of Heavily Doped n-Type Silicon, Phys. Rev. Lett. **49**(8), 586–589 (Aug 1982).

[194] J. Wagner, Photluminescence and excitation spectroscopy in heavily doped n- and p-type silicon, Phys. Rev. B **29**, 2002–2009 (Feb 1984).

[195] Y. Z. Miguel Levy, P. Y. Yu and M. P. Sarachik, Photluminescence of heavily doped, compensated Si:P,B, Phys. Rev. B **49**(3).

[196] K. Thompson, J. H. Booske, D. J. Larson, and T. F. Kelly, Three-dimensional atom mapping of dopants in Si nanostructures, Applied Physics Letters **87**, 52108–52110 (2005).

[197] F. Buda, J. Kohanoff, and M. Parinello, Optical Properties of Porous Silicon: A First-Principles Study, Phys. Rev. Lett. **69**(8), 1272–1275 (Aug. 1992).

[198] A. J. Read, R. J. Needs, K. J. Nash, L. T. Canham, P. D. J. Calcott, and A. Qteish, First-principles calculations of the electronic properties of silicon quantum wires, Phys. Rev. Lett. **69**(8), 1232–1235 (Aug 1992).

[199] R. Rurali and N. Lorente, Metallic and Semimetallic Silicon ¡100¿ Nanowires, Physical Review Letters **94**(2), 026805 (2005).

[200] X. Zhao, Y. Liu, S. Inoue, T. Suzuki, R. O. Jones, and Y. Ando, Smallest Carbon Nanotube Is 3 Åin Diameter, Phys. Rev. Lett. **92**(12), 125502 (Mar. 2004).

[201] M. V. Fernandez-Serra, C. Adessi, and X. Blase, Surface Segregation and Backscattering in Doped Silicon Nanowires, Physical Review Letters **96**(16), 166805 (2006).

[202] A. B. Filonov, G. V. Petrov, V. A. Novikov, and V. E. Borisenko, Orientation effect in electronic properties of silicon wires, Applied Physics Letters **67**(8), 1090–1091 (1995).

[203] A. Singh, V. Kumar, R. Note, and Y. Kawazoe, Effects of Morphology and Doping on the Electronic and Structural Properties of Hydrogenated Silicon Nanowires, Nano Letters **6**(5), 920–925 (2006).

[204] J. Zhong and G. Stocks, Localization/Quasi-Delocalization Transitions and Quasi-Mobility-Edges in Shell-Doped Nanowires, Nano Letters **6**(1), 128–132 (2006).

[205] N. Fukata, J. Chen, T. Sekiguchi, N. Okada, K. Murakami, T. Tsurui, and S. Ito, Doping and hydrogen passivation of boron in silicon nanowires synthesized by laser ablation, Applied Physics Letters **89**(20), 203109 (2006).

[206] N. Fukata, J. Chen, T. Sekiguchi, S. Matsushita, T. Oshima, N. Uchida, K. Murakami, T. Tsurui, and S. Ito, Phosphorus doping and hydrogen passivation of donors and defects in silicon nanowires synthesized by laser ablation, Applied Physics Letters **90**(15), 153117 (2007).

[207] H. Peelaers, B. Partoens, and F. M. Peeters, Properties of B and P doped Ge nanowires, Applied Physics Letters **90**(26), 263103 (2007).

[208] C. A. Rozzi, D. Varsano, A. Marini, E. K. U. Gross, and A. Rubio, Exact Coulomb cutoff technique for supercell calculations, Phys. Rev. B **73**(20), 205119 (2006).

Ringraziamenti

Con l' ultima pagina di questa tesi, dopo tre anni intensi di dottorato trascorsi qui a Modena, si apre un nuovo capitolo. Un capitolo che quasi sicuramente sarà all' estero, lontano dall' Italia e dalla mia città ma che senza dubbio contribuirà ad arricchirmi e a farmi crescere. Durante questi tre anni ho avuto la fortuna di vivere situazioni completamente nuove in cui mai mi sarei visto come attore protagonista, di ritrovarmi in luoghi stranieri ma al tempo stesso resi familiari dal contatto con persone nuove diverse da me con cui confrontarmi. Ho iniziato davvero a "vedere il mondo", non solo attraverso gli occhi della Fisica, ma anche attraverso gli occhi delle persone che "fanno la fisica". Il mondo rappresentato dalla mia piccola città, sembra banale a dirlo, ma é realmente solo una minuscola, sebben importante, parte di ciò che mi circonda. Tutte queste magnifiche ed importanti esperienze le devo al mio gruppo di lavoro a Modena che mi ha ospitato e accolto prima per la tesi di laurea, quindi anche "sopportato" nei tre anni successivi per svolgere la mia tesi di dottorato. Dire semplicemente *grazie* può sembrare riduttivo ma la semplicità della parola racchiude tutta la mia gratitudine ed affetto per il prof. Stefano Ossicini: perché mi ha fatto da guida nel campo della fisica del Silicio!! con grande professionalità ed onestà, perchè riesce sempre ad accompagnare la serietà sul lavoro non solo ad una profonda sensibiltà ed umanità nei rapporti personali, ma anche ad una accattivante curiosità per il mondo attorno, scienza, fatti e persone. Suoi sono gli incoraggiamenti e sue le opportunità offerte attraverso i tanti progetti scritti che mi hanno consentito davvero di crescere, di affacciarmi alla vita. A Stefano va tutto il mio affetto e la mia grande stima di cuore. Il mio grazie é per Elena che mi ha sempre supportato come "capo piccolo" ma anche come amica; per Ivan con cui si ride, si discute, si parla di fotografia, di politica, di precarietà (sic). Grazie a Roberto per la cordialità

sempre dimostrata e gli pseudo fatti e l'appoggio e le chiacchere! Vi voglio bene come ad una famiglia.
Un grazie sentito per le persone con cui ho avuto la fortuna di lavorare insieme e che hanno davvero contribuito in modo prezioso al mio lavoro di tesi, Olivia e Maurizia a Roma e Giovanni a Napoli. A Lucia e Christine per la pazienza con i "fiori" e per la meravigliosa possibilità offerta per il prossimo postdoc in Paris. C'est tres chic!

Voglio poi qui ricordare le altre persone che mi hanno *fatto stare bene* in questi anni al Dipartimento di Fisica, che hanno colorato le giornate davanti al computer o durante le conferenze. I miei *compagni di merende*, Lorenzo ed Enzo, (pure la rima ho fatto!) e Deborah e Valentina che condividono lo studio con me. Vi debbo tanto. Tutti gli altri ragazzi che ho conosciuto in questi 3 anni, alcuni sono ormai lontani da Modena (ma ci ricontreremo per il mondo) altri sono ancora qui: Cando (sempre vicino da una vita, anche se le strade si allontanano il filo rosso non si spezzerà), Stefania, Diego, Ghiro, Benedetta (one dollar one beer!) e Andrea (la strana coppia?!), David, Daniele, Andrea Ferretti, i "tritoni" Giulio-Emiliano-Marcello (tovaric!), Gianmarco e i mitici bitter a mezzanotte allo Juta, la punta d'attaco della squadra, brasileira Rosangela, Valerio, Andrea Vanossi, Davide, Elisa e MariaGrazia, Layla e Francesco e Marco, Maddalena, Max. Quante risate...si perché qui ho trovato amici cordiali, carini e gentili, e questo sarà il piùn bel ricordo che porto con me nel salutarvi tutti.

A coloro che sono a Parigi e che presto raggiungerò, Eleonora e Matteo, l'amicizia e il calore che mi avete trasmesso, lo sapete, rimangono un punto saldo e fermo. A bien tot!

Concludo dedicando questo lavoro alla mia famiglia, alle persone che più mi sono state vicino e che più mi stanno amando. La mamma e il papà, Gisella e Umberto, che mi hanno assecondato e incoraggiato in tutte le scelte e in tutte le esperienze, lungimiranti e pieni di fiducia, che mi hanno e mi sostengono senza cedimenti, come hanno fatto i miei nonni, Benilde e Gino in tutti gli anni preziosi trascorsi assieme. Vi abbraccio. A Francesca, che non solo ha pensato bene di condividere la fisica con me e pure i passi della vita! Che si dimostra una persona speciale anche nelle scelte difficili ed impegnative da me prese. Con affetto e riconoscenza.

A tutte le persone che mi hanno accompagnato fino a qui con affetto.
A tutte quelle che mi accompagneranno.

Federico